JAIST Repository
https://dspace.jaist.ac.jp/

Title	サクランにおける機能性ナノ粒子の形成とハイブリッド化
Author(s)	Saosamniang, Pruetsakorn
Citation	
Issue Date	2024-09
Type	Thesis or Dissertation
Text version	ETD
URL	http://hdl.handle.net/10119/19397
Rights	
Description	Supervisor: 松村 和明, 先端科学技術研究科, 博士

JAIST
JAPAN
ADVANCED INSTITUTE OF
SCIENCE AND TECHNOLOGY

Japan Advanced Institute of Science and Technology

Doctoral Dissertation

Functional Nanoparticle Formation in Sacran and Hybridization

Pruetsakorn SAOSAMNIANG

Supervisor: Kazuaki Matsumura

Graduate School of Advanced Science and Technology

Japan Advanced Institute of Science and Technology

Materials Science

September 2024

Referee-in-chief: Professor Dr. Kazuaki Matsumura
Japan Advanced Institute of Science and Technology

Referees: Associate Professor Dr. Kosuke Okeyoshi
Japan Advanced Institute of Science and Technology
Professor Dr. Masayuki Yamaguchi
Japan Advanced Institute of Science and Technology
Professor Dr. Toshiaki Taniike
Japan Advanced Institute of Science and Technology

External referee: Professor Dr. Pakorn Opaprakasit
Sirindhorn International Institute of Technology

Abstract

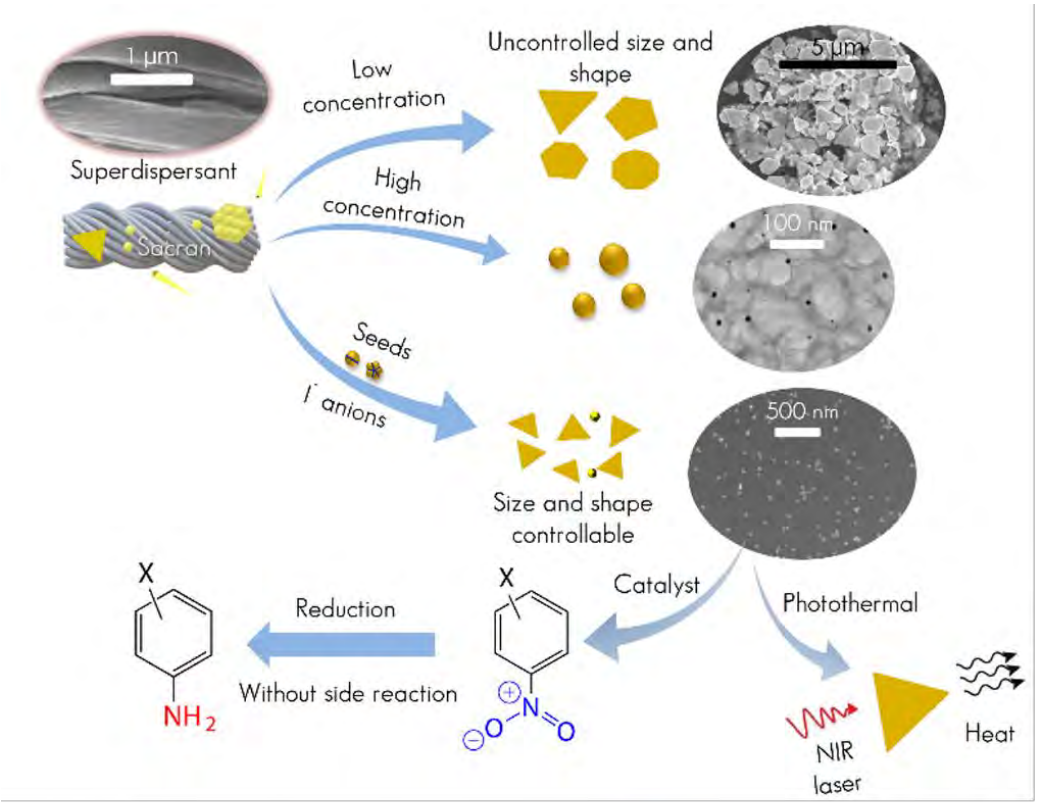

Graphical abstract

The size and shape of nanoparticles play a pivotal role in determining their properties and applications. Gold nanotriangles (AuNTs), in particular, exhibit anisotropic electrical conductivity, generating potent electric field enhancements at their vertices and surface plasmon resonance (SPR) in the near-infrared (NIR) region. These distinctive attributes render them exceptionally promising across various fields, including catalysis, sensors, cancer therapy, and as robust substrates for surface-enhanced Raman spectroscopy (SERS). The most effective method documented in the literature for synthesizing nanoparticles with high yields involves template-assited synthesis, where a surfactant is used as the morphology-controlling agent. However, the toxicity of some surfactants highlights the need to establish a green synthesis process for AuNPs that ensures both high yield and precise control over shape and size distribution. The complexity arising from various components, such as reducing and stabilizing agents found in bio-products, presents a challenge for nanoparticle synthesis.

Polysaccharides are the most abundant group of bio-products. Despite their prevalence, there have been limited studies in recent decades investigating the utilization of pure polysaccharides for synthesizing Au nanoplates, and these studies often lack elucidation on the factors influencing nanoparticle shape control. The anisotropic shape formation are strongly affected by the hydroxyl or caboxyl functional groups in polysaccharide. Sacran is one of the fascinating cyanobacteria polysaccharide that is extracted from the freshwater cyanobacteria Aphanothece sacrum. It possesses remarkable attributes, including its high molecular weight (10^6 – 10^8 g mol^{-1}) and a composition comprising more than ten types of sugars. Unlike other polysaccharides, sacran contains two types of anions, carboxylic acid and sulfate groups (22 mol% and 11 mol% to sugar residues in total, respectively), as well as neutral hexose and pentose units. The 11,000 sulfates efficiently attract cations in water, while the 22,000 carboxylates strongly bind with them. Sacran also posseses other functional groups, such as –OH and $–NH_2$, which likely influence the control of AuNPs shape. In addition, ultrahigh dispersion properties of sacran have been demonstrated using carbon-nanotubes. These multifunctional characteristics motivated us to investigate the development of AuNPs in the presence of sacran.

This study investigates a method for inducing morphological changes in anisotropic AuNPs using sacran and elucidates its mechanism. Initially, the morphology of anisotropic AuNPs was manipulated by varying the concentration of sacran-to-gold precursor to influence

the shape outcomes. While this approach did not afford complete control over the morphologies of anisotropic AuNPs, it did enable size control over specific morphologies at particular operating temperatures. Subsequently, controlled morphologies of Au nanoplates were attained by employing seeds and halide anions as shape-directing agents, ensuring high shape purity. **This green synthesis of AuNPs holds significant potential as an eco-friendly catalyst and shows promise for diverse applications in plasmonic photothermal therapy and biomedicine.**

Another invesion was focused on the synthesis of ZnO nanocomposite materials. Sacran, a supergiant polysaccharide, serves as a green reducing agent for the formation of ZnO nanoparticles (NPs) within the sacran matrix. The incorporation of ZnO NPs significantly influences the physicochemical properties of the resulting xerogels. The liquid crystalline structure of sacran contributes to the formation of anisotropic xerogels. Through systematic studies, including swelling behavior analysis and mechanical testing, the impact of various parameters, such as pH variations and DVS-to-OH ratios, on the performance of sacran-ZnO nanocomposite xerogels is thoroughly evaluated. Additionally, cell viability studies using A549 cancer cells shed light on the biocompatibility and potential use of these nanocomposite xerogels as wound dressing. The comprehensive characterization and evaluation presented in this chapter provide valuable insights into the development of sacran-based materials for biomedical applications.

Keywords: Sacran Polysaccharide, Gold nanoplates, Shape controller, Cancer selective, Photothermal therapy.

Acknowledgements

I am deeply thankful to Professor Tatsuo Kaneko, my former thesis advisor, and Professor Kazuaki Matsumura, my current thesis advisor, for their exceptional mentorship, steadfast encouragement, and valuable insights during this research endeavor.

I express my heartfelt gratitude to the members of the committee, with special gratitude to my minor research advisor, Professor Goro Mizutani, whose guidance proved invaluable throughout the minor research. I also express gratitude to Associate Professor Dr. Kosuke Okeyoshi, Professor Dr. Masayuki Yamaguchi, and Professor Dr. Toshiaki Taniike at JAIST for serving as my committee members during the pre-defense examination. Their dedicated time and invaluable advice during the defense were pivotal to the successful completion of this thesis.

During my research journey at JAIST, I extend my heartfelt gratitude to my second supervisor, Professor Toshiaki Taniike, and Senior Lecturer Kenji Takada, for their invaluable suggestions and generous assistance. I also appreciate all my colleagues at the Kaneko lab for their assistance and encouragement.

Above all, I am profoundly grateful to my family for their unwavering support and encouragement throughout the challenges and successes of my academic journey.

Pruetsakorn Saosamniang

Contents

CHAPTER I
GENERAL INFORMATION

1.1. Bio-products as the reducers for anisotropic gold nanoparticles

Various components derived from natural sources, particularly bio-products, contribute significantly to the reduction of the gold precursor. These bio-products, including plant extracts, green reactants, nitrogen compounds, surfactants, and carboxylate compounds, play a crucial role in this process.[1] The formation of anisotropic gold nanoparticles (AuNPs) depends on various key parameters, encompassing **reactant components, concentration, reaction time, pH, temperature, and the effects of external ions.** In this study, we elucidate the contribution of several bio-products to the formation of anisotropic AuNPs. Table 1.1 illustrates various bio-products contributing to nanoparticle formation. These approaches often yield a variety of AuNP outcomes, indicating the need for further refinement of reaction conditions.

Achieving reproducibility in bio-synthesis methodologies employing natural sources presents a common challenge.[2] This arises due to the diverse conditions under which plants are grown and the varied protocols employed for extraction. These variables, including environmental factors, geographical location, growth conditions, and extraction techniques, introduce uncertainties that can significantly impact nanoparticle growth.[3] While the use of natural products has a low environmental impact, the presence of multi-components or residual small molecules after extracting natural products may influence the shape outcome of nanoparticles, posing a challenge in discerning the specific components or molecules that contribute to shaping outcomes. Furthermore, achieving good uniformity and purity of anisotropic AuNPs proves challenging.

Table 1.1 Diversity of Anisotropic AuNPs generated by different bio-products.

Extraction Source	Reducing or Stabilizing Agent	Shape outcome	Size (nm)	Reference
Plant extracts	*Artemisia dracunculus*	Triangles, Hexagons, Spherical	35-50	[4]
Plant extracts	Bael gum	Triangles, Hexagons, Spherical	250-700	[5]
Plant extracts	Flavonoid derivatives	Triangles, Hexagons, Spherical, Cubes, Rectangles	5.86-17.54	[6]
Plant extracts	Red beetroot	Triangles, Icosahedra, Spherical	50-65	[7]
Green reactants	Hordenine	Quasi spherical, Triangles, Hexagons,	130-140	[8]
Green reactants	Carboxymethyl cellulose	Triangles, Spherical	8.9-94	[9]
Extraction Source	**Reducing or Stabilizing Agent**	**Shape outcome**	**Size (nm)**	**Reference**
Green reactants	Cinnamon	Spherical, Triangles, Hexagons,	17	[10]
Green reactants	Chitosan	Triangles	30	[11]
Nitrogen compounds	Serum albumin	Quasi spherical	67	[12]
Nitrogen compounds	PVP	Spherical, Triangles, Hexagons,	75	[13]
Surfactants	Oleylamine	Nanorods	5-20	[14]
Carboxylate compounds	Oxalic acid	Dodecahedral	58-64	[15]

Subsequently, we aim to present a concise overview of the critical parameters influencing the anisotropic growth of AuNPs in various shapes, as previously described. This understanding constitutes a valuable toolkit for advancing the development of innovative synthesis methods.

Reactant components play a crucial role in the reduction of AuNPs which involves a complex interplay of various factors in influencing the outcome. The process typically utilizes green reactants or plant extracts containing secondary metabolites such as glycosides, amino acids, flavonoids, alkaloids, saponins, tannins, steroids, carbohydrates, and other compounds with phenolic groups.

1. **Reduction Potential:** Many of the aforementioned reactant components possess inherent reduction potentials. The potential reducing agents should have the reduction potential between the reduction of $HAuCl_4$ to Au^0 and the oxidation of Au^0 to Au^+. These organic compounds can act as reducing agents, facilitating the conversion of gold ions (Au^{3+}) to metallic gold (Au^0), which leads to the formation of AuNPs.

2. **Stabilization and Capping:** Some reactant components also contribute to the stabilization and capping of the formed AuNPs. Certain compounds have affinity for the nanoparticle surface, creating a protective layer that helps prevent aggregation and stabilizes the particles in solution.

3. **Nucleation and Growth:** The presence of specific reactant components can influence the nucleation and subsequent growth stages of AuNPs. These components may act as nucleation sites or growth modifiers, affecting the size and shape of the nanoparticles formed during the process.

4. **Chemical Environment:** The chemical environment created by the reactant components, including factors like pH and temperature, plays a significant role in determining the reduction kinetics and the resulting morphology of the AuNPs.

5. **Surface Chemistry:** The functional groups of the reactant components can interact with the gold ions and the growing nanoparticles, influencing the surface chemistry of the AuNPs. This, in turn, affects their physicochemical properties and potential applications.

The effect of pH also promotes different AuNPs morphologies and referred to as the important factor in green synthesis. For example, the pH level affects the protonation and deprotonation of functional groups on the surface of reactant components and nanoparticles. This, in turn, influences the binding affinities of these groups, which play a role in directing the anisotropic growth of AuNPs. For example, acidic conditions can alter the reduction kinetics of

gold ions. The presence of excess protons in an acidic environment can influence the rate of the reduction reaction, leading to controlled nucleation and growth processes. This control over the reaction kinetics is crucial for achieving anisotropic shapes.

The influence of temperature stands out as a crucial parameter directly impacting the production kinetics of gold nanoparticles (AuNPs), thereby shaping the mechanisms governing particle growth. Changes in temperature during the synthesis process significantly affect the length, and width of gold nanorods. For instance, at temperatures ranging from 21 to 35 °C, lower temperatures yield smaller nanorods in terms of length and diameter. This phenomenon is linked to the activation energy required to initiate particle growth. Specifically, the process involves the deposition of a gold atom at one end of the rod, followed by migration to the sides to attain the desired morphology.[16]

The growth of anisotropic gold nanoparticles (AuNPs) is notably influenced by **the presence of external ions**, such as halide anions. Existing literature suggests that the introduction of iodide or bromide ions induces a transformation of gold precursor or $[AuCl_4]^-$ into $[AuCl_{4-x}X_x]^-$, ultimately progressing toward the more stable $[AuX_4]^-$, where X = I^- or Br^- ions.[17] It is noteworthy to emphasize the steric hindrance effect arising from the partial or complete substitution of Cl^- by X^-, significantly impacting the anisotropic growth process. This steric hindrance effect results in the formation of $[AuCl_{4-x}X_x]^-$, where $0 < x \leq 4$, as illustrated in the following chemical reaction (Eq. (3)):

$$[AuCl_4]^-_{(aq)} + xKX_{(aq)} \rightarrow [AuCl_{4-x}X_x]^-_{(aq)} + xKCl_{(aq)} \quad (3)$$

In the growth process of anisotropic gold nanoparticles (AuNPs), bromide and iodide ions are well-established contributors, while the roles of chlorine and silver ions have also garnered significance. The presence of Cl^- and Ag^+ ions play crucial roles in synthesizing Au nanoarrows. Specifically, Ag+ ions have been observed to induce the formation of pyramidal heads exposing (1 1 1)[18] facets. On the other hand, Cl^- ions primarily form Au^+Cl^- complexes, characterized by a higher reduction potential. This facilitates favorable kinetic pathways for cetyltrimethylammonium chloride (CTAC), promoting growth along the four (110) directions.[19]

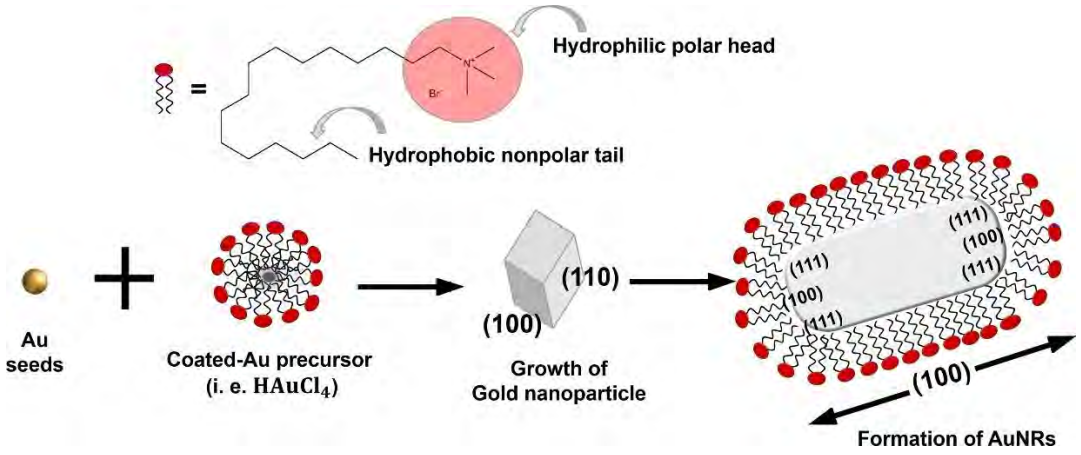

Fig.1. The example of growth mechanism of gold nanorods in 100 direction by using CTAC.

In summary, green reactants and plant extracts serve dual roles as both reducing and stabilizing agents in the formation of anisotropic gold nanoparticles (AuNPs). While certain green reactants and plant extracts have been extensively studied for their chemical structures and their roles in the growth mechanisms of AuNPs, the majority of plant extracts remain inadequately characterized regarding their components and chemical structures. This lack of comprehensive knowledge poses challenges in identifying specific components responsible for shaping AuNPs. Additionally, issues such as the purity and uniformity of the resulting shapes prove challenging to control when using green reactants. To address these concerns, we propose exploring strategies to mitigate these challenges by introducing well-known green reactants or plant extracts with defined structures for the production of anisotropic AuNPs.

1.2. Polysaccharides as the reducers for gold nanoparticles

Polysaccharides are frequently utilized in the construction of bio-nanocomposites for various applications. Derived from natural sources, polysaccharides offer significant advantages such as low toxicity and biodegradability. These versatile biomaterials can be classified into three categories based on their ionic properties: neutral examples include Starch, Dextran, Agarose, and Pullulan; anionic, represented by Gum Arabic, Carrageenan, Alginate, Heparin, and Hyaluronan; cationic, typified by Chitosan. The ionic nature of the utilized polysaccharide imparts distinct properties and chemical functionalities to the resulting nanocomposites, making them superior biological macromolecules.[20] To synthesize anisotropic AuNPs, polysaccharides must be carefully selected based on their intended

purposes. The main selective factors include (a) stability and solubility, (b) toxicity, biodegradability, and biocompatibility, and (c) surface charge characteristics. Most commonly use polysaccharides for AuNPs synthesis has been displayed in Fig.2. and their applications in Table.2.

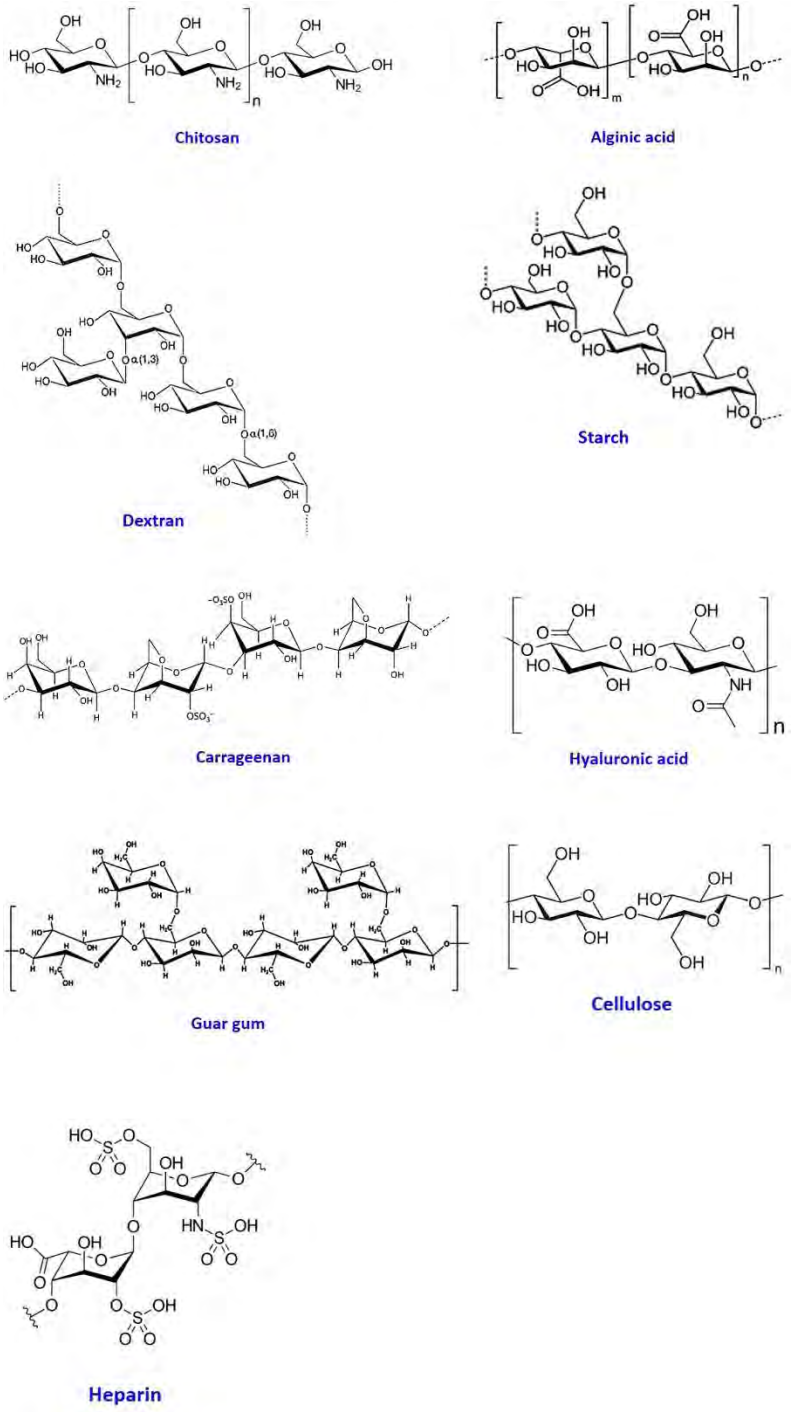

Fig.2. Structural diagrams of polysaccharides employed in gold nanoparticle synthesis.[21]

Table 2. A brief summary of polysaccharides roles for AuNPs synthesis and their applications.[21]

Polysaccharide	Role	Particle size (nm)	Application	References
Heparin	Reducer/stabilizer	12–52	n.d.	Guo et al., 2008
	Reducer/stabilizer	14 ± 4	Raman activity and photochemical reduction	Maria et al., 2014
	Reducer/stabilizer	20–300	n.d.	Rodríguez-Torres et al., 2014
	Reducer/stabilizer	20	Enhancement of computed tomography images	Sun et al., 2009
	Reducer/stabilizer	10 ± 3	Anticoagulant activities	Kemp et al., 2009b
	Reducer/stabilizer	10 ± 3	Anti-angiogenesis	Kemp et al., 2009a
	Reducer/stabilizer	14 ± 4	Acceleration of cell disorders in cancer and inflammatory diseases	Melissa et al., 2015
Chitosan	Reducer/stabilizer	10–1000	Penetration enhancer for proteins and vaccines	Huang and Yang 2004
	Reducer/stabilizer	10–50	Nano-carrier for insulin	Bhumkar et al., 2007
	Reducer/stabilizer	n.d.	Analysis of amino acids by surface-enhanced Raman scattering	Potara et al., 2009
	Reducer/stabilizer	n.d.	Antibacterial and catalytic properties	Wang et al., 2013
	Trisodium citrate as reducer Chitosan as stabilizer	2–200	Detection the concentration of heparin	Chen et al., 2013
	Trisodium citrate as reducer Chitosan as stabilizer	19–26	Anticancer drug delivery	Aldea et al., 2018
	Sodium borohydride as reducer Chitosan as stabilizer	10.2 ± 2.9	Drug delivery	Yazid et al., 2014
	Reducer/stabilizer ultrasonic assistance	34.5	n.d.	Wu et al., 2014
Hyaluronic acid (HA)	Reducer/stabilizer via thermal treatment	5–30	n.d.	Kemp et al., 2009b
	Sodium borohydride as reducer HA as stabilizer	98 ± 18	Imaging of urothelial tissue	Guelfi et al., 2017
	2-Propanol as reducer HA as stabilizer	17.9	Promoters of skin recovery	Cardenas et al., 2017

Polysaccharide	Role	Particle size (nm)	Application	References
Carrageenan	Sodium borohydride as reducer carrageenan as stabilizer	n.d.	Hydrogels	Infante-Rivera et al., 2012
	Reducer/stabilizer	120	Enhancement of the electrochemical response of conductive polymers	Farias et al. 2017
	Reducer/stabilizer	35 ± 8	In-vitro antitumor activities on colorectal cancer and breast cancer	Chen et al., 2018
Guar gum	Reducer/stabilizer	5–25	Optical sensor for detection of aqueous ammonia	Pandey et al., 2013
	Reducer/stabilizer under microwave irradiation	12.78 ± 4.26	Targeted drug delivery for colon cancer	Ganeshkumar et al., 2018
	Reducer/stabilizer	2.26–27.1	Biocidal activities	Ahmed, 2019
Alginic acid	Reducer/stabilizer under UV-radiation	10	Catalytic reactivities	Saha et al., 2010
	Amino-poly-carboxylic acids-alginate composite reducer/stabilizer	15–20	Biosensing	Malkar et al., 2015
	Sodium alginate-g-poly-(*N*,*N*-dimethyl acrylamide-co-acrylic acid) as reducer/stabilizer	n.d.	Antimicrobial activity	Kolya et al. 2015
	Reducer/stabilizer under microwave irradiation	150–185	n.d.	Valdez and Gómez, 2016
	Oxidized alginate as reducer/stabilizer	0.7 ± 1.1	n.d.	Ahmed et al., 2016
	Reducer/stabilizer	n.d.	Heterogeneous catalyst	Li et al., 2015
Starch	Reducer/stabilizer	n.d.	Detection concentration of α-amylase	Deka et al., 2008
	Buffered glucose and starch as reducer/stabilizer	4 ± 1	Bio-electrochemistry	Engelbrekt et al., 2009
	Hydrazine as reducer Starch and ethylene glycol as stabilizers	3.5	n.d.	Hussain et al., 2009
	Reducer/stabilizer	11.7	Catalytic and antimicrobial actions	Emam et al. 2016
	Reducer/stabilizer	10	Heterogeneous catalyst	Chairam et al. 2017

Polysaccharide	Role	Particle size (nm)	Application	References
Dextran	Carboxylated dextran as reducer/stabilizer	n.d.	Biosensing	Lee et al., 2005
	Aminated dextran as reducer/stabilizer	n.d.	Biosensing	Ma et al., 2005
	Aminated dextran as reducer/stabilizer	20	n.d.	Morrow et al., 2009
	Reducer/stabilizer under ultrasonic irradiation	13.6 ± 1.4	Colorimetric detection of dihydralazine sulfate	Wang et al., 2010
	Reducer/stabilizer under gamma irradiation	6–35	n.d.	Diem et al., 2017
	Reducer/stabilizer	12.1	n.d.	Tang et al., 2017
Cellulose and its derivatives	Cellulose nano-crystals reducer/stabilizer	n.d.	Catalytic purposes	Wu et al., 2014
	Amidoxime surface functionalized bacterial cellulose as reducer/stabilizer	n.d.	Catalytic purposes	Chen et al., 2015
	Unbleached kraft pulp as reducer/stabilizer	12–21	n.d.	Bumbudsanpharoke et al., 2015
	Extracted cellulose as reducer/stabilizer	26.1	Catalytic reactivity	Emam et al., 2017
	Viscose fibers as reducer/stabilizer	14–100	Anti-pathogenic action	Emam et al., 2017
	Carboxymethylated cellulose as reducer/stabilizer	8.8–14.0	Catalytic reactivity	Emam and Ahmed, 2017

n.d. not determined.

As presented in Table 2, polysaccharides are extensively employed as biological macromolecules in the synthesis of AuNPs due to their biocompatibility, non-toxic nature, and hydrophilicity. Additionally, they possess unique functional chemical groups that can serve as scaffolds for creating multifunctional systems by introducing reactive and bioactive groups onto composite surfaces. Polysaccharides find valuable applications in hydrogels, forming nanogels with various types of nanometals. These resulting nanogels can be utilized in biosystems responsive to physiological changes in mechanical stress, temperature, and pH. Certain polysaccharides, featuring hemi-acetal and hydroxyl groups, act as reducers in the metal precursor reduction process, yielding desired nanoparticle outcomes. On the other hand, polysaccharides with amino

groups can bind to the surface of the produced nanoparticles, creating a surrounding layer of hydrophilic molecules.[22]

In conclusion, polysaccharides emerge as versatile and effective agents in the synthesis of gold nanoparticles (AuNPs), serving dual roles as both reducers and stabilizers. The unique chemical functionalities of polysaccharides, including hydroxyl, amine, sulfate, and carboxyl groups, contribute to their multifaceted involvement in the reduction of gold precursors and the stabilization of resulting nanoparticles. The concentration of polysaccharides plays a pivotal role in influencing nucleation, growth kinetics, and the ultimate shape outcomes of AuNPs. Additionally, polysaccharides contribute to the prevention of particle aggregation and the maintenance of colloidal stability. Their ability to selectively bind to specific crystal facets further allows for the tailored control of nanoparticle shapes. Moreover, the high biocompatibility and low toxicity of polysaccharides make them particularly attractive for various biomedical and environmental applications. As we continue to unveil the intricate mechanisms behind polysaccharide as the reducing and stabilizing for AuNPs formation, the prospects for innovative and sustainable nanomaterial design remain promising.

1.3. Sacran supergiant polysaccharide as the reducers for anisotropic gold nanoparticles

Sacran, a supergiant water-soluble cyanobacterial polysaccharide, has been a focal point of our group's research for over 15 years.[23, 24] Comprising approximately 100,000 monosaccharides, Sacran incorporates two types of anions-carboxylic acid and sulfate groups (constituting 22 mol% and 11 mol% of the total sugar residues, respectively). Additionally, neutral hexose and pentose are present, showcasing a diverse array of sugar residues, including galactose, glucose, xylose, mannose, fucose, galacturonic acid, rhamnose, and glucuronic acid (as illustrated in Fig. 3). Traces of uronic acid, galactosamine, alanine, and sulfated muramic acid (approximately 1.0%) are also found, as depicted in Fig. 4. Sacran has found applications in various fields such as anti-inflammatory treatments,[25] transdermal drug carrier,[26] and metal adsorption.[27] Notably, sacran exhibits an exceptionally high molecular weight exceeding 10^7 g/mol, surpassing that of other reported polysaccharides to date.[28]

Sacran exhibits a unique structure with 11,000 sulfates efficiently attracting cations in water, while 22,000 carboxylates strongly bind with them. The additional functional groups of sacran, such as –OH and $–NH_2$, are anticipated to play a significant role in controlling the shape of AuNPs. Multiple –OH groups possess the capability to lower the redox potential, thereby enhancing their effectiveness in reducing gold ions. Moreover, these groups contribute to the colloidal stability of the nanoparticles. Concurrently, the lone electron pairs of $–NH_2$ groups interact or bind with the surface Au(0) atoms of the nanoparticles, promoting the formation of an Au(0) flat surface. This effect is facilitated by the steric hindrance from sacran's supergiant molecular structure.[29, 30] Additionally, the ultrahigh dispersion properties of sacran have been successfully demonstrated with carbon nanotubes.[31]

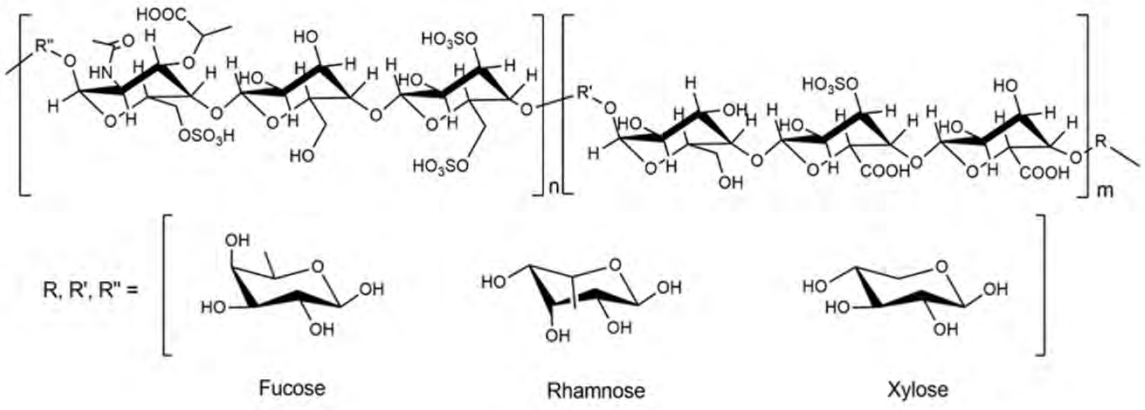

Fig. 3. Main structure of megamolecular polysaccharide, sacran, with anionic groups of sulfates and carboxylates.

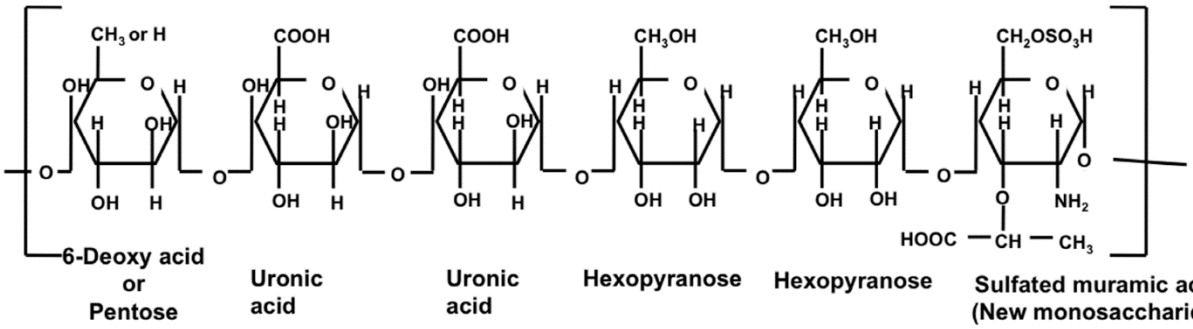

Fig. 4. Schematic illustration of the partial structure of sacran chains with the sugar residue and traces.[32]

To manipulate the outcomes of AuNPs shapes, one can adjust the concentration of sacran. The concentration of this supergiant polysaccharide can significantly impact the nucleation and growth processes during AuNPs synthesis. Higher concentrations may alter the rate of nucleation, influencing the number of nuclei formed and subsequently affecting the growth kinetics. Sacran serves as a stabilizing agent in the synthesis of AuNPs, and its concentration plays a crucial role in stabilizing the nanoparticles by forming a protective coating on their surfaces. Maintaining optimal concentrations is essential to prevent particle aggregation and ensure uniform growth. The concentration of sacran can also influence the sizes of resulting particles; for instance, higher concentrations may lead to the formation of smaller nanoparticles, while lower concentrations might result in larger particles. Different concentrations may favor the growth of specific crystal facets, consequently leading to the formation of distinct shapes. The concentration-dependent outcomes in shape are pivotal for tailoring the properties of the nanoparticles for various applications. Additionally, the concentration of sacran can impact the reduction potential, influencing its ability to effectively reduce gold ions and form nanoparticles. Maintaining optimal concentrations is necessary to achieve controlled and reproducible reduction.

The conformational dependence of sacran chains serves as a potential template for supporting AuNPs. Previous studies have reported critical concentrations in sacran aqueous solutions, with an overlap concentration (c^*) of approximately 0.004 wt% and an entanglement concentration (c_e) of about 0.015 wt%. Within the concentration range of 0.02 to 0.09 wt%, sacran chains have numerous opportunities to overlap without forming associations.[33] However, when the concentration exceeds 0.09 wt%, sacran chains adopt double-helical and rigid structures. At 0.25 wt%, the aqueous sacran solution enters a sol-gel critical state phase due to increased chain entanglement and fractions. Furthermore, a nematic liquid crystal (LC) phase appears to form at approximately 0.5 wt%, as illustrated in Fig. 5.

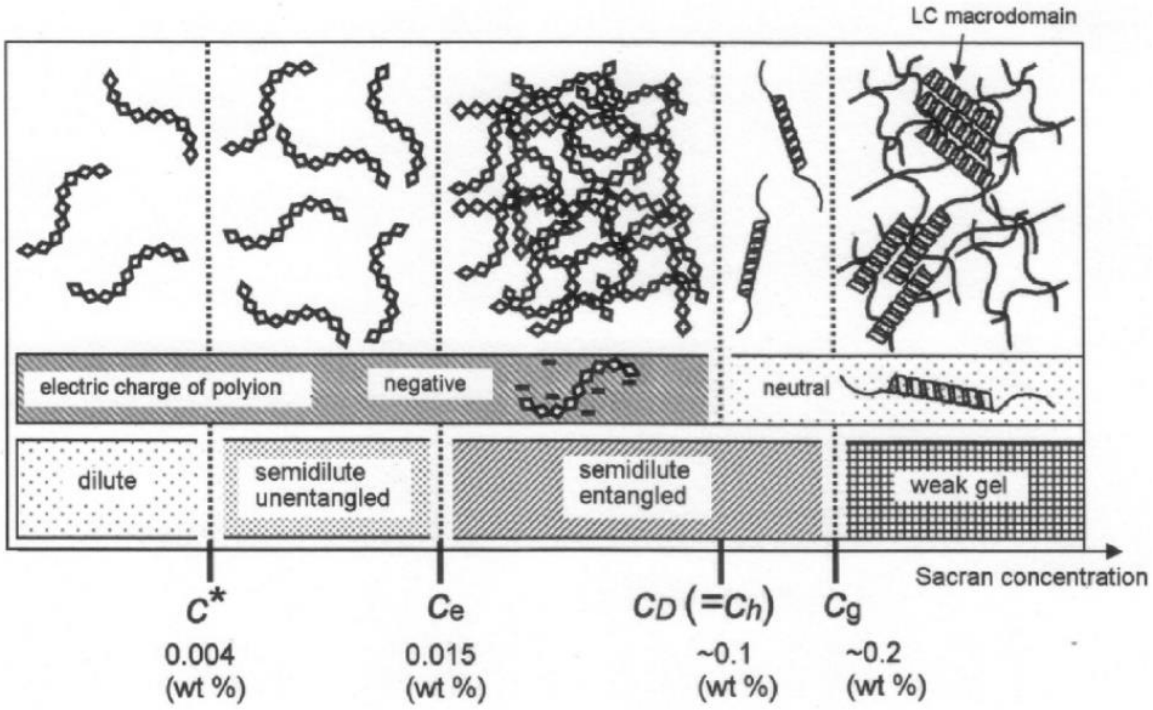

Fig. 5. Schematic illustrations representing the chain conformation of sacran in salt-free solutions [(c^*) overlap concentration, (c_e) entanglement concentration, (c_D) critical polyelectrolyte solution, (c_h) helix transition concentration, (c_g) gelation concentration].[33]

1.4. Objectives

As previously highlighted, sacran exhibits promising potential as both a reducing and stabilizing agent for AuNPs. The multifunctional nature of sacran has spurred our interest in exploring its role in guiding the development of AuNPs within a sacran medium. Our investigation aims to delve into how sacran influences anisotropic growth and identify the key parameters requiring control. Additionally, we will devise methodologies to enhance the precision and uniformity of AuNPs shapes, paving the way for their utilization as advanced materials.

1.5. References

1. Vijayan, R.; Joseph, S.; Mathew, B., Indigofera tinctoria leaf extract mediated green synthesis of silver and gold nanoparticles and assessment of their anticancer, antimicrobial, antioxidant and catalytic properties. *Artificial Cells, Nanomedicine, and Biotechnology* **2018,** *46* (4), 861-871.
2. Nadeem, M.; Abbasi, B. H.; Younas, M.; Ahmad, W.; Khan, T., A review of the green syntheses and anti-microbial applications of gold nanoparticles. *Green Chemistry Letters and Reviews* **2017,** *10* (4), 216-227.
3. Santhoshkumar, J.; Rajeshkumar, S.; Venkat Kumar, S., Phyto-assisted synthesis, characterization and applications of gold nanoparticles – A review. *Biochemistry and Biophysics Reports* **2017,** *11*, 46-57.
4. Wacławek, S.; Gončuková, Z.; Adach, K.; Fijałkowski, M.; Černík, M., Green synthesis of gold nanoparticles using Artemisia dracunculus extract: control of the shape and size by varying synthesis conditions. *Environmental Science and Pollution Research* **2018,** *25* (24), 24210-24219.
5. Balasubramanian, S.; Raghavachari, D., Green Synthesis of Triangular Au Nanoplates: Role of Small Molecules Present in Bael Gum. *ACS Sustainable Chem. Eng.* **2017,** *5* (11), 10317-10326.
6. Osonga, F. J.; Yazgan, I.; Kariuki, V.; Luther, D.; Jimenez, A.; Le, P.; Sadik, O. A., Greener synthesis and characterization, antimicrobial and cytotoxicity studies of gold nanoparticles of novel shapes and sizes. *RSC Adv.* **2016,** *6* (3), 2302-2313.
7. Deokar, G. K.; Ingale, A. G., Unveiling an unexpected potential of beetroot waste in green synthesis of single crystalline gold nanoplates: A mechanistic study. *Arabian Journal of Chemistry* **2018,** *11* (6), 950-958.
8. Rajkumari, J.; Meena, H.; Gangatharan, M.; Busi, S., Green synthesis of anisotropic gold nanoparticles using hordenine and their antibiofilm efficacy against Pseudomonas aeruginosa. *IET Nanobiotechnology* **2017,** *11* (8), 987-994.
9. Emam, H. E.; Ahmed, H. B., Carboxymethyl cellulose macromolecules as generator of anisotropic nanogold for catalytic performance. *Int. J. Biol. Macromol.* **2018,** *111*, 999-1009.
10. Goyal, D.; Saini, A.; Saini, G. S. S.; Kumar, R., Green synthesis of anisotropic gold nanoparticles using cinnamon with superior antibacterial activity. *Materials Research Express* **2019,** *6* (7), 075043.
11. Korir, D. K.; Gwalani, B.; Joseph, A.; Kamras, B.; Arvapally, R. K.; Omary, M. A.; Marpu, S. B., Facile Photochemical Syntheses of Conjoined Nanotwin Gold-Silver Particles within a Biologically-Benign Chitosan Polymer. *Nanomaterials* **2019,** *9* (4), 596.
12. Sasidharan, S.; Bahadur, D.; Srivastava, R., Rapid, One-Pot, Protein-Mediated Green Synthesis of Gold Nanostars for Computed Tomographic Imaging and Photothermal Therapy of Cancer. *ACS Sustainable Chem. Eng.* **2017,** *5* (11), 10163-10175.

13. Nehra, K.; Pandian, S. K.; Bharati, M. S. S.; Soma, V. R., Enhanced catalytic and SERS performance of shape/size controlled anisotropic gold nanostructures. *New J. Chem.* **2019,** *43* (9), 3835-3847.
14. Takahata, R.; Yamazoe, S.; Koyasu, K.; Imura, K.; Tsukuda, T., Gold Ultrathin Nanorods with Controlled Aspect Ratios and Surface Modifications: Formation Mechanism and Localized Surface Plasmon Resonance. *Journal of the American Chemical Society* **2018,** *140* (21), 6640-6647.
15. Praneeth, N. V. S.; Paria, S., Microwave-assisted one-pot synthesis of anisotropic gold nanoparticles with active high-energy facets for enhanced catalytic and metal enhanced fluorescence activities. *CrystEngComm* **2018,** *20* (30), 4297-4304.
16. Liu, X.; Yao, J.; Luo, J.; Duan, X.; Yao, Y.; Liu, T., Effect of Growth Temperature on Tailoring the Size and Aspect Ratio of Gold Nanorods. *Langmuir* **2017,** *33* (30), 7479-7485.
17. Holade, Y.; Hickey, D. P.; Minteer, S. D., Halide-regulated growth of electrocatalytic metal nanoparticles directly onto a carbon paper electrode. *Journal of Materials Chemistry A* **2016,** *4* (43), 17154-17162.
18. Shankar, S. S.; Rai, A.; Ankamwar, B.; Singh, A.; Ahmad, A.; Sastry, M., Biological synthesis of triangular gold nanoprisms. *Nature Materials* **2004,** *3* (7), 482-488.
19. Wang, Q.; Wang, Z.; Li, Z.; Xiao, J.; Shan, H.; Fang, Z.; Qi, L., Controlled growth and shape-directed self-assembly of gold nanoarrows. *Science Advances* **2017,** *3* (10), e1701183.
20. Bechtold, T.; Manian, A. P.; Öztürk, H. B.; Paul, U.; Široká, B.; Široký, J.; Soliman, H.; Vo, L. T. T.; Vu-Manh, H., Ion-interactions as driving force in polysaccharide assembly. *Carbohydr. Polym.* **2013,** *93* (1), 316-323.
21. Ahmed, H. B., Recruitment of various biological macromolecules in fabrication of gold nanoparticles: Overview for preparation and applications. *Int. J. Biol. Macromol.* **2019,** *140*, 265-277.
22. Kemp, M. M.; Kumar, A.; Mousa, S.; Park, T.-J.; Ajayan, P.; Kubotera, N.; Mousa, S. A.; Linhardt, R. J., Synthesis of Gold and Silver Nanoparticles Stabilized with Glycosaminoglycans Having Distinctive Biological Activities. *Biomacromolecules* **2009,** *10* (3), 589-595.
23. Okajima, M. K.; Nakamura, M.; Mitsumata, T.; Kaneko, T., Cyanobacterial Polysaccharide Gels with Efficient Rare-Earth-Metal Sorption. *Biomacromolecules* **2010,** *11* (7), 1773-1778.
24. Sornkamnerd, S.; Okajima, M. K.; Matsumura, K.; Kaneko, T., Surface-Selective Control of Cell Orientation on Cyanobacterial Liquid Crystalline Gels. *ACS Omega* **2018,** *3* (6), 6554-6559.
25. Kawashima, H.; Atarashi, K.; Hirose, M.; Hirose, J.; Yamada, S.; Sugahara, K.; Miyasaka, M., Oversulfated Chondroitin/Dermatan Sulfates Containing GlcAβ1/IdoAα1–3GalNAc(4,6-O-disulfate) Interact with L- and P-selectin and Chemokines∗. *J. Biol. Chem.* **2002,** *277* (15), 12921-12930.

26. Astronomo, R. D.; Burton, D. R., Carbohydrate vaccines: developing sweet solutions to sticky situations? *Nature Reviews Drug Discovery* **2010,** *9* (4), 308-324.
27. Okajima, M. K.; Higashi, T.; Asakawa, R.; Mitsumata, T.; Kaneko, D.; Kaneko, T.; Ogawa, T.; Kurata, H.; Isoda, S., Gelation Behavior by the Lanthanoid Adsorption of the Cyanobacterial Extracellular Polysaccharide. *Biomacromolecules* **2010,** *11* (11), 3172-3177.
28. Sayko, R.; Jacobs, M.; Dobrynin, A. V., Quantifying Properties of Polysaccharide Solutions. *ACS Polymers Au* **2021,** *1* (3), 196-205.
29. Lyu, Y.; Becerril, L. M.; Vanzan, M.; Corni, S.; Cattelan, M.; Granozzi, G.; Frasconi, M.; Rajak, P.; Banerjee, P.; Ciancio, R.; Mancin, F.; Scrimin, P., The Interaction of Amines with Gold Nanoparticles. *Adv. Mater. n/a* (n/a), 2211624.
30. Zhang, J.; Xiong, B.; Fu, Z.; Ning, Y.; Li, D., Synergistic Effect of Hydroxyl and Carboxyl Groups on Promoting Nanoparticle Occlusion within Calcite. *Small* **2023,** *19* (18), 2207843.
31. Okajima, M. K.; Kumar, A.; Fujiwara, A.; Mitsumata, T.; Kaneko, D.; Ogawa, T.; Kurata, H.; Isoda, S.; Kaneko, T., Anionic complexes of MWCNT with supergiant cyanobacterial polyanions. *Biopolymers* **2013,** *99* (1), 1-9.
32. Puluhulawa, L. E.; Joni, I. M.; Mohammed, A. F. A.; Arima, H.; Wathoni, N., The Use of Megamolecular Polysaccharide Sacran in Food and Biomedical Applications. *Molecules* **2021,** *26* (11), 3362.
33. Mitsumata, T.; Miura, T.; Takahashi, N.; Kawai, M.; Okajima, M. K.; Kaneko, T., Ionic state and chain conformation for aqueous solutions of supergiant cyanobacterial polysaccharide. *Physical Review E* **2013,** *87* (4), 042607.

CHAPTER II

Optimizing Supergiant Polysaccharide Parameters for the Synthesis of Anisotropic Gold Nanoparticles: A Comprehensive Study of Variable Factors

2.1 Introduction

The size and shape of nanoparticles play a pivotal role in determining their properties and applications. Triangular gold nanoplates (AuNTs), for instance, exhibit unique characteristics such as anisotropic electrical conductivity, heightened electric field enhancement at their vertices, and surface plasmon resonance (SPR) in the near-infrared (NIR) region, hold great promise across various fields. These triangular nanoplates demonstrate potential applications in cancer treatment, owing to their unique features.[34, 35] Additionally, they exhibit versatility in areas such as serving as robust substrates for surface-enhanced Raman spectroscopy (SERS),[36-38] contributing to advancements in solar energy applications,[39] photothermal therapy, drug delivery, and sensors.[40] The production of AuNTs often involves the utilization of bio-products, including plant extracts, green reactants, nitrogen compounds, surfactants, and carboxylate compounds, as reducing and stabilizing agents. However, achieving precise control over size and size distribution remains a challenging pursuit. More critically, the understanding of the growth mechanism under these conditions is still in its early stages.

While the utilization of bio-products for nanoparticle synthesis faces a challenge due to the presence of multiple components or residual small molecules after extracting bio-products acting as stabilizing, and reducing agents, their significance in biological applications remains undeniable. It is imperative to further investigate the potential of various bio-products for the production of gold nanoplates (AuNTs) and discern which components or small molecules are instrumental in this process. The initial biological synthesis method employed citric acid as the reductant for the reduction of the gold precursor. Recent advancements include the utilization of lemongrass extract,[41] Chlorella vulgaris (unicellular green algae),[42] and natural gums[43] for AuNTs production. This suggests that the presence of carbonyl-containing organic components could be linked to the observed anisotropic behavior. However, the advancement of biological synthesis

techniques is still in its early phases. Moreover, the current literature lacks comprehensive insights into the factors that govern the modulation and regulation of nanoparticle morphology, as well as the formation of various shapes.

This chapter presents an environmentally friendly synthesis method for triangular gold nanoparticles (AuNTs) with a one-pot and seedless technique, utilizing the supergiant polysaccharide sacran. The well-established chemical structure of sacran is examined for its role in shaping selectivity and promoting anisotropic growth. The specific conditions conducive to the predominant formation of AuNTs are identified. Additionally, the potential mechanism responsible for AuNTs formation is explored, drawing insights from established mechanistic routes documented in the literature.

2.2 Materials and methods

2.2.1 Materials

Sacran was extracted from the cyanobacterium Aphanothece sacrum (A. sacrum) cyanobacterium, which was dedicated from Kisendou Inc. (Asakura, Japan). Isopropanol, sodium hydroxide, and ethanol were used for sacran polysaccharide extraction. Gold precursor ($HAuCl_4 \cdot 3H_2O$, ≥99.9%), was procured from Sigma-Aldrich and TCI. Milli-Q water was used for preparation of all solutions.

2.2.2 Extraction of Sacran

Sacran polysaccharide was extracted using a procedure previously reported [44], [45], [46]. First, the *A. sacrum* sample was soaked in water followed by ethanol. Subsequently, the washed sample was added to an aqueous solution of 0.1 M NaOH for the elution of sacran. Obtained white solution was regulated to the pH of 8.0 using HCl. After filtration to remove insoluble material, rotary evaporator was used to concentrate the filtrate. Subsequently, the concentrated solution was gradually introduced into isopropanol to yield sacran fibers. This process was repeated twice to eliminate impurities and obtain pure white fibrous sacran. The fibrous sacran was dried in a vacuum oven for 2 min.

2.2.3 Synthesis of gold nanoparticles

A 0.05 wt% sacran solution was prepared in a vial. Subsequently, 1 mL of gold precursor aqueous solution ($HAuCl_4 \cdot 3H_2O$, 0.014 wt%) was carefully introduced into the sacran solution, maintaining a weight ratio of Sacran:$HAuCl_4$ at 3.5:1. The resultant mixture was left undisturbed at 25 °C for a duration of two days, leading to a transformation of color to purple and the observation of precipitate formation at the vial's bottom. Following this, the liquid above the sediment was poured off, and the sediment was dispersed in Milli-Q water, resulting in the formation of gold nanoplates with an approximate size of ≈2 μm. Control over the plate size was achieved by varying the temperature or adjusting the sacran concentration. For instance, increasing the sacran concentration from 0.05 wt% to 0.10 wt% and $HAuCl_4 \cdot 3H_2O$ same concentration (0.014 wt%), with a new Sacran:$HAuCl_4$ weight ratio of 7.0:1, produced nanoplates with a size of ≈1 μm. Further adjustment to a weight ratio of 14.0:1 resulted in the synthesis of approximately 500 nm sized AuNPLs. Additionally, temperature played a crucial role in size modulation; by adopting a 14.0:1 weight ratio and operating at 70 °C for 4 hours, ≈250 nm AuNPLs were obtained. Elevating the temperature from 70 to 90 °C resulted in the formation of pseudo-spherical shapes (≈20 nm). In all cases, the separation of AuNPLs was achieved either by simple decantation of the supernatant or by utilizing a centrifuge.

2.2.4 Measurements

UV-vis-NIR spectra were acquired using a Jasco V-770 spectrometer (Tsukuba, Japan) at wavelengths range from 200 to 1300 nm. Transmission electron microscope (TEM) was conducted using a Hitashi H-7650 with the beam current of 10 μA, operating voltage of 100 kV, and filament voltage of 20 V. JEM-ARM200F high-angle annular dark-field scanning transmission electron microscopy (HAADF-STEM) was employed, along with selected area electron diffraction (SAED), to investigate the crystallinity of AuNPs and elemental analyzer of energy dispersive X-ray spectroscopy (EDS) was utilized for elemental analysis. The specimen for TEM and STEM characterization were prepared by evaporation of 5 μL dilute solution onto a TEM grid. High-resolution scanning electron microscopy (HRSEM) images were recorded using a Hitachi S-5200 with the operating voltage of 10 kV. The average particle size of the AuNPs was measured using an Image-J analysis software. The process and mechanism of AuNPs formation were investigated using X-ray photoelectron spectroscopy (XPS) with a Kratos Axis Ultra DLD instrument. X-ray diffraction (XRD) pattern was measured on powder XRD diffractometer

(RINT-2500) operating at a voltage of 40 kV, the tube current of 30 mA, and the degree of measurement is between 10–90º. Dynamic light scattering (DLS) was performed on a Zetasizer Nano ZS90 instrument (Malvern Instruments Ltd., England) to determine the hydrodynamic size distribution, zeta potential (ζ) values, and molecular weight of all samples. The analyzed concentration of sacran was 0.5 mg/mL or 0.05 wt.%, and the sacran-AuNPs colloidal solution was diluted 100 times before analysis.

2.3 Results and discussion

Purified sacran, as revealed by its UV-vis-NIR spectra (Fig. 6a), exhibits an absence of discernible peaks within the 225–350 nm range, affirming the absence of contaminating chromophore molecules. The XRD pattern of sacran (Fig. 6b) further supports its amorphous nature, indicated by the absence of sharp diffraction peaks. The considerable presence of sulfate groups along sacran chains creates a profound negative ionic potential in any solution condition, robustly attracting cations, including metal ions. Additionally, the strong metal-binding ability of carboxylates contributes to this interaction.[27], [47] The efficient collection of Au ions around sacran chains, coupled with their robust uptake by sacran carboxylates, potentially results in particulation through intrinsic sugar functions during reduction. Investigating the synthesis of AuNPs under the influence of sacran using $HAuCl_4$, we anticipated diverse AuNP morphologies, considering the potential influence of organic molecule additives on their shapes.

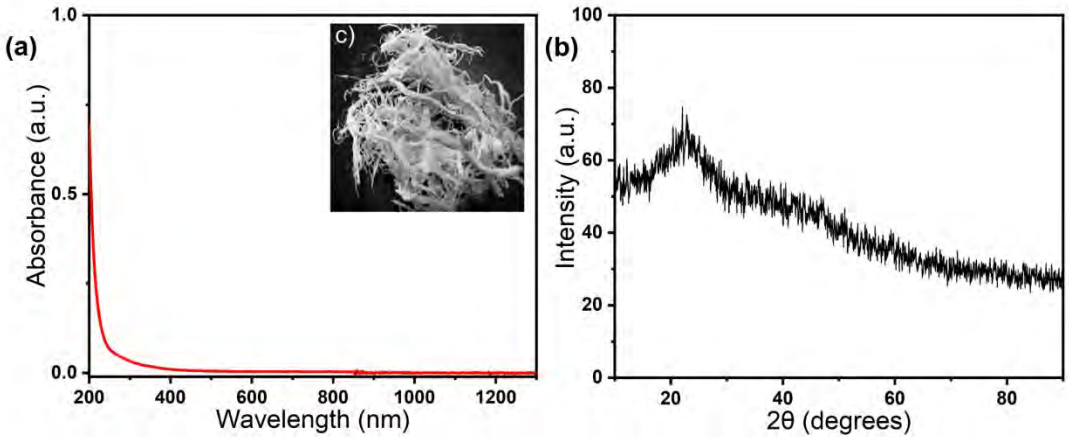

Fig. 6. UV-visible-near infrared (NIR) absorbance spectrum of functional polysaccharide sacran (a), Powder X-ray diffraction (XRD) pattern of sacran (b) and Dry-state sacran fibers extracted from A. sacrum (c, inset).

2.3.1 Formation of AuNPLs

Darya et al. [48] observed the formation of a triangular plate structure through the binding of multiple charged macromolecules to a specific facet. In this study, we explored the impact of the reaction between the entanglement concentration of the functional supergiant polysaccharide sacran and $HAuCl_4$ (a gold precursor) on the morphology of flat gold nanoplates (AuNPLs). The template size of sacran with different concentration was considered as the factors which influence the size and shape of anisotropic growth. We utilized the zetasizer to measure the hydrodynamic size of sacran at various concentrations (0.05, 0.10, 0.20, 0.40, and 0.80 wt%), yielding sizes of 295.4 nm, 363.0 nm, 506.1 nm, 714.2 nm, and 824.8 nm, respectively. Concurrently, the zeta potential became increasingly negative, measuring -23.5 mV, -28.7 mV, -30.6 mV, -40.3 mV, and -51.7 mV at the corresponding concentrations. Interestingly, the sizes of AuNPLs decreased with higher sacran concentrations. This phenomenon can be attributed to variations in reduction potential; as sacran concentration increases, the reduction potential of the gold precursor changes accordingly. At higher reduction rates, surface energy increases uniformly in all directions, leading to the preferential formation of pseudo-spherical and spherical shapes, particularly evident at elevated sacran concentrations. Consequently, the larger hydrodynamic size of sacran as a growth template for gold nanoparticles does not promote the anisotropic growth of gold nanoplates.

The optimization of AuNPL production was achieved by varying sacran-to-gold precursor weight ratios and reaction temperatures (Sacran: $HAuCl_4$ weight ratios of 3.5:1, 7.0:1, 14.0:1, 28.0:1, and 56.0:1) at temperatures of 25, 70, and 90 ºC). The sacran and $HAuCl_4$ mixture exhibited diverse color changes, transitioning from yellow to brownish, purple, and red under different conditions, signifying the formation of AuNPLs with a range of shapes. These included hexagonal, triangular, triangular with a truncated apex, and triangular with a tail. Moreover, the synthesis process yielded nanoparticles with various shapes, including icosahedral, pentagonal, cylindrical, pyramidal, and elongated spheres. The conversion of $HAuCl_4$ by sacran (at a weight ratio of sacran:$HAuCl_4$ = 3.5:1) at 25 ºC resulted in slow formation, producing AuNPLs with a tail, as depicted in Fig. 7. The images of TEM and SEM depicting all the synthesized AuNPs are presented in Fig. 7. By elevating the sacran: $HAuCl_4$ weight ratio from 3.5:1 to 28.0:1 at 25 ºC, well-defined gold nanoplates (AuNPLs, ≈300 nm) were successfully synthesized. The transition

in the shape of AuNPs, progressing from those with a tail to pristine AuNPLs, can be ascribed to the accelerated generation rate of Au(0) under room temperature conditions. Subsequent increases in the sacran to $HAuCl_4$ weight ratio, especially at 56.0:1, resulted in the formation of less anisotropic particles, giving rise to spherical AuNPs ≈20 nm, as illustrated in Fig. 7. A comprehensive visual summary of these findings is presented in Fig. 8.

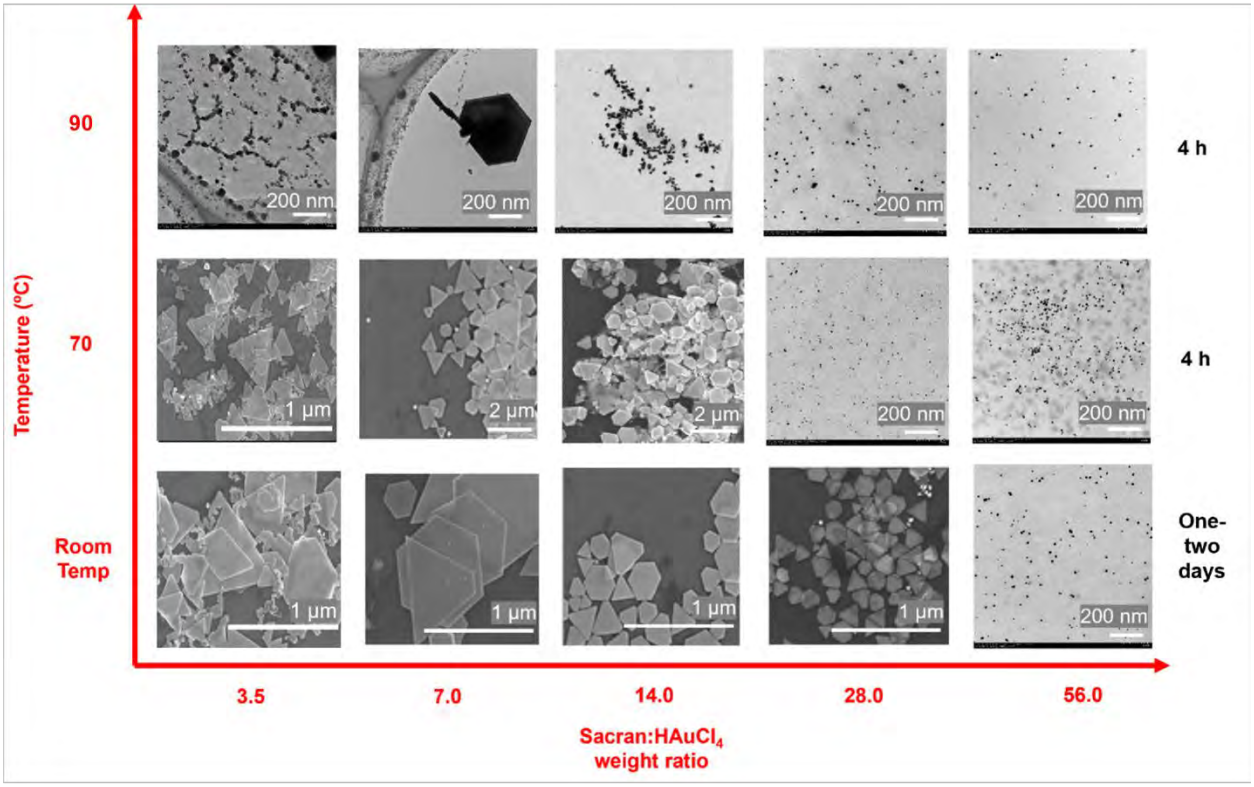

Fig. 7. TEM and SEM images of AuNPs obtained by varied sacran:$HAuCl_4$ weight ratios and temperature.

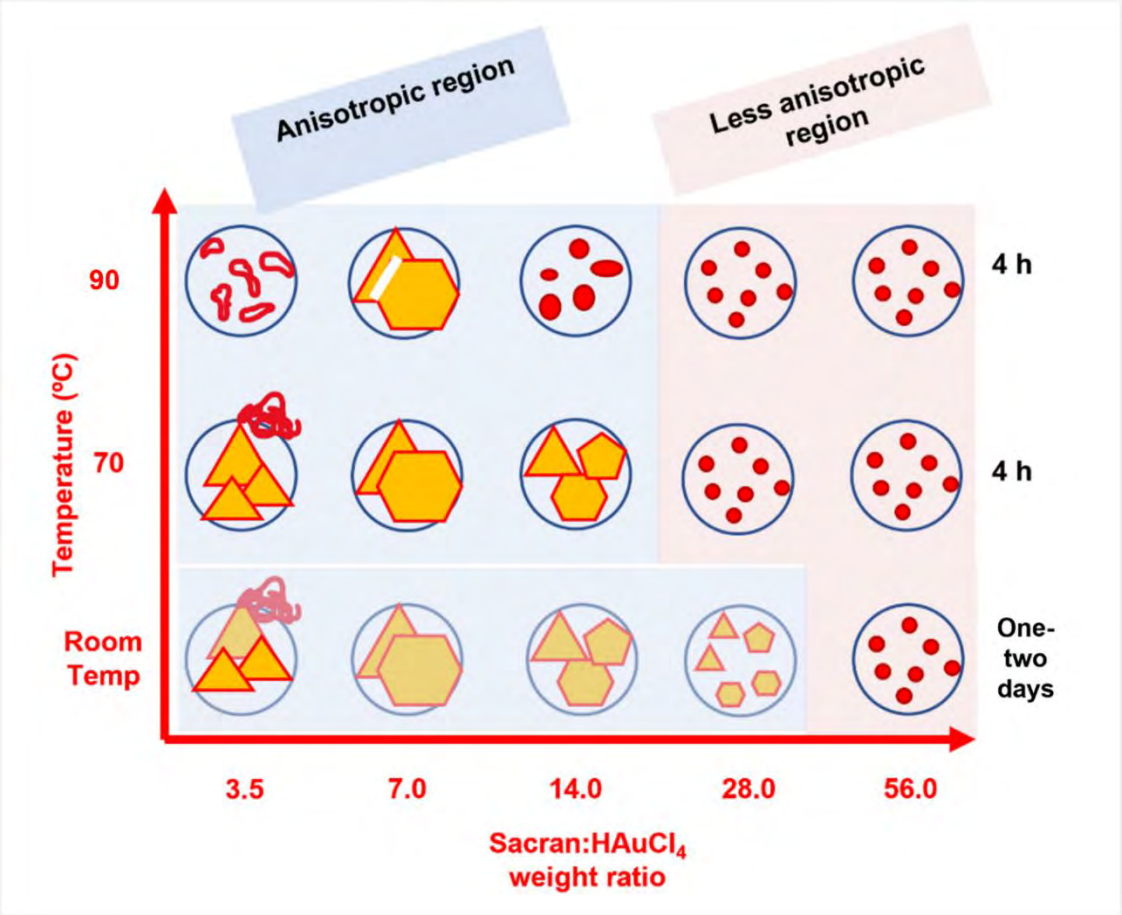

Fig. 8. Overview illustration of obtained AuNPs shapes.

Table 3. The summary of obtained AuNPs size of every conditions.

Weight ratio of sacran:$HAuCl_4$ and Temp.	Size distribution
3.5:1, Room Temp	0.9 ± 0.76 μm
3.5:1, 70 °C	0.5 ± 0.32 μm
3.5:1, 90 °C	Undefined
7.0:1, Room Temp	1.1 ± 0.22 μm
7.0:1, 70 °C	960 ± 66 nm
7.0:1, 90 °C	890 ± 27 nm
14.0:1, Room Temp	530 ± 38 nm
14.0:1, 70 °C	417 ± 57 nm
14.0:1, 90 °C	30.4 ± 2.8 nm
28.0:1, Room Temp	260 ± 51 μm
28.0:1, 70 °C	11.6 ± 1.7 nm
28.0:1, 90 °C	10.1 ± 0.8 nm
56.0:1, Room Temp	20.7 ± 5.2 nm
56.0:1, 70 °C	10.4 ± 0.7 nm
56.0:1, 90 °C	10.6 ± 0.3 nm

By adjusting the reaction temperature and increasing sacran concentration, the size of AuNPs was modified. Under the conditions of a sacran to $HAuCl_4$ (14.0:1) ratio at 70 °C, we deliberately chose specific parameters to clarify the growth mechanism dictating the generation of Au nanoplates (AuNPLs) through sacran-mediated reduction. Over the initial 4 hours, the mixture color transitioned from yellowish to a brownish hue, indicative of sacran's capability to reduce Au(III) species to Au(0) atoms by oxidizing sacran molecules. Within the initial hour of the reaction, gold nuclei were generated and stabilized by sacran, forming spherical Au nanospheres (AuNSs) evident in the UV-vis-NIR spectra at 520 nm (Fig. 9a)[49, 50, 51]. The initial Au seed particles exhibited a mix of polycrystalline characteristics with noticeable defects (Fig. 10a) and pristine single-crystalline structures without defects (Fig. 10c). Examination of lattice fringes at various locations revealed the presence of a combination of both (111) and (200) surface facets (Fig. 10b) and the (111) orientation (Fig. 10d). This observation is attributed to the slow progression of the reaction, favoring the prevalence of the lowest-energy surface facets during the early stages. However, the lack of a specific twinning order makes it challenging to quantify these twin formations in each particle. Subsequently, the appearance of a peak at 788 nm after 2 hours suggested the development of AuNPLs[52], supported by the increasing intensity of the UV-vis-NIR spectra over time (Fig. 9a). The distinct SPR bands at λ_{max} ~520 nm and ~788 nm in the visible and near-infrared regions, respectively, signified the SPR of AuNSs and AuNPLs. The synthesis mechanism of AuNPLs, as reported previously, aligns with the observed SPR bands [53, 54, 55, 56]. The two distinct SPR bands observed at ~520 nm and ~788 nm in the UV-vis-NIR spectra represented the presence of spherical, triangular, and hexagonal AuNPs, each exhibiting independent growth. Fig. 11A illustrates the polycrystalline pattern of aggregated AuNPs after a 2-hour reaction. To elucidate the mechanism, multiple-shaped particles aggregate form Au nanoplates. Because of the gradual manner of the reduction process, these diverse particles have the freedom to rotate and diffuse, aiming to achieve the optimal lattice alignment, as previously observed.[57] Certain plates display forbidden spots, suggesting the existence of stacking faults. Previous studies have shown that the emergence of observable 1/3(422) forbidden reflections on AuNPLs implies the existence of symmetry breaking aligned (111) indices.[58] Stacking faults are illustrated in Fig. 11C, alongside their SAED pattern in Fig. 11D. However, providing insight into the generation of symmetry breaking and their influence on shaping anisotropic NPs remains a complex task. Remarkably, even after 24 hours, these SPR bands exhibited minimal changes

compared to the 4-hour reaction period, implying the completion of the reduction process within the initial 4 hours. This stability in the SPR bands over time suggests the possibility that the observed morphologies may have originated from distinct initial seed structures.

The formation of AuNPLs and AuNSs is depicted in Fig. 9b. After 4 hours, the mean diameters of AuNPLs and AuNSs measured 317 ± 57 nm and 30 ± 4 nm, respectively. The kinetics of AuNPL evolution were scrutinized by observing morphological changes over time, as presented in Fig. 12. During the initial 4 hours, the diameter of the AuNPs increased from 12 ± 7 nm to 317 ± 57 nm (Fig. 12). High-resolution scanning electron microscopy (HRSEM) images in Fig. 12F. revealed the edge thickness of the AuNPLs, signifying the presence of the (200) plane on the side face, with a thickness of approximately 76 nm. To control the gradual formation and enlargement mechanisms, a low concentration of sacran was strategically employed, avoiding the generation of excess nuclei. This deliberate approach facilitated the growth of minute gold nuclei, with additional Au(0) atoms being absorbed on the (220) surfaces, resulting in size augmentation. This growth pattern is evident in the hexagonal nanoplate morphology and diffraction spots showcased in Fig. 9c and d, along with growth along specific (111) facets, as indicated by the XRD pattern in Fig. 12E for the obtained AuNPLs.

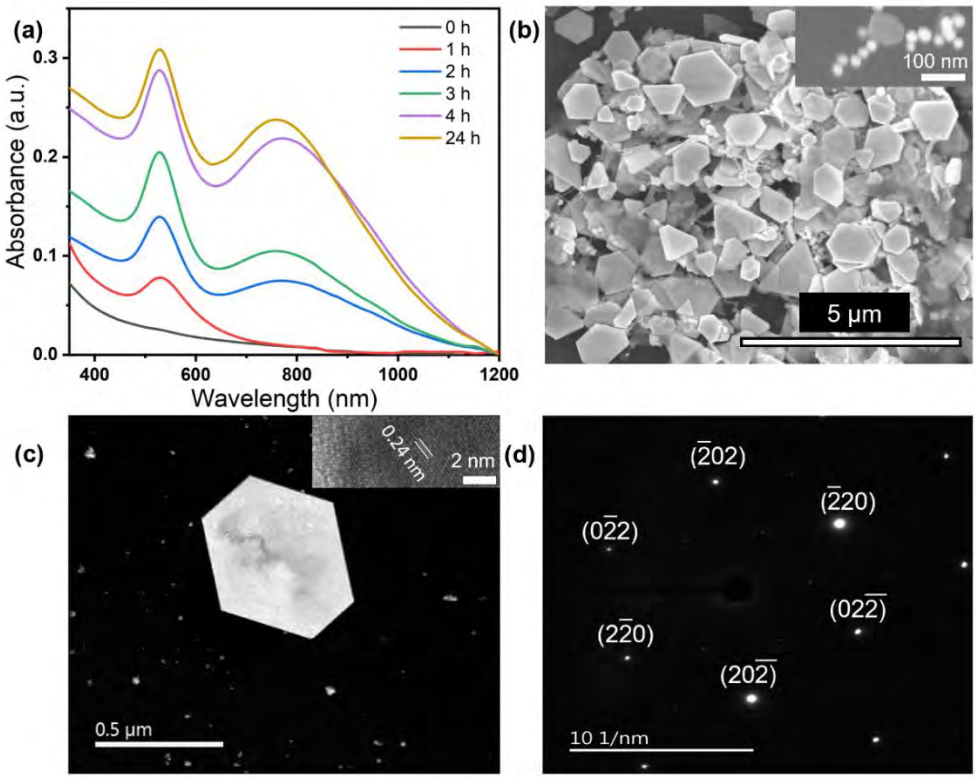

Fig. 9. UV-vis-NIR absorbance measured at different time intervals (a). High-resolution scanning electron microscopy (HRSEM) image depicting post-centrifugal separation of the AuNLPs, with the inset showcasing the spherical AuNPs obtained after 4 hours of reaction (b). Scanning transmission electron microscopy (STEM) image displaying a single hexagon at a reaction time of 4 hours, revealing an interplanar spacing of 0.24 nm (c) along with its associated selected-area electron diffraction (SAED) pattern (d).

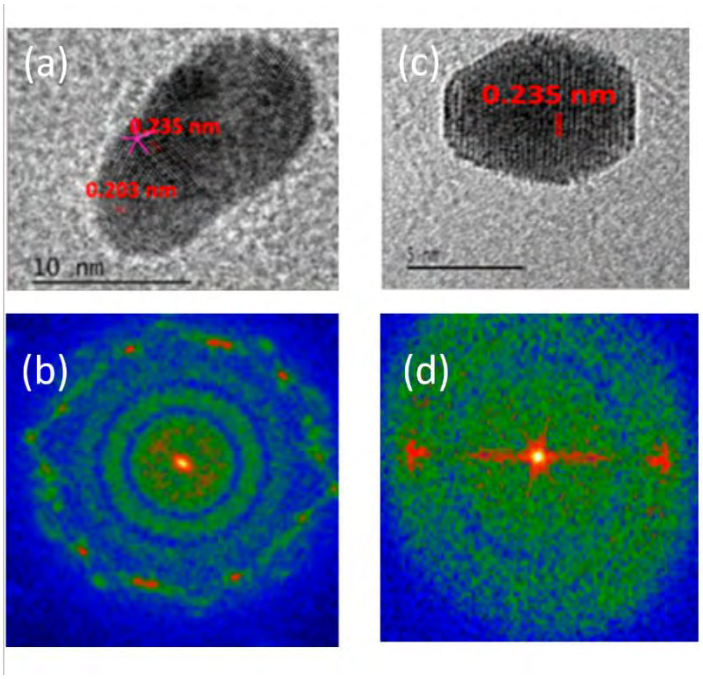

Fig. 10. The seed single particle formed exhibits polycrystalline characteristics (a) and single crystalline features (b).

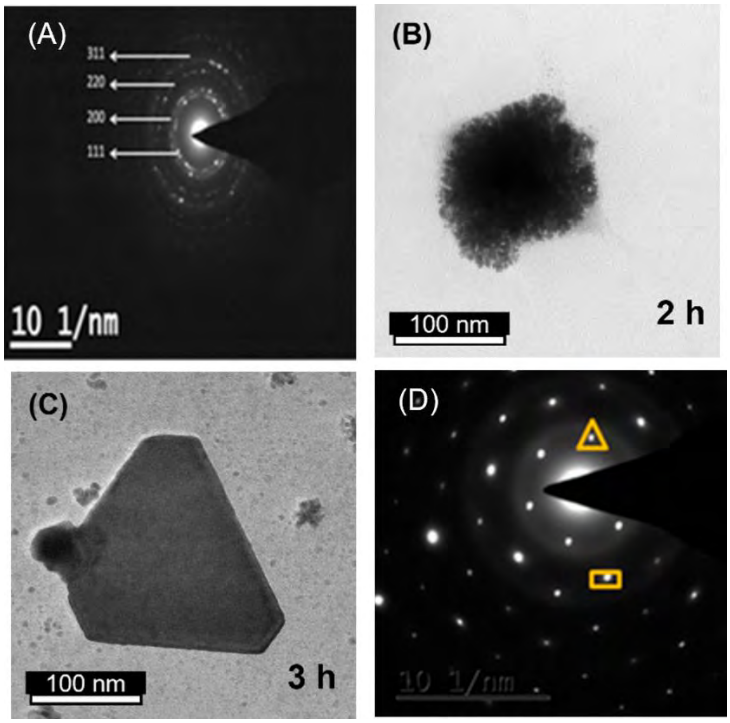

Fig. 11. SAED pattern of the aggregation of AuNPs formed after the reaction time of 2 h (A), its TEM image (B). The AuNPLs formation during 3 h of reaction (C) and its associated SAED pattern: cube spot represents (220) plane and triangle spot represents hidden 1/3(422) hidden plane (D).

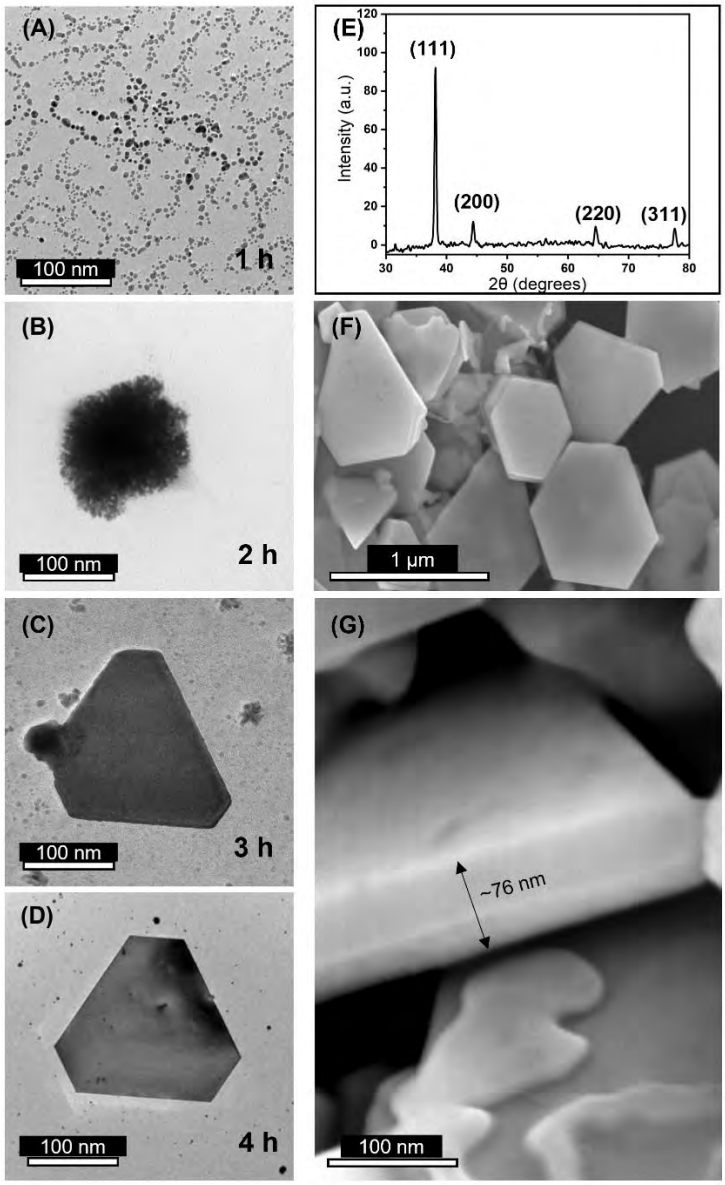

Fig. 12. Morphological changes of the gold nanoparticles at different time intervals from 1 h to 4 h (A-D). SEM images of the synthesized gold nanoplates (E) and the edge thickness (F).

Elevating the reduction temperature to 90 °C consistently yields elongated spherical AuNPs, with their size diminishing as sacran concentration increases. To investigate the influence of sacran concentrations on gold morphology, the sacran-to-$HAuCl_4$ weight ratio was adjusted to 28.0:1 acting as both the capping and reducing agent for AuNPs. This adjustment was made without introducing other reducers or altering additional parameters. The resultant AuNPs exhibited a spherical shape (11.6 ± 1.7 nm) without apparent AuNPLs. Sacran functioned as a capping agent, preventing the aggregation of AuNSs, as depicted in Fig. 13. Notably, the UV-vis-NIR spectra showed no SPR peak at 788 nm within the initial 4 hours of growth. The heightened reducing properties of sacran at elevated concentrations fostered the generation of new nuclei, bypassing primary nuclei formation. Furthermore, the infusion of a higher sacran concentration impeded the aggregation of primary nuclei, offering stability to the AuNSs. EDX images revealed carbon atoms, signifying sacran fibers enshrouding the AuNSs, as illustrated in Fig. 13C. Additionally, the AuNSs showcased a polycrystalline structure with defects (Fig. 13b, d).

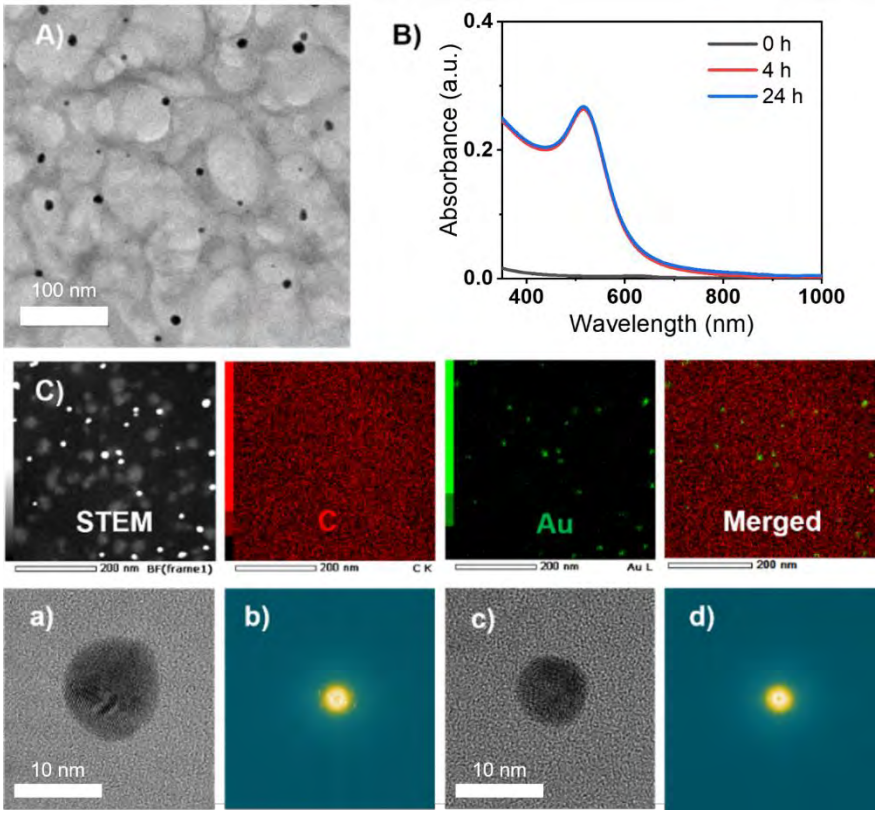

Fig. 13. TEM image of AuNSs formed using 0.40 wt.% entrapped within sacran fibers (A). UV-vis spectra of AuNSs obtained using sacran as the reducer and stabilizer (B). STEM images and EDS mapping of spherical AuNPs (C). HR-TEM images of multiply–twinned of single AuNS (a, c) and its respective fourier transform (FFT) pattern (b, d).

Under acidic conditions (pH: 3-5), the protonated state of the hydroxyl groups leads to a reduction in their capability, impacting the reduction of adsorbed molecules on preferential facets. This, in turn, influences asymmetric growth or stacking faults. Conversely, in basic conditions (pH: 8-12), the deprotonated state of the hydroxyl groups results in an increased reduction rate and the uniform accumulation of these groups on all facets of growing nuclei, contributing to the formation of spherical nanoparticles. However, our specific pH range (between 6.64 and 6.92) may exhibit less effectiveness when compared to the reduction capability determined by sacran concentration. A higher concentration of sacran solution could impede the growth process through a capping effect, resulting in spherical-shaped nanoparticles. Our observations indicate that small changes in pH do not significantly impact the promotion or control of the shape and size of AuNTs. Consequently, adjusting the pH of the medium to a specific value can be neglected.

Table 4 details the hydrodynamic size, zeta potential, and average molecular weight of sacran, sacran-to-$HAuCl_4$ weight ratios of 14.0:1, and 28.0:1 at 70 °C. Sacran exhibits a highly polydisperse particle size, attributed to its relatively low reduction potential, leading to varied sizes of Au seeds and a resulting polydisperse size distribution in AuNPLs. Zeta potential (ζ) is critical for evaluating colloidal stability, where values above +30 mV or below -30 mV indicate highly dispersed AuNPs. The ζ value of the sacran solution signifies a high degree of stability for sacran particles. In contrast, AuNPLs show higher negative ζ values, indicating lower stability, while AuNSs exhibit ζ values below -30 mV. Visually, sacran maintains the large size of AuNPLs for up to 1 week, whereas it stabilizes AuNSs for more than 1 month. Sacran's mega-polysaccharide structures, with a molecular weight exceeding 20×10^6 Da, effectively prevent AuNP aggregation in the sacran medium. Notably, sacran's molecular weight surpasses that of the highest commercially available polysaccharides by 10-100 times. To delve deeper into AuNP stability, viscosity measurements were conducted for carrageenan, chondroitin sulfate, sodium alginate, and sacran at the same concentration (Fig. 14). Sacran, among these polysaccharides, displayed the lowest viscosity. Importantly, viscosity appears to exert minimal influence on AuNP stability, with the primary factor being the molecular weight.

Another aspect we consider is whether the hydrodynamic sizes of sacran play a role as a template for gold nanoplates (AuNPLs). Intuitively, larger hydrodynamic sizes of sacran might be expected to favor the growth of larger AuNPLs. However, instead of AuNPLs, a significant portion of Au nanospheres (AuNSs) was observed. This outcome suggests that the hydrodynamic sizes of sacran

do not necessarily promote the growth of larger AuNPLs. Therefore, it is plausible that kinetic control, achieved through sacran-to-$HAuCl_4$ weight ratios and temperature adjustments, emerges as a crucial factor influencing shape selectivity.

We then investigated the stability properties of sacran in comparison with other polysaccharides, elucidating the capping effects of each polysaccharide under various conditions. To elaborate, three types of stabilization forces were considered: 1) Charge stabilization force: This involves the addition of charged molecules or polymers to the surface of nanoparticles, generating a repulsive electrostatic force between the particles. 2) Steric stabilization force: Utilizing polymer chains or surfactant molecules adsorbed onto the nanoparticle surface, such as thiolated PEG or thiolated DNA, to prevent agglomeration and 3) Depletion forces: These forces come into play in the presence of large molecules, like polymers or proteins. In comparison to charge and steric stabilization techniques, the surface retains its accessibility without undergoing covalent alterations or strong polymer adsorption. Depletion forces can maintain exceptionally high colloidal stability, even in conditions of extreme ionic strength and pH, all while preserving surface accessibility. Fig. 15 illustrates the stabilization properties of sacran under different salt and pH conditions. Sacran demonstrates outstanding resistance to salt (Na^+) induced AuNPs aggregation, exceeding 320 M, which is higher than observed with other polysaccharides. Furthermore, sacran effectively inhibits AuNPs aggregation under varying pH conditions. In summary, sacran exhibits a distinctive capacity for depletion forces, which enables remarkable colloidal stability, even under conditions of extreme pH and ionic strength. Additionally, sacran's low viscosity enhances its effectiveness in stabilizing nanoparticles, establishing it as a favorable selection for a range of industrial and biomedical applications.

Table 4. Hydrodynamic size, stability, and molecular weight of sacran-stabilized gold nanoparticles

Samples	Average hydrodynamic size (nm)	PDI	Zeta potential (ζ/mV)	Molecular weight ($\times 10^3$ kDa)
Sacran 0.2 wt. %	506±17.4	0.39	-30.1±1.7	23.7
Resulting AuNPLs	435±12.6	0.45	-41.7±1.3	20.4
Sacran 0.4 wt. %	714±21.8	0.57	-40.4±1.1	21.6
Resulting AuNSs	24.0±1.6	0.25	-27.5±0.8	22.8

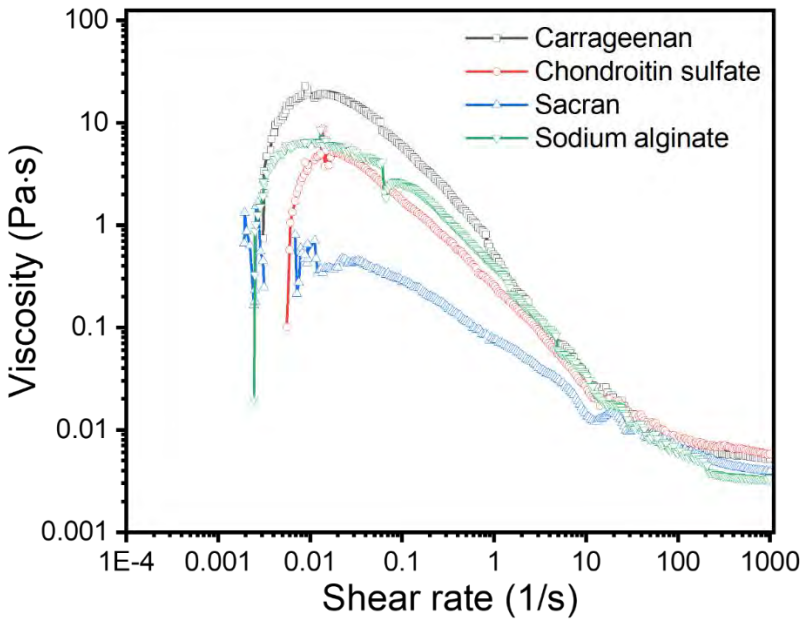

Fig. 14. Viscosity measurement of different polysaccharides with 0.05 % w/v.

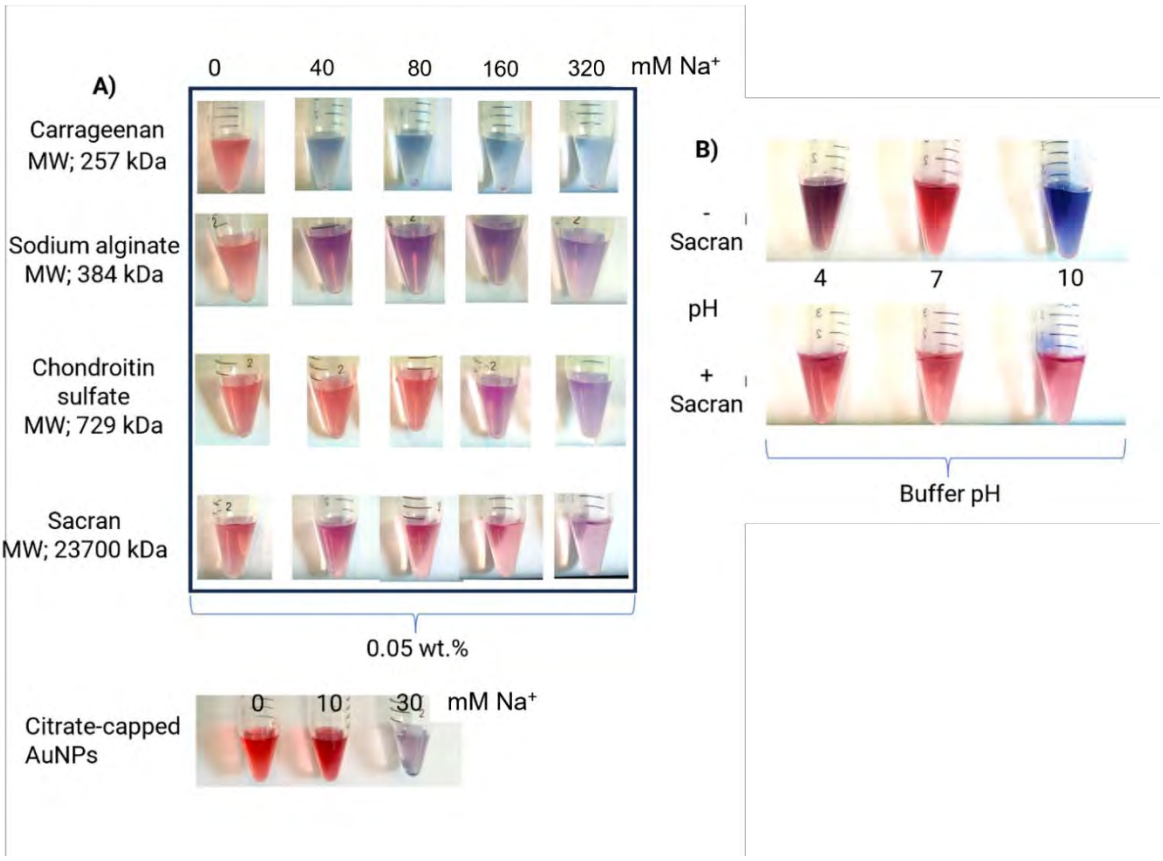

Fig. 15. Stability test of different polysaccharides on citrate-capped 50 nm AuNPs. (A) Stability of AuNPs in 0 to 320 M Na^+. Citrate-capped AuNPs could maintain their colloidal stability to only 30 M Na^+. (B) The stability of citrate and sacran megamolecules on 50 nm AuNPs as influenced by buffer pH.

We employed the XPS technique to investigate the oxidation of sacran during the formation of AuNPLs (Fig. 16) [59]. Before sacran oxidation (no reaction with Au(III)), the C 1s signals depicted aliphatic carbon atoms at 284.8 eV in the C 1s region. Additionally, peaks at 286.5, 288.0, and 289.5 eV corresponded to hydroxyl (–C–OH), acetal (O–C–O), and carboxylate (–C=OOH) carbon atoms within the sacran chemical structure, respectively (Fig. 15a) [60, 61]. Following sacran oxidation (Fig. 15a), C 1s signals demonstrated an increase in the carboxylate group fraction and a decrease in the hydroxyl group fraction, as indicated by area values (area CPS·eV). Furthermore, the atomic percentage of the carboxyl (–C=OOH) group at 289.7 eV increased from 1.33% to 5.60%, while that of the hydroxyl (–C–OH) group at 286.7 eV decreased from 43.42% to 36.00 % (Table 6). These findings suggest a partial conversion of –OH groups from the repeating sugar units at the C6 position of sacran[62, 63] to carboxyl groups, signifying the oxidation of the sacran

structure through the reduction of Au(III) species. On the contrary, the C 1s regions of the aliphatic carbon (284.8 eV) and acetal (288.0 eV) remained unchanged (Table 6), suggesting that the reduction of the Au(III) species did not impact these functional groups. The O 1s signals of oxidized sacran shifted from 532.9 to 533.2 eV, indicating a decrease in the alcoholic oxygen fraction at 533.2 eV and an increase in the carboxylic oxygen fraction at 531.9 eV, as reflected in terms of area value (Fig. 17b). The atomic percentage of the alcoholic (C<u>O</u>H) oxygen peak decreased from 68.03% to 38.71%, whereas that of the carboxylic (C=<u>O</u>OH) oxygen peak increased from 43.42% to 61.29%. Additionally, an examination of the chemical bonding energies and properties before and after the oxidation of sacran by Au(III) species was conducted. In the N 1s binding energy region, only a single peak at 399.8 eV corresponding to the amine (–<u>N</u>H_2) group was observed (Fig. 17a and b), suggesting that there was no significant binding between amino groups of sacran with Au(III).

In the S 2p binding energy region (Fig. 17c), the signal of sacran consists of a doublet ($2p_{3/2}$ and $2p_{1/2}$) with a 1.2 eV division and 2:1 peak area ratio.[64] After the oxidation of sacran (Fig. 17d), a doublet peak at 169.8 and 171.0 eV indicates spin-orbit coupling of the sulfate groups (–OSO_3^-) of the oxidized sacran, and the peak intensity remained unchanged when compared with the original sacran pattern (Fig. 17c). In addition, no new peaks corresponding to AuS were observed. Therefore, it can be inferred that the reduction of Au(III) was primarily influenced by the hydroxyl groups of sacran. The results revealed that carboxylate, sulfate, and amino groups do not strongly interact with the gold precursor for the reduction. However, these groups exhibit a strong binding affinity to metallic gold (Au^0). This interaction influences the surface energies of the gold nanoparticles, particularly reducing the surface energy of the (110) planes. As a result, the growth of gold nanoparticles is directed in a way that favors the formation of nanoplate (AuNPL) shapes.[65]

The formation mechanism of AuNPLs is depicted in Fig. 18. Initially, one sacran macromolecule consisted of ca. 33,000 applicable negative charges, which strongly attracted the positive electric charges of Au(III). Ionic adsorption induces the reduction of Au(III) species to form Au(0) atoms via the oxidation of sacran [66, 67], initiating the nucleation of single-crystal gold, which contributes to symmetry breaking, and the gold nuclei continue to grow by absorbing other unreduced Au(III) gathered under strong negative electrical fields. The reduction process can be catalyzed by applying heat [68, 69]. The negative charge of sacran functional groups, such as sulfate and carboxylate groups, should have individual roles; the sulfate group can be attracted under any

aqueous condition, even acidic or high ionic strength, while carboxylate groups can bind strongly with metal ions. Nanoparticles can undergo growth through either a thermodynamically or kinetically controlled process. Thermodynamic conditions lead to uniform growth, typically resulting in the formation of spherical structures. Conversely, anisotropic nanostructures or gold nanoplates arise through directional growth, primarily occurring in the kinetically controlled manner [70]. Despite these observations, the overall mechanism for the formation of nanoparticles with such diverse morphologies remains unclear [71]. In contrast, the growth process is retarded in a highly concentrated sacran solution (0.4 wt.%), attributable to a capping effect. This condition maintains the gold in a spherical shape, as illustrated in Fig. 13. The obtained particles were triangular with a tail, broken plates, and quasi-elongated plates. Moreover, the particles were polydisperse (328–1030 nm). Therefore, we investigated a new method for eliminating these nanostructures.

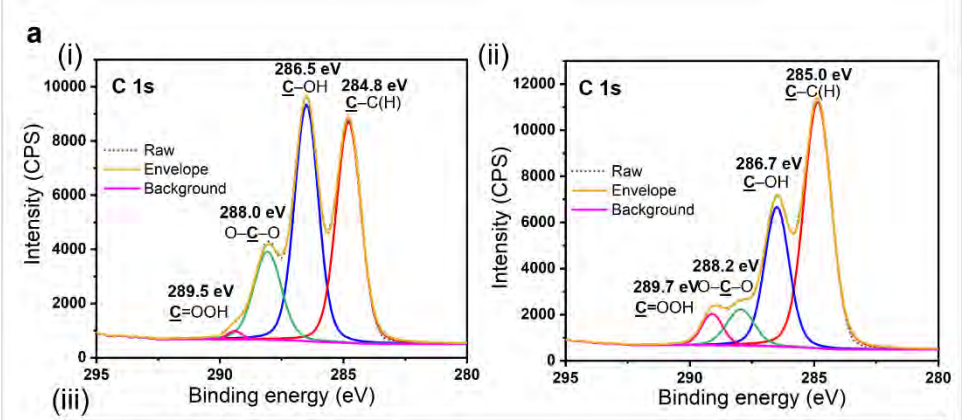

(iii)

Sample	Sacran		Oxidized sacran	
Peaks	Binding energy (eV)	Area CPS·eV	Binding energy (eV)	Area CPS·eV
C–C(H)	284.8	9700.2	285.0	11100.5
C–OH	286.5	9960.9	286.7	7830.6
O–C–O	288.0	3805.5	288.2	3371.7
C=OOH	289.5	245.7	289.7	2788.9

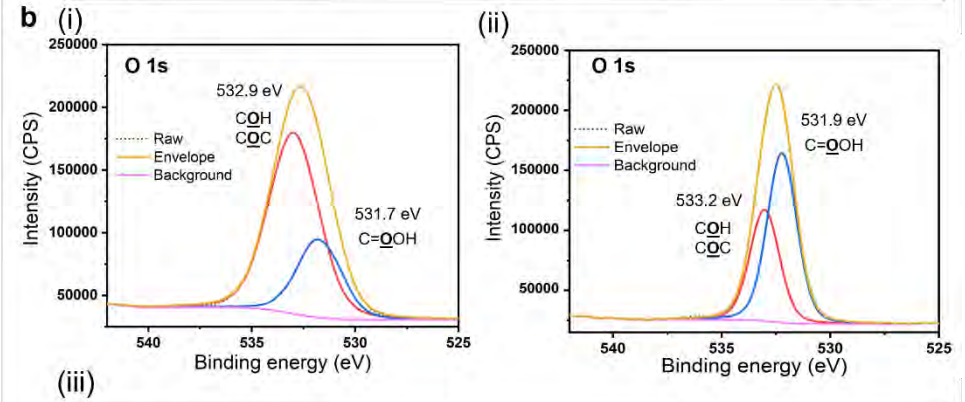

(iii)

Sample	Sacran		Oxidized sacran	
Peaks	Binding energy (eV)	Area CPS·eV	Binding energy (eV)	Area CPS·eV
COH	532.9	465141.6	533.2	178210.8
C=OOH	531.7	159540.8	531.9	231798.5

Fig. 16. High resolution XPS profiles before and after oxidation of sacran in the formation of AuNPLs. C 1s spectra of (i) sacran and (ii) oxidized sacran (iii) C 1s table of area values for the peaks (C–C(H), C–OH, O–C–O, C=OOH) of each sample (a). O 1s spectra of (i) sacran and (ii) oxidized sacran. (iii) O 1s table of area values for the peaks (COH, C=OOH) of each sample (b).

Table 5. Quantification of the chemical state of C 1s of sacran and oxidized sacran.

Sample	**Sacran**		**Oxidized sacran**	
Peaks	**Binding energy (eV)**	**Atomic concentration (%)**	**Binding energy (eV)**	**Atomic concentration (%)**
C–C(H)	284.8	39.46	285.0	43.89
C–OH	286.5	43.42	286.7	36.00
O–C–O	288.0	15.79	288.2	14.51
C=OOH	289.5	1.33	289.7	5.60

Table 6. Quantification of the chemical state of O 1s of sacran and oxidized sacran.

Sample	**Sacran**		**Oxidized sacran**	
Peaks	**Binding energy (eV)**	**Atomic concentration (%)**	**Binding energy (eV)**	**Atomic concentration (%)**
COH	532.9	68.03	533.2	38.71
C=OOH	531.7	43.42	531.9	61.29

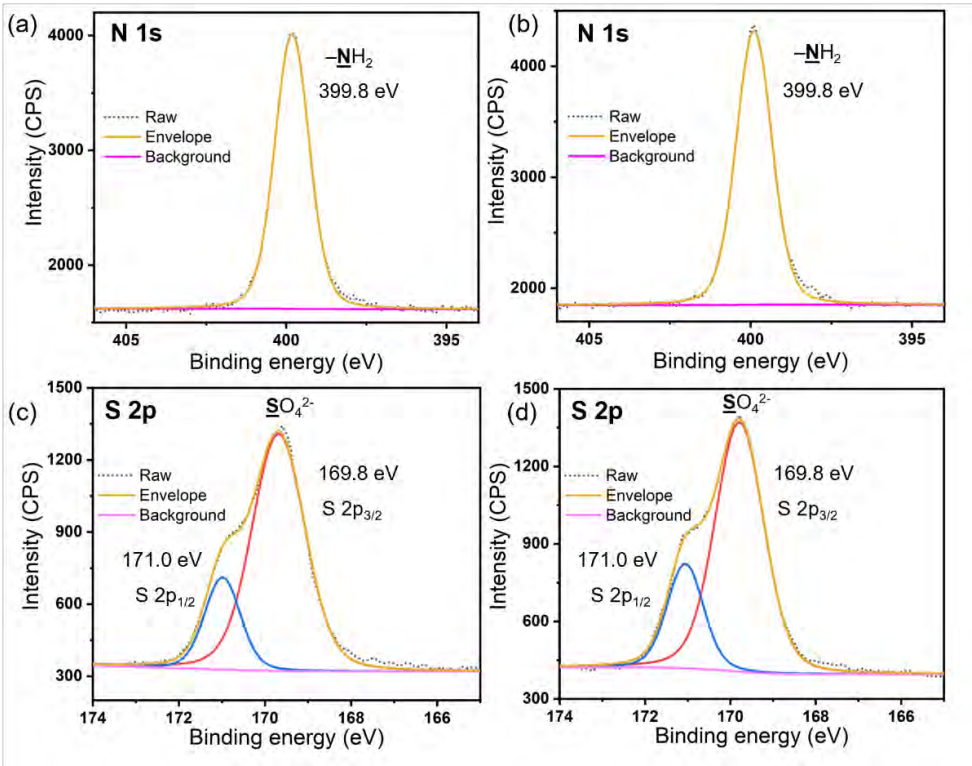

Fig. 17. High resolution XPS profiles spectrum of before and after oxidation of sacran in the formation of AuNPLs; N 1s spectra of sacran (a) and oxidized sacran (b), and S 2p spectra of sacran (c) and oxidized sacran (d).

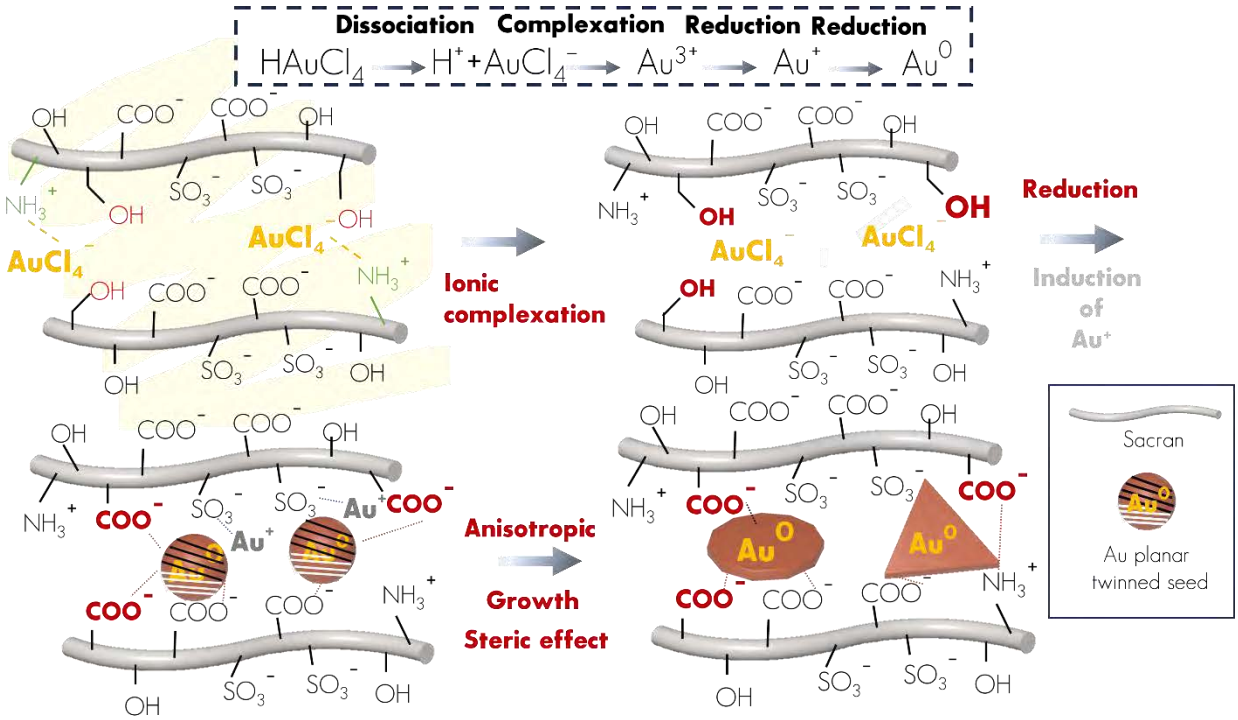

Fig. 18. Proposed mechanism of AuNPL formation using sacran. First, sacran induces Au(III) species. Second, hydroxyl groups can interact with Au(III) to reduce them to Au(0) via sacran oxidation. Third, Au(0) atoms start to aggregate or cluster together owing to the attractive forces between them to form the initial building blocks for the growth of AuNPLs. Finally, Au(0) atoms continuously added to the nucleus, leading to the anisotropic growth and sacran serves as a stabilizer of AuNPLs.

2.4 Conclusion

Sacran, a supergiant polysaccharide, exhibits unique properties that position it as a promising agent for the controlled formation of anisotropic gold nanoplates (AuNPLs). The multifunctional characteristics of sacran, encompassing its substantial molecular weight, sulfate groups, and carboxylates, play pivotal roles in the synthesis process. Functioning as both a reducing and stabilizing agent, sacran facilitates the growth of well-defined AuNPLs. The hydrodynamic size, zeta potential, and low viscosity of sacran collectively contribute to the stability of the resulting AuNPLs. The sacrificial oxidation of sacran during the reduction of Au(III) species influences its molecular structure, leading to the formation of carboxyl groups. The deliberately slow reduction kinetics of sacran enable the controlled growth of AuNPLs, offering the flexibility to tailor their size and shape by adjusting sacran-to-$HAuCl_4$ weight ratios and reaction temperature. Furthermore, sacran exhibits excellent stability against various environmental conditions, underscoring its potential applications in diverse fields such as catalysis, sensing, and photothermal therapy. This chapter addresses a challenging aspect, focusing on the control of shape uniformity and selectivity of AuNPLs. To overcome this challenge, we will explore controlling agents that promote shape/size purity and delve deeper into the effects of individual parameters in order to enhance our understanding and control over the synthesis process and explore their potential applications in catalysis.

2.5 References

1. Vijayan, R.; Joseph, S.; Mathew, B., Indigofera tinctoria leaf extract mediated green synthesis of silver and gold nanoparticles and assessment of their anticancer, antimicrobial, antioxidant and catalytic properties. *Artificial Cells, Nanomedicine, and Biotechnology* **2018,** *46* (4), 861-871.
2. Nadeem, M.; Abbasi, B. H.; Younas, M.; Ahmad, W.; Khan, T., A review of the green syntheses and anti-microbial applications of gold nanoparticles. *Green Chemistry Letters and Reviews* **2017,** *10* (4), 216-227.
3. Santhoshkumar, J.; Rajeshkumar, S.; Venkat Kumar, S., Phyto-assisted synthesis, characterization and applications of gold nanoparticles – A review. *Biochemistry and Biophysics Reports* **2017,** *11*, 46-57.
4. Wacławek, S.; Gončuková, Z.; Adach, K.; Fijałkowski, M.; Černík, M., Green synthesis of gold nanoparticles using Artemisia dracunculus extract: control of the shape and size by varying synthesis conditions. *Environmental Science and Pollution Research* **2018,** *25* (24), 24210-24219.
5. Balasubramanian, S.; Raghavachari, D., Green Synthesis of Triangular Au Nanoplates: Role of Small Molecules Present in Bael Gum. *ACS Sustainable Chem. Eng.* **2017,** *5* (11), 10317-10326.
6. Osonga, F. J.; Yazgan, I.; Kariuki, V.; Luther, D.; Jimenez, A.; Le, P.; Sadik, O. A., Greener synthesis and characterization, antimicrobial and cytotoxicity studies of gold nanoparticles of novel shapes and sizes. *RSC Adv.* **2016,** *6* (3), 2302-2313.
7. Deokar, G. K.; Ingale, A. G., Unveiling an unexpected potential of beetroot waste in green synthesis of single crystalline gold nanoplates: A mechanistic study. *Arabian Journal of Chemistry* **2018,** *11* (6), 950-958.
8. Rajkumari, J.; Meena, H.; Gangatharan, M.; Busi, S., Green synthesis of anisotropic gold nanoparticles using hordenine and their antibiofilm efficacy against Pseudomonas aeruginosa. *IET Nanobiotechnology* **2017,** *11* (8), 987-994.
9. Emam, H. E.; Ahmed, H. B., Carboxymethyl cellulose macromolecules as generator of anisotropic nanogold for catalytic performance. *Int. J. Biol. Macromol.* **2018,** *111*, 999-1009.
10. Goyal, D.; Saini, A.; Saini, G. S. S.; Kumar, R., Green synthesis of anisotropic gold nanoparticles using cinnamon with superior antibacterial activity. *Materials Research Express* **2019,** *6* (7), 075043.
11. Korir, D. K.; Gwalani, B.; Joseph, A.; Kamras, B.; Arvapally, R. K.; Omary, M. A.; Marpu, S. B., Facile Photochemical Syntheses of Conjoined Nanotwin Gold-Silver Particles within a Biologically-Benign Chitosan Polymer. *Nanomaterials* **2019,** *9* (4), 596.
12. Sasidharan, S.; Bahadur, D.; Srivastava, R., Rapid, One-Pot, Protein-Mediated Green Synthesis of Gold Nanostars for Computed Tomographic Imaging and Photothermal Therapy of Cancer. *ACS Sustainable Chem. Eng.* **2017,** *5* (11), 10163-10175.
13. Nehra, K.; Pandian, S. K.; Bharati, M. S. S.; Soma, V. R., Enhanced catalytic and SERS performance of shape/size controlled anisotropic gold nanostructures. *New J. Chem.* **2019,** *43* (9), 3835-3847.
14. Takahata, R.; Yamazoe, S.; Koyasu, K.; Imura, K.; Tsukuda, T., Gold Ultrathin Nanorods with Controlled Aspect Ratios and Surface Modifications: Formation Mechanism and Localized Surface Plasmon Resonance. *Journal of the American Chemical Society* **2018,** *140* (21), 6640-6647.
15. Praneeth, N. V. S.; Paria, S., Microwave-assisted one-pot synthesis of anisotropic gold nanoparticles with active high-energy facets for enhanced catalytic and metal enhanced fluorescence activities. *CrystEngComm* **2018,** *20* (30), 4297-4304.
16. Liu, X.; Yao, J.; Luo, J.; Duan, X.; Yao, Y.; Liu, T., Effect of Growth Temperature on Tailoring the Size and Aspect Ratio of Gold Nanorods. *Langmuir* **2017,** *33* (30), 7479-7485.
17. Holade, Y.; Hickey, D. P.; Minteer, S. D., Halide-regulated growth of electrocatalytic metal nanoparticles directly onto a carbon paper electrode. *Journal of Materials Chemistry A* **2016,** *4* (43), 17154-17162.
18. Shankar, S. S.; Rai, A.; Ankamwar, B.; Singh, A.; Ahmad, A.; Sastry, M., Biological synthesis of triangular gold nanoprisms. *Nature Materials* **2004,** *3* (7), 482-488.

19. Wang, Q.; Wang, Z.; Li, Z.; Xiao, J.; Shan, H.; Fang, Z.; Qi, L., Controlled growth and shape-directed self-assembly of gold nanoarrows. *Science Advances* **2017,** *3* (10), e1701183.
20. Bechtold, T.; Manian, A. P.; Öztürk, H. B.; Paul, U.; Široká, B.; Široký, J.; Soliman, H.; Vo, L. T. T.; Vu-Manh, H., Ion-interactions as driving force in polysaccharide assembly. *Carbohydr. Polym.* **2013,** *93* (1), 316-323.
21. Ahmed, H. B., Recruitment of various biological macromolecules in fabrication of gold nanoparticles: Overview for preparation and applications. *Int. J. Biol. Macromol.* **2019,** *140*, 265-277.
22. Kemp, M. M.; Kumar, A.; Mousa, S.; Park, T.-J.; Ajayan, P.; Kubotera, N.; Mousa, S. A.; Linhardt, R. J., Synthesis of Gold and Silver Nanoparticles Stabilized with Glycosaminoglycans Having Distinctive Biological Activities. *Biomacromolecules* **2009,** *10* (3), 589-595.
23. Okajima, M. K.; Nakamura, M.; Mitsumata, T.; Kaneko, T., Cyanobacterial Polysaccharide Gels with Efficient Rare-Earth-Metal Sorption. *Biomacromolecules* **2010,** *11* (7), 1773-1778.
24. Sornkamnerd, S.; Okajima, M. K.; Matsumura, K.; Kaneko, T., Surface-Selective Control of Cell Orientation on Cyanobacterial Liquid Crystalline Gels. *ACS Omega* **2018,** *3* (6), 6554-6559.
25. Kawashima, H.; Atarashi, K.; Hirose, M.; Hirose, J.; Yamada, S.; Sugahara, K.; Miyasaka, M., Oversulfated Chondroitin/Dermatan Sulfates Containing GlcAβ1/IdoAα1–3GalNAc(4,6-O-disulfate) Interact with L- and P-selectin and Chemokines∗. *J. Biol. Chem.* **2002,** *277* (15), 12921-12930.
26. Astronomo, R. D.; Burton, D. R., Carbohydrate vaccines: developing sweet solutions to sticky situations? *Nature Reviews Drug Discovery* **2010,** *9* (4), 308-324.
27. Okajima, M. K.; Higashi, T.; Asakawa, R.; Mitsumata, T.; Kaneko, D.; Kaneko, T.; Ogawa, T.; Kurata, H.; Isoda, S., Gelation Behavior by the Lanthanoid Adsorption of the Cyanobacterial Extracellular Polysaccharide. *Biomacromolecules* **2010,** *11* (11), 3172-3177.
28. Sayko, R.; Jacobs, M.; Dobrynin, A. V., Quantifying Properties of Polysaccharide Solutions. *ACS Polymers Au* **2021,** *1* (3), 196-205.
29. Lyu, Y.; Becerril, L. M.; Vanzan, M.; Corni, S.; Cattelan, M.; Granozzi, G.; Frasconi, M.; Rajak, P.; Banerjee, P.; Ciancio, R.; Mancin, F.; Scrimin, P., The Interaction of Amines with Gold Nanoparticles. *Adv. Mater. n/a* (n/a), 2211624.
30. Zhang, J.; Xiong, B.; Fu, Z.; Ning, Y.; Li, D., Synergistic Effect of Hydroxyl and Carboxyl Groups on Promoting Nanoparticle Occlusion within Calcite. *Small* **2023,** *19* (18), 2207843.
31. Okajima, M. K.; Kumar, A.; Fujiwara, A.; Mitsumata, T.; Kaneko, D.; Ogawa, T.; Kurata, H.; Isoda, S.; Kaneko, T., Anionic complexes of MWCNT with supergiant cyanobacterial polyanions. *Biopolymers* **2013,** *99* (1), 1-9.
32. Puluhulawa, L. E.; Joni, I. M.; Mohammed, A. F. A.; Arima, H.; Wathoni, N., The Use of Megamolecular Polysaccharide Sacran in Food and Biomedical Applications. *Molecules* **2021,** *26* (11), 3362.
33. Mitsumata, T.; Miura, T.; Takahashi, N.; Kawai, M.; Okajima, M. K.; Kaneko, T., Ionic state and chain conformation for aqueous solutions of supergiant cyanobacterial polysaccharide. *Physical Review E* **2013,** *87* (4), 042607.
34. AshaRani, P. V.; Low Kah Mun, G.; Hande, M. P.; Valiyaveettil, S., Cytotoxicity and Genotoxicity of Silver Nanoparticles in Human Cells. *ACS Nano* **2009,** *3* (2), 279-290.
35. Verano-Braga, T.; Miethling-Graff, R.; Wojdyla, K.; Rogowska-Wrzesinska, A.; Brewer, J. R.; Erdmann, H.; Kjeldsen, F., Insights into the Cellular Response Triggered by Silver Nanoparticles Using Quantitative Proteomics. *ACS Nano* **2014,** *8* (3), 2161-2175.
36. Singh, A.; Pasricha, R.; Sastry, M., Ultra-low level optical detection of mercuric ions using biogenic gold nanotriangles. *Analyst* **2012,** *137* (13), 3083-3090.
37. Yan, Z.; Yuen, M.-F.; Hu, L.; Sun, P.; Lee, C.-S., Advances for the colorimetric detection of Hg2+ in aqueous solution. *RSC Adv.* **2014,** *4* (89), 48373-48388.
38. Zhang, Y.; Charles, D. E.; Ledwith, D. M.; Aherne, D.; Cunningham, S.; Voisin, M.; Blau, W. J.; Gun'ko, Y. K.; Kelly, J. M.; Brennan-Fournet, M. E., Wash-free highly sensitive detection of C-reactive protein using gold derivatised triangular silver nanoplates. *RSC Adv.* **2014,** *4* (55), 29022-29031.

39. Jiang, X.; Liu, R.; Tang, P.; Li, W.; Zhong, H.; Zhou, Z.; Zhou, J., Controllably tuning the near-infrared plasmonic modes of gold nanoplates for enhanced optical coherence imaging and photothermal therapy. *RSC Adv.* **2015,** *5* (98), 80709-80718.
40. Fazal, S.; Jayasree, A.; Sasidharan, S.; Koyakutty, M.; Nair, S. V.; Menon, D., Green Synthesis of Anisotropic Gold Nanoparticles for Photothermal Therapy of Cancer. *ACS Appl. Mater. Interfaces* **2014,** *6* (11), 8080-8089.
41. Shankar, S. S.; Rai, A.; Ahmad, A.; Sastry, M., Controlling the Optical Properties of Lemongrass Extract Synthesized Gold Nanotriangles and Potential Application in Infrared-Absorbing Optical Coatings. *Chem. Mater.* **2005,** *17* (3), 566-572.
42. Xie, J.; Lee, J. Y.; Wang, D. I. C.; Ting, Y. P., Identification of Active Biomolecules in the High-Yield Synthesis of Single-Crystalline Gold Nanoplates in Algal Solutions. *Small* **2007,** *3* (4), 672-682.
43. Wu, C.-C.; Chen, D.-H., Facile green synthesis of gold nanoparticles with gum arabic as a stabilizing agent and reducing agent. *Gold Bulletin* **2010,** *43* (4), 234-240.
44. Okajima, M. K.; Bamba, T.; Kaneso, Y.; Hirata, K.; Fukusaki, E.; Kajiyama, S. i.; Kaneko, T., Supergiant Ampholytic Sugar Chains with Imbalanced Charge Ratio Form Saline Ultra-absorbent Hydrogels. *Macromolecules* **2008,** *41* (12), 4061-4064.
45. Okajima, M. K.; Kaneko, D.; Mitsumata, T.; Kaneko, T.; Watanabe, J., Cyanobacteria That Produce Megamolecules with Efficient Self-Orientations. *Macromolecules* **2009,** *42* (8), 3057-3062.
46. Okajima, M. K.; Miyazato, S.; Kaneko, T., Cyanobacterial Megamolecule Sacran Efficiently Forms LC Gels with Very Heavy Metal Ions. *Langmuir* **2009,** *25* (15), 8526-8531.
47. Okajima, M. K.; Miyazato, S.; Kaneko, T., Cyanobacterial megamolecule sacran efficiently forms LC gels with very heavy metal ions. *Langmuir* **2009,** *25* (15), 8526-31.
48. Radziuk, D.; Skirtach, A.; Sukhorukov, G.; Shchukin, D.; Möhwald, H., Stabilization of Silver Nanoparticles by Polyelectrolytes and Poly(ethylene glycol). *Macromol. Rapid Commun.* **2007,** *28* (7), 848-855.
49. Ershov, B. G.; Abkhalimov, E. V.; Solovov, R. D.; Roldughin, V. I., Gold nanoparticles in aqueous solutions: influence of size and pH on hydrogen dissociative adsorption and Au(iii) ion reduction. *Physical Chemistry Chemical Physics* **2016,** *18* (19), 13459-13466.
50. Mzwd, E.; Ahmed, N. M.; Suradi, N.; Alsaee, S. K.; Altowyan, A. S.; Almessiere, M. A.; Omar, A. F., Green synthesis of gold nanoparticles in Gum Arabic using pulsed laser ablation for CT imaging. *Scientific Reports* **2022,** *12* (1), 10549.
51. Panariello, L.; Radhakrishnan, A. N. P.; Papakonstantinou, I.; Parkin, I. P.; Gavriilidis, A., Particle Size Evolution during the Synthesis of Gold Nanoparticles Using In Situ Time-Resolved UV–Vis Spectroscopy: An Experimental and Theoretical Study Unravelling the Effect of Adsorbed Gold Precursor Species. *The Journal of Physical Chemistry C* **2020,** *124* (50), 27662-27672.
52. Stangherlin, S.; Cathcart, N.; Sato, F.; Kitaev, V., Gold Nanoprisms: Synthetic Approaches for Mastering Plasmonic Properties and Implications for Biomedical Applications. *ACS Appl. Nano Mater.* **2020,** *3* (8), 8304-8318.
53. DuChene, J. S.; Niu, W.; Abendroth, J. M.; Sun, Q.; Zhao, W.; Huo, F.; Wei, W. D., Halide Anions as Shape-Directing Agents for Obtaining High-Quality Anisotropic Gold Nanostructures. *Chem. Mater.* **2013,** *25* (8), 1392-1399.
54. Chen, L.; Ji, F.; Xu, Y.; He, L.; Mi, Y.; Bao, F.; Sun, B.; Zhang, X.; Zhang, Q., High-Yield Seedless Synthesis of Triangular Gold Nanoplates through Oxidative Etching. *Nano Lett.* **2014,** *14* (12), 7201-7206.
55. Millstone, J. E.; Hurst, S. J.; Métraux, G. S.; Cutler, J. I.; Mirkin, C. A., Colloidal Gold and Silver Triangular Nanoprisms. *Small* **2009,** *5* (6), 646-664.
56. Millstone, J. E.; Park, S.; Shuford, K. L.; Qin, L.; Schatz, G. C.; Mirkin, C. A., Observation of a Quadrupole Plasmon Mode for a Colloidal Solution of Gold Nanoprisms. *Journal of the American Chemical Society* **2005,** *127* (15), 5312-5313.

57. Tangeysh, B.; Moore Tibbetts, K.; Odhner, J. H.; Wayland, B. B.; Levis, R. J., Triangular Gold Nanoplate Growth by Oriented Attachment of Au Seeds Generated by Strong Field Laser Reduction. *Nano Lett.* **2015,** *15* (5), 3377-3382.
58. Germain, V.; Li, J.; Ingert, D.; Wang, Z. L.; Pileni, M. P., Stacking Faults in Formation of Silver Nanodisks. *The Journal of Physical Chemistry B* **2003,** *107* (34), 8717-8720.
59. Stevens, J. S.; Schroeder, S. L. M., Quantitative analysis of saccharides by X-ray photoelectron spectroscopy. *Surf. Interface Anal.* **2009,** *41* (6), 453-462.
60. Kang, F.; Qu, X.; Alvarez, P. J. J.; Zhu, D., Extracellular Saccharide-Mediated Reduction of Au3+ to Gold Nanoparticles: New Insights for Heavy Metals Biomineralization on Microbial Surfaces. *Environ. Sci. Technol.* **2017,** *51* (5), 2776-2785.
61. Xu, Z.; Uddin, K. M. A.; Kamra, T.; Schnadt, J.; Ye, L., Fluorescent Boronic Acid Polymer Grafted on Silica Particles for Affinity Separation of Saccharides. *ACS Appl. Mater. Interfaces* **2014,** *6* (3), 1406-1414.
62. Amat Yusof, F. A.; Yamaki, M.; Kawai, M.; Okajima, M. K.; Kaneko, T.; Mitsumata, T., Rheopectic Behavior for Aqueous Solutions of Megamolecular Polysaccharide Sacran. *Biomolecules* **2020,** *10* (1).
63. Doi, M.; Sagawa, Y.; Momose, S.; Tanaka, T.; Mizutani, T.; Okano, Y.; Masaki, H., Topical treatment with sacran, a sulfated polysaccharide from Aphanothece sacrum, improves corneocyte-derived parameters. *The Journal of Dermatology* **2017,** *44* (12), 1360-1367.
64. Biesinger, M. C., Advanced analysis of copper X-ray photoelectron spectra. *Surf. Interface Anal.* **2017,** *49* (13), 1325-1334.
65. Xia, J.; Dong, Z.; Cai, Y.; Guan, G.; Zhang, S.; Kovács, A.; Boothroyd, C.; Phang, I. Y.; Liu, S.; Wu, M.; Zhang, Y. W.; Hu, X.; Han, M.-Y., Morphological Growth and Theoretical Understanding of Gold and Other Noble Metal Nanoplates. *Chemistry – A European Journal* **2018,** *24* (58), 15589-15595.
66. Emam, H. E.; El-Bisi, M. K., Merely Ag nanoparticles using different cellulose fibers as removable reductant. *Cellulose* **2014,** *21* (6), 4219-4230.
67. Hebeish, A. A.; El-Rafie, M. H.; Abdel-Mohdy, F. A.; Abdel-Halim, E. S.; Emam, H. E., Carboxymethyl cellulose for green synthesis and stabilization of silver nanoparticles. *Carbohydr. Polym.* **2010,** *82* (3), 933-941.
68. Ahmed, H. B.; Abdel-Mohsen, A. M.; Emam, H. E., Green-assisted tool for nanogold synthesis based on alginate as a biological macromolecule. *RSC Adv.* **2016,** *6* (78), 73974-73985.
69. Ahmed, H. B.; Zahran, M. K.; Emam, H. E., Heatless synthesis of well dispersible Au nanoparticles using pectin biopolymer. *Int. J. Biol. Macromol.* **2016,** *91*, 208-219.
70. Berhault, G.; Bausach, M.; Bisson, L.; Becerra, L.; Thomazeau, C.; Uzio, D., Seed-Mediated Synthesis of Pd Nanocrystals: Factors Influencing a Kinetic- or Thermodynamic-Controlled Growth Regime. *The Journal of Physical Chemistry C* **2007,** *111* (16), 5915-5925.
71. Sajanlal, P. R.; Sreeprasad, T. S.; Samal, A. K.; Pradeep, T., Anisotropic nanomaterials: structure, growth, assembly, and functions. *Nano Reviews* **2011,** *2* (1), 5883.
72. Li, N.; Zhao, P.; Astruc, D., Anisotropic Gold Nanoparticles: Synthesis, Properties, Applications, and Toxicity. *Angew. Chem. Int. Ed.* **2014,** *53* (7), 1756-1789.
73. Xue, C.; Métraux, G. S.; Millstone, J. E.; Mirkin, C. A., Mechanistic Study of Photomediated Triangular Silver Nanoprism Growth. *Journal of the American Chemical Society* **2008,** *130* (26), 8337-8344.
74. Chu, H.-C.; Kuo, C.-H.; Huang, M. H., Thermal Aqueous Solution Approach for the Synthesis of Triangular and Hexagonal Gold Nanoplates with Three Different Size Ranges. *Inorg. Chem.* **2006,** *45* (2), 808-813.
75. Zhu, J.; Jin, X.-l., Electrochemical synthesis of gold triangular nanoplates and self-organized into rhombic nanostructures. *Superlattices Microstruct.* **2007,** *41* (4), 271-276.
76. Miranda, A.; Malheiro, E.; Skiba, E.; Quaresma, P.; Carvalho, P. A.; Eaton, P.; de Castro, B.; Shelnutt, J. A.; Pereira, E., One-pot synthesis of triangular gold nanoplates allowing broad and fine tuning of edge length. *Nanoscale* **2010,** *2* (10), 2209-2216.

77. Millstone, J. E.; Métraux, G. S.; Mirkin, C. A., Controlling the Edge Length of Gold Nanoprisms via a Seed-Mediated Approach. *Adv. Funct. Mater.* **2006,** *16* (9), 1209-1214.
78. Millstone, J. E.; Wei, W.; Jones, M. R.; Yoo, H.; Mirkin, C. A., Iodide Ions Control Seed-Mediated Growth of Anisotropic Gold Nanoparticles. *Nano Lett.* **2008,** *8* (8), 2526-2529.
79. Piella, J.; Bastús, N. G.; Puntes, V., Size-Controlled Synthesis of Sub-10-nanometer Citrate-Stabilized Gold Nanoparticles and Related Optical Properties. *Chem. Mater.* **2016,** *28* (4), 1066-1075.
80. Hendel, T.; Wuithschick, M.; Kettemann, F.; Birnbaum, A.; Rademann, K.; Polte, J., In Situ Determination of Colloidal Gold Concentrations with UV–Vis Spectroscopy: Limitations and Perspectives. *Anal. Chem.* **2014,** *86* (22), 11115-11124.
81. Jones, M. R.; Mirkin, C. A., Bypassing the Limitations of Classical Chemical Purification with DNA-Programmable Nanoparticle Recrystallization. *Angew. Chem. Int. Ed.* **2013,** *52* (10), 2886-2891.
82. Cheng, W.; Dong, S.; Wang, E., Iodine-Induced Gold-Nanoparticle Fusion/Fragmentation/Aggregation and Iodine-Linked Nanostructured Assemblies on a Glass Substrate. *Angew. Chem. Int. Ed.* **2003,** *42* (4), 449-452.
83. Alloyeau, D.; Dachraoui, W.; Javed, Y.; Belkahla, H.; Wang, G.; Lecoq, H.; Ammar, S.; Ersen, O.; Wisnet, A.; Gazeau, F.; Ricolleau, C., Unravelling Kinetic and Thermodynamic Effects on the Growth of Gold Nanoplates by Liquid Transmission Electron Microscopy. *Nano Lett.* **2015,** *15* (4), 2574-2581.
84. Choi, B. K.; Kim, J.; Luo, Z.; Kim, J.; Kim, J. H.; Hyeon, T.; Mehraeen, S.; Park, S.; Park, J., Shape Transformation Mechanism of Gold Nanoplates. *ACS Nano* **2023,** *17* (3), 2007-2018.
85. Baral, A.; Cavalieri, F.; Chattopadhyay, S.; Ashokkumar, M., Synthesis of Gold Nanosheets with Controlled Morphology by Combining a Natural Amino Acid with High-Frequency Ultrasound. *ACS Sustainable Chem. Eng.* **2021,** *9* (41), 13953-13962.
86. Khan, M.; Al-hamoud, K.; Liaqat, Z.; Shaik, M. R.; Adil, S. F.; Kuniyil, M.; Alkhathlan, H. Z.; Al-Warthan, A.; Siddiqui, M. R. H.; Mondeshki, M.; Tremel, W.; Khan, M.; Tahir, M. N., Synthesis of Au, Ag, and Au–Ag Bimetallic Nanoparticles Using Pulicaria undulata Extract and Their Catalytic Activity for the Reduction of 4-Nitrophenol. *Nanomaterials* **2020,** *10* (9), 1885.
87. Hervés, P.; Pérez-Lorenzo, M.; Liz-Marzán, L. M.; Dzubiella, J.; Lu, Y.; Ballauff, M., Catalysis by metallic nanoparticles in aqueous solution: model reactions. *Chem. Soc. Rev.* **2012,** *41* (17), 5577-5587.
88. Zhao, B.; Mele, G.; Pio, I.; Li, J.; Palmisano, L.; Vasapollo, G., Degradation of 4-nitrophenol (4-NP) using Fe–TiO2 as a heterogeneous photo-Fenton catalyst. *J. Hazard. Mater.* **2010,** *176* (1), 569-574.
89. Pandey, A. K.; Gaur, V. K.; Udayan, A.; Varjani, S.; Kim, S.-H.; Wong, J. W. C., Biocatalytic remediation of industrial pollutants for environmental sustainability: Research needs and opportunities. *Chemosphere* **2021,** *272*, 129936.
90. Salehi, S.; Abdollahi, K.; Panahi, R.; Rahmanian, N.; Shakeri, M.; Mokhtarani, B., Applications of Biocatalysts for Sustainable Oxidation of Phenolic Pollutants: A Review. *Sustainability* **2021,** *13* (15), 8620.
91. Ali, F.; Khan, S. B.; Kamal, T.; Anwar, Y.; Alamry, K. A.; Asiri, A. M., Anti-bacterial chitosan/zinc phthalocyanine fibers supported metallic and bimetallic nanoparticles for the removal of organic pollutants. *Carbohydr. Polym.* **2017,** *173*, 676-689.
92. Wunder, S.; Lu, Y.; Albrecht, M.; Ballauff, M., Catalytic Activity of Faceted Gold Nanoparticles Studied by a Model Reaction: Evidence for Substrate-Induced Surface Restructuring. *ACS Catal.* **2011,** *1* (8), 908-916.
93. Wunder, S.; Polzer, F.; Lu, Y.; Mei, Y.; Ballauff, M., Kinetic Analysis of Catalytic Reduction of 4-Nitrophenol by Metallic Nanoparticles Immobilized in Spherical Polyelectrolyte Brushes. *The Journal of Physical Chemistry C* **2010,** *114* (19), 8814-8820.
94. Zhou, X.; Xu, W.; Liu, G.; Panda, D.; Chen, P., Size-Dependent Catalytic Activity and Dynamics of Gold Nanoparticles at the Single-Molecule Level. *Journal of the American Chemical Society* **2010,** *132* (1), 138-146.

95. Monti, G. A.; Correa, N. M.; Falcone, R. D.; Silbestri, G. F.; Moyano, F., New Insights into the Catalytic Activity and Reusability of Water-Soluble Silver Nanoparticles. *ChemistrySelect* **2021,** *6* (29), 7436-7442.
96. Blanco, E.; Atienzar, P.; Hernández, P.; Quintana, C., The Langmuir–Hinshelwood approach for kinetic evaluation of cucurbit[7]uril-capped gold nanoparticles in the reduction of the antimicrobial nitrofurantoin. *Physical Chemistry Chemical Physics* **2017,** *19* (29), 18913-18923.
97. Rashid, M. H.; Mandal, T. K., Templateless Synthesis of Polygonal Gold Nanoparticles: An Unsupported and Reusable Catalyst with Superior Activity. *Adv. Funct. Mater.* **2008,** *18* (15), 2261-2271.
98. Bai, X.; Gao, Y.; Liu, H.-g.; Zheng, L., Synthesis of Amphiphilic Ionic Liquids Terminated Gold Nanorods and Their Superior Catalytic Activity for the Reduction of Nitro Compounds. *The Journal of Physical Chemistry C* **2009,** *113* (41), 17730-17736.
99. Kundu, S.; Lau, S.; Liang, H., Shape-Controlled Catalysis by Cetyltrimethylammonium Bromide Terminated Gold Nanospheres, Nanorods, and Nanoprisms. *The Journal of Physical Chemistry C* **2009,** *113* (13), 5150-5156.
100. Kaur, R.; Pal, B., Improved surface properties and catalytic activity of anisotropic shapes of photoetched Au nanostructures formed by variable energy laser exposure. *J. Mol. Catal. A: Chem.* **2014,** *395*, 7-15.
101. Bhosale, M. A.; Chenna, D. R.; Ahire, J. P.; Bhanage, B. M., Morphological study of microwave-assisted facile synthesis of gold nanoflowers/nanoparticles in aqueous medium and their catalytic application for reduction of p-nitrophenol to p-aminophenol. *RSC Adv.* **2015,** *5* (65), 52817-52823.
102. Zhu, Q.; Zhang, W.; Cai, J.; Li, J.; Zhong, L.; Pu, S.; Li, A., Morphology-controlled synthesis of gold nanoparticles with chitosan for catalytic reduction of nitrophenol. *Colloids and Surfaces A: Physicochemical and Engineering Aspects* **2022,** *640*, 128471.
103. Cárdenas-Lizana, F.; Hao, Y.; Crespo-Quesada, M.; Yuranov, I.; Wang, X.; Keane, M. A.; Kiwi-Minsker, L., Selective Gas Phase Hydrogenation of p-Chloronitrobenzene over Pd Catalysts: Role of the Support. *ACS Catal.* **2013,** *3* (6), 1386-1396.
104. Zhong, R.-Y.; Sun, K.-Q.; Hong, Y.-C.; Xu, B.-Q., Impacts of Organic Stabilizers on Catalysis of Au Nanoparticles from Colloidal Preparation. *ACS Catal.* **2014,** *4* (11), 3982-3993.
105. Fountoulaki, S.; Daikopoulou, V.; Gkizis, P. L.; Tamiolakis, I.; Armatas, G. S.; Lykakis, I. N., Mechanistic Studies of the Reduction of Nitroarenes by NaBH4 or Hydrosilanes Catalyzed by Supported Gold Nanoparticles. *ACS Catal.* **2014,** *4* (10), 3504-3511.
106. Arif, M.; Shahid, M.; Irfan, A.; Nisar, J.; Wu, W.; Farooqi, Z. H.; Begum, R., Polymer microgels for the stabilization of gold nanoparticles and their application in the catalytic reduction of nitroarenes in aqueous media. *RSC Adv.* **2022,** *12* (9), 5105-5117.
107. Kemas, C. U.; Ngwuluka, N. C.; Ochekpe, N. A.; Nep, E. I., Starch-based xerogels: Effect of acetylation on Physicochemical and rheological properties. *Int. J. Biol. Macromol.* **2017,** *98*, 94-102.
108. de Resende, M. A.; Pedroza, G. A.; Macêdo, L. H. G. M. C.; de Oliveira, R.; Amela-Cortes, M.; Molard, Y.; Molina, E. F., Design of polyurea networks containing anticancer and anti-inflammatory drugs for dual drug delivery purposes. *J. Appl. Polym. Sci.* **2022,** *139* (16).
109. Ibeaho, W. F.; Chen, M.; Shi, J.; Chen, C.; Duan, Z.; Wang, C.; Xie, Y.; Chen, Z., Multifunctional Magnetic Hydrogels Fabricated by Iron Oxide Nanoparticles Mediated Radical Polymerization. *ACS Applied Polymer Materials* **2022,** *4* (6), 4373-4381.
110. Islam, F.; Wong, S. Y.; Li, X.; Arafat, M. T., Pectin and mucin modified cellulose-based superabsorbent hydrogel for controlled curcumin release. *Cellulose* **2022,** *29* (9), 5207-5222.
111. Yu, Y.; Chau, Y., One-Step "Click" Method for Generating Vinyl Sulfone Groups on Hydroxyl-Containing Water-Soluble Polymers. *Biomacromolecules* **2012,** *13* (3), 937-942.
112. Mondal, S.; Das, S.; Nandi, A. K., A review on recent advances in polymer and peptide hydrogels. *Soft Matter* **2020,** *16* (6), 1404-1454.
113. Kong, J.-H.; Oh, E. J.; Chae, S. Y.; Lee, K. C.; Hahn, S. K., Long acting hyaluronate – exendin 4 conjugate for the treatment of type 2 diabetes. *Biomaterials* **2010,** *31* (14), 4121-4128.

114. Yadollahi, M.; Farhoudian, S.; Barkhordari, S.; Gholamali, I.; Farhadnejad, H.; Motasadizadeh, H., Facile synthesis of chitosan/ZnO bio-nanocomposite hydrogel beads as drug delivery systems. *Int. J. Biol. Macromol.* **2016,** *82*, 273-278.
115. Yadollahi, M.; Namazi, H.; Aghazadeh, M., Antibacterial carboxymethyl cellulose/Ag nanocomposite hydrogels cross-linked with layered double hydroxides. *Int. J. Biol. Macromol.* **2015,** *79*, 269-277.
116. Nagaraja, K.; Tae Hwan, O., Green synthesis of Multifunctional Zinc oxide Nanoparticles from Cordia myxa gum; and their Catalytic Reduction of Nitrophenol, Anticancer and Antimicrobial Activity. *Int. J. Biol. Macromol.* **2023,** *253*, 126788.
117. Wirunchit, S.; Koetniyom, W., ZnO Nanoparticles Synthesis and Characterization by Hydrothermal Process for Biological Applications. *physica status solidi (a)* **2023,** *220* (10), 2200364.
118. Wathoni, N.; Motoyama, K.; Higashi, T.; Okajima, M.; Kaneko, T.; Arima, H., Physically crosslinked-sacran hydrogel films for wound dressing application. *Int. J. Biol. Macromol.* **2016,** *89*, 465-470.
119. Wathoni, N.; Motoyama, K.; Higashi, T.; Okajima, M.; Kaneko, T.; Arima, H., Enhancing effect of γ-cyclodextrin on wound dressing properties of sacran hydrogel film. *Int. J. Biol. Macromol.* **2017,** *94*, 181-186.
120. Amornwachirabodee, K.; Okajima, M. K.; Kaneko, T., Uniaxial Swelling in LC Hydrogels Formed by Two-Step Cross-Linking. *Macromolecules* **2015,** *48* (23), 8615-8621.
121. Saosamniang, P.; Singh, M.; Ali, M. A.; Takada, K.; Okajima, M. K.; Kaneko, T., Gold nanoparticle morphology adjusted as high-performance catalyses in supergiant dispersant. *Surfaces and Interfaces* **2024,** *45*, 103904.
122. Dodero, A.; Scarfi, S.; Pozzolini, M.; Vicini, S.; Alloisio, M.; Castellano, M., Alginate-Based Electrospun Membranes Containing ZnO Nanoparticles as Potential Wound Healing Patches: Biological, Mechanical, and Physicochemical Characterization. *ACS Appl. Mater. Interfaces* **2020,** *12* (3), 3371-3381.
123. Gholamali, I.; Yadollahi, M., Doxorubicin-loaded carboxymethyl cellulose/Starch/ZnO nanocomposite hydrogel beads as an anticancer drug carrier agent. *Int. J. Biol. Macromol.* **2020,** *160*, 724-735.
124. P, M. R.; Muraleedaran, K.; Mujeeb, V. M. A., Applications of chitosan powder with in situ synthesized nano ZnO particles as an antimicrobial agent. *Int. J. Biol. Macromol.* **2015,** *77*, 266-272.
125. Sudheesh Kumar, P. T.; Lakshmanan, V.-K.; Anilkumar, T. V.; Ramya, C.; Reshmi, P.; Unnikrishnan, A. G.; Nair, S. V.; Jayakumar, R., Flexible and Microporous Chitosan Hydrogel/Nano ZnO Composite Bandages for Wound Dressing: In Vitro and In Vivo Evaluation. *ACS Appl. Mater. Interfaces* **2012,** *4* (5), 2618-2629.
126. Li, S.-D.; Huang, L., Pharmacokinetics and Biodistribution of Nanoparticles. *Molecular Pharmaceutics* **2008,** *5* (4), 496-504.
127. Rasmussen, J. W.; Martinez, E.; Louka, P.; Wingett, D. G., Zinc oxide nanoparticles for selective destruction of tumor cells and potential for drug delivery applications. *Expert Opin Drug Deliv* **2010,** *7* (9), 1063-77.
128. Cho, K.; Wang, X.; Nie, S.; Chen, Z.; Shin, D. M., Therapeutic Nanoparticles for Drug Delivery in Cancer. *Clinical Cancer Research* **2008,** *14* (5), 1310-1316.
129. High Resolution XPS of Organic Polymers: The Scienta ESCA300 Database (Beamson, G.; Briggs, D.). *J. Chem. Educ.* **1993,** *70* (1), A25.
130. Gobbo, P.; Mossman, Z.; Nazemi, A.; Niaux, A.; Biesinger, M. C.; Gillies, E. R.; Workentin, M. S., Versatile strained alkyne modified water-soluble AuNPs for interfacial strain promoted azide–alkyne cycloaddition (I-SPAAC). *Journal of Materials Chemistry B* **2014,** *2* (13), 1764-1769.
131. Elumalai, K.; Velmurugan, S., Green synthesis, characterization and antimicrobial activities of zinc oxide nanoparticles from the leaf extract of Azadirachta indica (L.). *Appl. Surf. Sci.* **2015,** *345*, 329-336.

132. Lin, B.; Chen, H.; Liang, D.; Lin, W.; Qi, X.; Liu, H.; Deng, X., Acidic pH and High-H2O2 Dual Tumor Microenvironment-Responsive Nanocatalytic Graphene Oxide for Cancer Selective Therapy and Recognition. *ACS Appl. Mater. Interfaces* **2019,** *11* (12), 11157-11166.
133. Ono, S.; Imai, R.; Ida, Y.; Shibata, D.; Komiya, T.; Matsumura, H., Increased wound pH as an indicator of local wound infection in second degree burns. *Burns* **2015,** *41* (4), 820-824.
134. Vandebriel, R. J.; De Jong, W. H., A review of mammalian toxicity of ZnO nanoparticles. *Nanotechnol Sci Appl* **2012,** *5*, 61-71.
135. Dodero, A.; Alloisio, M.; Castellano, M.; Vicini, S., Multilayer Alginate–Polycaprolactone Electrospun Membranes as Skin Wound Patches with Drug Delivery Abilities. *ACS Appl. Mater. Interfaces* **2020,** *12* (28), 31162-31171.
136. Paul, K. B.; Singh, V.; Vanjari, S. R. K.; Singh, S. G., One step biofunctionalized electrospun multiwalled carbon nanotubes embedded zinc oxide nanowire interface for highly sensitive detection of carcinoma antigen-125. *Biosens. Bioelectron.* **2017,** *88*, 144-152.
137. Yazdi, A. S.; Guarda, G.; Riteau, N.; Drexler, S. K.; Tardivel, A.; Couillin, I.; Tschopp, J., Nanoparticles activate the NLR pyrin domain containing 3 (Nlrp3) inflammasome and cause pulmonary inflammation through release of IL-1α and IL-1β. *Proceedings of the National Academy of Sciences* **2010,** *107* (45), 19449-19454.
138. Chi, L.; Wolff, J. J.; Laremore, T. N.; Restaino, O. F.; Xie, J.; Schiraldi, C.; Toida, T.; Amster, I. J.; Linhardt, R. J., Structural Analysis of Bikunin Glycosaminoglycan. *Journal of the American Chemical Society* **2008,** *130* (8), 2617-2625.

CHAPTER III

Controlling Gold Nanoparticle Morphology with Supergiant Polysaccharide: A Potential Way for Catalysis.

3.1 Introduction

The distinctive anisotropic configuration of gold nanoparticles (AuNPs), deviating from the conventional spherical shape, results in shape-dependent optical, magnetic, and catalytic attributes. These distinct characteristics position anisotropic AuNPs as compelling candidates for a myriad of applications, spanning biosensing, drug delivery, imaging, and environmental monitoring.[72] Additionally, the ability to functionalize anisotropic AuNPs with different molecules further enhances their potential applications. Therefore, researchers are actively exploring the synthesis, characterization, and applications of anisotropic AuNPs to advance our understanding of their features and promising applications across diverse fields.

Particularly noteworthy are gold nanotriangles (AuNTs), which have garnered significant attention due to their exceptional localized surface plasmon resonance (LSPR) property and extremely high anisotropy.[73] Although various synthetic techniques exist for producing gold nanoplates, achieving highly monodispersed AuNTs remains a considerable challenge. The initial report on AuNT synthesis using bio-products dates back to the 2000s when Sastry et al. utilized lemongrass plant extract for the preparation of AuNTs.[18] Synthetic strategies have continued to evolve, encompassing approaches such as thermal reduction approach,[74] electrochemical approach,[75] photocatalytic approach,[76] and seed-mediated growth method.[77, 78] Among these, the seed-mediated growth method stands out as the most popular due to its relatively higher throughput and straightforward setup. In the realm of AuNTs bio-synthesis, persistent challenges have hampered progress. Several challenges impede progress in the practical application and further development of AuNTs, including incomplete comprehension of the growth mechanism, suboptimal shape purity (below 70%), and the intricacies involved in synthesizing AuNTs with a small size, specifically with less than 100 nm edge length. These combined hurdles pose obstacles to the broader utilization and advancement of AuNTs.

We explored innovative insights into a novel green synthesis approach for producing Au nanotriangles (AuNTs) and Au nanodecahedrons (AuNDs) with high shape selectivity (size distribution: 62 ± 10 nm), utilizing supergiant polysaccharide sacran as the main reducing and super-stabilizing agent. The key factors ensuring elevated shape purity and selectivity involve leveraging the reduction properties of anionic super dispersant mega-polysaccharides, sacran, in conjunction with the gold precursor to regulate the Au(I) species. This control is further enhanced by the use of uniform Au seeds as the growth template and iodide anions as the shape-directing agents, resulting in distinctive Au morphologies compared to the low shape purity and selectivity method, as detailed in the section on Au nanoplates formation using only sacran as the reducing and stabilizing agent. Moreover, the varied Au shapes obtained enhance the catalytic activity of 4-nitrophenol when compared to common reducing or stabilizing agents, attributed to the high stability in the sacran medium, as indicated by a zeta potential value of -22 mV. The catalytic performances of obtained Au shapes also show higher specific rate compared to recent other polysaccharide media such as carboxymethyl cellulose or chitosan, owing to the more uniform size and shape of the catalysts. The high conversion rate of chloro-substituted nitroarenes (> 99%) is attributed to their superior uniformity, high active surface area accessibility, and dispersion within the catalytic system of super dispersant mega-saccharides. The high shape purity AuNTs may open new avenues for applications in photothermal therapy owing to the high intensity of surface plasmons in the Near-IR region and the development of eco-friendly catalysts due to the large active surface area.

3.2 Materials and methods

3.2.1 Materials

Sacran was extracted from the cyanobacterium Aphanothece sacrum (A. sacrum) cyanobacterium, which was dedicated from Kisendou Inc. (Asakura, Japan). Isopropanol, sodium hydroxide, and ethanol were used for sacran polysaccharide extraction. Gold precursor ($HAuCl_4 \cdot 3H_2O$, ≥99.9%), sodium borohydride ($NaBH_4$, Reagentplus, 99%), trisodium citrate dihydrate ($C_6H_9Na_3O_9$, 99%), tannic acid ($C_{76}H_{52}O_{46}$, ACS reagent), potassium carbonate (K_2CO_3, >99%), potassium iodide (KI, >99.5%), 4-Nitrophenol (TCI, >99.0%), 4-Chloronitrobenzene (TCI, >98.0%), 2,4-Dichloronitrobenzene (TCI, >99.0%), and 1,4-Dichloro-2-nitrobenzene (TCI,

>99.0%) were procured from Sigma-Aldrich and TCI. Milli-Q water was used for preparation of all solutions.

3.2.2 Synthesis of AuNTs

$HAuCl_4$ solution (10 µL, 25 mM) was added to a mixture of sodium citrate solution (1.5 mL, 2 mM), tannic acid (1 µL, 2.5 mM), and potassium carbonate (10 µL, 150 mM). The mixture was heated to 70 °C and stirred for 2 min. After stirring, it was allowed to stand at 70 °C for 5 min [79]. The solution exhibited a reddish color, signaling the generation of Au seeds (Solution A). At 70 °C, an aqueous solution of $HAuCl_4$ (0.014 wt. %) was introduced into a sacran solution (10 ml, 0.10 wt. %), and the mixture was stirred for 30 min. The subtle yellow hue of the initial solution disappeared (Solution B). Thereafter, 20 µL of solution A was added to solution B. An aqueous solution of KI (20 µL, 10 mM) was then added to the resulting mixture. The obtained solution was left to stand at 25 °C for 24 h.

3.2.3 Catalytic ability evaluation of 4-NP

The reduction of 4-NP to 4-AP by AuNPs was assessed with the participation of $NaBH_4$. Initially, a 20 mL glass vial was used to prepare a solution containing 4-NP (10 mL, 0.17 mM). Subsequently, carefully measured volumes of the AuNP dispersions and $NaBH_4$ aqueous solution (1 mL, 100 mM) were introduced into the same glass vial. The progression of the gold catalytic reduction was monitored using an ultraviolet-visible-near-infrared (UV–vis–NIR) spectrometer, by observing the changes in the reaction mixture.

The colloidal gold concentrations were determined using a UV-vis-NIR spectrometer. The molar concentration of AuNPs was determined according to Equation 1

$$A = \varepsilon CL, \tag{1}$$

where A is the absorbance of light at a specific wavelength, ε is the molar absorptivity($M^{-1}cm^{-1}$) for specific Au morphologies previously measured by Jones et al. and Hendel et al., [80, 81] C is the molar concentration of the absorbing material (M), and L represents the optical path length (cm).

The number concentration of the gold nanoparticles was determined by Equation 2:

$$C = N/6.02 \times 10^{23}, \tag{2}$$

N represents the number concentration of the AuNPs (particles/L) and 6.02×10^{23} is the Avogadro's number.

The volume of each Au morphology was estimated by measuring its dimensions. We utilized transmission electron microscopy (TEM) images and a software (Image–J) to measure the particle dimensions, allowing the volume to be calculated.

The mass of single AuNPs was determined according Equation 3

$$\rho = m/V, \tag{3}$$

where ρ is the density of the AuNP (19.3 g/cm^3), m represents the weight of a single AuNP (g), and V represents the dimension of a single AuNP (cm^3).

Calculation of The Usage Catalyst Mass Concentration

Samples	Absorbance	Molar extinction coefficient (ε, $M^{-1}cm^{-1}$)	Particle molarity (C, M)	Number concentration (particles/mL)	Surface area of the catalyst (nm^2)	Mass of the catalyst used (μg)
AuNSs	0.273	3.36×10^{9}	8.03×10^{-11}	4.83×10^{10}	1256.83	5.64
AuNDs	0.620	3.69×10^{10}	1.68×10^{-11}	1.01×10^{10}	1635.61	5.64
AuNTs	0.531	2.41×10^{10}	2.19×10^{-11}	1.31×10^{10}	2610.16	5.64

The final concentration of Au nanospheres (AuNSs), AuNTs, and Au nanodecahedrons (AuNDs) was 5.64 mg/L.

The reaction rate of the AuNPs was determined by Pseudo-first-order kinetics according to Equation 4

$$ln\left(\frac{A_t}{A_0}\right) = -kt, \tag{4}$$

k represents the pseudo-first-order reaction constant, A_0, A_t are the maximum absorbance of product at the specified times 0 and t, respectively.

The AuNSs, AuNTs, and AuNDs were separated from 4-AP solution through centrifugation. Subsequently, they were dried, redispersed, and examined for recyclability under identical experimental conditions.

3.2.4 Catalytic ability evaluation of nitroarenes

10 mL of various nitroarenes (0.17 mM) were introduced into a glass vial. Subsequently, the previously determined concentration of AuNPs and a 1 mL aqueous solution containing 100 mM $NaBH_4$ were added to the same glass vial. The reduction progress was monitored using UV–vis–NIR spectrometer, which recorded the time-dependent changes in absorbance spectra until reaching a stable state. The kinetics analysis of a series of nitroarenes with different positions of chlorine substitution, was conducted employing eq.4. The obtained solutions were subjected to mixing with 10 mL of ethyl acetate to facilitate the extraction of the reactant and product. Subsequently, the organic layer was evaluated using gas chromatography mass spectrometry (GC-MS) to ascertain the conversion and selectivity of each nitroarene reduction.

3.2.5 Cell Culture Experiments

A549, HDF, and L929 cells were cultured using Dulbecco's Modified Eagle Medium (DMEM). Each cell line was grown in media supplemented with 10% fetal bovine serum (FBS) and maintained in cell culture plates. The incubation took place in a biological incubator set at 37°C with a humidified atmosphere.

3.2.6 Cytotoxicity studies

A549, HDF, and L929 cells were detached using trypsin and seeded in 96-well plates at a density of 10,000 cells per well. After 24 hours, the cells were exposed to varying concentrations of gold nanotriangles (10, 25, 50, and 100 µg/mL) in a 0.05 wt.% sacran solution prepared in DMEM with 10% FBS. Each concentration was tested in triplicate. Untreated cells served as negative controls, and cells exposed to laser treatment served as an additional control. Following 24 hours of treatment, the media was replaced with a 10 µg/mL MTT reagent solution prepared in DMEM without FBS. The plates were shaken for 10 minutes, and absorbance was measured using a microplate reader (Infinite 200 Pro Nano Plus) after 4 hours of incubation at 540 nm. The percentage of cell viability was calculated using the following equation:

$$\% \text{ Cell viability} = \left(\frac{\text{Absorbance of control wells}}{\text{Absorbance of test wells}}\right) \times 100 \quad (1)$$

3.2.7 Photothermal Heating

To investigate photothermal heating, gold nanotriangle (AuNT) dispersions were irradiated using a (808 nm, 1 W) laser. Various concentrations of AuNTs (5, 10, 25, 50, and 100 μg/mL, expressed as gold concentrations) were prepared, and 500 μL aliquots were placed in quartz cuvettes with a 1 cm optical path length. These cuvettes were positioned along the optical axis of the laser. Once the samples reached thermal equilibrium with their surroundings, the temperature of the colloidal dispersions was measured using a thermometer placed at the top of the cuvettes. The temperature increase during laser irradiation was recorded over a period of 300 seconds.

3.2.8 Evaluation of Laser Irradiation Effects

The impact of laser irradiation was assessed on A549, HDF, and L929 cells cultured under the same conditions as those used in the cytotoxicity studies. Following 24 hours of incubation with gold nanotriangles (AuNTs) at concentrations of 5, 10, 25, 50, and 100 μg/mL, the cells were subjected to a 10-minute irradiation using a laser (808 nm, 1 W). Three hours post-irradiation, the cells were stained with Ethidium Homodimer-1 (EtHD-1) and Calcein AM to assess viability. Cell viability was immediately examined using all-in-one fluorescence microscope (Keyence, BZ-X810).

3.2.9 Measurements

UV-vis-NIR spectra were acquired using a Jasco V-770 spectrometer (Tsukuba, Japan) at wavelengths range from 200 to 1300 nm. Transmission electron microscope (TEM) was conducted using a Hitashi H-7650 with the beam current of 10 μA, operating voltage of 100 kV, and filament voltage of 20 V. JEM-ARM200F high-angle annular dark-field scanning transmission electron microscopy (HAADF-STEM) was employed, along with selected area electron diffraction (SAED), to investigate the crystallinity of AuNPs and elemental analyzer of energy dispersive X-ray spectroscopy (EDS) was utilized for elemental analysis. The specimen for TEM and STEM characterization were prepared by evaporation of 5 μL dilute solution onto a TEM grid. High-resolution scanning electron microscopy (HRSEM) images were recorded using a Hitachi S-5200 with the operating voltage of 10 kV. The average particle size of the AuNPs was measured using an Image-J analysis software. The process and mechanism of AuNPs formation were investigated

using X-ray photoelectron spectroscopy (XPS) with a Kratos Axis Ultra DLD instrument. X-ray diffraction (XRD) pattern was measured on powder XRD diffractometer (RINT-2500) operating at a voltage of 40 kV, the tube current of 30 mA, and the degree of measurement is between 10–90º. Dynamic light scattering (DLS) was performed on a Zetasizer Nano ZS90 instrument (Malvern Instruments Ltd., England) to determine the hydrodynamic size distribution, zeta potential (ζ) values, and molecular weight of all samples. The analyzed concentration of sacran was 0.5 mg/mL or 0.05 wt.%, and the sacran-AuNPs colloidal solution was diluted 100 times before analysis. The catalytic reaction products underwent testing and analysis using a JMS-T200GC AccuTOF system equipped with gas chromatography mass spectrometry (GC-MS).

3.3 Results and Discussion

3.3.1 Formation of controllable shape AuNTs

As discussed previously, the concentration of sacran significantly influences the morphology of gold, primarily because of the strong binding interactions between Au(III) species and the carboxyl anion, as well as the hydroxyl coordination of sacran. These interactions guide Au(0) atoms to specific crystalline facets, ultimately shaping the gold morphology. Alterations in the sacran aqueous solution concentration relative to $HAuCl_4$ concentration, under varied conditions, result in the development of anisotropic gold nanoparticles (AuNPs). However, the particle size of Au nanoplates (AuNPLs) exhibits a wide range, spanning from 2.1 μm to 207 nm. Diverse AuNP morphologies, including triangular with a tail (639 ± 32 nm), broken plates (679 ± 213 nm), quasi-elongated plates (402 ± 23 nm), and spherical AuNPs (20 ± 14 nm), account for approximately 30 ± 5% compared to hexagonal and triangular AuNPLs. To address the challenges of achieving uniform sizes in AuNPL morphology, a modified synthesis method involving iodide anions as size-controlling and shape-directing ligands was employed.[52]

Here, we discuss AuNPs formation steps as follows. First, a nanoparticle precursor ($HAuCl_4$) is partially reduced from Au(III) to Au(I) species and Au(0) atoms by sacran:$HAuCl_4$ (14.0:1) during stirring and heating at 70 ºC for 30 min. The reduction prevented secondary nucleation of Au(0) during growth. Second, the injected Au seeds were used as scaffolds, which confirmed the existence of Au(I) intermediate species on their surfaces during the final reduction. Third, iodide anions were added to the remaining non-reduced gold precursor to reduce Au(I) to Au(0) atoms

completely and adsorb onto gold seeds to govern the morphology and dimensions of the AuNTs. Iodide anions are known to strongly adsorb on the (100) facets of gold. This preferential adsorption can inhibit the growth of (100) facets, leading to the selective growth of other facets like (111).

The anisotropic growth along specific crystallographic directions results in the formation of triangular shapes [53]. Fig. 19a and b present high-resolution SEM images and UV-vis-NIR spectra of the AuNTs. The reduction in the absorbance at λ_{max} ~520 nm suggests that the concentration of AuNSs decreased compared to the previous synthesis method. During synthesis, the intensity in the near-infrared region at λ_{max} ~903 nm increased sharply over time up to 24 h owing to the high production of AuNTs. The oxidation states of Au after reduction by sacran and after the addition of iodide anions were determined using XPS (Fig. 20). After the reduction of the Au(III) species by sacran, the Au 4f region presented two sets of doublets of Au species at 83.7 and 87.4 eV, corresponding to the binding energies of Au(0) $4f_{7/2}$ and Au(0) $4f_{5/2}$, respectively, indicating the stable form of Au(0). Additionally, the peaks at 84.7 and 88.5 eV correspond to Au(I) $4f_{7/2}$ and Au(I) $4f_{5/2}$, which indicate the intermediate species of gold ions during the reduction using sacran alone as the reducing agent. After adding iodide anions, two strong fitted XPS peaks at 83.7 and 87.4 eV corresponding to Au(0) $4f_{7/2}$ and Au(0) $4f_{5/2}$ increased while the peaks correspond to intermediate gold species (Au(I) $4f_{7/2}$ and Au(I) $4f_{5/2}$) disappeared. In addition, the atomic percentages of Au(0) $4f_{7/2}$ and Au(0) $4f_{5/2}$ increased from 28.84 and 21.77% to 55.20 and 44.80% , respectively (Table 7). These results indicate that the complete reduction of gold ions using sacran and iodide anions as reducing and shape-directing agents induces the uniform formation of AuNTs. In addition, the reduction of Au(III) to Au(I) using sacran as the reducing agent under 70 ºC for 30 min can also be seen by the disappearance in color from pale yellow gold precursor. To elucidate the importance of Au(I) as an intermediate species in the growth of AuNTs, we performed control experiments using seeds and iodide as the reducing agent, without the addition of sacran. We found that the gold precursor could not be completely reduced to Au(0) because a pale yellow color was still observed, and new nuclei were formed instead of the seeds growth that became AuNSs. This was owing to the ability of iodide anions to reduce the gold precursor (Fig. 20a) [52, 82]. Another control experiment involved the utilization of seeds, sacran, and iodide without catalyzed by temperature of the first reduction step by sacran. The added seeds grew and became penta-twinned decahedrons at high aspect ratios because of the uncontrollable Au(I) species (Fig. 20b). Therefore, it can be inferred that sacran performs a crucial role in reducing Au(III) to Au(I),

which is an intermediate species that controls the reduction rate for the growth of AuNTs. Furthermore, the supergiant size of sacran can impart nanoparticles with high dispersion stability to induce efficient growth of nanoparticles.We also studied the effect of iodide on gold facets. Energy-dispersive spectroscopy (EDS) of the STEM image (Fig. 19c) was used to determine the elemental distribution on the AuNTs, as shown in Fig. 19d-f, which presents the iodide anions absorbed on the AuNT surfaces and high density of oxygen on the edges and corners of AuNTs.

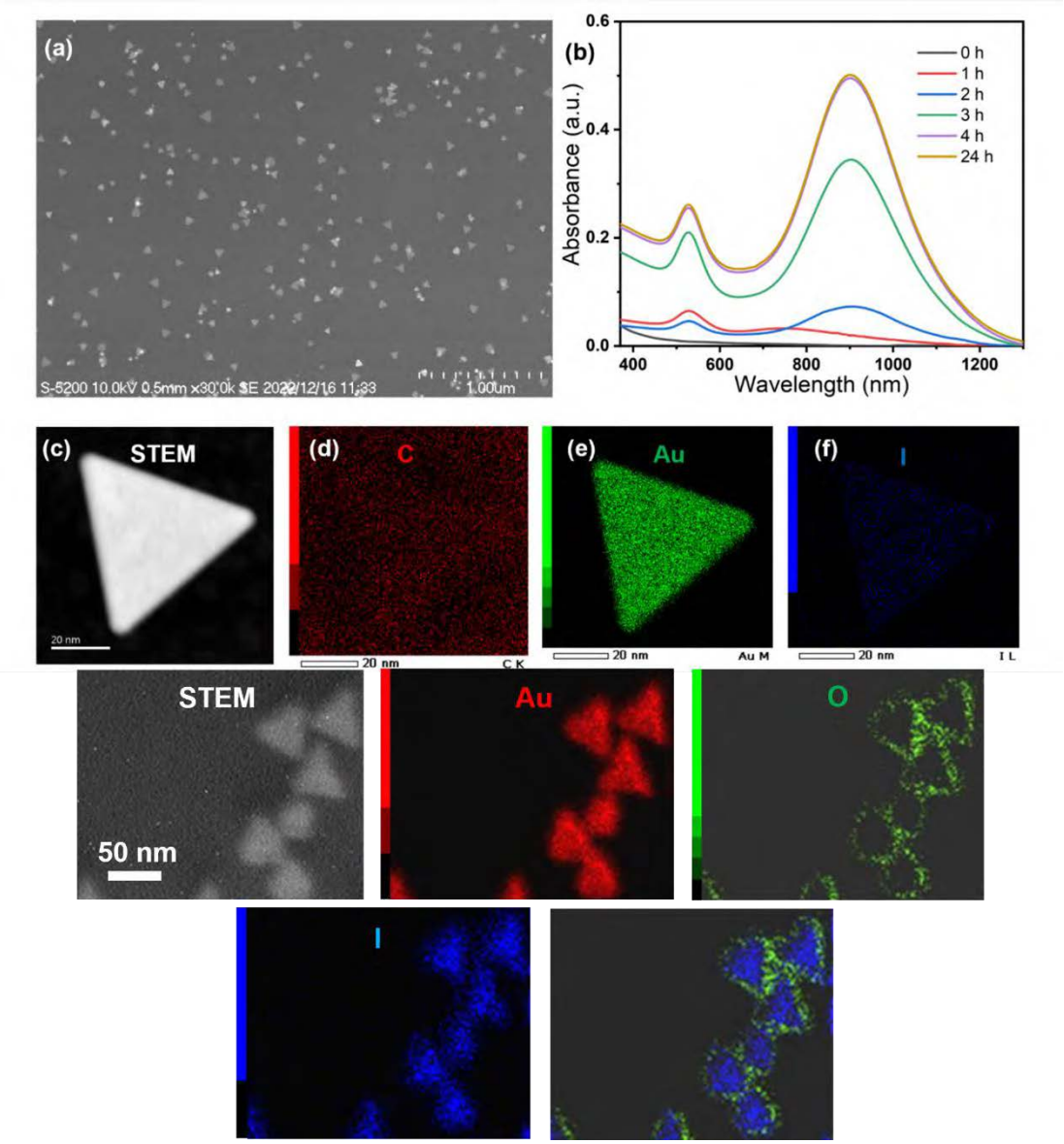

Fig. 19. HRSEM image of the AuNTs formed after 4 h at 25°C using sacran and iodide anions as the reducing agents (a). UV-vis-NIR spectra of the obtained AuNTs (b). HAADF–STEM image of a single gold nanotriangle (c). and EDS mapping of the distribution of C, Au, O and I elements on AuNT (d-f).

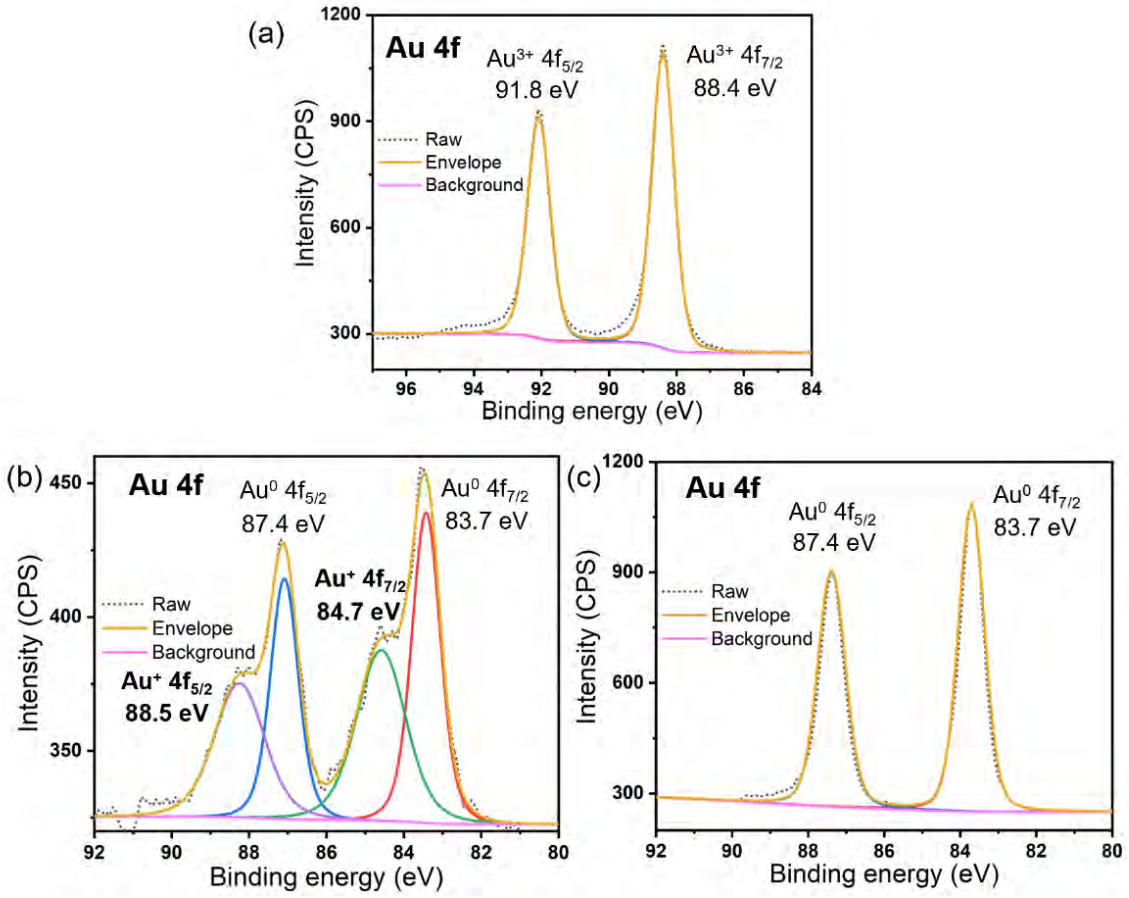

Fig. 20. High resolution XPS profiles spectrum of Au 4f regions: gold precursor before reduction (a) gold ions before addition of iodide anions (b) and after addition of iodide anions (c).

Table 7. Quantification of the chemical state of Au 4f of gold ions after reduction by sacran and gold ions after complete reduction with sacran and iodide.

Sample	Before addition of iodide anions		After addition of iodide anions	
Peaks	**Binding energy (eV)**	**Atomic concentration (%)**	**Binding energy (eV)**	**Atomic concentration (%)**
Au^0 $4f_{7/2}$	83.4	28.84	83.7	55.20
Au^0 $4f_{5/2}$	87.1	21.77	87.4	44.80
Au^+ $4f_{7/2}$	84.6	27.46	x	x
Au^+ $4f_{5/2}$	88.2	21.93	x	x

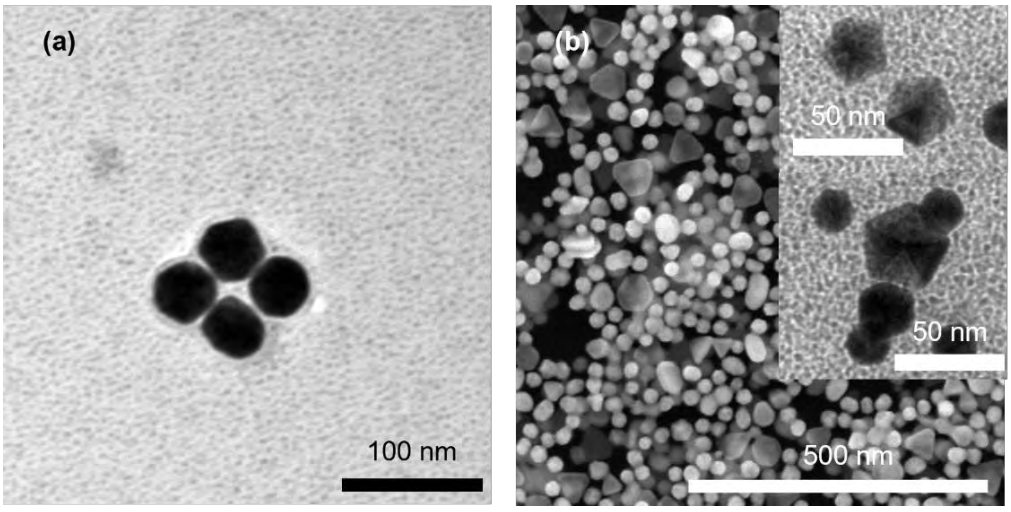

Fig. 21. TEM image of AuNS formed using gold template seeds and only iodide as a reducing agent without the addition of sacran (a) and HRSEM image of gold penta-twinned decahedrons formed using the seeds, sacran, and iodide, without the first reduction step by sacran (b).

The STEM images, including the inset images, elucidate the individual gold nanotriangle (AuNT) particle, revealing an interplanar spacing of 0.24 nm, consistent with the (111) facet, as depicted in Fig. 22a. The selected-area electron diffraction (SAED) pattern confirms the capping of these AuNTs by atomically flat gold (111) facets, as illustrated in Fig. 22b. Notably, the presence of a 1/3(422) SAED spot indicates a stacking fault parallel to the (111) facet, aligning with previous observations [83], [84], [58]. An additional factor contributing to anisotropic growth is the structure of the template seeds. As showcased in Fig. 22c-d, the gold seeds exhibit two distinct structures: penta- and planar-twinned morphologies. The growth mechanism suggests that the penta- and planar-twinned seed morphologies transform into penta-twinned decahedral nanoparticles and hexagonal or triangular nanoparticles, respectively [53]. This transformation is influenced by the reduction rate of sacran and iodide reducing agents, as illustrated in Fig. 23 and Fig. 24. Remarkably, the modified synthesis method achieved high yields of AuNTs (approximately 92% area ratio) and decahedral gold nanoparticles (AuNDs) (approximately 8% area ratio), as demonstrated in Fig. 25. The uniform sizes of AuNTs and AuNDs were found to be 62 ± 10 nm and 26 ± 8 nm, respectively. This suggests that oxidized sacran molecules, in conjunction with iodide anions acting as both reducing and shape-directing agents, are crucial in regulating the growth of gold seeds into AuNTs, obviating the necessity for supplementary reducing or capping agents.

The stability of sacran-partially reduced AuNTs and AuNDs was evaluated, and the findings are summarized in Table 8. Both Au nanostructures exhibited stability in sacran medium, as evidenced by their zeta potential (ζ) values of -24.47 ± 0.88 and -22.05 ± 0.90. The recorded average hydrodynamic sizes were larger than those determined by electron microscopy due to sacran's high water-absorbing capacity, leading to its coating around AuNPs. Moreover, low polydispersity index (PDI) values indicated the production of nearly monodisperse AuNPs. This achievement was realized through a modified synthesis method incorporating sacran as the reducing agent, aided by iodide anions. The resulting colloidal solutions of sacran-AuNPs are depicted in Fig. 26.

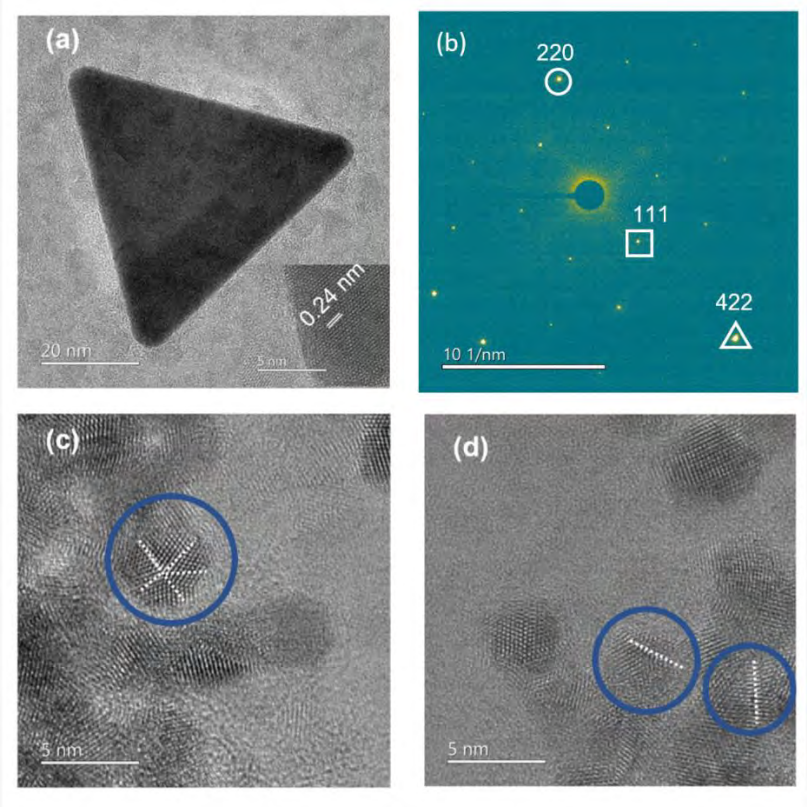

Fig. 22. STEM and inset images of the AuNT surface, which display a lattice spacing (a). SAED pattern of the AuNT (b). STEM image of gold template seeds structures with a penta-twinned structure (c). Planar-twinned and single-crystalline structure (d). Dashed white lines act as markers to emphasize the boundaries.

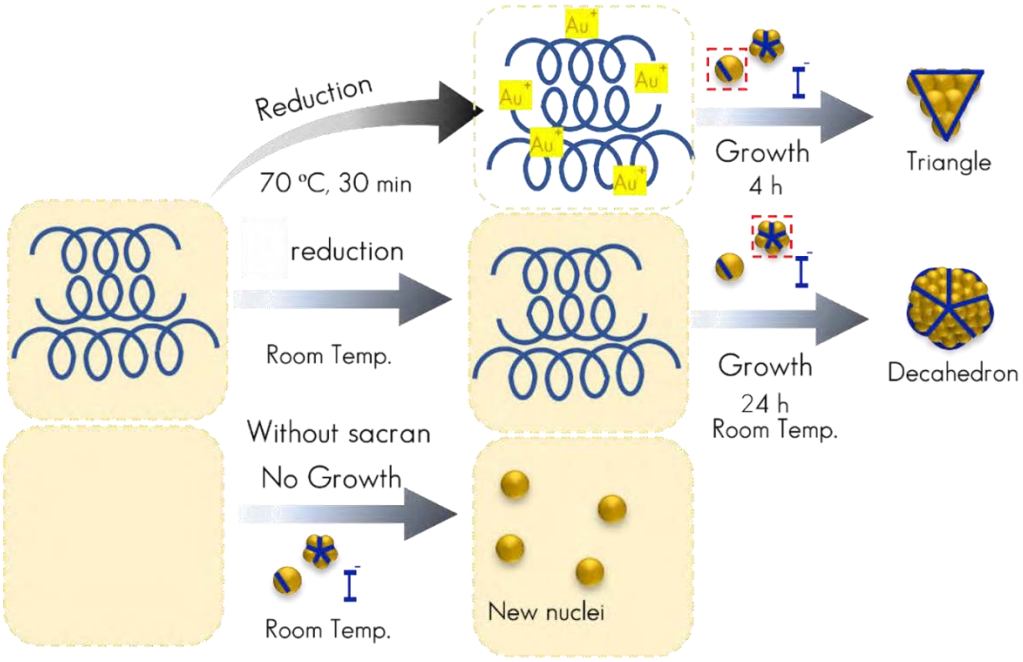

Fig. 23. Possible growth mechanism of the penta- and planar-twinned seeds morphologies transform into decahedral nanoparticles, hexagonal, and triangular nanoparticles depend on the reduction rate by sacran and iodide as the reducing and shape-directing agent. No AuNPs growth were observed without sacran.

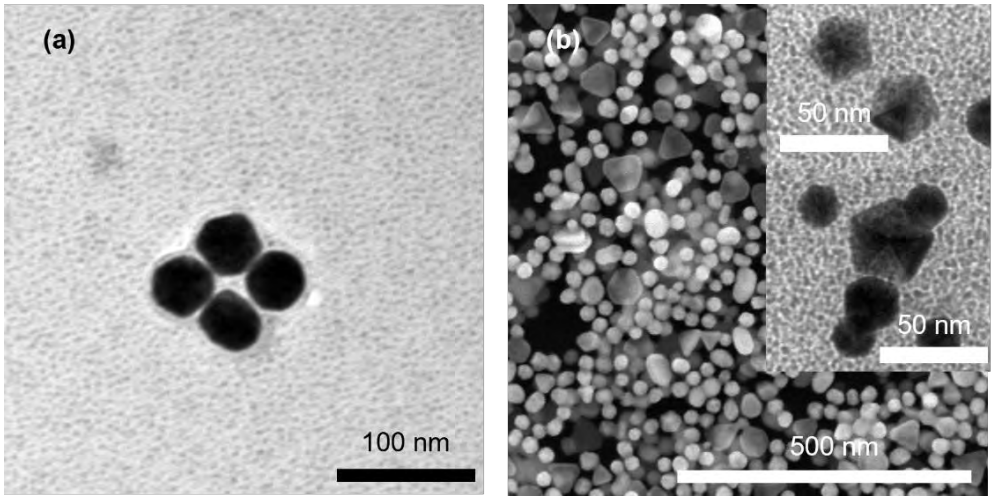

Fig. 24. TEM image of AuNS formed using gold template seeds and only iodide as a reducing agent without the addition of sacran (a) and HRSEM image of gold penta-twinned decahedrons formed using the seeds, sacran, and iodide, without the first reduction step by sacran (b).

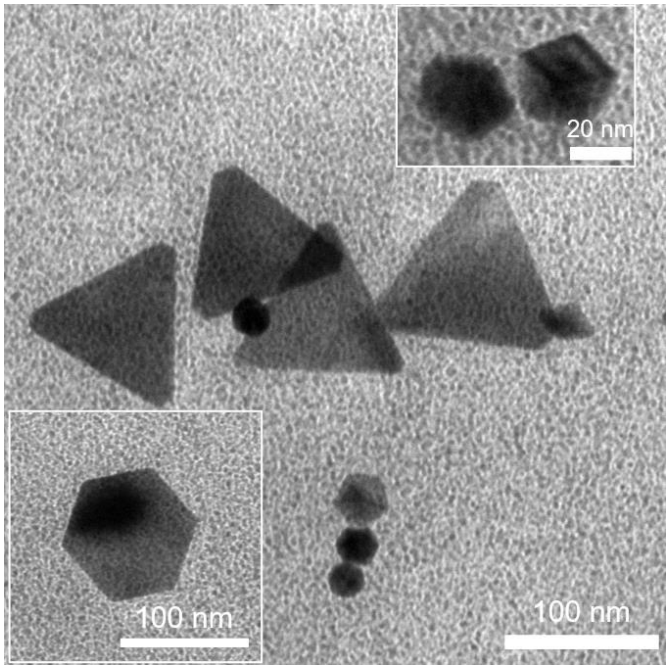

Fig. 25. TEM image of AuNTs obtained using the modified synthesis method along with hexagonal-shaped nanoparticle and penta twinned-decahedrons.

Table 8. Hydrodynamic size, PDI, and zeta potential of obtained AuNPs.

Samples	Average hydrodynamic size (nm)	PDI	Zeta potential (ζ/mV)
Sacran	506±17.47	0.39	-30.07±1.73
Sacran-partially reduced AuNTs	85.80±0.93	0.23	-24.84±0.80
Sacran-partially reduced AuNDs	34.21±0.81	0.20	-22.05±0.90

Fig. 26. Sacran-AuNPs colloidal solutions images.

The solutions containing partially reduced gold ions facilitated by sacran were then utilized to examine how iodide anions affect the preference for the formation of gold nanotriangles (AuNTs). Varying amounts of iodide, ranging from 5 to 20 mM, were employed to discern their impact on shape selectivity. It was observed that lower concentrations of iodide were insufficient to control the inhibition of growth on the (111) crystalline plane, as depicted in the UV-vis-NIR spectrum (Fig. 27). Employing increased concentrations of KI, reaching up to 20 mM, facilitated the successful and high-yield production of AuNTs, as depicted in Fig. 25. The UV-Vis-NIR spectra revealed a distinct surface plasmon resonance (SPR) in the near-IR region at 930 nm, confirming the exceptional purity of the resulting AuNTs. Nevertheless, elevating the KI concentration to 30 mM resulted in the deterioration of the obtained AuNTs due to the etching effect caused by I_3^- species (as per equation 6). This led to the formation of rounded gold nanoplates and the disappearance of the SPR band at 930 nm. Within the range of 10-20 mM KI, effective promotion of anisotropic growth of AuNTs from low to high purity was observed in the UV-vis-NIR spectra. Additionally, iodide anions demonstrated the ability to reduce the gold precursor through a redox equilibrium mechanism (equation 5). The redox equilibrium was instrumental in shaping AuNTs as they grew through sacran reduction under room temperature conditions. Among the halide anions, iodide emerged as the most efficient in promoting anisotropic growth, attributed to its larger size and higher polarizability compared to other

halides. Iodide exhibited effective capping and stabilizing effects throughout the growth process of AuNTs.[53]

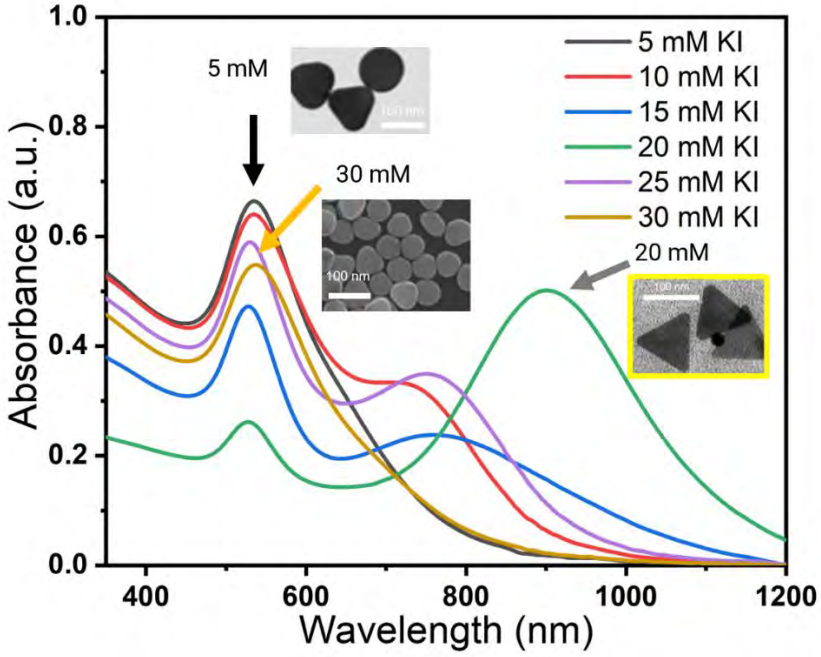

Fig. 27. The influence of iodide anions on the selectivity of AuNTs.

$2[AuCl_4]^- + 3I^- \rightleftharpoons 2Au^0 + 3I_2 + 4Cl^-$ (5) Iodide-mediated reduction of the gold precursor

$Au^0 + 3I_3^- \rightleftharpoons AuI_3 + 3I^-$ (6) Etching of AuNPs by I_3^-

3.3.2 Catalytic activity in the reduction of 4-NP and nitroarenes.

Owing to the high active surface area of the catalytic sites, anisotropic AuNPs have been widely used for catalytic purposes [85, 86]. One harmful non-biodegradable pollutant is 4-nitrophenol (4-NP), which is commonly found in wastewater [87, 88]. Conversely, 4-aminophenol (4-AP) is a less toxic and essential intermediate in various industrial applications, such as the manufacturing of dyes and medications. It also serves as a building block for the synthesis of other compounds. The conversion of 4-NP to 4-AP allows for the modification of the chemical structure to enable further reactions and formation of the desired product. 4-NP can be converted to 4-AP using a metallic

catalyst. Therefore, the advancement of catalytic systems to convert 4-NP to 4-AP provides an opportunity to promote ecofriendly and sustainable technologies [89, 90].

To investigate the impact of gold morphology on the catalytic performance, (a) AuNTs were synthesized using sacran and iodide anions as the reducing and shape-directing agents, as shown in Fig. 19a; (b) AuNDs (Fig. 24b); (c) AuNSs were synthesized using sacran at 0.40 wt.% as the reducing and capping agent (Fig. 13A). The catalytic activities of both morphologies were compared. Before starting the catalytic reduction experiment, 4-NP was transformed into its corresponding 4-nitrophenolate species by the addition of $NaBH_4$ solution. The UV-vis spectra exhibited a shift in the absorbance of 4-NP from 320 nm to 400 nm, as shown in Fig. 28. The resulting solution was left undisturbed for 24 h to ensure that no reduction took place in the absence of the catalyst. The catalytic reduction occurred upon the addition of AuNTs, as evidenced by the diminishment of the peak at 400 nm and the enhancement of the peak at 298 nm in the UV-vis spectra. The appearance of an additional absorption band at 298 nm represented the generation of 4-AP. Surprisingly, within a mere 3 minutes, a trace amount of AuNTs achieved complete reduction of 4-AP (Fig. 29a, d). The pseudo-first-order kinetics equation was used to determine the reaction rate constant (k), which was 16.3×10^{-3} s^{-1}. Additionally, AuNDs also exhibit good catalytic performance, as shown in Fig. 29b, e. It took approximately 9 min to complete the reduction of 4-AP, and the reaction rate constant (k) was 5.3×10^{-3} s^{-1}. Conversely, AuNSs took approximately 240 s to be ready as an active catalyst, and it completely reduced to 4-NP after 12 min (Fig. 29c, f). The supporting UV-vis-NIR graphs, with wavelengths ranging from 500 to 1300 nm, are presented in Fig. 30. Despite sharing the same sacran medium concentration (0.05 wt.%) as AuNDs and AuNTs, Gold nanospheres have a symmetrical shape and a high degree of uniformity, which can contribute to their structural stability. This intrinsic stability might help maintain consistent catalytic activity in the early stages of the reaction. The surface energy of gold nanospheres might be lower compared to other shapes (like nanotriangles), leading to a slower rate of surface reconstruction initially.[91], [92], [93], [94]. AuNSs tend to have fewer high-energy reactive sites compared to nanotriangles, leading to comparatively lower catalytic activity compared to AuNTs and AuNDs.

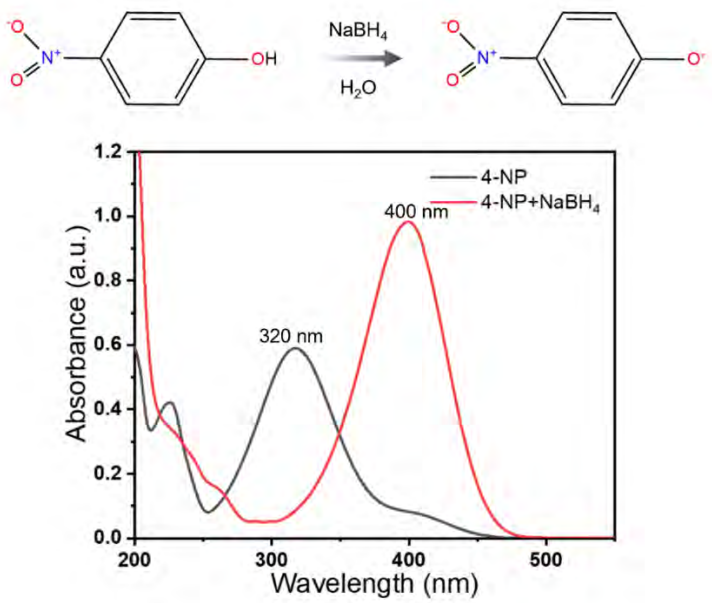

Fig. 28. The reaction between 4-NP with $NaBH_4$ to form 4–nitrophenolate ions and UV–vis spectra obtained from 4-NP and 4–nitrophenolate ions.

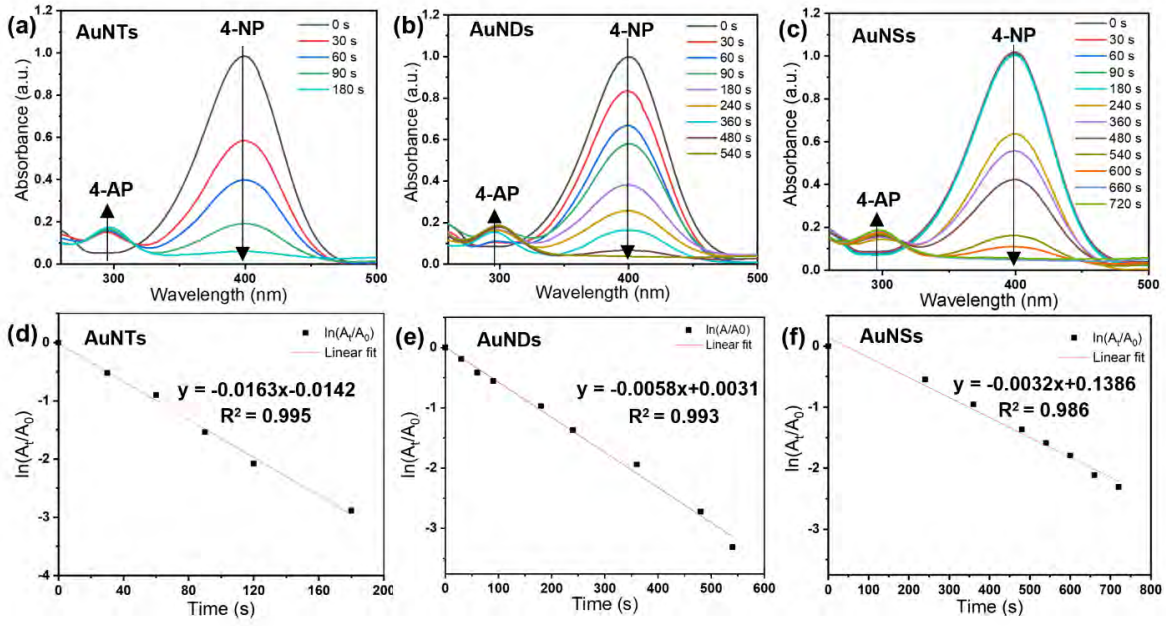

Fig. 29. UV-vis spectra at different intervals of time present the reduction of 4-NP using AuNTs (a), AuNDs (b), and AuNSs (c) as catalysts. Pseudo-first-order reduction kinetics plot of 4-NP by AuNTs (d), AuNDs (e), and AuNSs (f) in the participation of $NaBH_4$

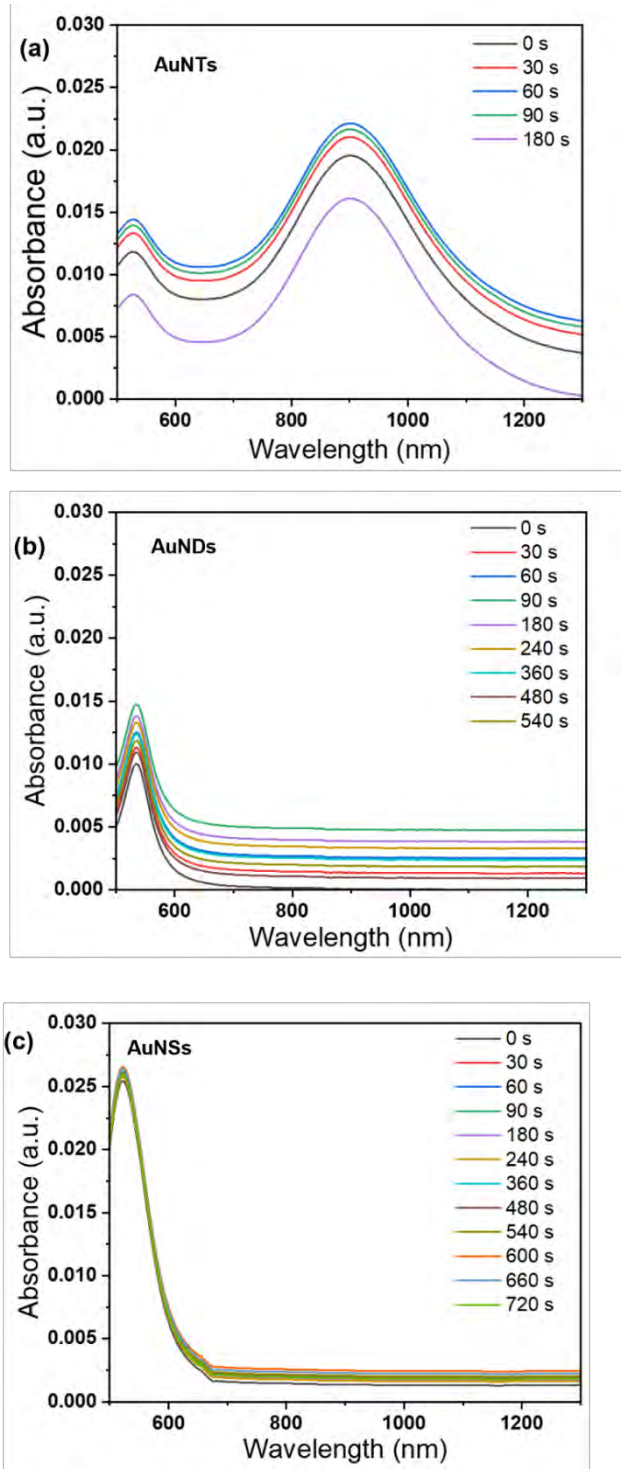

Fig. 30. UV-vis spectra from 500 to 1300 nm at different time intervals depict the reduction of 4-NP using AuNTs (a), AuNDs (b), and AuNSs (c) as catalysts.

Fig. 31 shows the TEM images of the AuNSs and AuNTs after their use as catalysts. Evidently, the morphologies of AuNSs and AuNTs remained intact with their other nanoparticles, which keep active surface area in the stable state. This behavior could be owing to the sacran structures, which act as inhibitors of nanoparticle aggregation. These results demonstrate the high possibility of the catalyst reuse. The conversion of 4-NP decreased from over 98% to 88% after three cycles for all Au morphologies (Fig. 32). This reduction can be attributed to the weight loss upon drying or aggregation of the catalysts. Nevertheless, the recyclability of AuNTs, AuNDs, and AuNSs remained satisfactory. Here catalytic behavior of sacran without any gold nanoparticles was checked, and UV-vis-NIR revealed that sacran lacks catalytic ability for the reduction of 4-AP to 4-NP (Fig. 33). UV-vis-NIR additionally revealed no specific influence of iodide anions on the AuNTs catalyst for the 4-AP reduction (Fig. 34). In summary, the AuNTs with the highest active surface area are excellent candidates for catalytic reduction (Table 9). The results indicate that the specific rate constant (k) towards 4-nitrophenol (4-NP) for the gold nanotriangles (AuNTs), calculated from the Pseudo-first-order model, is remarkably high at 2.90×10^{3} $s^{-1}g^{-1}$. This value surpasses that of Au anisotropic shapes generated using common reducing or stabilizing agents, such as sodium borohydride (0.65×10^{3} $s^{-1}g^{-1}$) or ascorbic acid (1.00×10^{3} $s^{-1}g^{-1}$), by a factor of above 2.9. Furthermore, it exceeds the rates observed with other polysaccharides like carboxymethyl cellulose (1.01×10^{3} $s^{-1}g^{-1}$) or chitosan (1.23×10^{3} $s^{-1}g^{-1}$). Turnover frequency (TOF) stands as a critical metric for comparing the efficiency of active sites among different catalysts. It denotes the average number of chemical reactions occurring on active sites per hour. TOF evaluation entails product conversion, typically determined through gas chromatography (GC), and the quantification of active sites on the catalyst. For metal catalysts, active site quantification typically involves H_2 adsorption. However, obtaining comprehensive data from prior research on various gold (Au) morphologies' effects on 4-nitrophenol (4-NP) reduction proves challenging. To circumvent this limitation, we estimate the TOF value using this equation for comparison with our synthesized Au nanotriangles (AuNTs), nanodecahedrons (AuNDs), and nanospheres (AuNSs) (Table 9).

$$TOF(h^{-1}) = \text{mol (substrate)}/(\text{mol (catalyst)}\times\text{time (h)})$$

In our analysis, we find that two crucial parameters exert a substantial influence on turnover frequency (TOF): the quantity of nanoparticles within the catalyst system and the dispersion of these nanoparticles. In our particular catalyst system, we employ a relatively low quantity of

AuNTs, while benefiting from a high dispersion (active surface area). This enhanced dispersion is attributed to the effective stabilizing ability of sacran, distinguishing our system from others.

The reduction mechanism of 4–NP to 4–AP in the presence of AuNTs as the catalyst is elucidated through the Langmuir–Hinshelwood (LH) model [93], [95], [96] (Fig. 35). The process initiates with the adsorption of borohydride ions onto the surface of AuNTs, facilitating the transfer of surface–hydrogen species. Following this, 4-nitrophenolate molecules adsorb onto the active surface of AuNTs, initiating the reduction of 4–NP to 4–AP. Subsequently, 4–AP desorbs from the surface into the solution, liberating the AuNTs surface for further catalytic reduction cycles. We compared our synthesized gold nanostructure using the polysaccharide sacran with other previously reported gold nanostructures as catalysts to reduce 4-NP, as presented in Table 9. AuNTs show remarkable catalytic activities, and their activities are enhanced by sacran molecules, which inhibit the aggregation and surface oxidation of the nanoparticles.

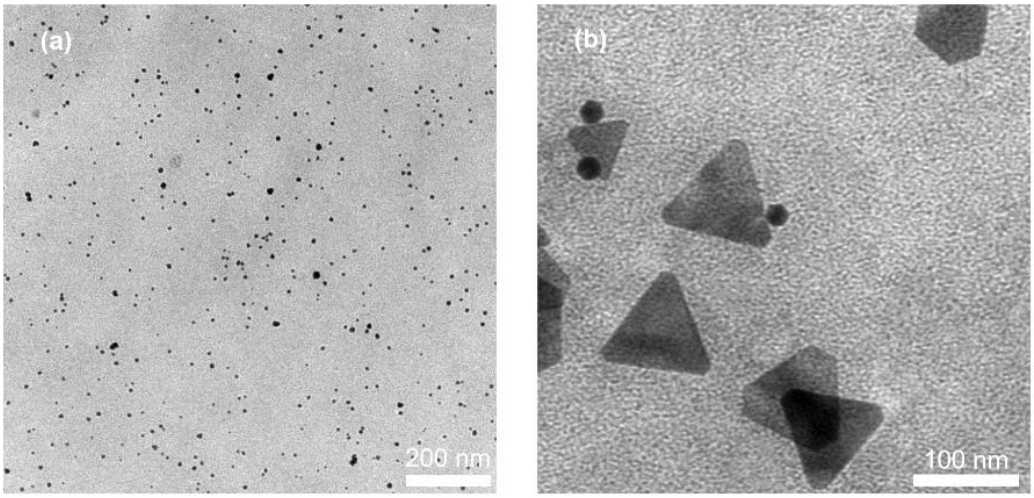

Fig. 31. TEM images of AuNSs (a) and AuNTs (b) after being used as catalysts.

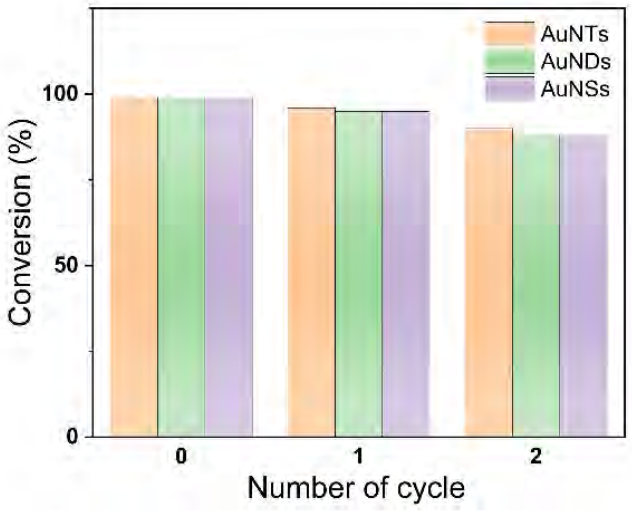

Fig. 32. The recyclability of AuNTs, AuNDs and AuNSs, respectively.

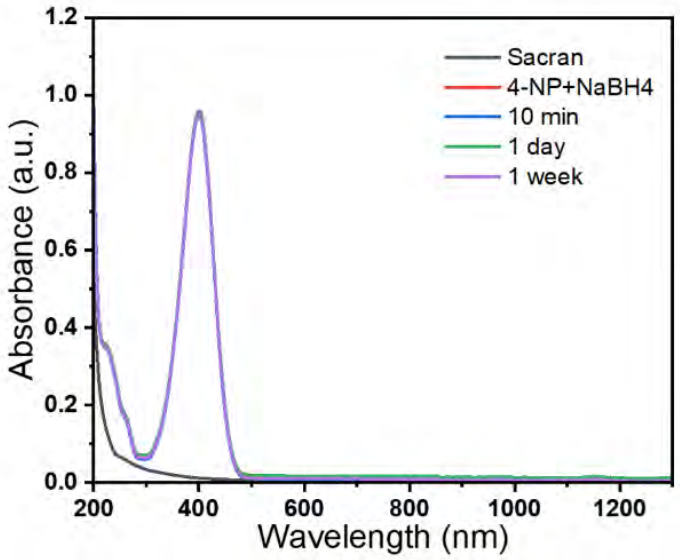

Fig. 33. UV-vis-NIR spectra at different intervals of time present the reduction of 4-NP using sacran over a period ranging from 10 minutes to 1 week.

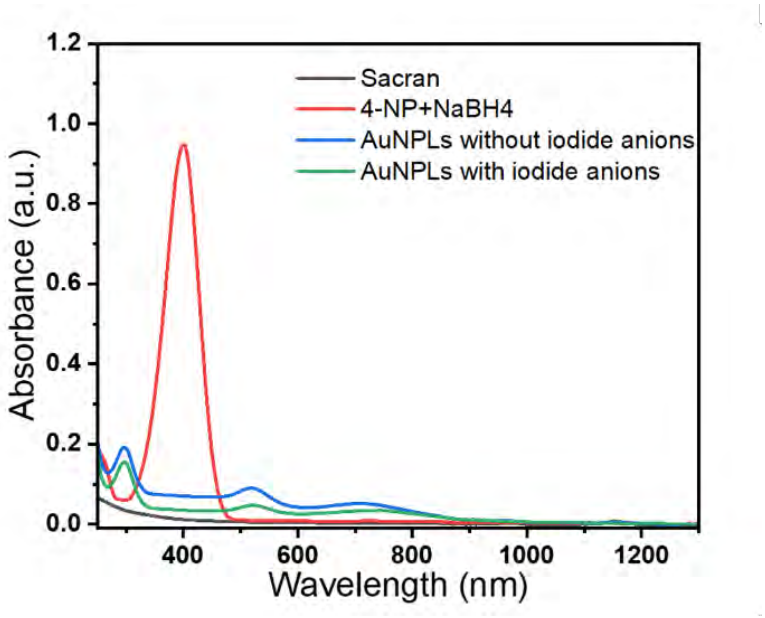

Fig. 34. UV-vis-NIR spectra following the catalytic reduction of 4-AP to 4-NP by AuNPLs with and without the assistance of iodide anions.

Table 9. Comparison of the catalytic performances of our produced AuNPs by functional polysaccharide sacran with other literature reviews.

Gold morphologies	Reducing or capping agents	Mass of the catalyst used (μg)	Rate constant (10^{-3} k, s^{-1})	Rate constant per unit mass (10^{3} $s^{-1}gAu^{-1}$)	TOF (h^{-1})	Reference
Gold nanopolygons	Ferric ammonium citrate	328	11.0	0.03	53.68	[97]
Gold nanorods	Ascorbic acid	35	44.0	1.25	37.29	[98]
Gold nanoprisms	Ascorbic acid	20.7	20.8	1.00	84.61	[99]
Gold nanospheres	Sodium borohydride	10	6.6	0.65	21.89	[100]
Gold nanoflowers	DMSO	394	16.3	0.04	74.63	[101]
Gold nanotriangles	Carboxymethyl cellulose	5.2	5.3	1.01	120.42	[9]
Gold nanotriangles	Chitosan	9.5	11.7	1.23	82.44	[102]
Gold nanospheres	Sacran	5.64	3.27	0.58	25.54	Our work
Gold nano-decahedrons	Sacran	5.64	5.80	1.02	109.09	Our work
Gold nanotriangles	Sacran	5.64	16.3	2.90	240.52	Our work

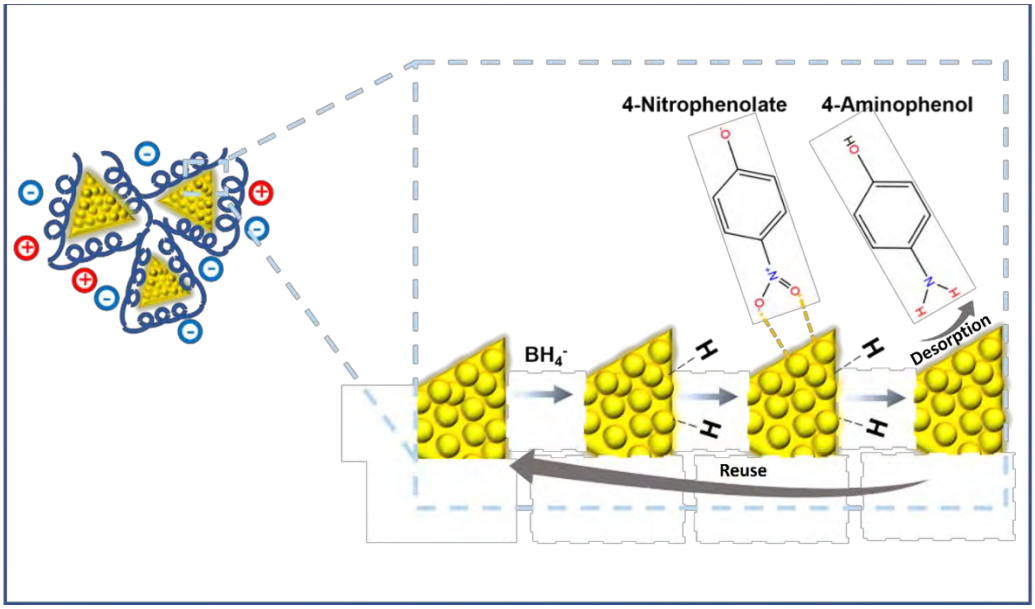

Fig.35. Langmuir–Hinshelwood (LH) model of catalytic reduction by AuNTs.

Chloro-substituted anilines allow for diverse chemical modifications, facilitating the creation of complex drug molecules. These compounds are also used as precursors in the production of herbicides, insecticides, and fungicides due to their reactivity, which enables the introduction of functional groups necessary for biological activity.[103] Recognizing the importance of chloro-substituted anilines, we investigated the possibility of using our synthesized AuNPs as catalysts. Therefore, we employed the reduction of nitroarenes with various chlorine substitution positions to further explore their catalytic activities and practical applications. We evaluated the conversion and selectivity of the reduction process across all gold morphologies. Three distinct gold nanomorphologies (AuNTs, AuNDs, and AuNSs) were employed to catalyze the conversion of chlorine-substituted nitrobenzenes into the corresponding aromatic amines. Remarkably, excellent conversion rates of up to 99% were achieved within 10 minutes of reaction at room temperature, as depicted in Table 10. During the reduction of nitroarenes with varying substitution positions of chlorine, no dehalogenation occurred. The main reaction yielded high conversion rates and satisfactory selectivity. Conversion and selectivity were quantified by the complete dataset obtained from GC-MS. The time-dependent changes in absorbance spectra until reaching a stable state of the catalysts were recorded as shown in Fig. 39-41. GC-MS for reaction solution of 2,4-dichloronitrobenzene conversion showed a small, unexpected peak at 7.17 minutes, which can be

assigned to 2,4-dichloroacetanilide based on library search. Our investigation reveals that the selectivity did not over 99 % but still kept high. The values were much higher than those of other stabilizer on gold nanoparticles reported in the literatures on hydrogenation catalysis of PVP stabilized on AuNPs (conversion of 18.4 %) [104], organosilicon ligand supported AuNPs [105] (k = 2.81×10^{-3} s^{-1}, conversion of 98 %), and poly(N-isopropylmethacrylamide) stabilized on AuNPs with the participation of $NaBH_4$ (k = 6.33×10^{-3} s^{-1}, conversion of 85.5 %) [106], presumably due to ultrahigh dispersion ability of sacran for avoiding unwanted coagulation of gold nanoparticles.

Table 10. Catalytic reductions of nitroarenes with various positions of chlorine substitution by AuNTs, AuNDs, and AuNSs[a]

Reactant	Product	Catalyst	Conversion (%)	Selectivity (%)	Reaction time (s)	Rate constant (10^{-3} k, s^{-1})
		AuNTs	>99	>99	~ 360	6.30
		AuNDs	>99	>99	~ 480	3.94
		AuNSs	>99	>99	~ 600	3.31
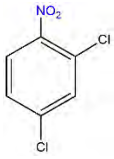	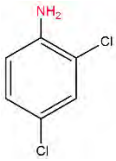	AuNTs	>99	96.2	~ 240	4.63
		AuNDs	>99	96.2	~ 360	2.92
		AuNSs	>99	95.5	~ 600	1.43
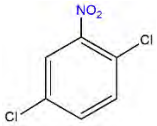	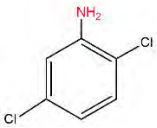	AuNTs	>99	>99	~ 240	2.63
		AuNDs	>99	>99	~ 360	1.71
		AuNSs	>99	>99	~ 600	1.00

[a]Reaction conditions: 5.64 mg/L of each catalyst, 0.17 mM nitroarene, 15 mM $NaBH_4$, 10 mL ($EtOH/H_2O$ 70% v/v) solvent.

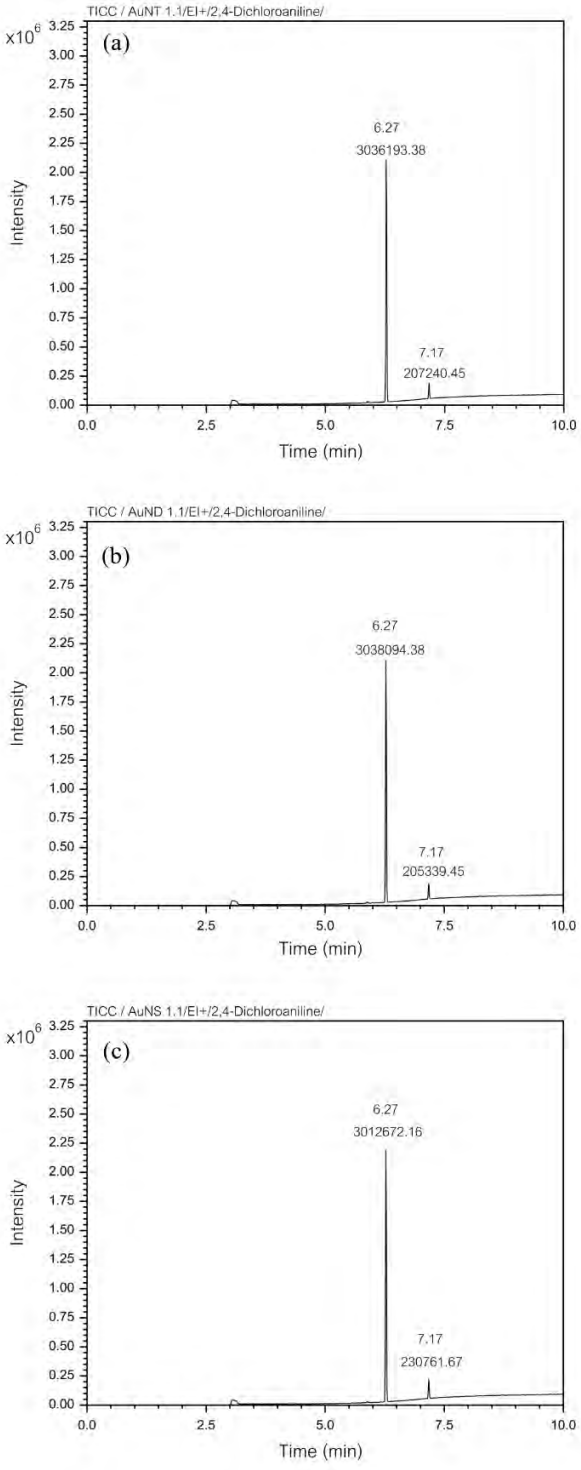

Fig. 36. The analysis of 2,4-dichloroaniline after reduction by AuNT (a), AuND (b), and AuNS (c).

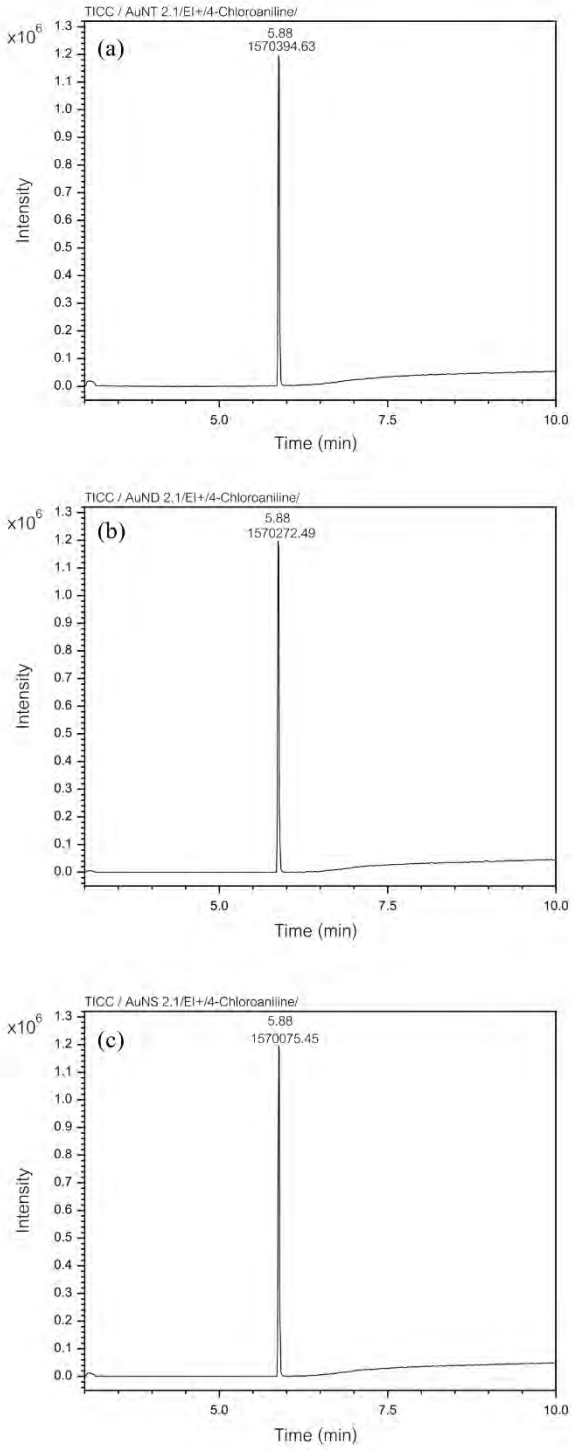

Fig. 37. The analysis of 4-chloroaniline after reduction by AuNT (a), AuND (b), and AuNS (c).

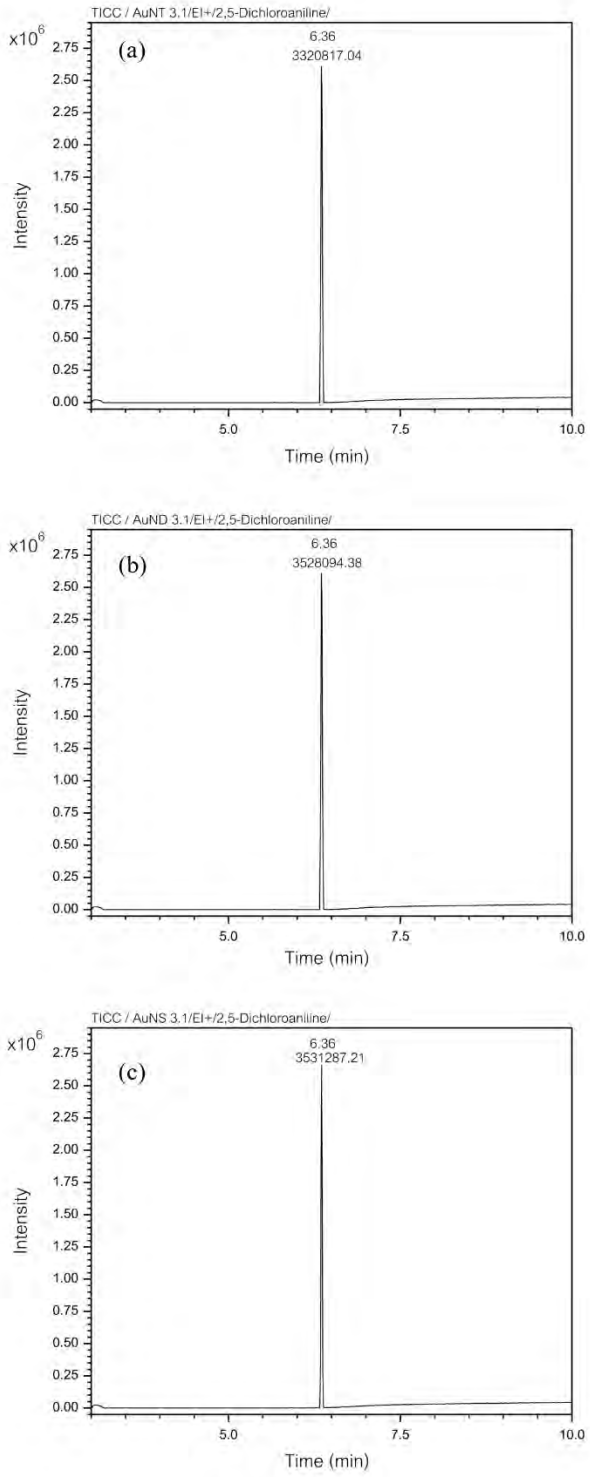

Fig. 38. The analysis of 2,5-dichloroaniline after reduction by AuNT (a), AuND (b), and AuNS (c).

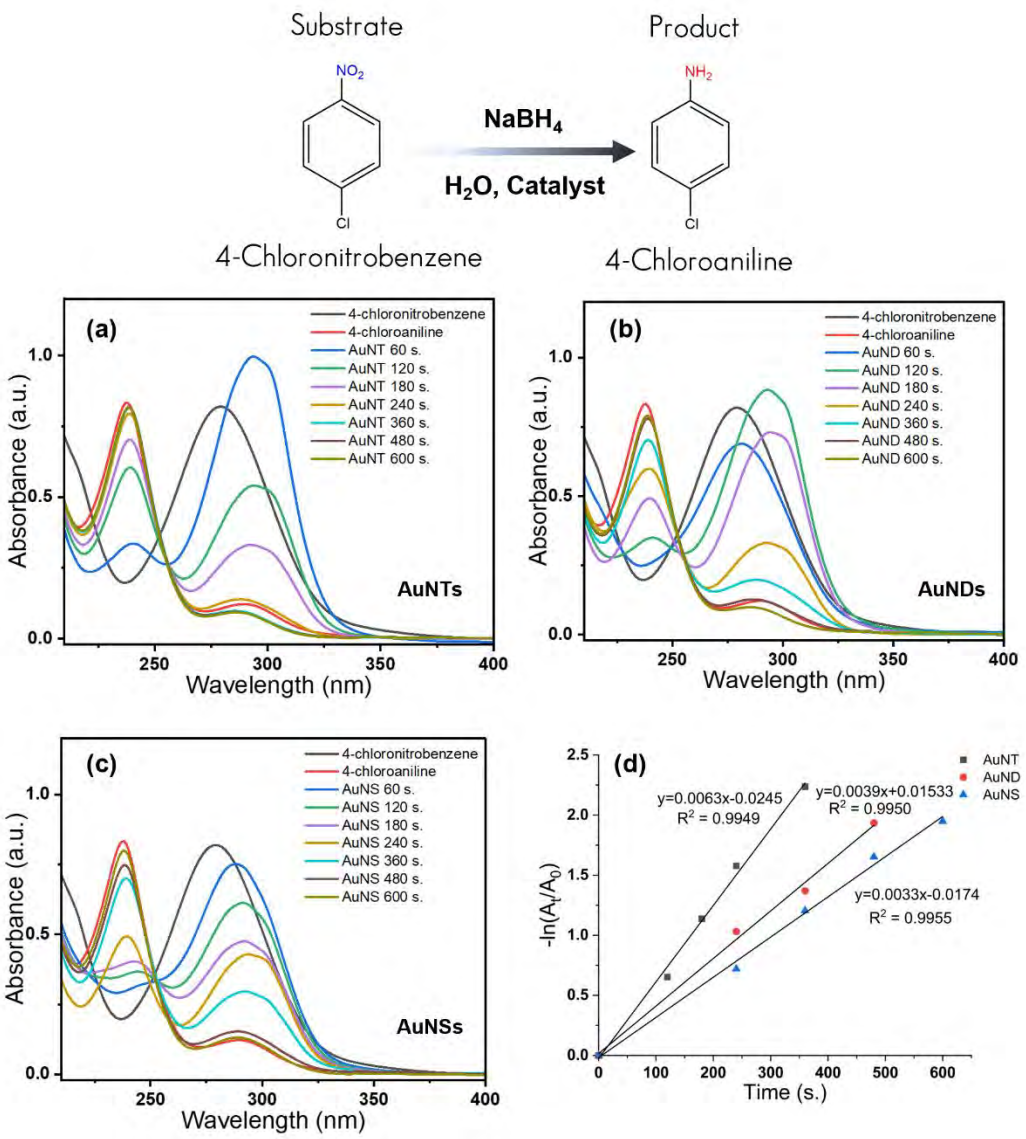

Fig. 39. UV-vis-NIR spectra following the catalytic reduction of 4-Chloronitrobenzene to 4-Chloroaniline by AuNTs (a), AuNDs (b) and AuNSs (c), respectively. Kinetic plots for AuNT, AuND and AuNS (d).

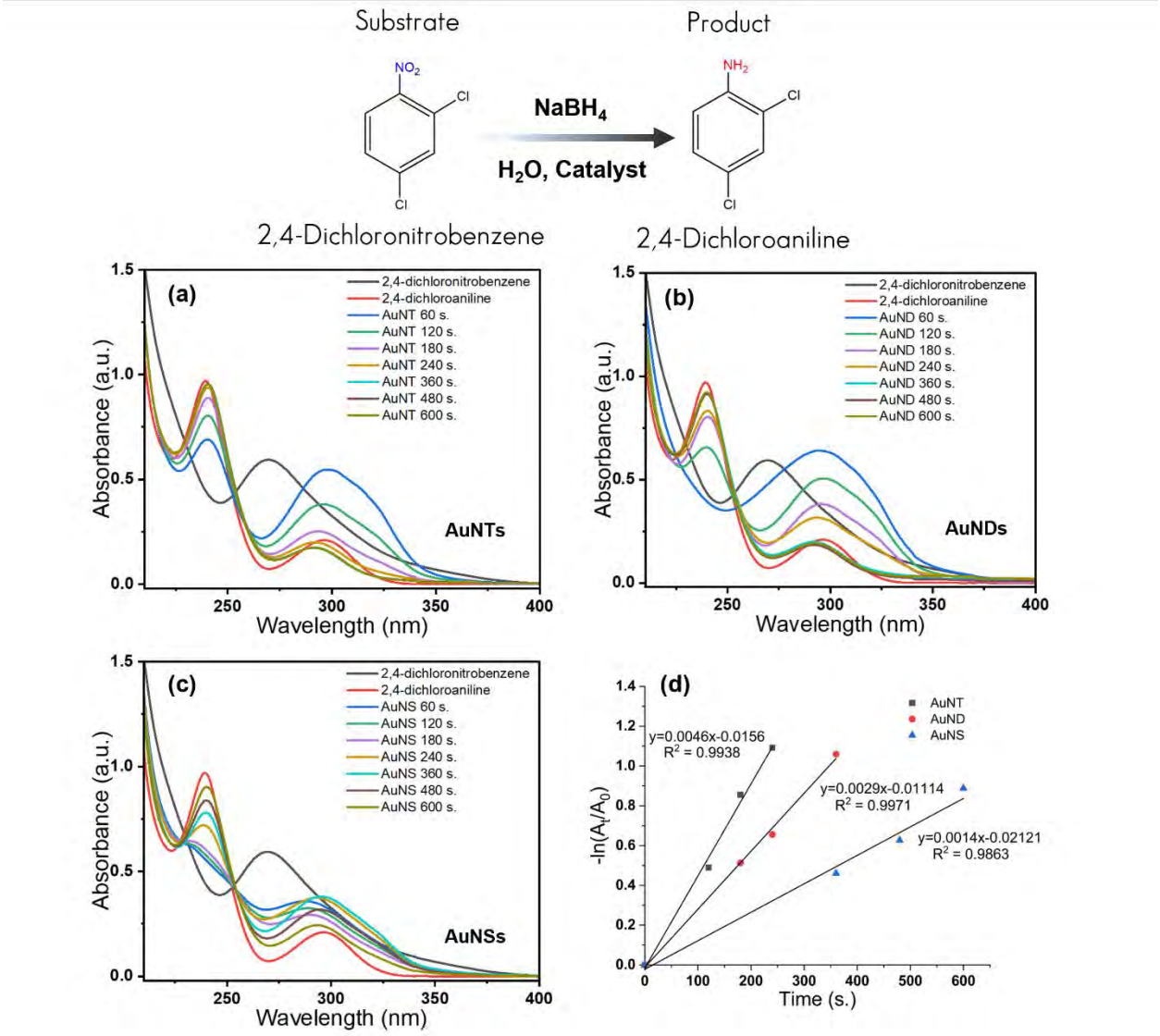

Fig. 40. UV-vis spectra following the catalytic reduction of 2,4-Dichloronitrobenzene to 2,4-Dichloroaniline by AuNTs (a), AuNDs (b) and AuNSs (c), respectively. Kinetic plots for AuNT, AuND and AuNS (d)

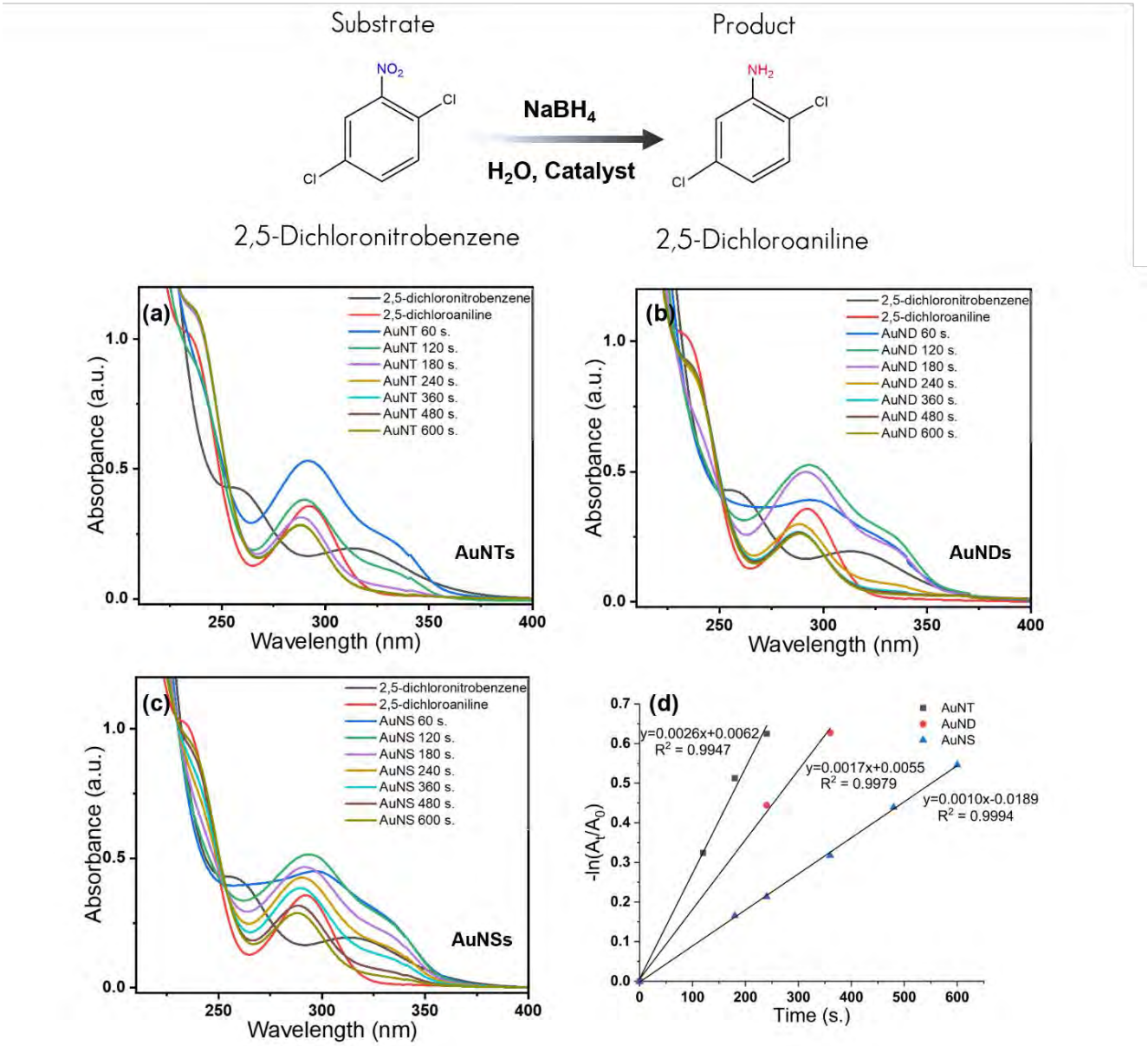

Fig. 41. UV-vis-NIR spectra following the catalytic reduction of 2,5-Dichloronitrobenzene to 2,5-Dichloroaniline by AuNTs (a), AuNDs (b) and AuNSs (c), respectively. Kinetic plots for AuNT, AuND and AuNS (d)

3.3.3 Photothermal therapy studies

The sacran-AuNTs solution at different nanoparticle concentrations exhibits a response to the laser and generates heating energy. The maximum concentration shows the highest temperature difference of about 13°C (24°C to 37°C), while the lowest concentration shows a temperature difference of 5°C.

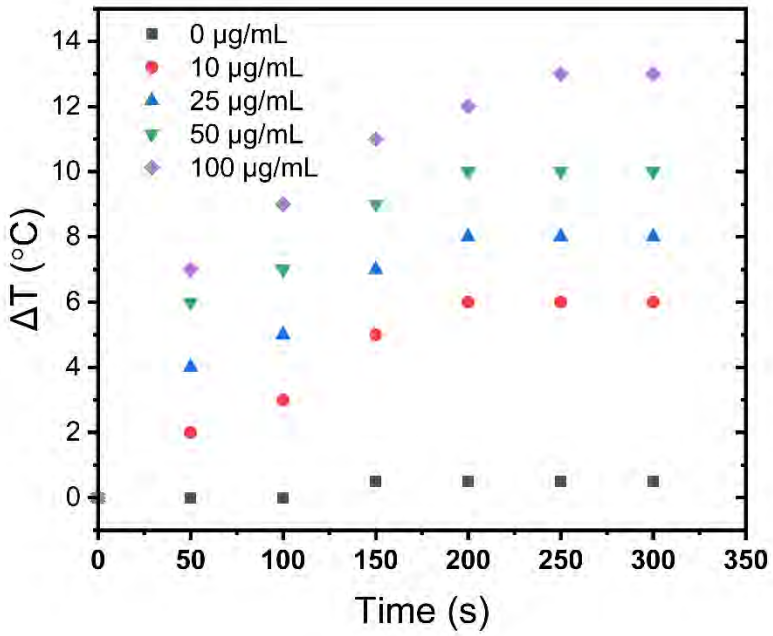

Fig. 42. Temperature changes during laser irradiation of sacran-AuNTs solution. The graph plots the temperature variation over time during exposure to an 808 nm laser at 1 W power.

The biocompatibility of sacran-coated gold nanotriangles (sacran-AuNTs), produced via an eco-friendly synthesis method, was tested on A549, L929, and HDF cell lines. Fig. 43 displays the cell viability percentages corresponding to various AuNTs concentrations after 24 hours of treatment. Fig. 43 shows that sacran-AuNTs maintained good biocompatibility for up to 24 hours at concentrations up to 100 µg/mL. At this highest concentration, HDF cells exhibited a slight decrease in cell viability (around 85%). This observed biocompatibility is likely due to the sacran coating on the AuNTs, which enhances stability and reduces cytotoxicity. Additionally, the NIR absorbance properties of sacran-AuNTs make them promising candidates for photothermal therapy.

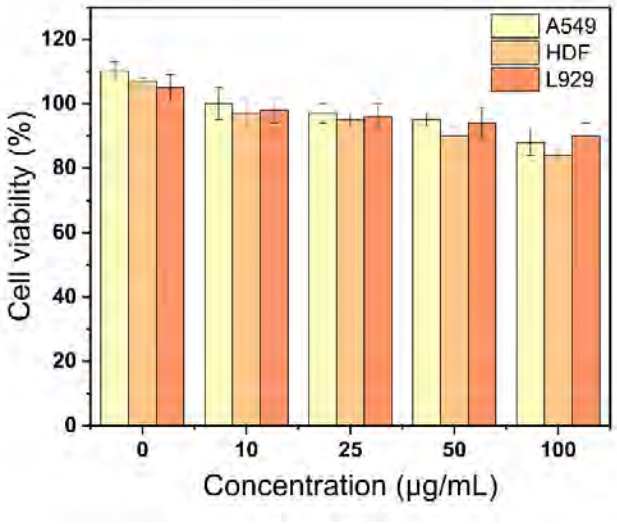

Fig. 43. Cell viability (%) was assessed as a function of AuNT concentration after a 24-hour treatment period. The graph illustrates the impact of varying AuNT concentrations on cell viability.

The biocompatibility of green-synthesized sacran-coated gold nanotriangles (sacran-AuNTs) was evaluated on A549, HDF, and L929 cell lines. As shown in Fig. 44-55, cells were treated with sacran-AuNTs at concentrations of 10, 25, 50, and 100 µg/mL for 24 hours, both before and after laser irradiation. The NIR laser irradiation was performed at 1 W and 808 nm for 10 minutes.

Prior to laser irradiation, sacran-coated AuNTs exhibited good biocompatibility across all three cell lines, maintaining high cell viability at all tested concentrations. Following laser irradiation, treated cells displayed notable morphological alterations, including the retraction of cellular appendages, membrane rupture, blebbing, and cytoplasmic fluid leakage, as indicated by arrows in Fig. 45, 49, and 53. Conversely, untreated cells showed no discernible morphological changes after laser exposure.

The reduced cell viability and observed morphological changes in cells treated with sacran-AuNTs following laser irradiation are attributed to the buildup of NIR-absorbing AuNTs within the cells. This buildup induces localized photothermal effects when exposed to the laser, ultimately causing cell death.

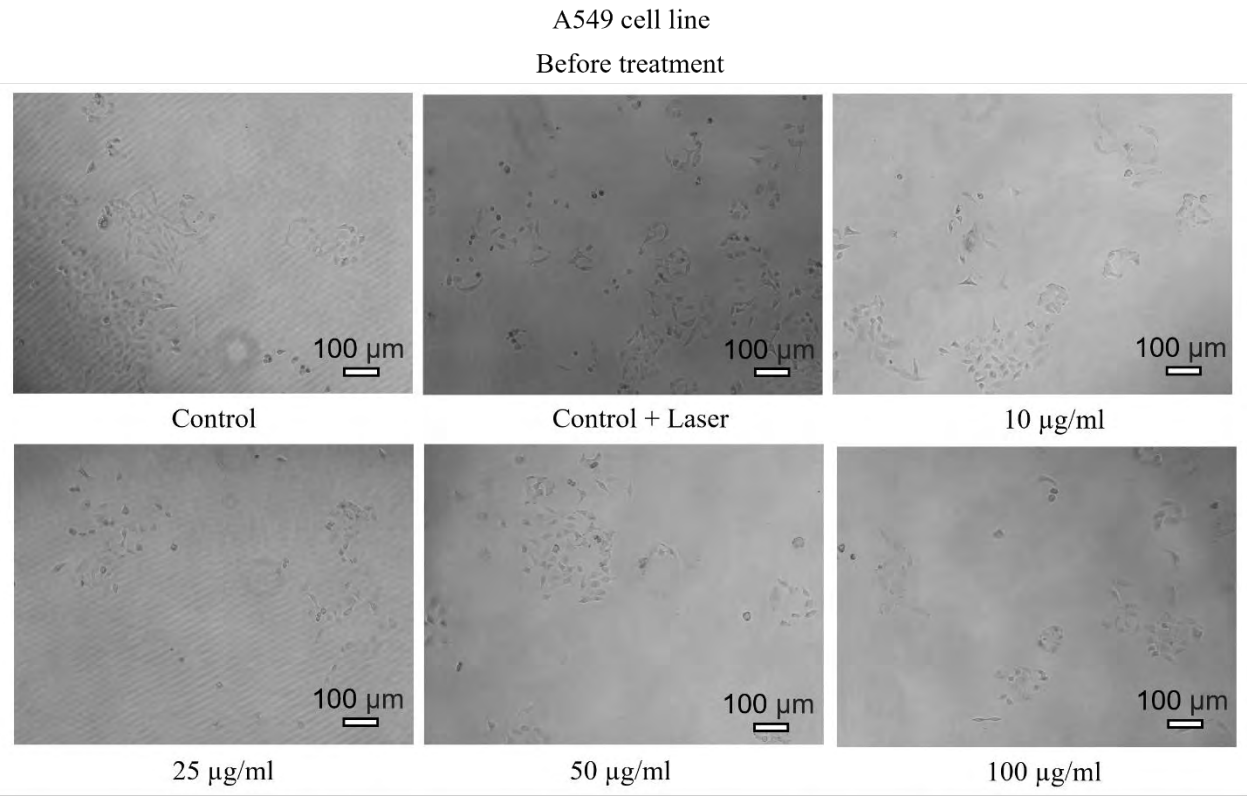

Fig. 44. Viability of A549 cells treated with AuNTs at concentrations of 10, 25, 50, and 100 µg/mL for 24 hours, compared to untreated controls, both with and without laser irradiation.

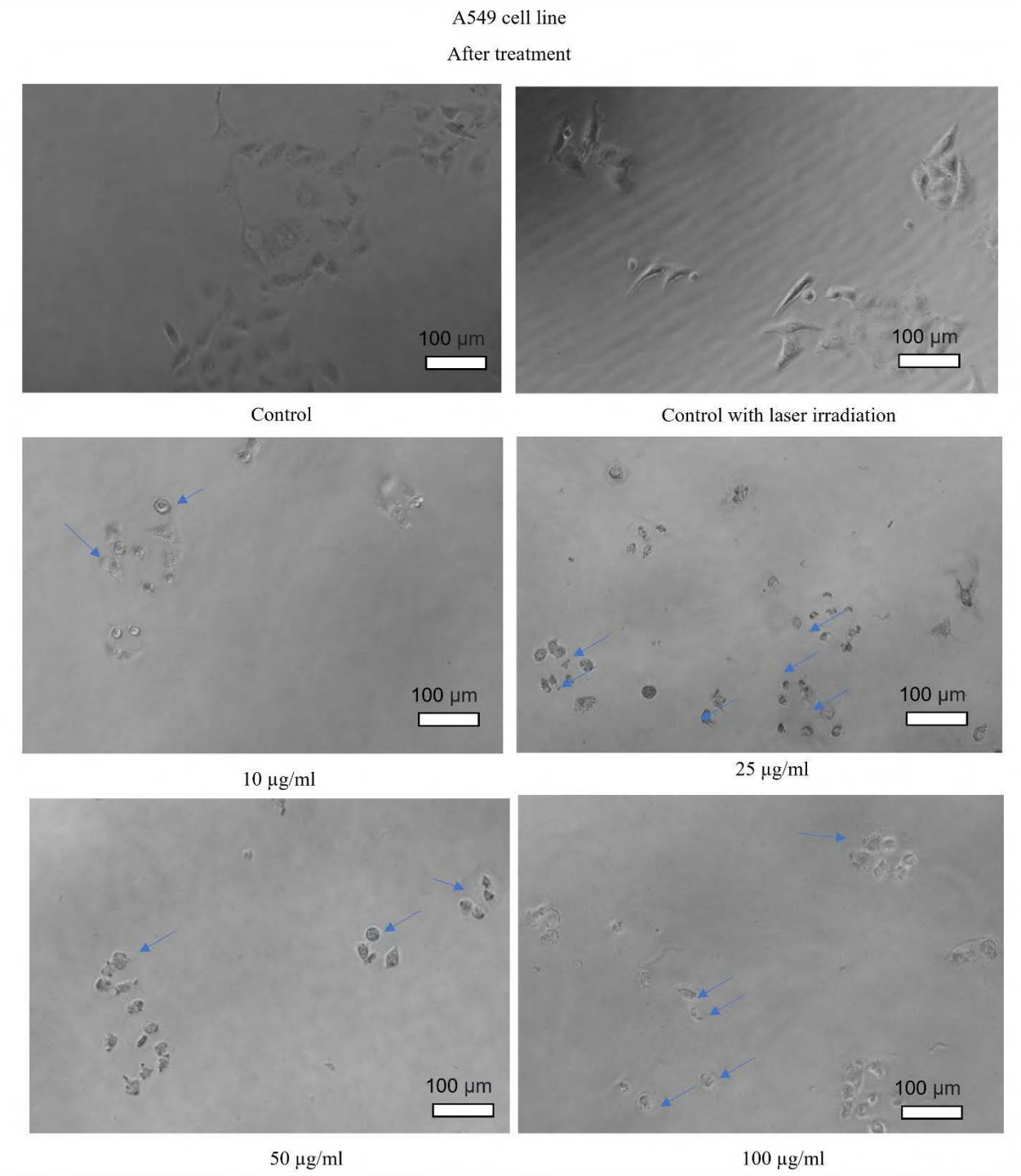

Fig. 45. Morphological changes in A549 cells after laser irradiation following treatment with AuNTs at concentrations of 10, 25, 50, and 100 µg/mL for 24 hours, compared to untreated controls with and without laser exposure. Significant changes were noticed (indicated by arrows) after 10 minutes of laser irradiation at 1 W.

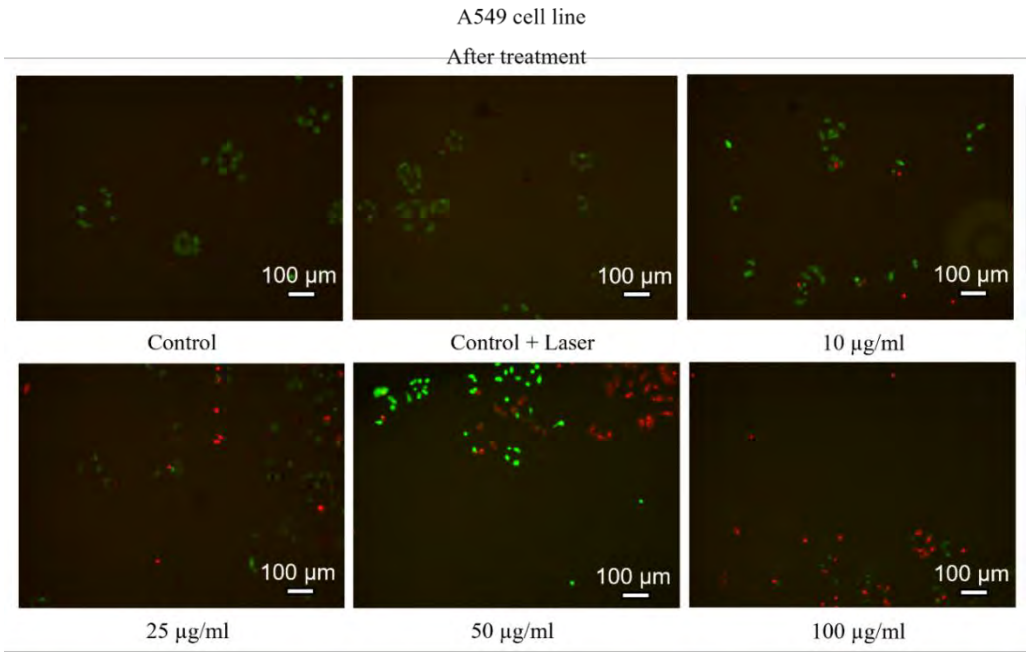

Fig. 46. Live/dead staining of A549 cells was performed after 10 minutes of 808 nm laser irradiation at 1 W power. Cells were treated with AuNTs at concentrations of 0, 10, 25, 50, and 100 µg/mL. The reduction in red fluorescence at lower AuNT concentrations indicates the effectiveness of the nanoparticles' photothermal activity in inducing cell death.

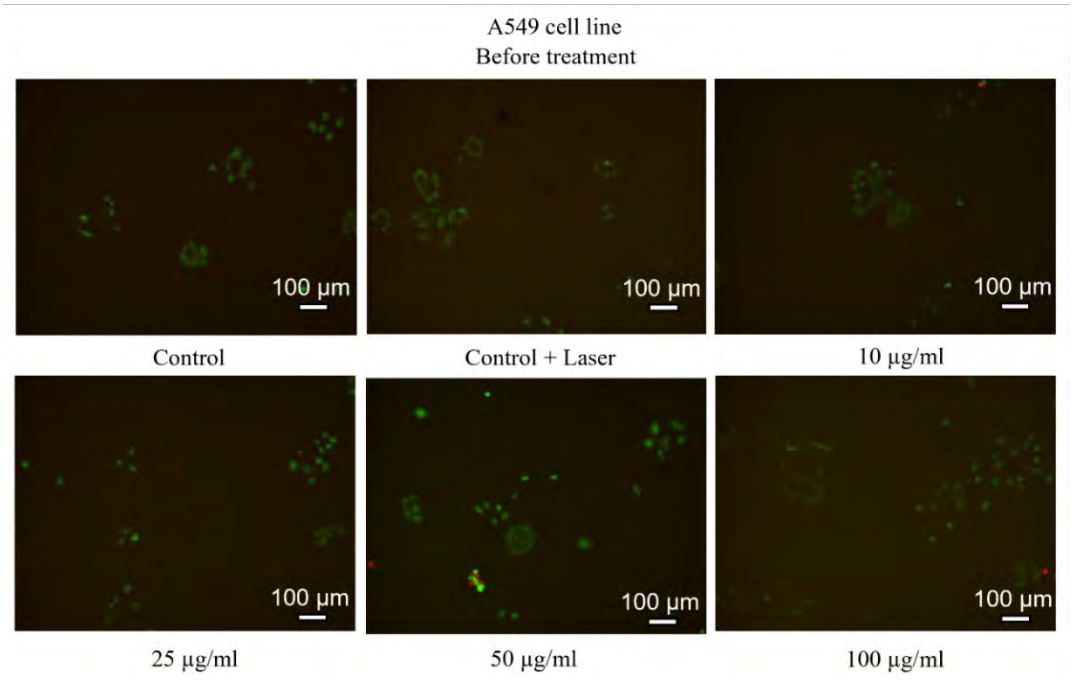

Fig. 47. Live/dead staining of A549 cells prior to 10 minutes of 808 nm laser irradiation at 1 W power. Cells were treated with AuNTs at concentrations of 0, 10, 25, 50, and 100 µg/mL.

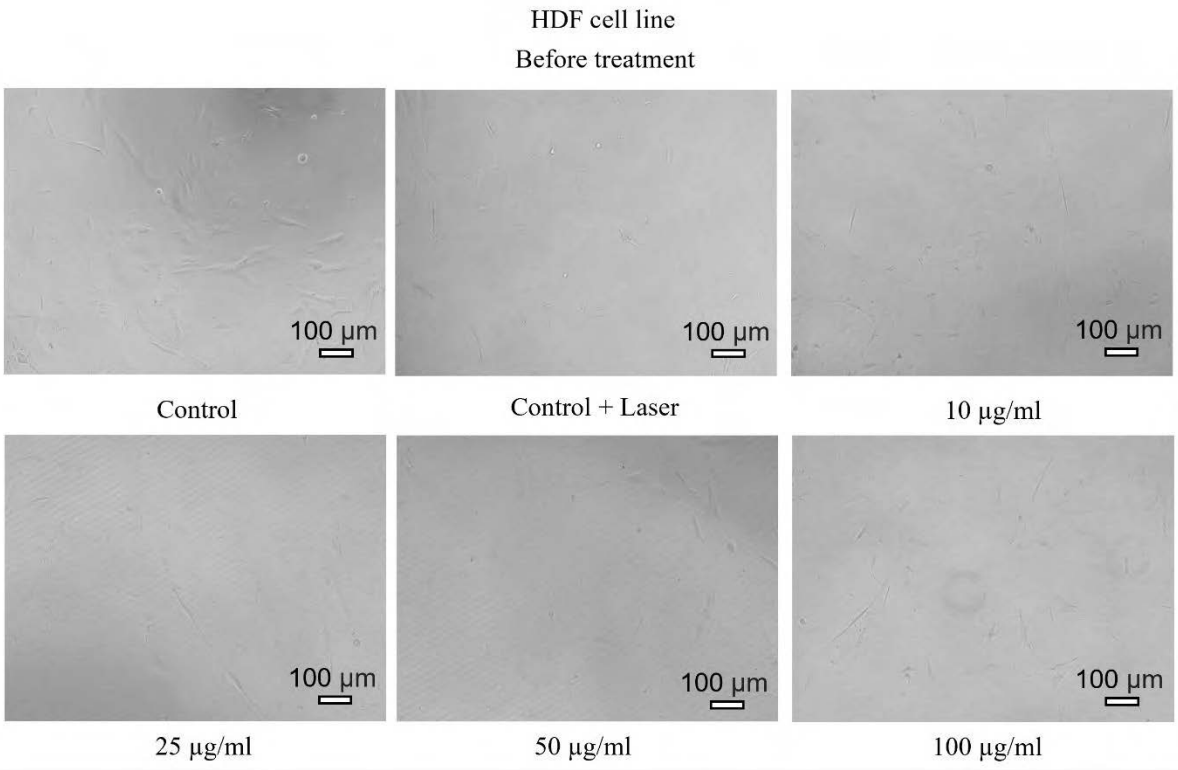

Fig. 48. Viability of HDF cells treated with AuNTs at concentrations of 10, 25, 50, and 100 µg/mL for 24 hours, compared to untreated controls, both with and without laser irradiation.

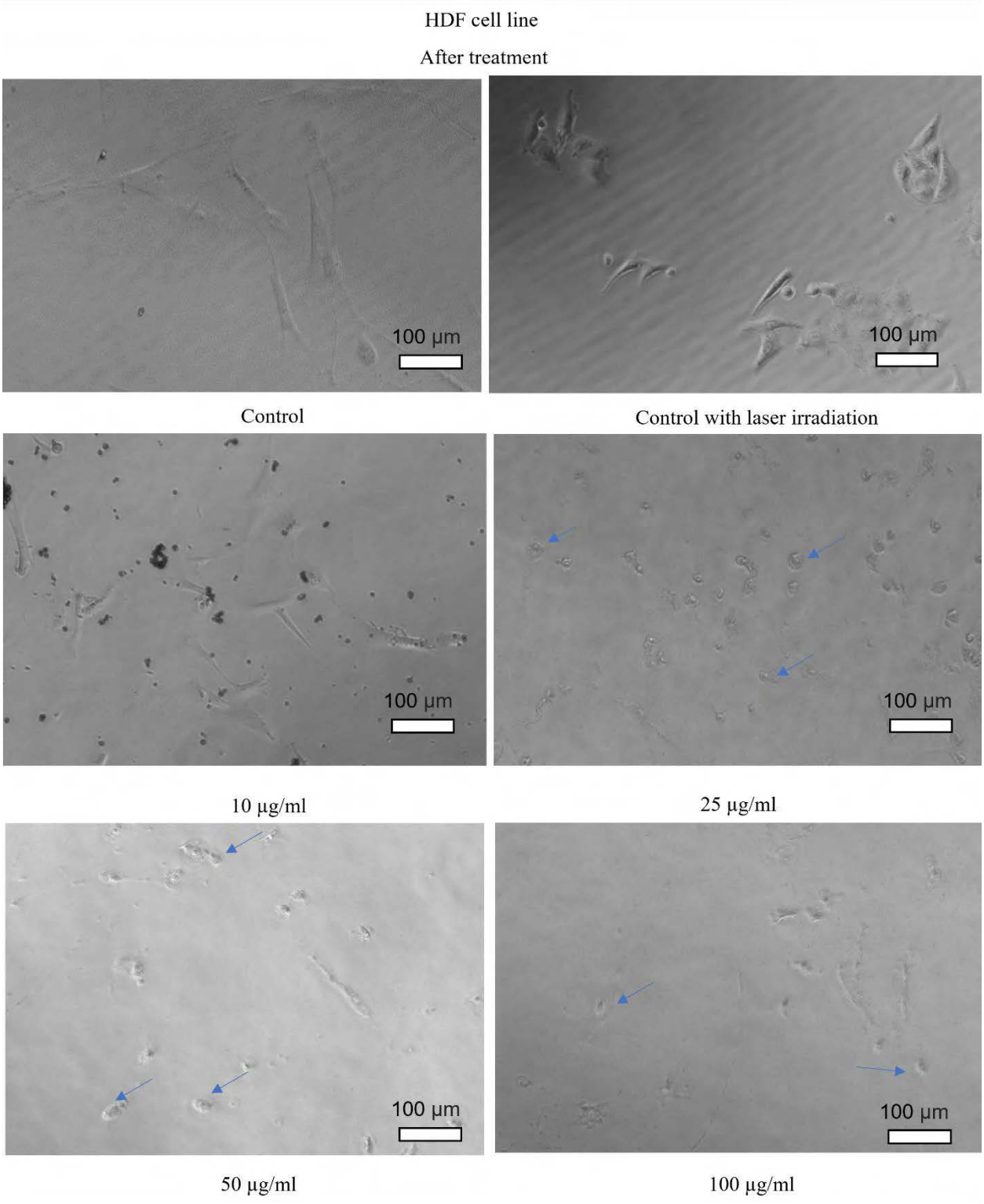

Fig. 49. Morphological changes in HDF cells after laser irradiation following treatment with AuNTs at concentrations of 10, 25, 50, and 100 µg/mL for 24 hours, compared to untreated controls with and without laser exposure. Significant changes were noticed (indicated by arrows) after 10 minutes of laser irradiation at 1 W.

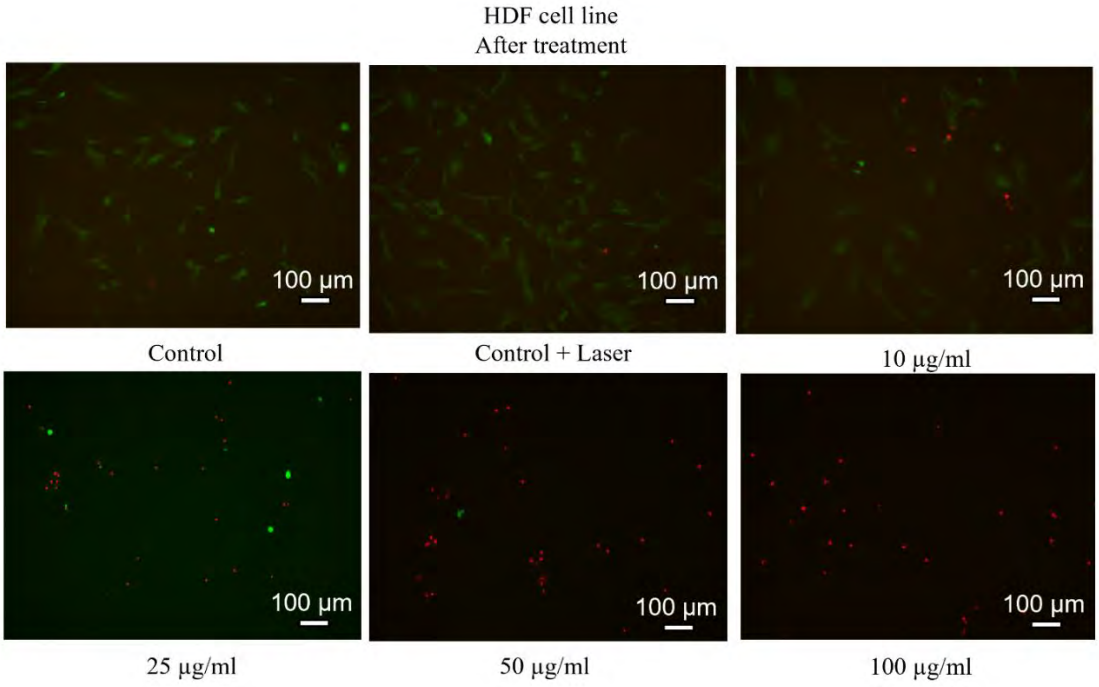

Fig. 50. Live/dead staining of HDF cells was performed after 10 minutes of 808 nm laser irradiation at 1 W power. Cells were treated with AuNTs at concentrations of 0, 10, 25, 50, and 100 µg/mL. The reduction in red fluorescence at lower AuNT concentrations indicates the effectiveness of the nanoparticles' photothermal activity in inducing cell death.

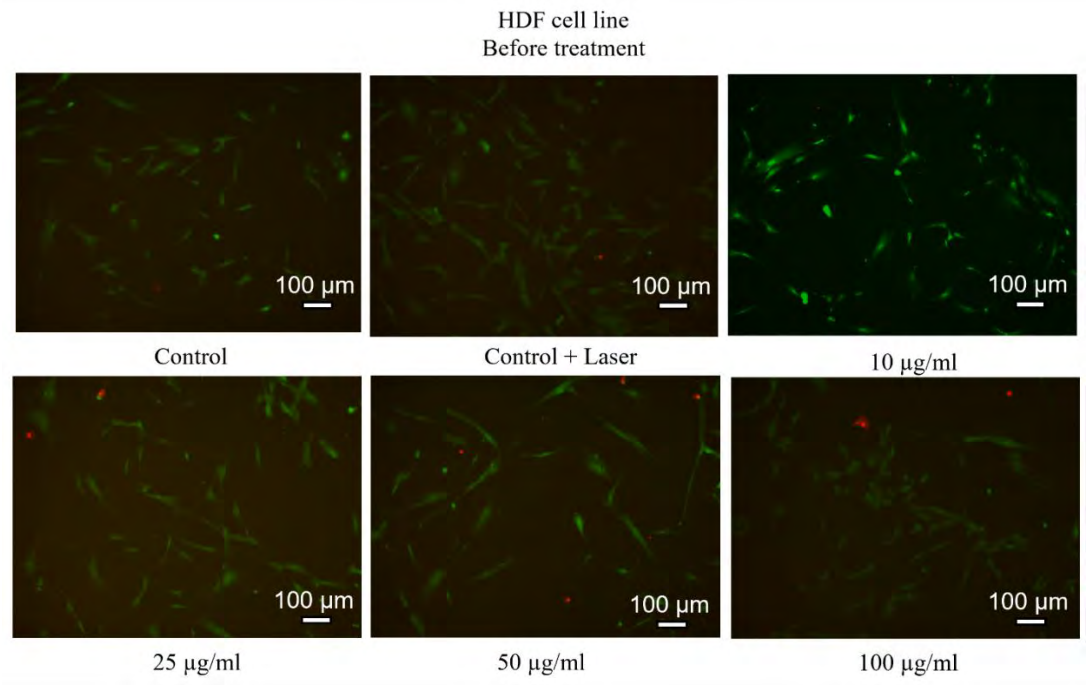

Fig. 51. Live/dead staining of HDF cells prior to 10 minutes of 808 nm laser irradiation at 1 W power. Cells were treated with AuNTs at concentrations of 0, 10, 25, 50, and 100 µg/mL.

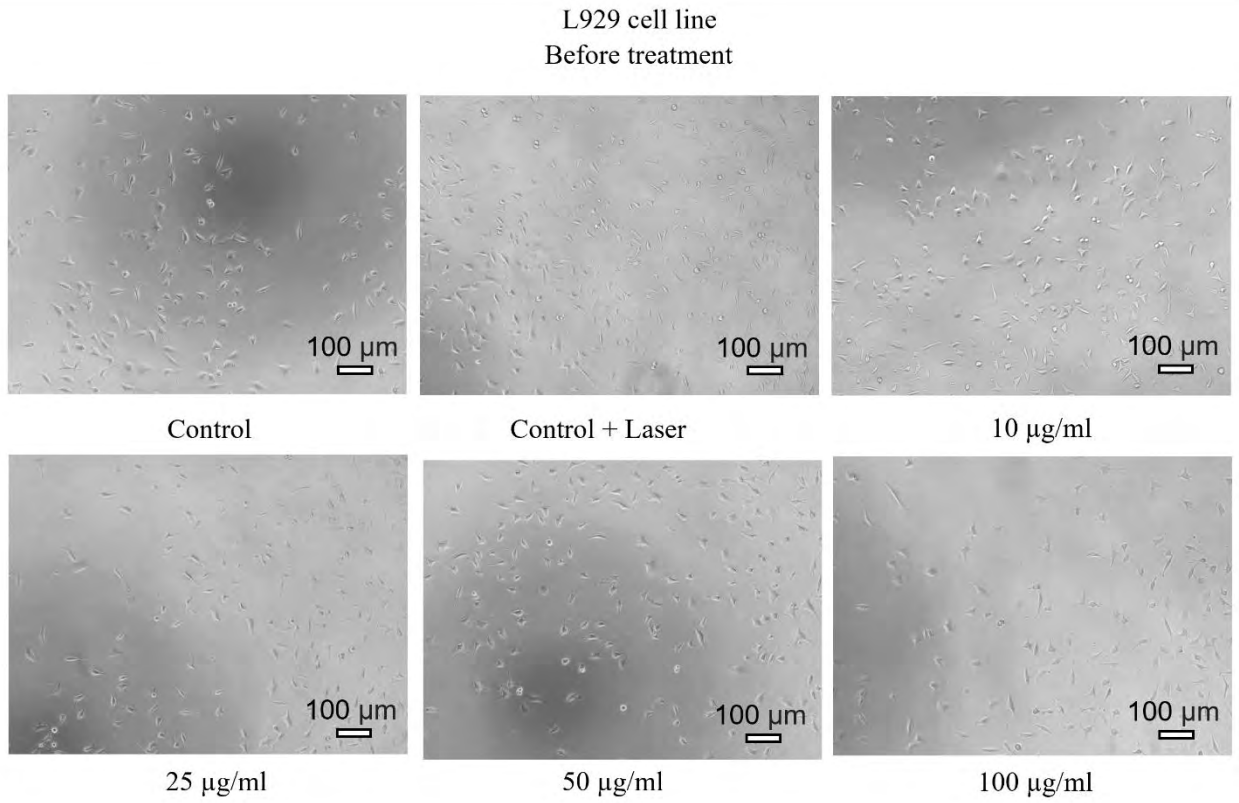

Fig. 52. Viability of L929 cells treated with AuNTs at concentrations of 10, 25, 50, and 100 µg/mL for 24 hours, compared to untreated controls, both with and without laser irradiation.

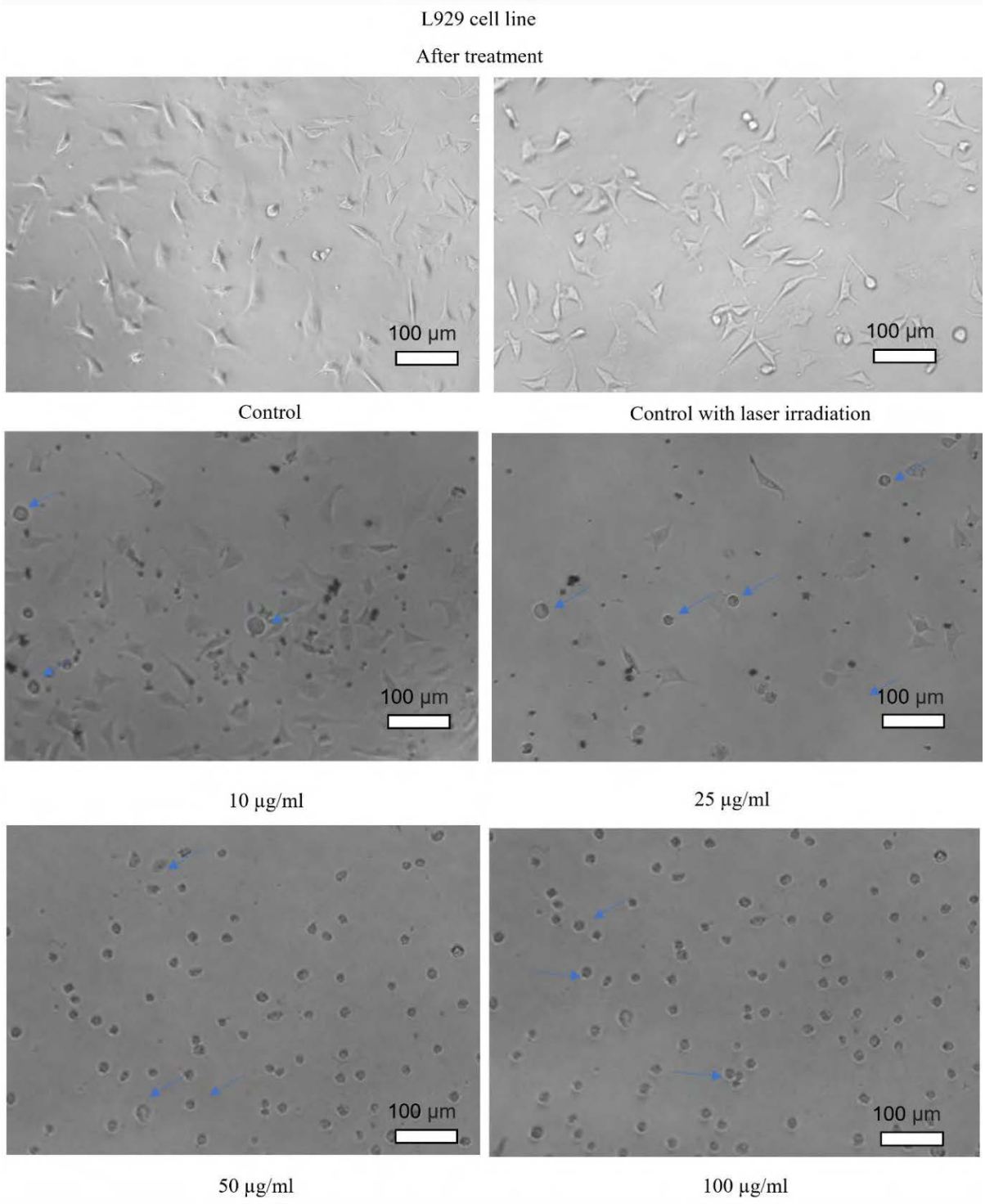

Fig. 53. Morphological changes in L929 cells after laser irradiation following treatment with AuNTs at concentrations of 10, 25, 50, and 100 µg/mL for 24 hours, compared to untreated controls with and without laser exposure. Significant changes were noticed (indicated by arrows) after 10 minutes of laser irradiation at 1 W.

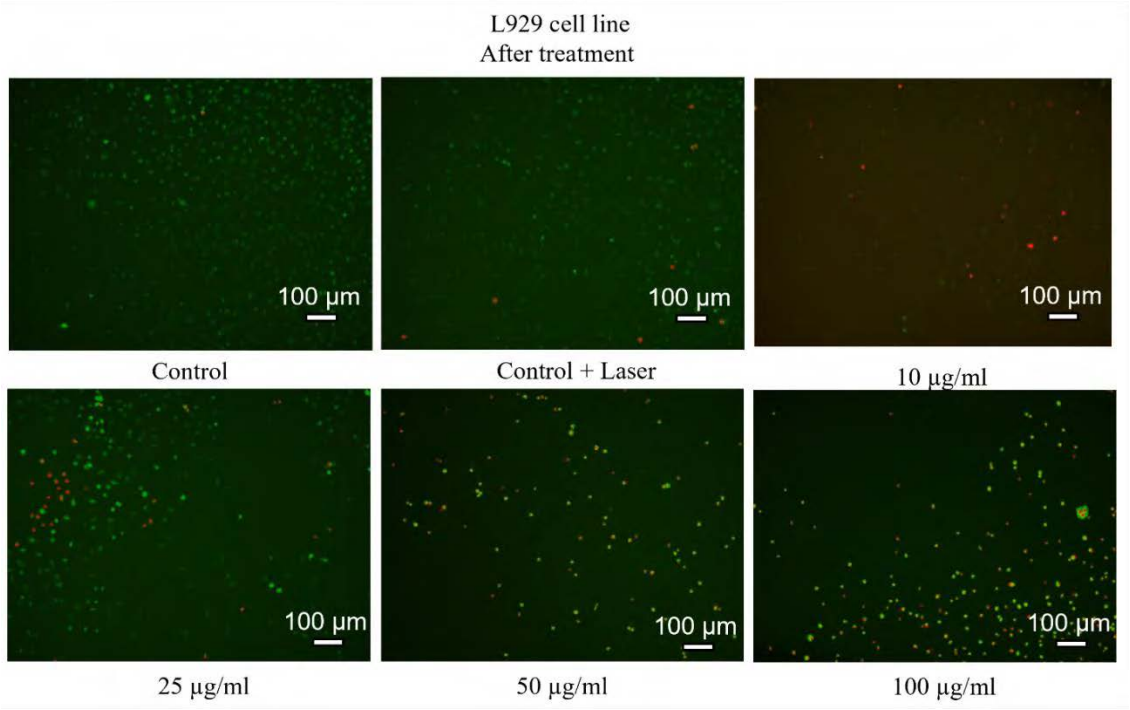

Fig. 54. Live/dead staining of L929 cells was performed after 10 minutes of 808 nm laser irradiation at 1 W power. Cells were treated with AuNTs at concentrations of 0, 10, 25, 50, and 100 µg/mL. The reduction in red fluorescence at lower AuNT concentrations indicates the effectiveness of the nanoparticles' photothermal activity in inducing cell death.

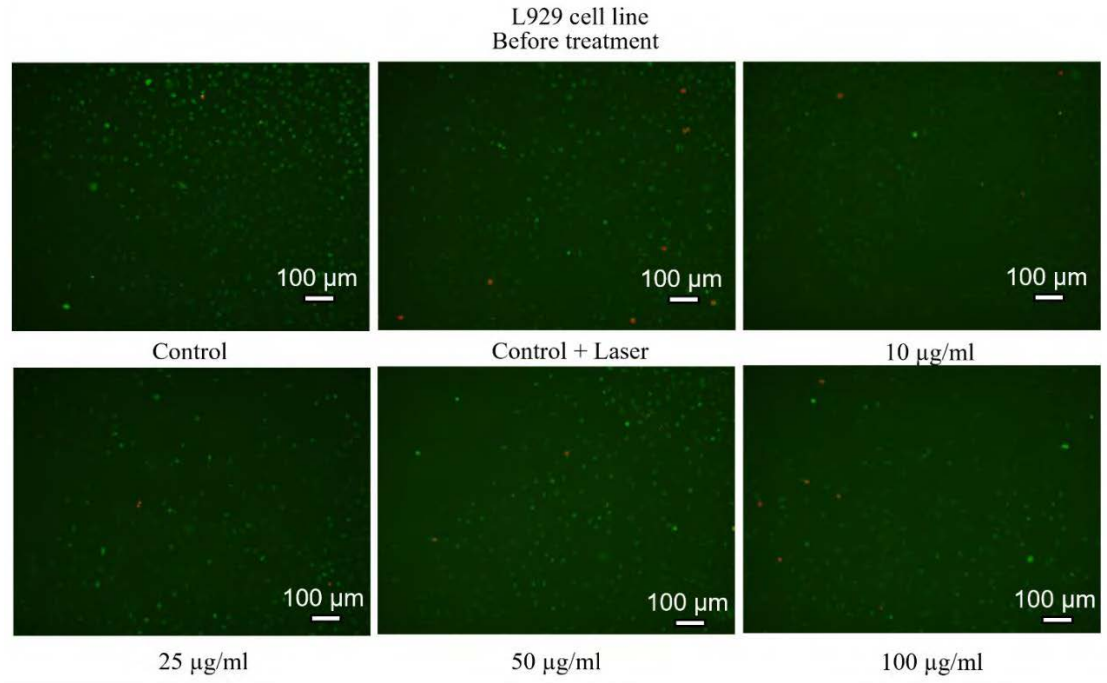

Fig. 55. Live/dead staining of L929 cells prior to 10 minutes of 808 nm laser irradiation at 1 W power. Cells were treated with AuNTs at concentrations of 0, 10, 25, 50, and 100 µg/mL.

The biocompatibility of eco-friendly synthesized sacran-coated gold nanotriangles (sacran-AuNTs) was tested on A549, HDF, and L929 cell lines under NIR laser irradiation (1 W, 808 nm for 10 minutes). Fig. 56 shows cell viability percentages in relation to nanoparticle concentrations following a 24-hour treatment period.

From Fig. 56, it is evident that AuNTs can induce cytotoxicity in A549 cells, particularly at higher concentrations. The combination of AuNTs and NIR radiation leads to enhanced cytotoxicity and membrane rupture in A549 cells, primarily due to the photothermal effect and increased reactive oxygen species (ROS) production. These cytotoxic effects can cause significant cell membrane damage, ROS generation, and apoptosis.

L929 cells exhibit resilience at lower concentrations of sacran-AuNTs (10 and 25 μg/mL). However, at higher concentrations, these cells experience membrane damage and increased cytotoxic effects. The enhanced cytotoxicity at higher concentrations can be attributed to the accumulation of AuNTs and their interaction with the cell membrane, leading to cellular damage.

HDF cells are more sensitive to sacran-AuNT exposure compared to the immortalized cell lines A549 and L929. The higher sensitivity of HDF cells results in more pronounced cytotoxic effects and membrane damage, even at lower concentrations of sacran-AuNTs. These findings underscore the potential of sacran-AuNTs for photothermal therapy.

To improve the selectivity of sacran-AuNTs for photothermal therapy of A549 cancer cells, it is recommended to conjugate targeting ligands and load chemotherapeutic drugs onto the AuNTs. For practical use, it is essential to study the nanoparticle uptake by cells. Cancer cells (A549) have abnormal, highly permeable blood vessels with large fenestrations, allowing nanoparticles like AuNTs to penetrate the tumor tissue more easily compared to normal tissues. Tumor tissues also exhibit impaired lymphatic drainage, which means that once the nanoparticles enter the tumor site, they tend to accumulate and are retained for longer periods. This phenomenon is known as the Enhanced Permeability and Retention (EPR) effect.

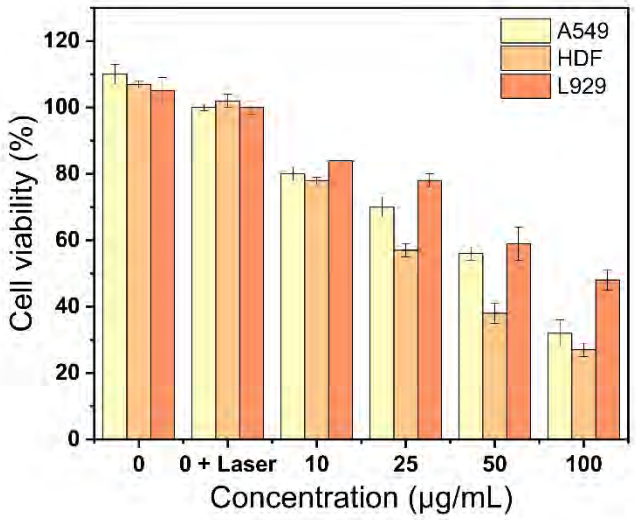

Fig. 56. The graph depicts the relationship between AuNT concentration and cell viability (%) following a 24-hour treatment period, showing the impact of varying AuNT concentrations on cell viability.

3.4 Conclusion

Here we found AuNPLs generation in the presence of supergiant polysaccharides, sacran, without any additional additives. Sacran, even in a low concentration, acted as the reducing and stabilizing agent for the formation and inhibition of aggregation of AuNPLs when compared with high reducing performance (high sacran concentration). We controlled morphology of anisotropic AuNPs using sacran and iodide anions, resulting in highly uniform AuNTs with a size of 62 ± 10 nm. This groundbreaking method, unprecedented in the literature, combines polysaccharide and iodide anion reduction, enabling precise control of AuNT morphology. Notably, our room-temperature process, with its easy parameter adjustments for morphology control, distinguishes itself from existing methods.

Our AuNTs exhibited exceptional catalytic performance, converting 4-NP to 4-AP with a specific rate constant (k) of 2.90×10^3 $s^{-1}g^{-1}$, outperforming Au nanoprisms (k = 1.00×10^3 $s^{-1}g^{-1}$) and Au nanorods (k = 1.25×10^3 $s^{-1}g^{-1}$) under ascorbic acid capping agent. Furthermore, they displayed high recyclability and excellent catalytic reduction activities towards various chloro-substituted nitroarenes, with conversion and selectivity rates exceeding 95%.

This novel synthesis approach, characterized by its high catalytic stability and can be applied in plasmonic photothermal therapy. Our findings pave the way for innovative research and practical applications in these fields.

3.5 References

1. Vijayan, R.; Joseph, S.; Mathew, B., Indigofera tinctoria leaf extract mediated green synthesis of silver and gold nanoparticles and assessment of their anticancer, antimicrobial, antioxidant and catalytic properties. *Artificial Cells, Nanomedicine, and Biotechnology* **2018,** *46* (4), 861-871.
2. Nadeem, M.; Abbasi, B. H.; Younas, M.; Ahmad, W.; Khan, T., A review of the green syntheses and anti-microbial applications of gold nanoparticles. *Green Chemistry Letters and Reviews* **2017,** *10* (4), 216-227.
3. Santhoshkumar, J.; Rajeshkumar, S.; Venkat Kumar, S., Phyto-assisted synthesis, characterization and applications of gold nanoparticles – A review. *Biochemistry and Biophysics Reports* **2017,** *11*, 46-57.
4. Wacławek, S.; Gončuková, Z.; Adach, K.; Fijałkowski, M.; Černík, M., Green synthesis of gold nanoparticles using Artemisia dracunculus extract: control of the shape and size by varying synthesis conditions. *Environmental Science and Pollution Research* **2018,** *25* (24), 24210-24219.
5. Balasubramanian, S.; Raghavachari, D., Green Synthesis of Triangular Au Nanoplates: Role of Small Molecules Present in Bael Gum. *ACS Sustainable Chem. Eng.* **2017,** *5* (11), 10317-10326.
6. Osonga, F. J.; Yazgan, I.; Kariuki, V.; Luther, D.; Jimenez, A.; Le, P.; Sadik, O. A., Greener synthesis and characterization, antimicrobial and cytotoxicity studies of gold nanoparticles of novel shapes and sizes. *RSC Adv.* **2016,** *6* (3), 2302-2313.
7. Deokar, G. K.; Ingale, A. G., Unveiling an unexpected potential of beetroot waste in green synthesis of single crystalline gold nanoplates: A mechanistic study. *Arabian Journal of Chemistry* **2018,** *11* (6), 950-958.
8. Rajkumari, J.; Meena, H.; Gangatharan, M.; Busi, S., Green synthesis of anisotropic gold nanoparticles using hordenine and their antibiofilm efficacy against Pseudomonas aeruginosa. *IET Nanobiotechnology* **2017,** *11* (8), 987-994.
9. Emam, H. E.; Ahmed, H. B., Carboxymethyl cellulose macromolecules as generator of anisotropic nanogold for catalytic performance. *Int. J. Biol. Macromol.* **2018,** *111*, 999-1009.
10. Goyal, D.; Saini, A.; Saini, G. S. S.; Kumar, R., Green synthesis of anisotropic gold nanoparticles using cinnamon with superior antibacterial activity. *Materials Research Express* **2019,** *6* (7), 075043.
11. Korir, D. K.; Gwalani, B.; Joseph, A.; Kamras, B.; Arvapally, R. K.; Omary, M. A.; Marpu, S. B., Facile Photochemical Syntheses of Conjoined Nanotwin Gold-Silver Particles within a Biologically-Benign Chitosan Polymer. *Nanomaterials* **2019,** *9* (4), 596.
12. Sasidharan, S.; Bahadur, D.; Srivastava, R., Rapid, One-Pot, Protein-Mediated Green Synthesis of Gold Nanostars for Computed Tomographic Imaging and Photothermal Therapy of Cancer. *ACS Sustainable Chem. Eng.* **2017,** *5* (11), 10163-10175.

13. Nehra, K.; Pandian, S. K.; Bharati, M. S. S.; Soma, V. R., Enhanced catalytic and SERS performance of shape/size controlled anisotropic gold nanostructures. *New J. Chem.* **2019,** *43* (9), 3835-3847.
14. Takahata, R.; Yamazoe, S.; Koyasu, K.; Imura, K.; Tsukuda, T., Gold Ultrathin Nanorods with Controlled Aspect Ratios and Surface Modifications: Formation Mechanism and Localized Surface Plasmon Resonance. *Journal of the American Chemical Society* **2018,** *140* (21), 6640-6647.
15. Praneeth, N. V. S.; Paria, S., Microwave-assisted one-pot synthesis of anisotropic gold nanoparticles with active high-energy facets for enhanced catalytic and metal enhanced fluorescence activities. *CrystEngComm* **2018,** *20* (30), 4297-4304.
16. Liu, X.; Yao, J.; Luo, J.; Duan, X.; Yao, Y.; Liu, T., Effect of Growth Temperature on Tailoring the Size and Aspect Ratio of Gold Nanorods. *Langmuir* **2017,** *33* (30), 7479-7485.
17. Holade, Y.; Hickey, D. P.; Minteer, S. D., Halide-regulated growth of electrocatalytic metal nanoparticles directly onto a carbon paper electrode. *Journal of Materials Chemistry A* **2016,** *4* (43), 17154-17162.
18. Shankar, S. S.; Rai, A.; Ankamwar, B.; Singh, A.; Ahmad, A.; Sastry, M., Biological synthesis of triangular gold nanoprisms. *Nature Materials* **2004,** *3* (7), 482-488.
19. Wang, Q.; Wang, Z.; Li, Z.; Xiao, J.; Shan, H.; Fang, Z.; Qi, L., Controlled growth and shape-directed self-assembly of gold nanoarrows. *Science Advances* **2017,** *3* (10), e1701183.
20. Bechtold, T.; Manian, A. P.; Öztürk, H. B.; Paul, U.; Široká, B.; Široký, J.; Soliman, H.; Vo, L. T. T.; Vu-Manh, H., Ion-interactions as driving force in polysaccharide assembly. *Carbohydr. Polym.* **2013,** *93* (1), 316-323.
21. Ahmed, H. B., Recruitment of various biological macromolecules in fabrication of gold nanoparticles: Overview for preparation and applications. *Int. J. Biol. Macromol.* **2019,** *140*, 265-277.
22. Kemp, M. M.; Kumar, A.; Mousa, S.; Park, T.-J.; Ajayan, P.; Kubotera, N.; Mousa, S. A.; Linhardt, R. J., Synthesis of Gold and Silver Nanoparticles Stabilized with Glycosaminoglycans Having Distinctive Biological Activities. *Biomacromolecules* **2009,** *10* (3), 589-595.
23. Okajima, M. K.; Nakamura, M.; Mitsumata, T.; Kaneko, T., Cyanobacterial Polysaccharide Gels with Efficient Rare-Earth-Metal Sorption. *Biomacromolecules* **2010,** *11* (7), 1773-1778.
24. Sornkamnerd, S.; Okajima, M. K.; Matsumura, K.; Kaneko, T., Surface-Selective Control of Cell Orientation on Cyanobacterial Liquid Crystalline Gels. *ACS Omega* **2018,** *3* (6), 6554-6559.
25. Kawashima, H.; Atarashi, K.; Hirose, M.; Hirose, J.; Yamada, S.; Sugahara, K.; Miyasaka, M., Oversulfated Chondroitin/Dermatan Sulfates Containing GlcAβ1/IdoAα1–3GalNAc(4,6-O-disulfate) Interact with L- and P-selectin and Chemokines∗. *J. Biol. Chem.* **2002,** *277* (15), 12921-12930.

26. Astronomo, R. D.; Burton, D. R., Carbohydrate vaccines: developing sweet solutions to sticky situations? *Nature Reviews Drug Discovery* **2010,** *9* (4), 308-324.
27. Okajima, M. K.; Higashi, T.; Asakawa, R.; Mitsumata, T.; Kaneko, D.; Kaneko, T.; Ogawa, T.; Kurata, H.; Isoda, S., Gelation Behavior by the Lanthanoid Adsorption of the Cyanobacterial Extracellular Polysaccharide. *Biomacromolecules* **2010,** *11* (11), 3172-3177.
28. Sayko, R.; Jacobs, M.; Dobrynin, A. V., Quantifying Properties of Polysaccharide Solutions. *ACS Polymers Au* **2021,** *1* (3), 196-205.
29. Lyu, Y.; Becerril, L. M.; Vanzan, M.; Corni, S.; Cattelan, M.; Granozzi, G.; Frasconi, M.; Rajak, P.; Banerjee, P.; Ciancio, R.; Mancin, F.; Scrimin, P., The Interaction of Amines with Gold Nanoparticles. *Adv. Mater. n/a* (n/a), 2211624.
30. Zhang, J.; Xiong, B.; Fu, Z.; Ning, Y.; Li, D., Synergistic Effect of Hydroxyl and Carboxyl Groups on Promoting Nanoparticle Occlusion within Calcite. *Small* **2023,** *19* (18), 2207843.
31. Okajima, M. K.; Kumar, A.; Fujiwara, A.; Mitsumata, T.; Kaneko, D.; Ogawa, T.; Kurata, H.; Isoda, S.; Kaneko, T., Anionic complexes of MWCNT with supergiant cyanobacterial polyanions. *Biopolymers* **2013,** *99* (1), 1-9.
32. Puluhulawa, L. E.; Joni, I. M.; Mohammed, A. F. A.; Arima, H.; Wathoni, N., The Use of Megamolecular Polysaccharide Sacran in Food and Biomedical Applications. *Molecules* **2021,** *26* (11), 3362.
33. Mitsumata, T.; Miura, T.; Takahashi, N.; Kawai, M.; Okajima, M. K.; Kaneko, T., Ionic state and chain conformation for aqueous solutions of supergiant cyanobacterial polysaccharide. *Physical Review E* **2013,** *87* (4), 042607.
34. AshaRani, P. V.; Low Kah Mun, G.; Hande, M. P.; Valiyaveettil, S., Cytotoxicity and Genotoxicity of Silver Nanoparticles in Human Cells. *ACS Nano* **2009,** *3* (2), 279-290.
35. Verano-Braga, T.; Miethling-Graff, R.; Wojdyla, K.; Rogowska-Wrzesinska, A.; Brewer, J. R.; Erdmann, H.; Kjeldsen, F., Insights into the Cellular Response Triggered by Silver Nanoparticles Using Quantitative Proteomics. *ACS Nano* **2014,** *8* (3), 2161-2175.
36. Singh, A.; Pasricha, R.; Sastry, M., Ultra-low level optical detection of mercuric ions using biogenic gold nanotriangles. *Analyst* **2012,** *137* (13), 3083-3090.
37. Yan, Z.; Yuen, M.-F.; Hu, L.; Sun, P.; Lee, C.-S., Advances for the colorimetric detection of Hg2+ in aqueous solution. *RSC Adv.* **2014,** *4* (89), 48373-48388.
38. Zhang, Y.; Charles, D. E.; Ledwith, D. M.; Aherne, D.; Cunningham, S.; Voisin, M.; Blau, W. J.; Gun'ko, Y. K.; Kelly, J. M.; Brennan-Fournet, M. E., Wash-free highly sensitive detection of C-reactive protein using gold derivatised triangular silver nanoplates. *RSC Adv.* **2014,** *4* (55), 29022-29031.
39. Jiang, X.; Liu, R.; Tang, P.; Li, W.; Zhong, H.; Zhou, Z.; Zhou, J., Controllably tuning the near-infrared plasmonic modes of gold nanoplates for enhanced optical coherence imaging and photothermal therapy. *RSC Adv.* **2015,** *5* (98), 80709-80718.

40. Fazal, S.; Jayasree, A.; Sasidharan, S.; Koyakutty, M.; Nair, S. V.; Menon, D., Green Synthesis of Anisotropic Gold Nanoparticles for Photothermal Therapy of Cancer. *ACS Appl. Mater. Interfaces* **2014,** *6* (11), 8080-8089.
41. Shankar, S. S.; Rai, A.; Ahmad, A.; Sastry, M., Controlling the Optical Properties of Lemongrass Extract Synthesized Gold Nanotriangles and Potential Application in Infrared-Absorbing Optical Coatings. *Chem. Mater.* **2005,** *17* (3), 566-572.
42. Xie, J.; Lee, J. Y.; Wang, D. I. C.; Ting, Y. P., Identification of Active Biomolecules in the High-Yield Synthesis of Single-Crystalline Gold Nanoplates in Algal Solutions. *Small* **2007,** *3* (4), 672-682.
43. Wu, C.-C.; Chen, D.-H., Facile green synthesis of gold nanoparticles with gum arabic as a stabilizing agent and reducing agent. *Gold Bulletin* **2010,** *43* (4), 234-240.
44. Okajima, M. K.; Bamba, T.; Kaneso, Y.; Hirata, K.; Fukusaki, E.; Kajiyama, S. i.; Kaneko, T., Supergiant Ampholytic Sugar Chains with Imbalanced Charge Ratio Form Saline Ultra-absorbent Hydrogels. *Macromolecules* **2008,** *41* (12), 4061-4064.
45. Okajima, M. K.; Kaneko, D.; Mitsumata, T.; Kaneko, T.; Watanabe, J., Cyanobacteria That Produce Megamolecules with Efficient Self-Orientations. *Macromolecules* **2009,** *42* (8), 3057-3062.
46. Okajima, M. K.; Miyazato, S.; Kaneko, T., Cyanobacterial Megamolecule Sacran Efficiently Forms LC Gels with Very Heavy Metal Ions. *Langmuir* **2009,** *25* (15), 8526-8531.
47. Okajima, M. K.; Miyazato, S.; Kaneko, T., Cyanobacterial megamolecule sacran efficiently forms LC gels with very heavy metal ions. *Langmuir* **2009,** *25* (15), 8526-31.
48. Radziuk, D.; Skirtach, A.; Sukhorukov, G.; Shchukin, D.; Möhwald, H., Stabilization of Silver Nanoparticles by Polyelectrolytes and Poly(ethylene glycol). *Macromol. Rapid Commun.* **2007,** *28* (7), 848-855.
49. Ershov, B. G.; Abkhalimov, E. V.; Solovov, R. D.; Roldughin, V. I., Gold nanoparticles in aqueous solutions: influence of size and pH on hydrogen dissociative adsorption and Au(iii) ion reduction. *Physical Chemistry Chemical Physics* **2016,** *18* (19), 13459-13466.
50. Mzwd, E.; Ahmed, N. M.; Suradi, N.; Alsaee, S. K.; Altowyan, A. S.; Almessiere, M. A.; Omar, A. F., Green synthesis of gold nanoparticles in Gum Arabic using pulsed laser ablation for CT imaging. *Scientific Reports* **2022,** *12* (1), 10549.
51. Panariello, L.; Radhakrishnan, A. N. P.; Papakonstantinou, I.; Parkin, I. P.; Gavriilidis, A., Particle Size Evolution during the Synthesis of Gold Nanoparticles Using In Situ Time-Resolved UV–Vis Spectroscopy: An Experimental and Theoretical Study Unravelling the Effect of Adsorbed Gold Precursor Species. *The Journal of Physical Chemistry C* **2020,** *124* (50), 27662-27672.
52. Stangherlin, S.; Cathcart, N.; Sato, F.; Kitaev, V., Gold Nanoprisms: Synthetic Approaches for Mastering Plasmonic Properties and Implications for Biomedical Applications. *ACS Appl. Nano Mater.* **2020,** *3* (8), 8304-8318.

53. DuChene, J. S.; Niu, W.; Abendroth, J. M.; Sun, Q.; Zhao, W.; Huo, F.; Wei, W. D., Halide Anions as Shape-Directing Agents for Obtaining High-Quality Anisotropic Gold Nanostructures. *Chem. Mater.* **2013,** *25* (8), 1392-1399.
54. Chen, L.; Ji, F.; Xu, Y.; He, L.; Mi, Y.; Bao, F.; Sun, B.; Zhang, X.; Zhang, Q., High-Yield Seedless Synthesis of Triangular Gold Nanoplates through Oxidative Etching. *Nano Lett.* **2014,** *14* (12), 7201-7206.
55. Millstone, J. E.; Hurst, S. J.; Métraux, G. S.; Cutler, J. I.; Mirkin, C. A., Colloidal Gold and Silver Triangular Nanoprisms. *Small* **2009,** *5* (6), 646-664.
56. Millstone, J. E.; Park, S.; Shuford, K. L.; Qin, L.; Schatz, G. C.; Mirkin, C. A., Observation of a Quadrupole Plasmon Mode for a Colloidal Solution of Gold Nanoprisms. *Journal of the American Chemical Society* **2005,** *127* (15), 5312-5313.
57. Tangeysh, B.; Moore Tibbetts, K.; Odhner, J. H.; Wayland, B. B.; Levis, R. J., Triangular Gold Nanoplate Growth by Oriented Attachment of Au Seeds Generated by Strong Field Laser Reduction. *Nano Lett.* **2015,** *15* (5), 3377-3382.
58. Germain, V.; Li, J.; Ingert, D.; Wang, Z. L.; Pileni, M. P., Stacking Faults in Formation of Silver Nanodisks. *The Journal of Physical Chemistry B* **2003,** *107* (34), 8717-8720.
59. Stevens, J. S.; Schroeder, S. L. M., Quantitative analysis of saccharides by X-ray photoelectron spectroscopy. *Surf. Interface Anal.* **2009,** *41* (6), 453-462.
60. Kang, F.; Qu, X.; Alvarez, P. J. J.; Zhu, D., Extracellular Saccharide-Mediated Reduction of Au3+ to Gold Nanoparticles: New Insights for Heavy Metals Biomineralization on Microbial Surfaces. *Environ. Sci. Technol.* **2017,** *51* (5), 2776-2785.
61. Xu, Z.; Uddin, K. M. A.; Kamra, T.; Schnadt, J.; Ye, L., Fluorescent Boronic Acid Polymer Grafted on Silica Particles for Affinity Separation of Saccharides. *ACS Appl. Mater. Interfaces* **2014,** *6* (3), 1406-1414.
62. Amat Yusof, F. A.; Yamaki, M.; Kawai, M.; Okajima, M. K.; Kaneko, T.; Mitsumata, T., Rheopectic Behavior for Aqueous Solutions of Megamolecular Polysaccharide Sacran. *Biomolecules* **2020,** *10* (1).
63. Doi, M.; Sagawa, Y.; Momose, S.; Tanaka, T.; Mizutani, T.; Okano, Y.; Masaki, H., Topical treatment with sacran, a sulfated polysaccharide from Aphanothece sacrum, improves corneocyte-derived parameters. *The Journal of Dermatology* **2017,** *44* (12), 1360-1367.
64. Biesinger, M. C., Advanced analysis of copper X-ray photoelectron spectra. *Surf. Interface Anal.* **2017,** *49* (13), 1325-1334.
65. Xia, J.; Dong, Z.; Cai, Y.; Guan, G.; Zhang, S.; Kovács, A.; Boothroyd, C.; Phang, I. Y.; Liu, S.; Wu, M.; Zhang, Y. W.; Hu, X.; Han, M.-Y., Morphological Growth and Theoretical Understanding of Gold and Other Noble Metal Nanoplates. *Chemistry – A European Journal* **2018,** *24* (58), 15589-15595.
66. Emam, H. E.; El-Bisi, M. K., Merely Ag nanoparticles using different cellulose fibers as removable reductant. *Cellulose* **2014,** *21* (6), 4219-4230.

67. Hebeish, A. A.; El-Rafie, M. H.; Abdel-Mohdy, F. A.; Abdel-Halim, E. S.; Emam, H. E., Carboxymethyl cellulose for green synthesis and stabilization of silver nanoparticles. *Carbohydr. Polym.* **2010,** *82* (3), 933-941.
68. Ahmed, H. B.; Abdel-Mohsen, A. M.; Emam, H. E., Green-assisted tool for nanogold synthesis based on alginate as a biological macromolecule. *RSC Adv.* **2016,** *6* (78), 73974-73985.
69. Ahmed, H. B.; Zahran, M. K.; Emam, H. E., Heatless synthesis of well dispersible Au nanoparticles using pectin biopolymer. *Int. J. Biol. Macromol.* **2016,** *91*, 208-219.
70. Berhault, G.; Bausach, M.; Bisson, L.; Becerra, L.; Thomazeau, C.; Uzio, D., Seed-Mediated Synthesis of Pd Nanocrystals: Factors Influencing a Kinetic- or Thermodynamic-Controlled Growth Regime. *The Journal of Physical Chemistry C* **2007,** *111* (16), 5915-5925.
71. Sajanlal, P. R.; Sreeprasad, T. S.; Samal, A. K.; Pradeep, T., Anisotropic nanomaterials: structure, growth, assembly, and functions. *Nano Reviews* **2011,** *2* (1), 5883.
72. Li, N.; Zhao, P.; Astruc, D., Anisotropic Gold Nanoparticles: Synthesis, Properties, Applications, and Toxicity. *Angew. Chem. Int. Ed.* **2014,** *53* (7), 1756-1789.
73. Xue, C.; Métraux, G. S.; Millstone, J. E.; Mirkin, C. A., Mechanistic Study of Photomediated Triangular Silver Nanoprism Growth. *Journal of the American Chemical Society* **2008,** *130* (26), 8337-8344.
74. Chu, H.-C.; Kuo, C.-H.; Huang, M. H., Thermal Aqueous Solution Approach for the Synthesis of Triangular and Hexagonal Gold Nanoplates with Three Different Size Ranges. *Inorg. Chem.* **2006,** *45* (2), 808-813.
75. Zhu, J.; Jin, X.-l., Electrochemical synthesis of gold triangular nanoplates and self-organized into rhombic nanostructures. *Superlattices Microstruct.* **2007,** *41* (4), 271-276.
76. Miranda, A.; Malheiro, E.; Skiba, E.; Quaresma, P.; Carvalho, P. A.; Eaton, P.; de Castro, B.; Shelnutt, J. A.; Pereira, E., One-pot synthesis of triangular gold nanoplates allowing broad and fine tuning of edge length. *Nanoscale* **2010,** *2* (10), 2209-2216.
77. Millstone, J. E.; Métraux, G. S.; Mirkin, C. A., Controlling the Edge Length of Gold Nanoprisms via a Seed-Mediated Approach. *Adv. Funct. Mater.* **2006,** *16* (9), 1209-1214.
78. Millstone, J. E.; Wei, W.; Jones, M. R.; Yoo, H.; Mirkin, C. A., Iodide Ions Control Seed-Mediated Growth of Anisotropic Gold Nanoparticles. *Nano Lett.* **2008,** *8* (8), 2526-2529.
79. Piella, J.; Bastús, N. G.; Puntes, V., Size-Controlled Synthesis of Sub-10-nanometer Citrate-Stabilized Gold Nanoparticles and Related Optical Properties. *Chem. Mater.* **2016,** *28* (4), 1066-1075.
80. Hendel, T.; Wuithschick, M.; Kettemann, F.; Birnbaum, A.; Rademann, K.; Polte, J., In Situ Determination of Colloidal Gold Concentrations with UV–Vis Spectroscopy: Limitations and Perspectives. *Anal. Chem.* **2014,** *86* (22), 11115-11124.
81. Jones, M. R.; Mirkin, C. A., Bypassing the Limitations of Classical Chemical Purification with DNA-Programmable Nanoparticle Recrystallization. *Angew. Chem. Int. Ed.* **2013,** *52* (10), 2886-2891.

82. Cheng, W.; Dong, S.; Wang, E., Iodine-Induced Gold-Nanoparticle Fusion/Fragmentation/Aggregation and Iodine-Linked Nanostructured Assemblies on a Glass Substrate. *Angew. Chem. Int. Ed.* **2003,** *42* (4), 449-452.
83. Alloyeau, D.; Dachraoui, W.; Javed, Y.; Belkahla, H.; Wang, G.; Lecoq, H.; Ammar, S.; Ersen, O.; Wisnet, A.; Gazeau, F.; Ricolleau, C., Unravelling Kinetic and Thermodynamic Effects on the Growth of Gold Nanoplates by Liquid Transmission Electron Microscopy. *Nano Lett.* **2015,** *15* (4), 2574-2581.
84. Choi, B. K.; Kim, J.; Luo, Z.; Kim, J.; Kim, J. H.; Hyeon, T.; Mehraeen, S.; Park, S.; Park, J., Shape Transformation Mechanism of Gold Nanoplates. *ACS Nano* **2023,** *17* (3), 2007-2018.
85. Baral, A.; Cavalieri, F.; Chattopadhyay, S.; Ashokkumar, M., Synthesis of Gold Nanosheets with Controlled Morphology by Combining a Natural Amino Acid with High-Frequency Ultrasound. *ACS Sustainable Chem. Eng.* **2021,** *9* (41), 13953-13962.
86. Khan, M.; Al-hamoud, K.; Liaqat, Z.; Shaik, M. R.; Adil, S. F.; Kuniyil, M.; Alkhathlan, H. Z.; Al-Warthan, A.; Siddiqui, M. R. H.; Mondeshki, M.; Tremel, W.; Khan, M.; Tahir, M. N., Synthesis of Au, Ag, and Au–Ag Bimetallic Nanoparticles Using Pulicaria undulata Extract and Their Catalytic Activity for the Reduction of 4-Nitrophenol. *Nanomaterials* **2020,** *10* (9), 1885.
87. Hervés, P.; Pérez-Lorenzo, M.; Liz-Marzán, L. M.; Dzubiella, J.; Lu, Y.; Ballauff, M., Catalysis by metallic nanoparticles in aqueous solution: model reactions. *Chem. Soc. Rev.* **2012,** *41* (17), 5577-5587.
88. Zhao, B.; Mele, G.; Pio, I.; Li, J.; Palmisano, L.; Vasapollo, G., Degradation of 4-nitrophenol (4-NP) using Fe–TiO2 as a heterogeneous photo-Fenton catalyst. *J. Hazard. Mater.* **2010,** *176* (1), 569-574.
89. Pandey, A. K.; Gaur, V. K.; Udayan, A.; Varjani, S.; Kim, S.-H.; Wong, J. W. C., Biocatalytic remediation of industrial pollutants for environmental sustainability: Research needs and opportunities. *Chemosphere* **2021,** *272*, 129936.
90. Salehi, S.; Abdollahi, K.; Panahi, R.; Rahmanian, N.; Shakeri, M.; Mokhtarani, B., Applications of Biocatalysts for Sustainable Oxidation of Phenolic Pollutants: A Review. *Sustainability* **2021,** *13* (15), 8620.
91. Ali, F.; Khan, S. B.; Kamal, T.; Anwar, Y.; Alamry, K. A.; Asiri, A. M., Anti-bacterial chitosan/zinc phthalocyanine fibers supported metallic and bimetallic nanoparticles for the removal of organic pollutants. *Carbohydr. Polym.* **2017,** *173*, 676-689.
92. Wunder, S.; Lu, Y.; Albrecht, M.; Ballauff, M., Catalytic Activity of Faceted Gold Nanoparticles Studied by a Model Reaction: Evidence for Substrate-Induced Surface Restructuring. *ACS Catal.* **2011,** *1* (8), 908-916.
93. Wunder, S.; Polzer, F.; Lu, Y.; Mei, Y.; Ballauff, M., Kinetic Analysis of Catalytic Reduction of 4-Nitrophenol by Metallic Nanoparticles Immobilized in Spherical Polyelectrolyte Brushes. *The Journal of Physical Chemistry C* **2010,** *114* (19), 8814-8820.

94. Zhou, X.; Xu, W.; Liu, G.; Panda, D.; Chen, P., Size-Dependent Catalytic Activity and Dynamics of Gold Nanoparticles at the Single-Molecule Level. *Journal of the American Chemical Society* **2010,** *132* (1), 138-146.
95. Monti, G. A.; Correa, N. M.; Falcone, R. D.; Silbestri, G. F.; Moyano, F., New Insights into the Catalytic Activity and Reusability of Water-Soluble Silver Nanoparticles. *ChemistrySelect* **2021,** *6* (29), 7436-7442.
96. Blanco, E.; Atienzar, P.; Hernández, P.; Quintana, C., The Langmuir–Hinshelwood approach for kinetic evaluation of cucurbit[7]uril-capped gold nanoparticles in the reduction of the antimicrobial nitrofurantoin. *Physical Chemistry Chemical Physics* **2017,** *19* (29), 18913-18923.
97. Rashid, M. H.; Mandal, T. K., Templateless Synthesis of Polygonal Gold Nanoparticles: An Unsupported and Reusable Catalyst with Superior Activity. *Adv. Funct. Mater.* **2008,** *18* (15), 2261-2271.
98. Bai, X.; Gao, Y.; Liu, H.-g.; Zheng, L., Synthesis of Amphiphilic Ionic Liquids Terminated Gold Nanorods and Their Superior Catalytic Activity for the Reduction of Nitro Compounds. *The Journal of Physical Chemistry C* **2009,** *113* (41), 17730-17736.
99. Kundu, S.; Lau, S.; Liang, H., Shape-Controlled Catalysis by Cetyltrimethylammonium Bromide Terminated Gold Nanospheres, Nanorods, and Nanoprisms. *The Journal of Physical Chemistry C* **2009,** *113* (13), 5150-5156.
100. Kaur, R.; Pal, B., Improved surface properties and catalytic activity of anisotropic shapes of photoetched Au nanostructures formed by variable energy laser exposure. *J. Mol. Catal. A: Chem.* **2014,** *395*, 7-15.
101. Bhosale, M. A.; Chenna, D. R.; Ahire, J. P.; Bhanage, B. M., Morphological study of microwave-assisted facile synthesis of gold nanoflowers/nanoparticles in aqueous medium and their catalytic application for reduction of p-nitrophenol to p-aminophenol. *RSC Adv.* **2015,** *5* (65), 52817-52823.
102. Zhu, Q.; Zhang, W.; Cai, J.; Li, J.; Zhong, L.; Pu, S.; Li, A., Morphology-controlled synthesis of gold nanoparticles with chitosan for catalytic reduction of nitrophenol. *Colloids and Surfaces A: Physicochemical and Engineering Aspects* **2022,** *640*, 128471.
103. Cárdenas-Lizana, F.; Hao, Y.; Crespo-Quesada, M.; Yuranov, I.; Wang, X.; Keane, M. A.; Kiwi-Minsker, L., Selective Gas Phase Hydrogenation of p-Chloronitrobenzene over Pd Catalysts: Role of the Support. *ACS Catal.* **2013,** *3* (6), 1386-1396.
104. Zhong, R.-Y.; Sun, K.-Q.; Hong, Y.-C.; Xu, B.-Q., Impacts of Organic Stabilizers on Catalysis of Au Nanoparticles from Colloidal Preparation. *ACS Catal.* **2014,** *4* (11), 3982-3993.

CHAPTER IV

Directing Mineralization of ZnO Nanoparticles in Cyanobacterial Liquid Crystals for Potential Cancer Therapies

4.1 Introduction

Xerogels synthesized from natural polymers combine the inherent properties of natural polymers with the unique attributes of xerogels. These materials, derived from abundant and renewable sources, offer exceptional biocompatibility, customizable porosity, extensive surface area, and versatile structural properties. Xerogels, which are dehydrated gels maintaining the three-dimensional network of the original hydrogel, provide a promising foundation for applications in biomedicine, catalysis, tissue scaffolding, wound dressing, biosensors, and drug delivery [107], [108], [109], [110].

The creation of xerogel networks demands a preparation process that is straightforward and efficient, and allows for controlled modification of the degree of cross-linking. Chemical cross-linking is widely utilized to enhance the anisotropic properties of naturally soluble polymers in hydrogel synthesis, primarily because it establishes a three-dimensional network structure within the polymer matrix [111]. This technique entails the creation of covalent bonds among polymer chains, thereby enhancing thermal, chemical, and mechanical properties [112]. Polysaccharides are commonly functionalized using divinyl sulfone (DVS) in a Michael-type reaction, where it serves as a primary acceptor for nucleophiles like thiols, alcohols, and amines under elevated pH conditions. Hyaluronic acid has been efficiently processed into hydrogels through this method and has been extensively explored for drug delivery, biocompatible coatings, and tissue scaffolds [113].

Recently, there has been growing interest in metal-oxide nanocomposite xerogels employing polysaccharides. Specifically, chitosan has been incorporated with zinc oxide (ZnO) and copper oxide (CuO) nanoparticles through redox reactions involving Zn^{2+}, and Cu^{2+} ions in the polymer solution medium [114]. Studies have also explored using carboxymethyl cellulose (CMC) in synthesizing nanocomposite xerogels incorporating ZnO and CuO [115]. ZnO nanoparticles (ZnO NPs) find widespread application in various products, including sunscreen formulations, electronic devices, shampoos, and antiseptic creams [116]. Their widespread use stems from their ability to generate reactive oxygen species (ROS), which cause oxidative damage to DNA, lipids,

and proteins, leading to loss of cellular integrity and function. Additionally, ROS can induce mitochondrial dysfunction and apoptosis [117].

Sacran, a remarkable water-soluble polysaccharide derived from cyanobacteria, has been under investigation for over 15 years [45], [46]. Comprising approximately 100,000 monosaccharides, sacran exhibits a unique composition featuring sulfate groups (11 mol%) and carboxylic acid groups (22 mol%), along with pentose and hexose sugars. In solution, sacran chains spontaneously self-assemble, forming a rigid rod structure and demonstrating liquid crystalline (LC) properties. Notably, the sacran chain has an impressive molar mass of 15×10^6 g/mol, showcasing strong water-retention capabilities [44] and exceptional metal-chelating whose efficiency was enhanced in LC arrangement [46]. Additionally, the LC structure contributes to improved mechanical strength and flexibility, enables controlled release of therapeutics, and serves as effective scaffolds for cell growth [24]. Beyond its intriguing physicochemical characteristics, sacran holds promise for biomedical applications. Previous studies have highlighted its physically crosslinked hydrogel [118], composite cyclodextrin [119], facilitating anti-inflammatory, wound-healing, and antiallergic activities. When chemically crosslinked and cast into xerogels from aqueous solutions, sacran demonstrates in-plane orientation and anisotropic properties [120]. More recently, sacran has been employed as a green stabilizer and reductant for the formation of anisotropic AuNPs with high dispersibility properties and tunable shapes [121]. These features highlight its versatility for diverse applications in material science and biomedicine, making sacran a compelling subject for further exploration and utilization.

In this study, we develop ZnO-incorporated sacran xerogels and explore their properties and applications, advancing materials science and technology. Sacran in LC state served as the stabilizing agent for synthesizing ZnO nanoparticles (NPs), while divinyl sulfone (DVS) functioned as a crosslinking agent during hydrogel formation. The resulting xerogels, with different ratios of DVS to OH concentration and ZnO nanoparticles, were characterized to control porosity, mechanical stability, swelling capability, and the utilization of ZnO NP properties. We evaluated the potential of sacran-ZnO nanocomposite xerogels for cancer treatment by studying their cell compatibility with primary dermal fibroblasts and their selective toxicity towards cancer cells.

4.2 Materials and methods

4.2.1 Materials

Sacran, sourced from the cyanobacterium Aphanothece sacrum (A. sacrum) and generously provided by Kisendou Inc. (Asakura, Japan). Zinc acetate dihydrate (CH3COO)2Zn□2H2O, 99.9%) was received from Fujifilm Wako Pure Chemical (Tokyo, Japan) and Divinylsulfone (DVS, >96%) was procured from TCI Chemical (Tokyo, Japan). DVS, employed for crosslinking, was used without purification throughout the experiment. Hydrochloric acid (HCl, 37%) and sodium hydroxide (NaOH, ≥96%) were used as received for pH adjustment purposes (Sigma-Aldrich). Dulbecco's modified Eagle's medium high glucose (DMEM, Sigma-Aldrich) with 10% fetal bovine serum (FBS, Sigma-Aldrich) were utilized the culture of human lung cancer cells (A549) and primary dermal fibroblasts (HDFa).

4.2.2 Extraction of sacran

The extraction of sacran polysaccharide adhered to a well-documented protocol [44], [45], [46]. Initially, the *A. sacrum* sample underwent water and ethanol soaking. The washed sample was then immersed in an aqueous solution of 0.1 M NaOH to elute sacran. The resultant solution was then adjusted to a pH of 8.0 with HCl. Insoluble materials were removed through filtration, and the filtrate was concentrated using a rotary evaporator. The resulting solution was then gradually added to isopropanol, precipitating sacran fibers. To enhance purity, this precipitation step was repeated twice, resulting in pristine white fibrous material. Sacran was then dried in a vacuum oven for 2 minutes. The final sacran fiber product and 0.8% w/v of sacran solution are shown in Fig. 57a and b.

4.2.3 Green synthesis of ZnO NPs from sacran

A 100 mM (10 mL) of zinc precursor ($(CH_3COO)_2Zn{\cdot}2H_2O$) solution as shown in Fig. 57c was carefully introduced into a 0.8% w/w sacran solution (100 mL) under stirring at 300 rpm for 10 minutes. The resulting solution was then placed in an autoclave and underwent hydrothermal treatment at 120°C for 20 minutes, facilitating the controlled precipitation of ZnO, as illustrated in Fig. 57d. Following the hydrothermal treatment, the resulting white solution underwent

centrifugation at 5000 rpm for 10 minutes. A portion of the resultant white powder was selectively gathered, rinsed with deionized (DI) water, and carefully dried in a vacuum oven at 50°C for 24 hours. The resulting powder was definitively identified as a unique crystalline substance through X-ray diffraction (XRD) analysis.

4.2.4 Preparation of chemical cross-linked ZnO NPs-sacarn xerogels with DVS

The sacran-ZnO mixture underwent pH adjustment from 7.4 to 13 by the gradual addition of 1.5 M NaOH dropwise while continuously stirring the solution. Subsequently, a 20 mL portion was extracted from the 100 mL solution and divided into four separate beakers. DVS crosslinking agent was introduced to these solutions with varying concentrations, as detailed in Table 11. Following a 5-minute stirring period and the removal of bubbles through a 1-minute centrifugation step, the resulting solutions were carefully poured into four molds for the casting of hydrogels. The hydrogels underwent a complete reaction over a 4-hour period. The hydrogels were neutralized by introducing 0.2 M hydrochloric acid (HCl), and then underwent a thorough rinsing process, being submerged in abundant Milli-Q water until the pH reached 6 with regular water changes every 12 hours. To induce orientation, additional cross-linking was activated during a drying procedure. This entailed gradual drying on polypropylene substrates for several days until dried at room temperature, culminating in the formation of composite sacran-ZnO xerogels.

To optimize the conditions for xerogel formation, we carefully regulated the nucleophilic alkoxide ion and the quantity of DVS relative to sacran hydroxyls. Details of the synthesized components and conditions for both xerogels and composite xerogels can be found in Table 11.

Table 11. Concentration of components in sacran-ZnO nanocomposite xerogels.

Sample	Conc. of sacran solution (w/v %)	Conc. of ZnO (w/w %)	DVS/OH (mol/mol)
S1	0.8	20	0.43
S2		20	0.63
S3		20	0.83
S4		20	1.10

4.2.5 Structural analysis of sacran-ZnO nanocomposite xerogels

The mechanical properties of sacran-ZnO nanocomposite xerogels were assessed using an Instron 3365 machine equipped with a 5 kN load cell, operated at a crosshead speed of 1.00 mm/min. FT-IR spectra were recorded with a Spectrum Spotlight 200 **(**ATR mode, PerkinElmer Inc.) between 4000-400 cm^{-1}. Before testing, dumbbell strips of the dried xerogels, measuring 3×1 cm, were prepared and securely positioned between grips, leaving a 1 cm gap. Following the measurement of each xerogel's thickness with a caliper, they were hydrated by soaking them in deionized water at room temperature for 30 minutes before measurements began. The determination of elastic modulus involved calculating the linear slope of the stress-strain curve. SEM measurements were conducted using a TM3030plus. The size of ZnO NPs incorporated in xerogels were measured by using HRSEM (Hitachi, S-5200). Examination of the distribution of ZnO within the sacran-ZnO nanocomposite xerogels was conducted using Energy dispersive X-ray spectroscopy (EDX). X-ray diffraction (XRD) analysis was performed using a powder XRD diffractometer (RINT-2500), with measurements taken in the range of 10 to 90 degrees at a voltage of 40 kV and a tube current of 30 mA.

$$D_p = (0.94 \times \lambda) / (\beta \times cos\theta) \quad (1)$$

where *Dp* represents the average crystallite size, β indicates line broadening in radians, θ signifies the Bragg angle, and λ denotes the X-ray wavelength.

4.2.6 Swelling ratio measurements

The xerogels, cut into 1×1 cm pieces, were immersed in milli-Q water for varying durations: 2 to 60 minutes. After immersion, the swollen gels were taken out, excess milli-Q water was carefully blotted dry, and the samples were promptly weighed. The following formula was used to determine the swelling percentage (%Q) of the xerogels:

$$\%Q = \left(\frac{W_s - W_d}{W_d}\right)100 \qquad (2)$$

All experiments were conducted in triplicate, with W_s representing the swollen gels weight under equilibrium condition and W_d representing dried weight of xerogels.

The calculation of the xerogels' anisotropic swelling ratio involved by

$$\alpha = \frac{l_1 - l_o}{l_0} \qquad (3)$$

The anisotropic swelling ratio of the xerogels was determined by calculating the ratio of the length after swelling (l_1) to the length before swelling (l_0). Additionally, the degree of anisotropy in swelling, represented by αt/αw, was calculated using the linear swelling ratio of thickness (α_t) to width (α_w).

The investigation into the swelling behavior of sacran-ZnO nanocomposite xerogels involved immersing them in buffer solutions with pH values ranging from 2 to 14 at 25°C until equilibrium was attained, typically within approximately 24 hours.

4.2.7 Cell Cytotoxicity, adhesion, and viability study on sacran-ZnO composite xerogel in primary dermal fibroblast cells (HDFa).

Xerogels of Sacran-ZnO nanocomposites with varying concentrations (0 to 20 wt.%) were first swelled in deionized (DI) water overnight. After swelling, the gels were cut into 5 mm discs. These discs were then placed into a 96-well plate, and 70% v/v ethanol was added to each well. The samples were left in ethanol for 72 hours before further use.

To assess cell adhesion, primary dermal fibroblast cells were seeded at a density of 10,000 cells/mL in 96-well plates and incubated onto the gels at 37°C for 72 hours. Images were taken after this incubation period.

To determine the cytotoxicity, xerogels with varying ZnO concentrations were positioned on Falcon cell culture inserts within 24-well extract plates. Subsequently, 1 mL of HDFa culture medium (DMEM supplemented with 10% FBS) was added to each well. After incubating at 37°C for 72 hours, all extracts were used for cell treatment. Empty wells, without any xerogel but containing only the HDFa culture medium, were included as negative controls for cytotoxicity. Following the incubation period, the cells were exposed to the xerogel extracts for 24 hours. Then, 100 µg/mL of MTT solution (3-(4,5-dimethylthiazol-2-yl)-2,5-diphenyltetrazolium bromide) was added to each well and incubated at 37°C for 4 hours. To dissolve the formazan salts, 100 µL of DMSO was added to each well and allowed to stand for 5 minutes at room temperature. The absorbance of the resulting solution in each well was then measured at 540 nm using a microplate reader.

For cell adhesion assessment, images were taken after 72 hours of incubation, the cells were stained with calcein AM (3',6'-Di(O-acetyl)-4',5'-bis[N,N-bis(carboxymethyl) aminomethyl]fluorescein, tetraacetoxymethyl ester, DMSO solution) and EthD-1 (Ethidium Homodimer-1) were added and incubated for an additional 15 minute.

4.2.8 Cytotoxicity study of sacran-ZnO composite xerogel extracts in human lung cancer cells (A549).

Initially, the swollen sacran-ZnO nanocomposite xerogels were trimmed into circles with a 5 mm diameter. Subsequently, they underwent a 3-day immersion in a 70% v/v ethanol solution to facilitate sterilization.

Human lung cancer cells (A549) were employed to assess the cytotoxicity of extracts derived from sacran-ZnO nanocomposite xerogels (with varying ZnO wt.% ranging from 0 to 20 wt.%). Xerogels with varying ZnO concentrations were positioned on Falcon cell culture inserts within 24-well extract plates. Subsequently, 1 mL of A549 culture medium (DMEM supplemented with 10% FBS) was added to each well. After incubating at 37°C for 72 hours, all extracts were used for cell treatment. Empty wells, without any xerogel, containing only the A549 culture medium, were also included as negative controls for cytotoxicity.

Initially, the seeding density of A549 cells was 1×10^4 cells per mL, and they were plated in 24-well plates filled with complete A549 culture medium. After incubating at 37°C for 72

hours, the A549 culture medium was substituted with pre-prepared xerogel extracts. Following this, the cells were exposed to the xerogel extracts for a period of 24 hours.

Following 24 hours of incubation, the contents of each well were aspirated, and MTT solution (3-(4,5-dimethylthiazol-2-yl)-2,5-diphenyltetrazolium bromide) was added, followed by incubation at 37°C for 4 hours. Afterward, dimethyl sulfoxide (DMSO) was used to replace the MTT solution, aiming to dissolve the formazan crystals. Subsequently, the absorbance of each well was measured at 540 nm using infinite 200 pro nano plus multiplate reader, enabling the determination of the average absorbance values, as per equation 3.

$$\% \text{ Cell viability} = \left(\frac{\text{Absorbance of control cells}}{\text{Absorbance of treated cells}}\right) \times 100 \quad (3)$$

After a 15-minute incubation period, the cells were stained with calcein AM (3',6'-Di(O-acetyl)-4',5'-bis[N,N-bis(carboxymethyl) aminomethyl]fluorescein, tetraacetoxymethyl ester, DMSO solution) and EthD-1 (Ethidium Homodimer-1) to observe viable and dead cells.

4.3 Results and Discusion

4.3.1. Proposed mechanism of sacran-ZnO nanocomposite xerogels

Sacran, an expansive water-soluble cyanobacterial polysaccharide, is biosynthesized within the cell colony of Aphanothece sacrum. The extracted sacran comprises diverse monosaccharide units, including glucose (25.9%), xylose (16.2%), galactose (11.0%), rhamnose (10.2%), mannose (10.0%), and fucose (6.9%). Furthermore, it contains traces of uronic acid (20-25%), galactosamine, alanine, and sulfated muramic acid (~1%). Predominantly, has the functional groups consist of hydroxyl groups (250 mol%), carboxyl groups (22 mol%), sulfate groups (11 mol%), and amino groups relative to the total sugar residues. The deionized functional groups, such as sulfate and carboxylates, form complexes with Zn^{2+}, effectively preventing particle aggregation and maintaining dispersion in LC state (0.8 % w/w). The pH of the sacran (0.8 % w/w) and Zn^{2+} mixture was adjusted from a weakly acidic condition (pH 5.2) to neutral (pH 7.4) using a 0.2 M NaOH solution. Under autoclave conditions, the hydrothermal environment provides the necessary energy to drive the forced hydrolysis and dehydration reactions, resulting in the synthesis of ZnO nanoparticles. Sacran adsorbs onto the surface of the

ZnO NPs, providing steric hindrance that limits particle growth and aggregation. All the following possible reactions were involved in the synthesis system.

$Zn(CH_3COO)_2 \cdot 2H_2O \rightarrow Zn^{2+} + 2CH_3COO^- + 2H_2O$ (Dissolution of zinc acetate dihydrate) (4)

$Zn^{2+} + 2OH^- \rightarrow Zn(OH)_2$ (Formation of zinc hydroxide) (5)

$Zn^{2+} + 2H_2O \rightarrow Zn(OH)_2 + 2H^+$ (Hydrolysis reaction) (6)

$Zn(OH)_2 \rightarrow ZnO + H_2O$ (Dehydration reaction) (7)

To prepare sacran-ZnO nanocomposite xerogels, divinyl sulfone (DVS) was utilized as the cross-linking agent. Under elevated pH conditions, divinyl sulfone acted as an acceptor in a Michael-type reactionaddition, reacting with the hydroxyl groups of sacran. This reaction formed ether bonds, contributing to the attainment of high mechanical properties and the creation of smooth hydrogels. Subsequently, the resulting hydrogels were gradually dried on a polypropylene substrate over a 5-day period at room temperature, resulting in the formation of xerogels, as depicted the digital photographic images in Fig. 58 and the proposed mechanism in Fig. 57e.

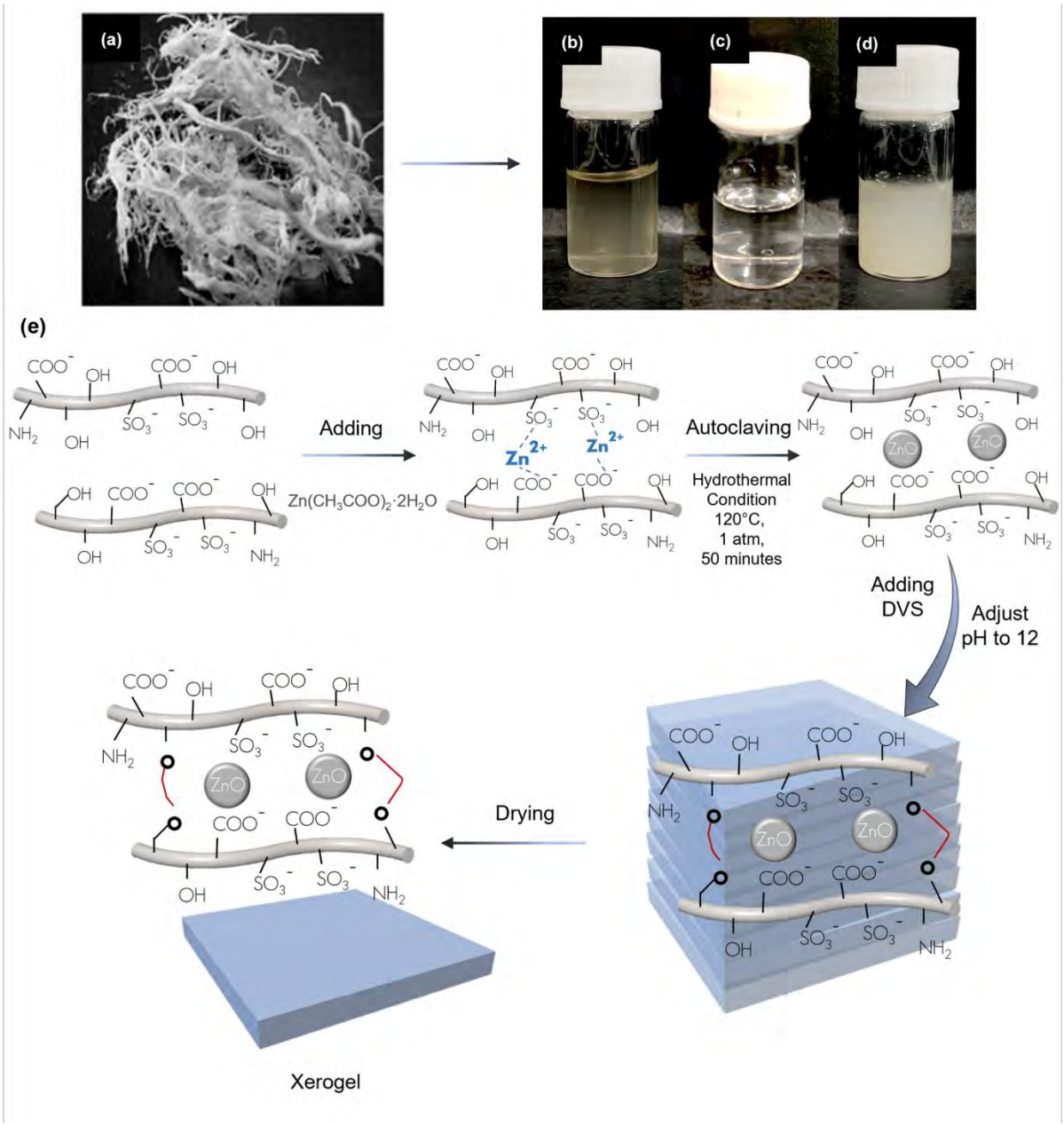

Fig. 57. Images of (A) extrated sacran fiber, (B) sacran 0.8 % w/w solution, (C) 100 mM Zinc acetate aqueous solution, (D) Sacran-ZnO NPs colloidal solution, (E) proposed reaction of sacran-ZnO nanocomposite xerogel.

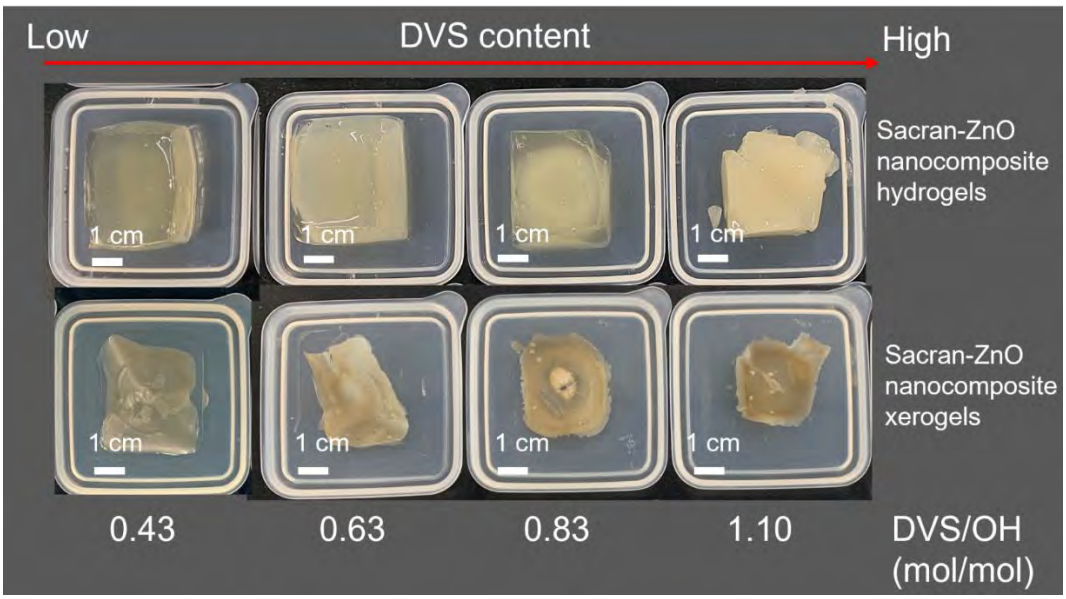

Fig. 58. Digital photographic images of resulting DVS cross-linked sacran-ZnO nanocomposite xerogels.

4.3.2. Functional groups analysis (FT-IR)

The comparison of FT-IR spectra was conducted to identify distinctive features of materials, including pure sacran film, and sacran-ZnO nanocomposite xerogels (Fig. 3a and b). The analysis of pure sacran reveals a broad peak at 3389 cm^{-1}, indicating the presence of free –OH groups, while the peak at 2928 cm^{-1} corresponds to aliphatic chains ($–CH_2$). Additionally, the peak at 1613 cm^{-1} signifies carbonyl groups (C=O), and sulfate ($–SO_3$) stretching is observed at 1411 and 1219 cm^{-1}. The asymmetric stretching of hydroxyls (C–O) is evident at 1034 cm^{-1} [46], [23], [27].

Confirmation of the addition reaction between DVS vinyls and sacran hydroxyls, resulting in the formation of an ether linkage, is evident from the appearance of an ether absorption shoulder around 1100 cm^{-1}. The increase in ether content is correlated with a higher concentration of DVS addition, as displayed in Fig. 3a. Furthermore, the observed IR absorptions around 1300 cm^{-1} (Fig. 3a), attributed to S=O, suggest the integration of the reaction involving sacran hydroxyls and DVS addition, increasing with higher concentrations of DVS.

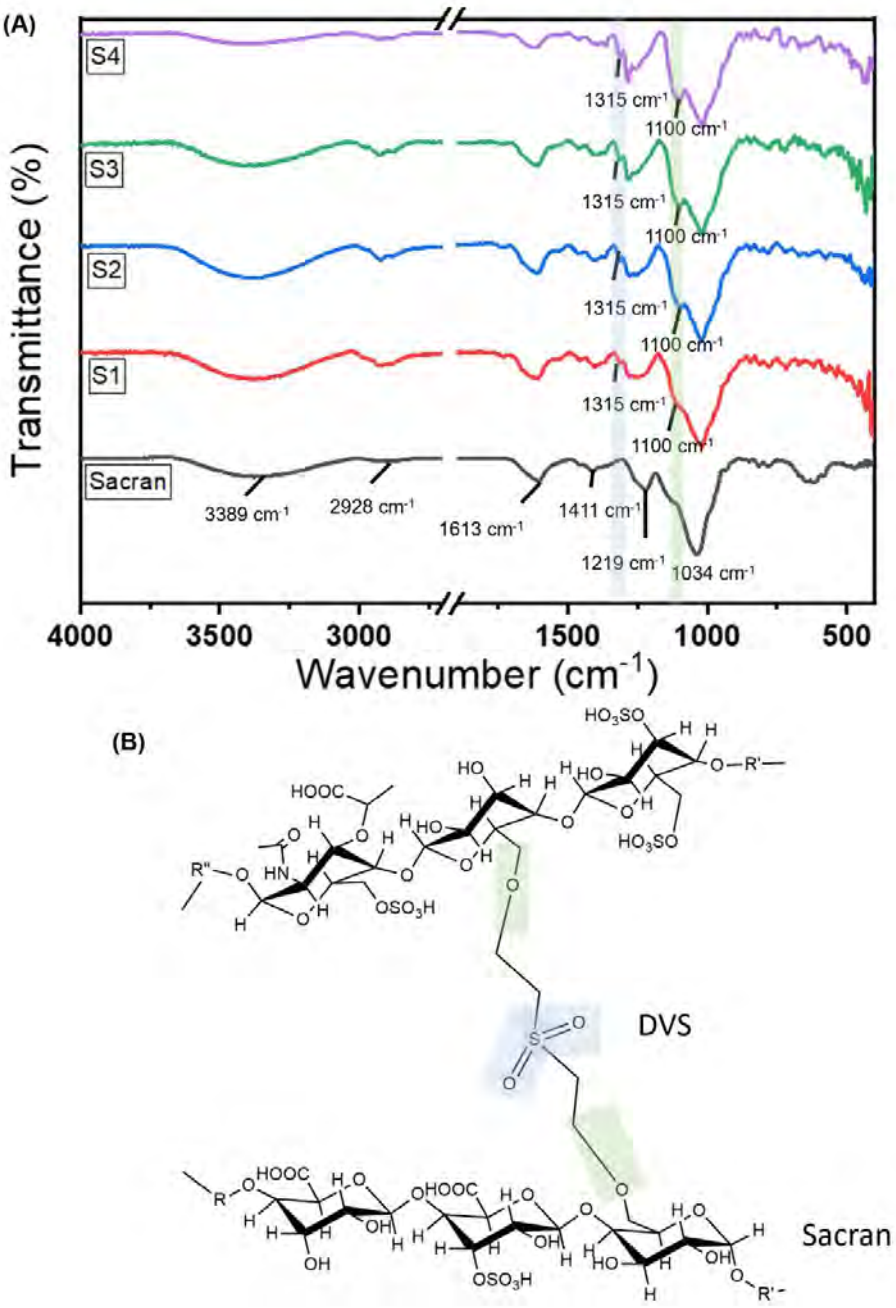

Fig. 59. The FTIR spectra of (a) original sacran film and sacran-ZnO nanocomposite xerogels with varying DVS to OH ratios from 0.43 (S1), 0.63 (S2), 0.83 (S3), and 1.10 (S4). (b) Chemical structure of DVS crosslinking sacran molecules.

4.3.3. Scanning electron microscopy (SEM) and energy dispersive X-ray spectroscopy (EDX)

Fig. 60 depicts the morphological characteristics of both the original sacran physically crosslinked by thermal treatment at 100°C and sacran-ZnO nanocomposite xerogels. Irrespective of varying DVS-to-OH sacran crosslinking ratios, top-view SEM images show a uniformly smooth surface without distinct structures (Fig. 60a-e). However, side-view images of cross-sectional samples unveil compact striped lines, indicating the formation of liquid crystalline layered structures at the micrometer scale, as illustrated in Fig. 60f-j. Surface analysis conducted using ImageJ software determined the interlayer spacing between these structures, measuring 0.56 ± 0.16 μm, 0.53 ± 0.12 μm, 0.47 ± 0.06 μm, 0.49 ± 0.05 μm, and 0.60 ± 0.04 μm for samples sacran film and the sacran-ZnO nanocomposite crosslinked with DVS-to-OH ratios of 0.43, 0.63, 0.83, and 1.10, respectively (Fig. 60f-j). The spacing between sacran layers do not show significant differences, indicating that the incorporation of ZnO NPs in xerogels does not significantly impact the crosslinking performance of DVS.

To examine their three-dimensional network structure, the xerogels were first swollen in water and then subjected to freeze-drying. Fig. 61 shows SEM images of the layered structures of sacran hydrogels and sacran-ZnO nanocomposite xerogels after freeze-drying. The porous pattern is predominantly observable from the side view, while the top and bottom surfaces display somewhat indistinct corrugated features, lacking visible pores. However, interconnecting pore structures were evident across all conditions of crosslinked samples. The absence of pores on the upper and lower surfaces can be attributed to an uncontrolled oriented pattern, unlike the anisotropic behavior observed on their side surfaces. Pore formation occurred through ice sublimation, with vapor preferentially venting out from the side faces without breaking through the upper and lower surfaces. This observation indicates the intrinsic toughness of the sacran primary layers due to robust interchain interactions. Concurrently, the appearance of undulating formations on the upper and lower surfaces resulted from pressure changes induced by water outflow. The pore size of sacran hydrogel was measured at 27.03 ± 4.84 μm. The density of pores appeared to increase with higher DVS-to-OH cross-linking ratios. Specifically, pore sizes were measured at 84.23 ± 39.09 1 μm, $70.89\ 9 \pm 25.82$ μm, and $33.86\ 9 \pm 9.991.0$ μm for samples cross-linked at ratios of 0.43, 0.63, and 0.83, respectively. In contrast, for samples cross-linked at

ratio of 1.10, pore formation was not observed (Fig. 61f-j). These findings suggest that higher DVS content influences the compactness and decreases the presence of porosity sites.

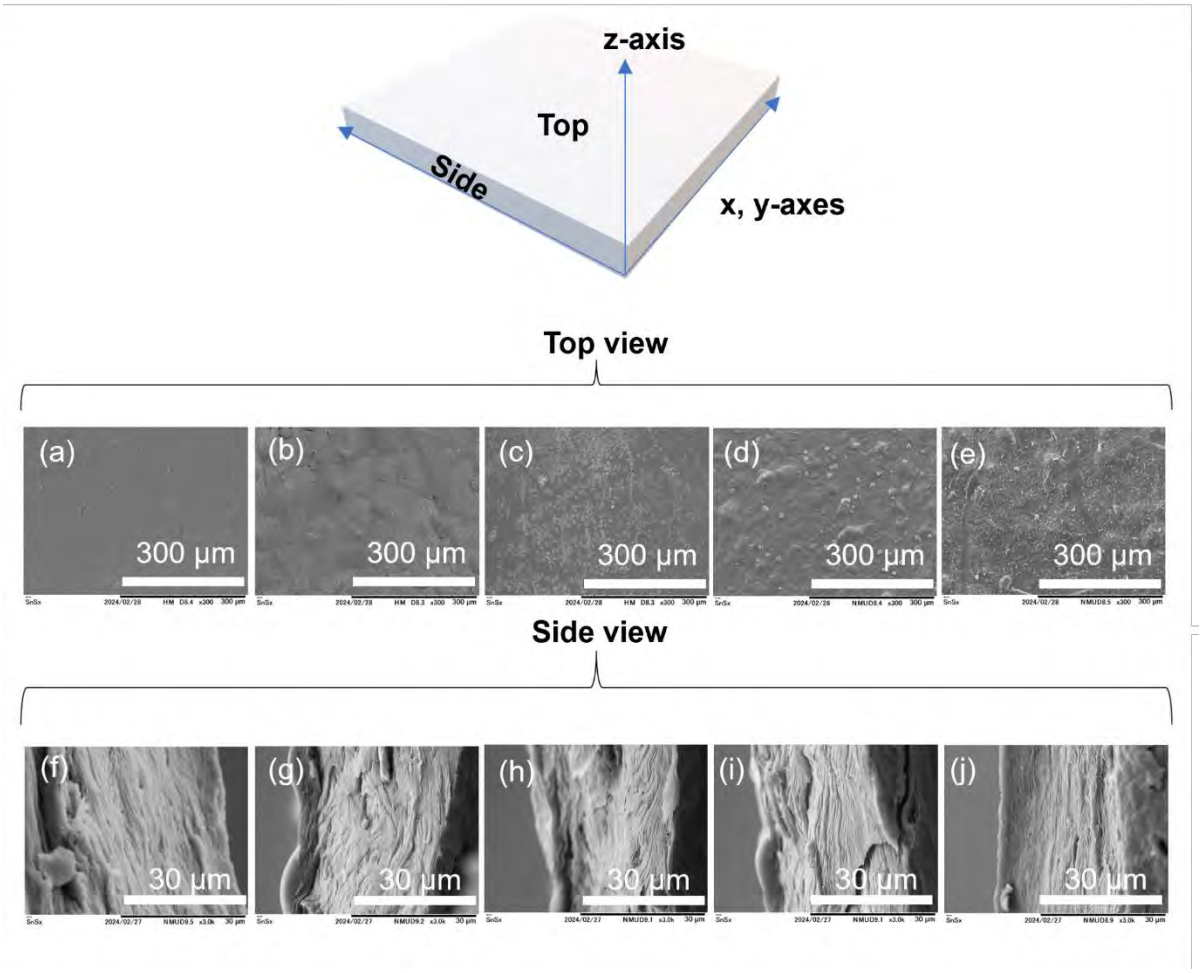

Fig. 60. SEM images of sacran film (a) and sacran-ZnO nanocomposite xerogels on the top faces (dimensions indicated above images) prepared at DVS to OH ratios of 0.43 (b), 0.63 (c), 0.83 (d), and 1.10 (e). sacran film (f) and sacran-ZnO nanocomposite xerogels on the side faces with the same range of DVS to OH ratios (g-j).

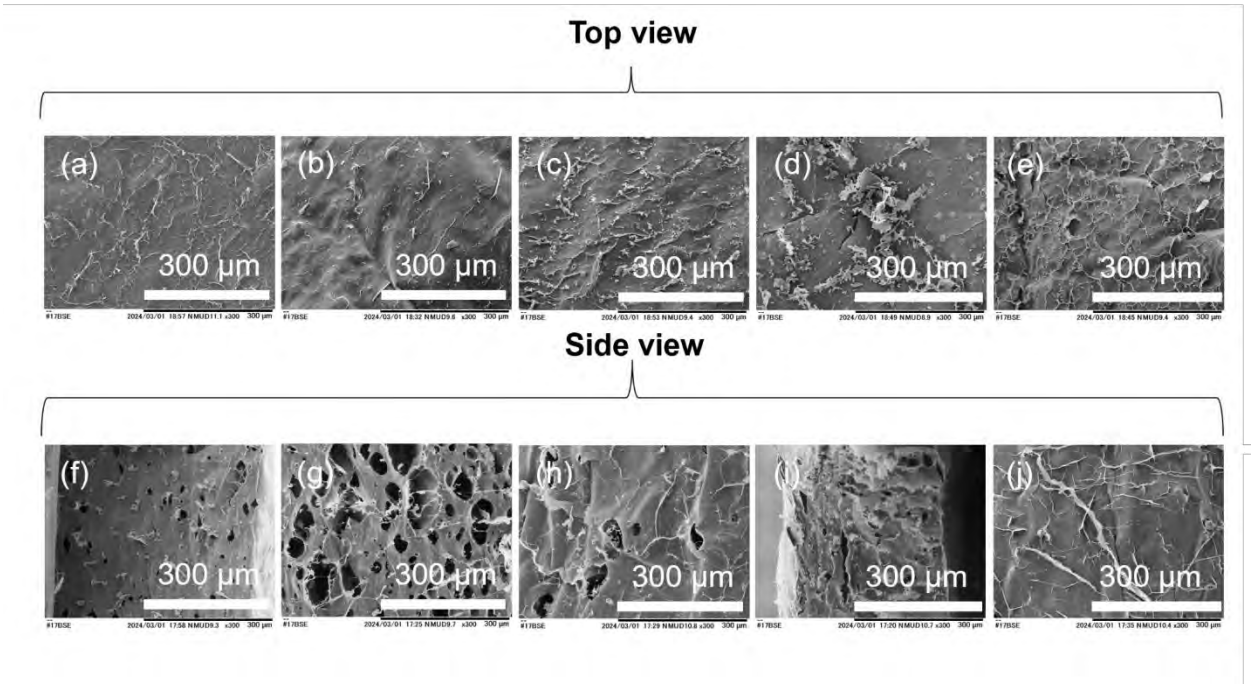

Fig. 61. SEM images of freeze-dried samples sacran film (a) and sacran-ZnO nanocomposite xerogels on the top faces (dimensions indicated above images) prepared at DVS to OH ratios of 0.43 (b), 0.63 (c), 0.83 (d), and 1.10 (e). sacran film (f) and sacran-ZnO nanocomposite xerogels on the side faces with the same range of DVS to OH ratios (g-j).

Elemental distribution analysis conducted through EDX confirms the incorporation of approximately 20% w/w ZnO NPs within the xerogel structure, as displayed in Fig. 62. The EDX elemental mapping analysis results are shown in Fig. 64-67. Further HRSEM imaging reveals the presence of block-like structures of ZnO NPs ranging in size from 258-370 nm. These blocks comprise individual ZnO NPs with sizes ranging from 25 to 70 nm (Fig. 63), which are smaller than those shown in the literatures. Typically, ZnO NPs are incorporated into polysaccharide matrices using the chemical precipitation method, forming complexes with chitosan, alginate, carboxymethyl cellulose, and gum, with sizes ranging from 100 to 300 nm [122], [123], [116], [124], [125]. The smaller size observed here is likely due to the mineralization of ZnO NPs under the restricted conditions of the sacran LC state. Studies have demonstrated that ZnO nanoparticles with sizes ranging from 50-200 nm can remain within the tumor interstitial space, achieving a tumor uptake rate four times higher than ZnO NPs larger than 300 nm [126]. Additionally, ZnO NPs smaller than 50 nm demonstrate increased toxicity, attributed to their high surface area to volume ratio [127], [128]. Our ZnO NPs are block-shaped with a high surface area to volume ratio compared to spherical or flake shapes. With sizes approximately 25-70 nm, which are smaller than those synthesized by other polysaccharide green methods, these characteristics might enhance cancer treatment

efficiency. We also compared the shape of our synthesized ZnO NPs with those reported in previous works that used similar forced hydrolysis under hydrothermal conditions with different reaction media [117]. The results showed that ZnO NPs in other studies exhibited dumbbell and rounded shapes, without the observation of block shapes. Therefore, the block shape observed in our study might be the effect of sacran complexation.

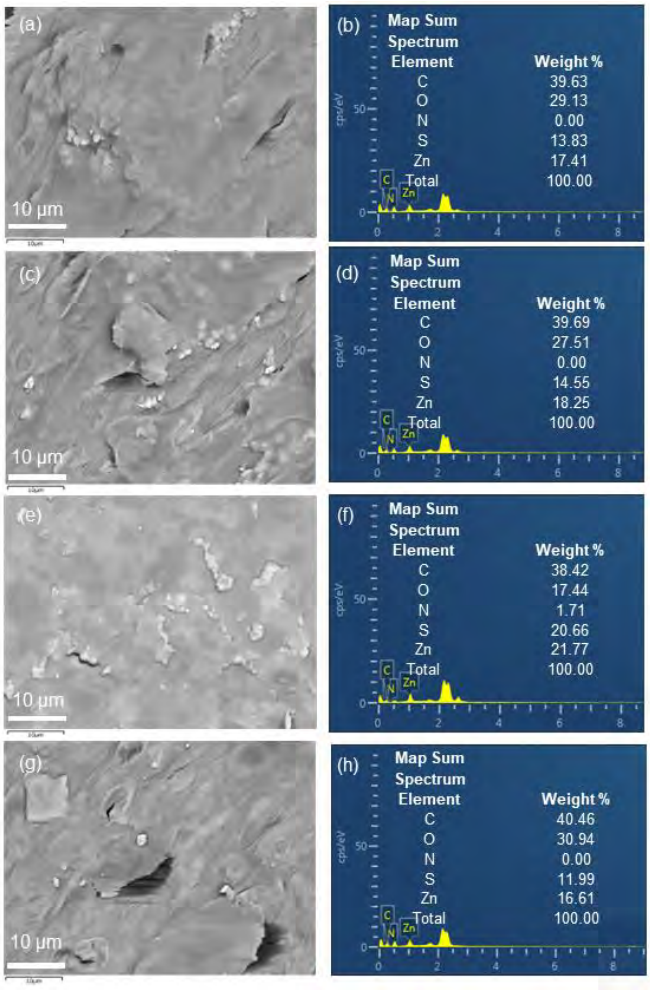

Fig. 62. Surface morphology assessed via SEM and corresponding EDX spectrum of sacran-ZnO nanocomposite xerogels prepared at DVS to OH ratios of 0.43 (a, b), 0.63 (c, d), 0.83 (e, f), and 1.10 (g, h).

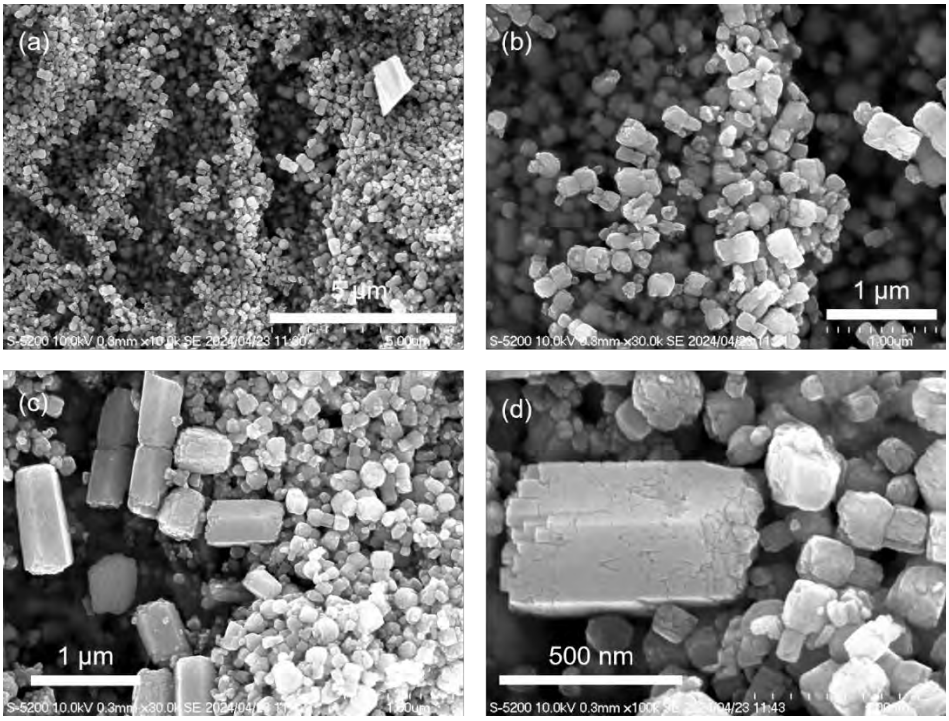

Fig. 63. FESEM images of ZnO incorporation in sacran-ZnO nanocomposite xerogels.

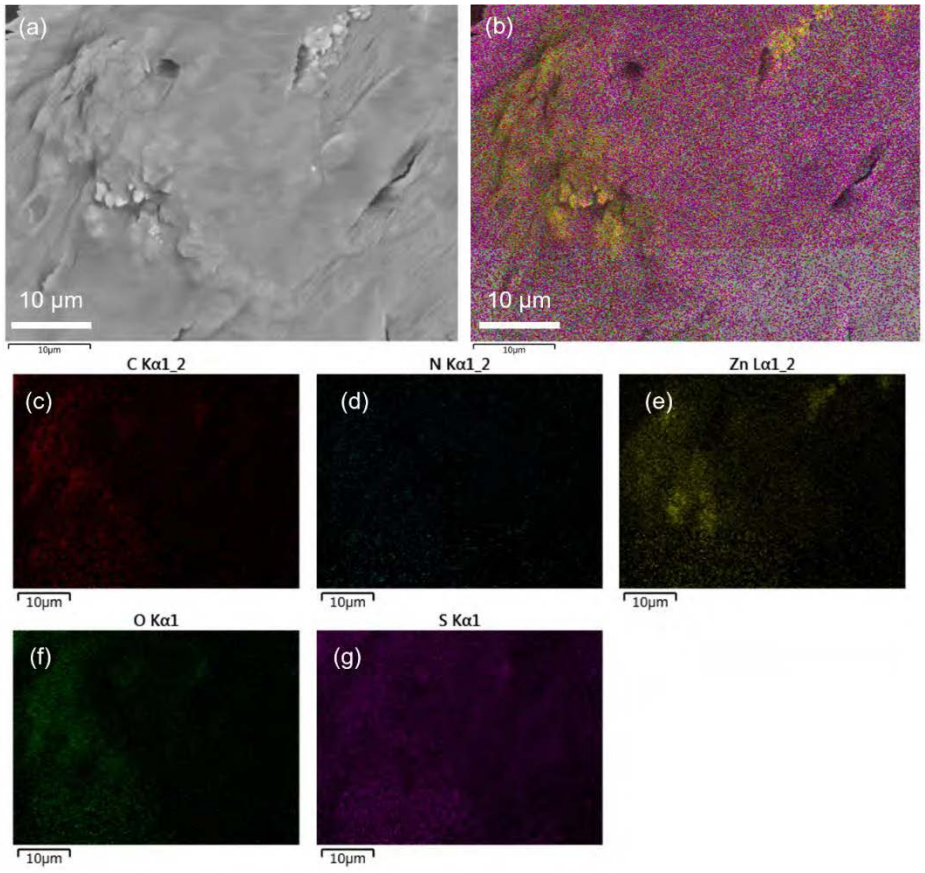

Fig. 64. Surface morphology assessed via SEM of sacran-ZnO nanocomposite xerogels prepared at DVS to OH ratios of 0.43 (a). Corresponding EDX elemental mapping depicting overall composition (b), carbon (c), nitrogen (d), zinc (e), oxygen (f), and sulfur distribution (g).

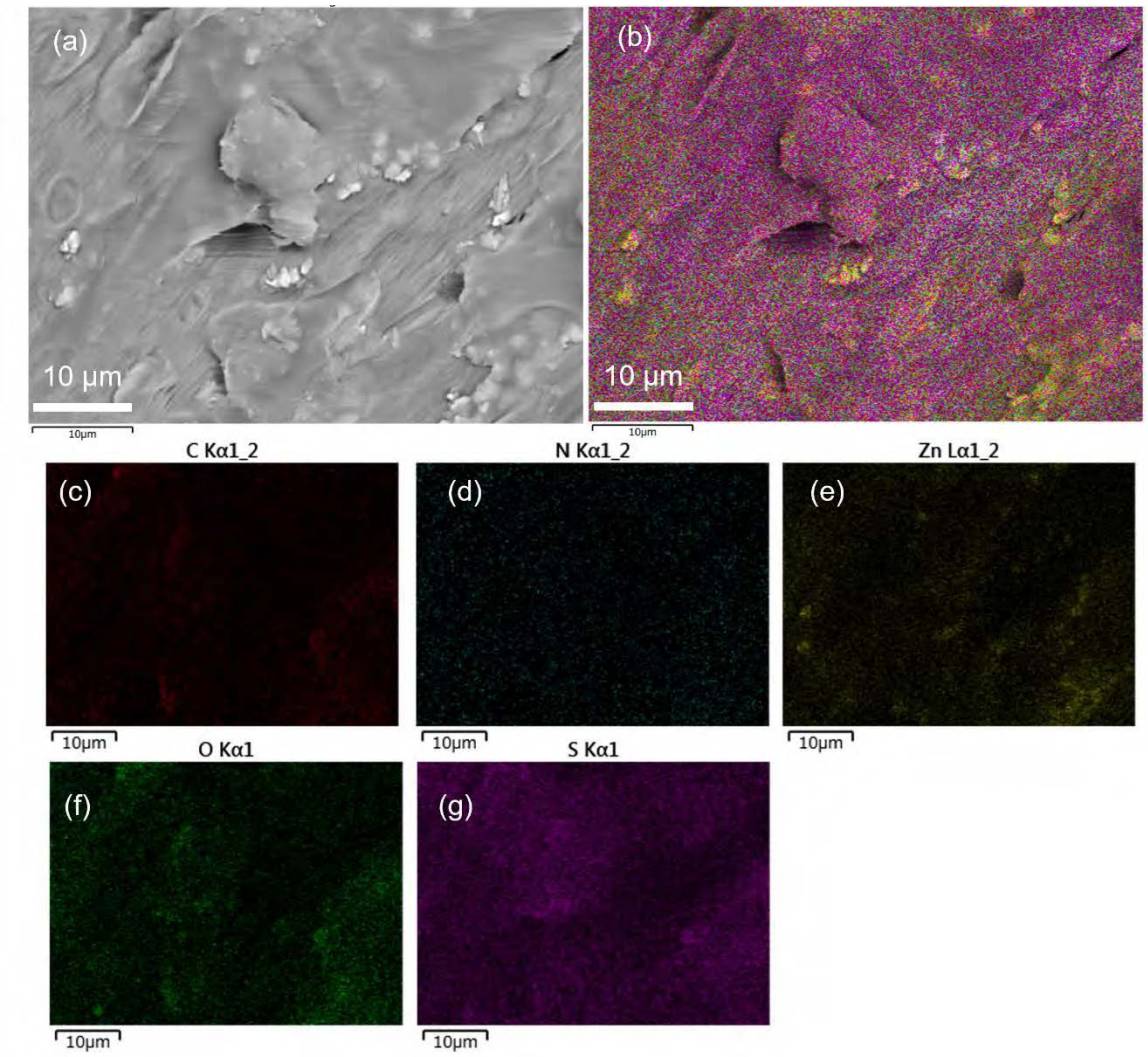

Fig. 65. Surface morphology assessed via SEM of sacran-ZnO nanocomposite xerogels prepared at DVS to OH ratios of 0.63 (a). Corresponding EDX elemental mapping depicting overall composition (b), carbon (c), nitrogen (d), zinc (e), oxygen (f), and sulfur distribution (g).

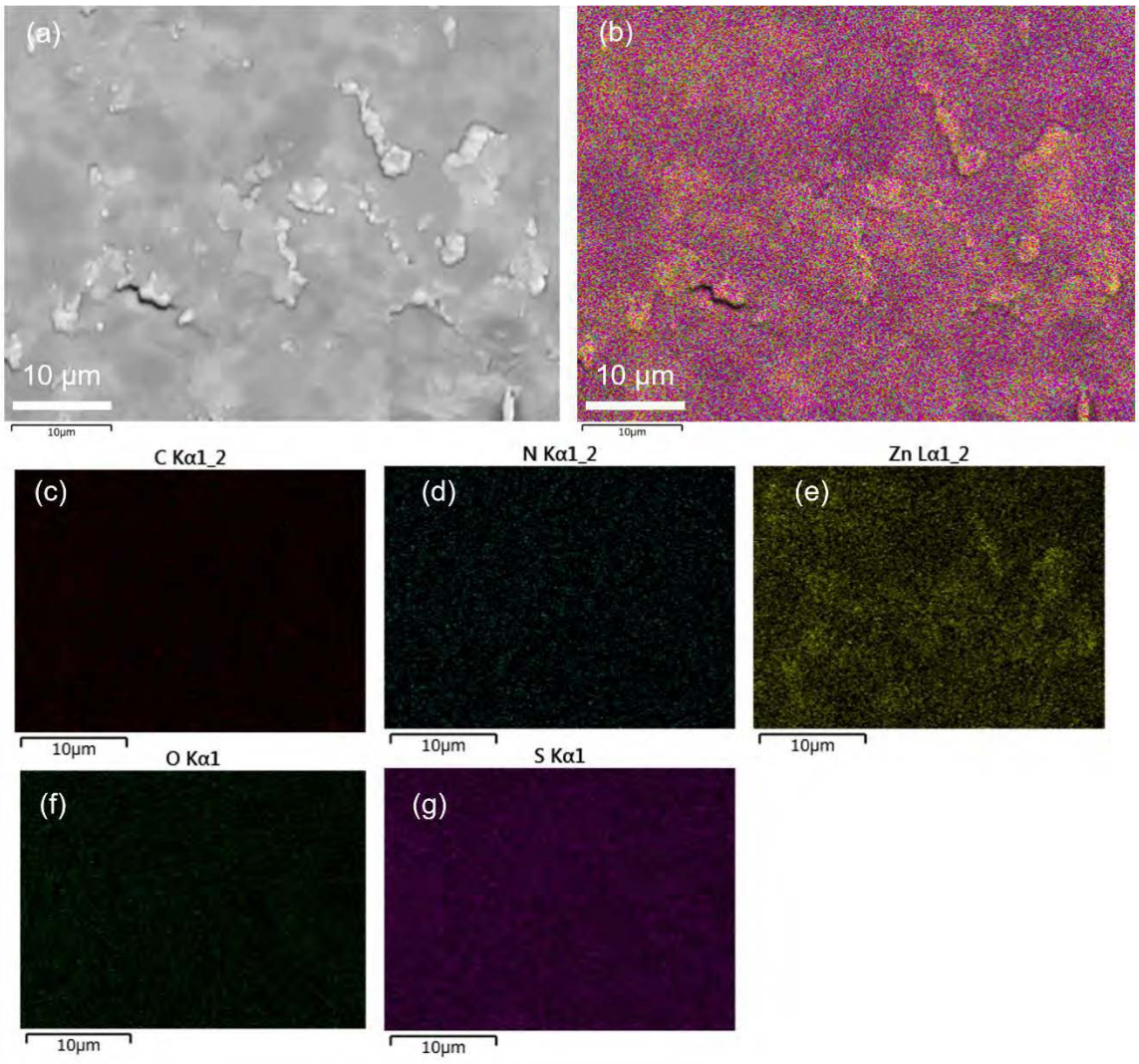

Fig. 66. Surface morphology assessed via SEM of sacran-ZnO nanocomposite xerogels prepared at DVS to OH ratios of 0.83 (a). Corresponding EDX elemental mapping depicting overall composition (b), carbon (c), nitrogen (d), zinc (e), oxygen (f), and sulfur distribution (g).

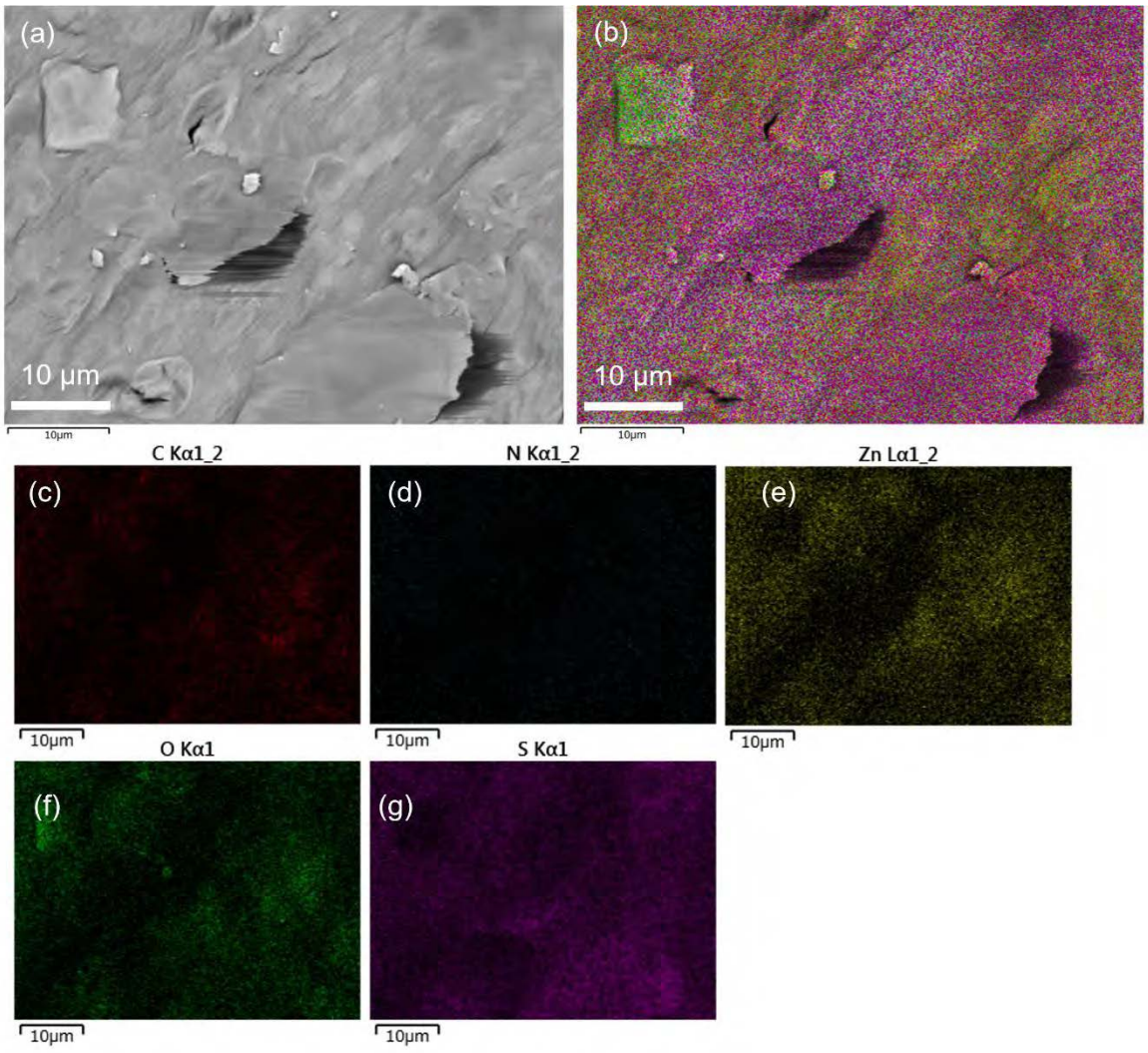

Fig. 67. Surface morphology assessed via SEM of sacran-ZnO nanocomposite xerogels prepared at DVS to OH ratios of 1.10 (a). Corresponding EDX elemental mapping depicting overall composition (b), carbon (c), nitrogen (d), zinc (e), oxygen (f), and sulfur distribution (g).

4.3.4. X-ray photoelectron spectroscopy (XPS) chemical state analysis

The XPS analysis revealed signals from sacran at specific binding energies: the peaks appeared at 285.0, 286.6, 288.0, and 289.0 eV corresponded to (C–C(H)), (C–OH), (O–C–O), and (C=OOH), respectively (Fig. 68) [60, 61]. Following the reaction of sacran with the DVS crosslinking agent (Fig.53b-e), there was a small change in the hydroxyl group fraction (C–OH), as evidenced by the area value (area CPS·eV) and the decreasing of atomic concentration (%) (Table 12). The higher the concentration of DVS, the greater the decrease in the hydroxyl group fraction, while the carboxylate groups remained almost constant. This decrease occurred because the vinyl groups of DVS reacted with nucleophiles, such as the high amount of hydroxyl groups present at the elevated pH of sacran. Interestingly, the peak at 285.0 eV and 288.0 eV, corresponding to (C–C(H)) and (O–C–O) respectively, remained relatively constant (Table 12), suggesting that the DVS reaction had minimal impact on these functional groups. Furthermore, sacran and Zn^{2+} ions do not show a strong interaction as determined by XPS technique. However, they could form a complex or be induced by electrostatic interaction.

Sacran-ZnO nanocomposite xerogels were analyzed to study the reaction of sacran molecules with the vinyl groups of the DVS crosslinking agent and identical ZnO NPs concentration. After the formation of ZnO NPs, the concentration of the crosslinking agent was varied from low to high, as depicted in the O1s signals of all samples (Fig. 69). A decrease in the alcoholic fraction at 533.2 eV was observed in terms of area value. This is attributed to sacran molecules reacting with the DVS crosslinking agent to form ether bonds. Table 13 demonstrates a shift in atomic percentages: the alcoholic (C**O**H) oxygen peak decreased substantially from 77.35% to 72.63%, while the carbonyl fraction (C=**O**) showed a small increase value. This might be because of the Zn-O bond formation that near the binding energy of carbonyl fraction (C=**O**)at 531.5 eV [129].

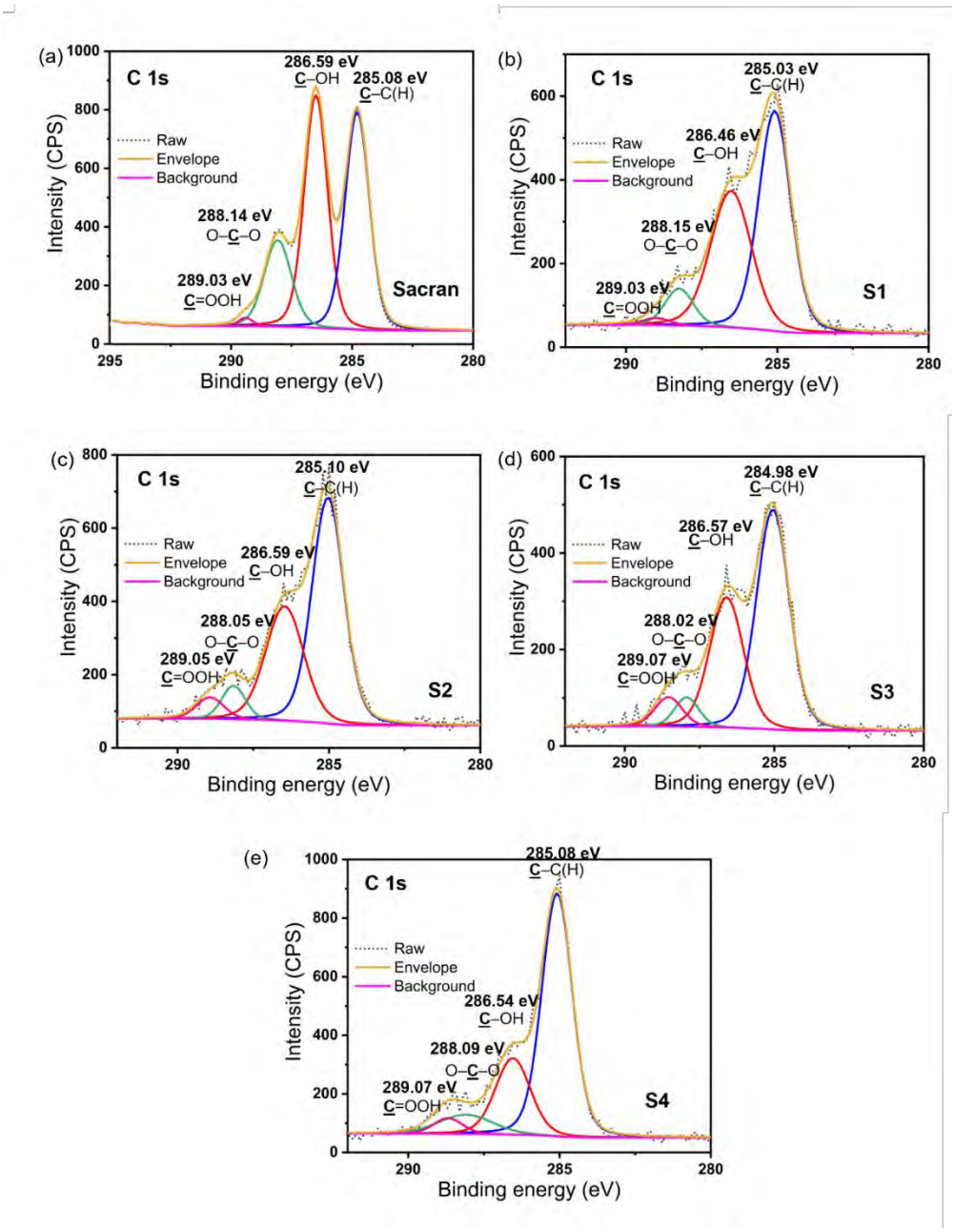

Fig. 68. XPS spectra in the C1s region of sacran (a) and sacran-ZnO nanocomposite xerogels with varying DVS-to-OH ratios: S1-1 (b), S1-2 (c), S1-3 (d), and S1-4 (e), corresponding to ratios of 0.43, 0.63, 0.83, and 1.10, respectively.

Table 12. The chemical composition of carbon (C 1s) region in sacran-ZnO nanocomposite xerogels was quantified for different DVS to OH ratios: 0.43 (S1), 0.63 (S2), 0.83 (S3), and 1.10 (S4).

Sample	Peaks	Binding energy (eV)	Area CPS·eV	Atomic concentration (%)
Sacran	C-C(H)	285.08	801.3	53.01
	C-OH	286.59	537.4	36.12
	O-C-O	288.14	96.3	6.48
	C=OOH	289.03	65.03	4.39
S1	C-C(H)	285.03	886.4	55.8
	C-OH	286.46	533.1	33.54
	O-C-O	288.15	97.118	6.10
	C=OOH	289.03	72.559	4.56
S2	C-C(H)	285.10	916.9	54.45
	C-OH	286.59	528.7	33.16
	O-C-O	288.05	130.1	7.72
	C=OOH	289.05	78.90	4.68
S3	C-C(H)	284.98	1028.1	57.43
	C-OH	286.57	515.9	30.79
	O-C-O	288.02	125.3	7.00
	C=OOH	289.07	85.6	4.78
S4	C-C(H)	285.08	1064.6	60.14
	C-OH	286.54	479.2	27.04
	O-C-O	288.09	141.0	7.94
	C=OOH	289.07	86.5	4.88

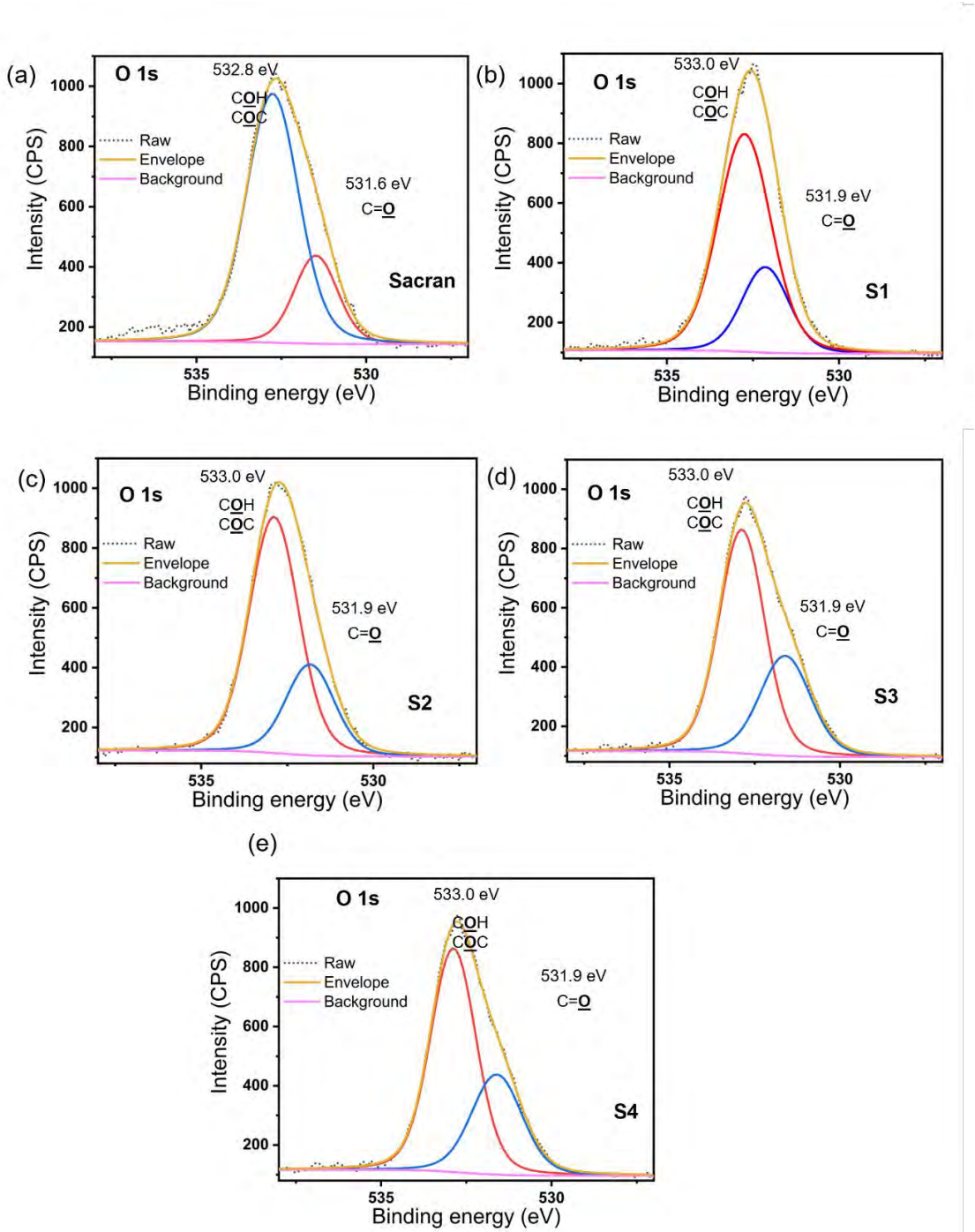

Fig. 69. XPS spectra in the O1s region of sacran (a) and sacran xerogels with varying DVS-to-OH ratios: S1 (b), S2 (c), S3 (d), and S4 (e), corresponding to ratios of 0.43, 0.63, 0.83, and 1.10, respectively.

Table 13. The chemical composition of oxygen (O 1s) region in sacran-ZnO nanocomposite xerogels was quantified for different DVS to OH ratios: 0.43 (S1), 0.63 (S2), 0.83 (S3), and 1.10 (S4).

Sample	Peaks	Binding energy (eV)	Area CPS·eV	Atomic concentration (%)
Sacran	C<u>O</u>H	532.8	1732.0	77.35
	C=<u>O</u>	531.6	507.0	22.65
S1	C<u>O</u>H	533.0	1584.0	74.25
	C=<u>O</u>	531.9	528.5	25.75
S2	C<u>O</u>H	533.0	1562.4	73.56
	C=<u>O</u>	531.9	561.7	26.44
S3	C<u>O</u>H	533.0	1542.6	72.63
	C=<u>O</u>	531.9	581.0	27.37
S4	C<u>O</u>H	533.0	1514.9	71.33
	C=<u>O</u>	531.9	608.6	28.67

We investigated the interaction between the nitrogen content in sacran, the DVS crosslinking agent, and ZnO NPs by examining the nitrogen region (N 1s) in sacran-ZnO nanocomposite xerogels. The amino groups ($–NH_2$) of sacran was identified at 399.8 eV (Fig. 70). This observation suggests that the amino groups ($–NH_2$) of sacran do not significantly interact with either the DVS crosslinking agent or ZnO NPs.

Fig. 71 shows a doublet signal for sacran with a 1.18 eV separation and a 2:1 peak area ratio in the sulfur (S 2p) region [130]. Upon sacran's reaction with the DVS crosslinking agent, a doublet peak emerged at 168.9 and 170.1 eV, indicating the presence of sulfate groups ($–SO_4–$) through their spin-orbit splitting. The sulfone groups ($SO_2–C$) enveloped at 167.6 eV near 168.9

eV increased with increasing DVS concentrations, as shown in Fig. 71. The total area value of the sulfate groups significantly increased, as displayed in Table 14. Therefore, the addition of the DVS crosslinking agent influenced the increment of the area value in terms of sulfone groups.

In the Zn 2p binding energy region, we conducted an investigation to ascertain the presence of ZnO formation on the surfaces of sacran-ZnO nanocomposite xerogels. Fig. 72. depicts the signal sulfates peak, confirming the formulation of ZnO NPs.

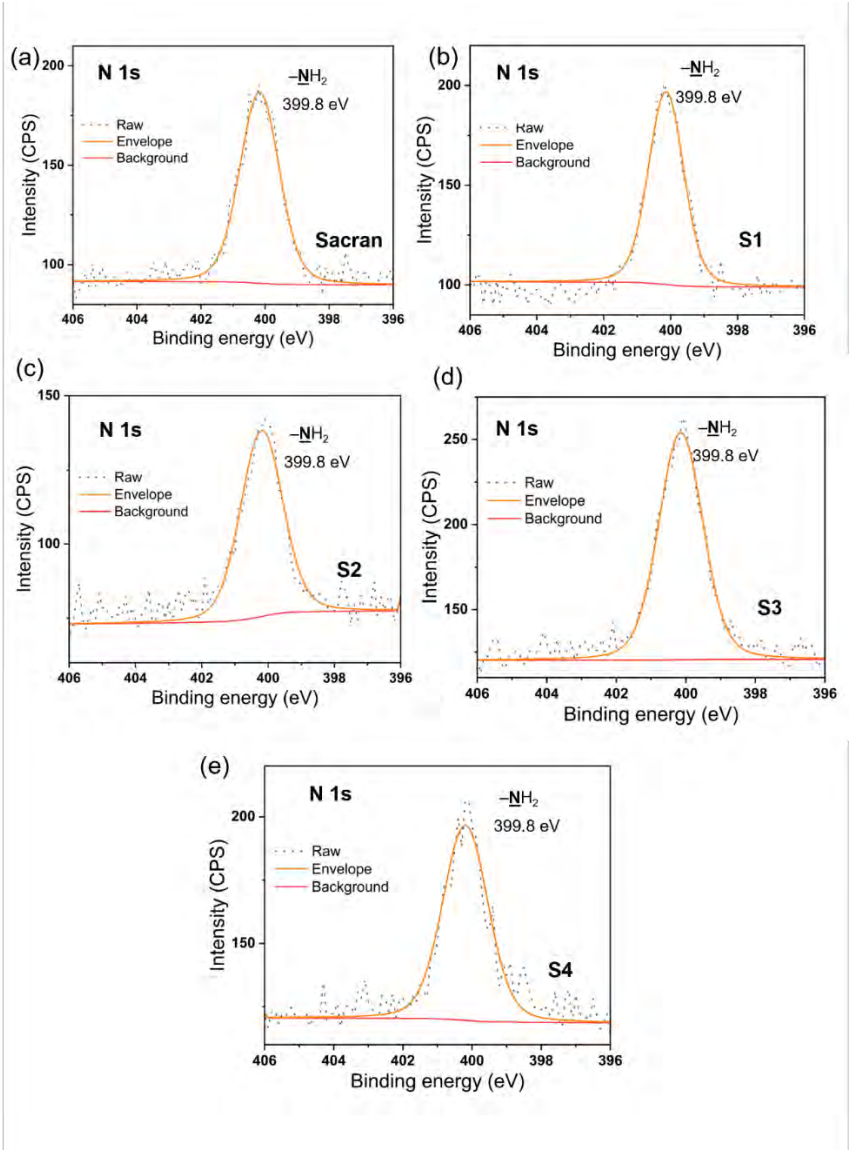

Fig. 70. XPS spectra in the N1s region of sacran (a) and sacran xerogels with varying DVS-to-OH ratios: S1 (b), S2 (c), S3 (d), and S4 (e), corresponding to ratios of 0.43, 0.63, 0.83, and 1.10, respectively.

Table 14. Quantification of the chemical composition of S 2p in sacran-ZnO nanocomposite xerogels.

Sample	Peaks	Binding energy (eV)	Area CPS·eV	Atomic concentration (%)
Sacran	$\underline{S}O_4^2(2p_{3/2})$	168.9	46.32	80.25
	$\underline{S}O_4^2(2p_{1/2})$	170.1	11.39	19.72
S1	$\underline{S}O_4^2(2p_{3/2})$	168.9	58.99	68.66
	$\underline{S}O_4^2(2p_{1/2})$	170.1	26.97	31.34
S2	$\underline{S}O_4^2(2p_{3/2})$	168.9	82.06	63.58
	$\underline{S}O_4^2(2p_{1/2})$	170.1	47.07	36.42
S3	$\underline{S}O_4^2(2p_{3/2})$	168.9	90.32	69.12
	$\underline{S}O_4^2(2p_{1/2})$	170.1	48.02	30.88
S4	$\underline{S}O_4^2(2p_{3/2})$	168.9	116.20	57.48
	$\underline{S}O_4^2(2p_{1/2})$	170.1	86.07	42.52

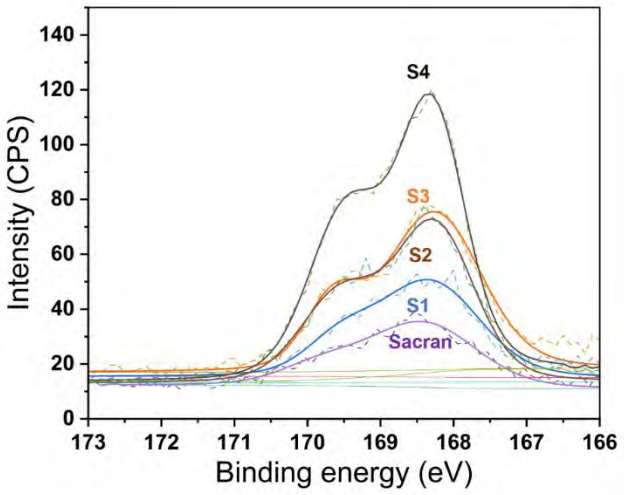

Fig. 71. XPS spectra in the S2p region of sacran and sacran-ZnO nanocomposite xerogels with varying DVS-to-OH ratios: S1, S2, S3, and S4, corresponding to ratios of 0.43, 0.63, 0.83, and 1.10, respectively.

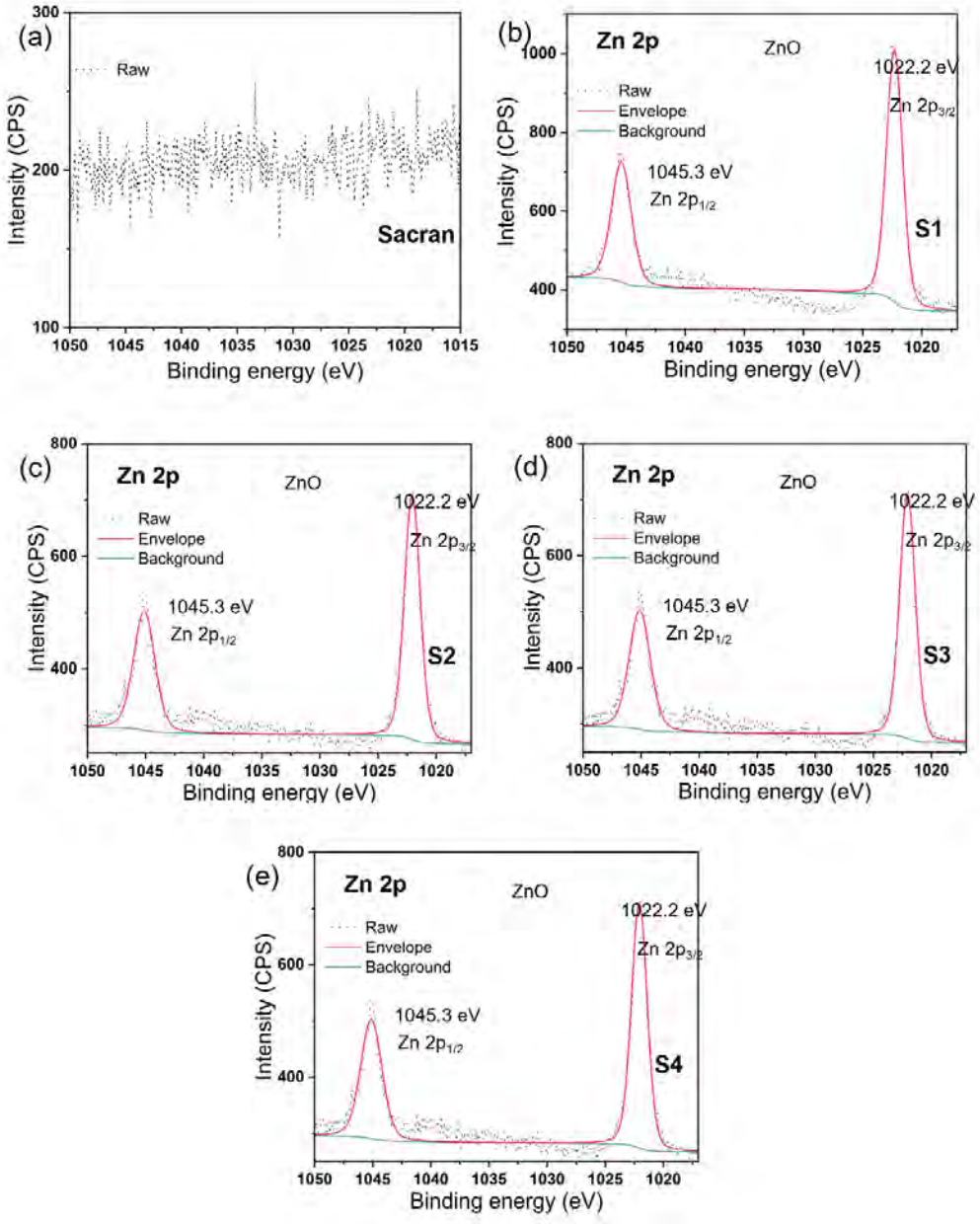

Fig. 72. XPS spectra in the Zn 2p region of sacran and sacran-ZnO nanocomposite xerogels with varying DVS-to-OH ratios: S1, S2, S3, and S4, corresponding to ratios of 0.43, 0.63, 0.83, and 1.10, respectively.

4.3.5. X-ray diffraction (XRD) analysis

Examining the crystalline structure of the sacran-ZnO nanocomposite xerogels involved X-ray diffraction (XRD) analysis. Fig. 73 illustrates the XRD patterns of sacran, sacran xerogel, and sacran-ZnO nanocomposite xerogel. Pristine sacran structure exhibits an amorphous nature. Similarly, the structure of sacran xerogel (crosslinked with DVS) also demonstrates an amorphous character within the range of 15–30°. The XRD patterns of the sacran-ZnO nanocomposite xerogel reveal distinct peaks at 31.93, 34.52, 36.37, 47.77, 56.68, 62.92, 66.47, 68.09, 69.15, 72.75, and 77.04 degrees, corresponding to the diffraction of ZnO in the planes (100), (002), (101), (102), (110), (103), (200), (112), (201), (004), and (202), respectively.[117] The alignment of these plane values is characteristic of ZnO nanoparticles. The sharp and narrow diffraction peaks indicate a well-ordered crystalline structure, with the relatively high intensity of the (101) peak suggesting anisotropic growth and a preferred orientation of the crystallites. The synthesis involved the reaction of zinc acetate with sacran polysaccharide, resulting in the formation of small ZnO crystals measuring approximately 25.174 nm.

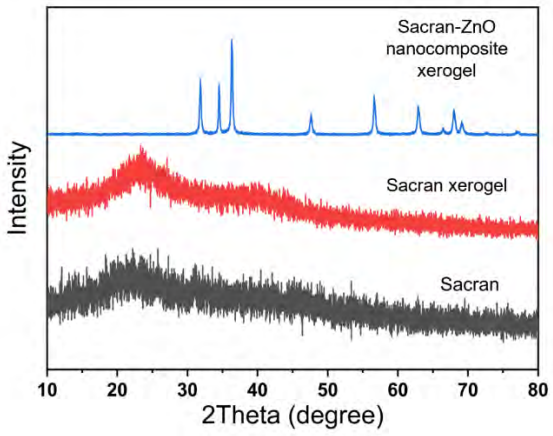

Fig. 73. The XRD pattern of pure sacran, sacran xerogel, and sacran-ZnO nanocomposite xerogel.

4.3.6. UV-vis spectroscopy analysis

Fig. 74 illustrates the absorption spectrum. A significant feature at 370 nm was observed in the Sacran-ZnO NPs solution, indicating the characteristic optical properties of ZnO. This feature reflects the intrinsic band-gap absorption of ZnO, suggesting electron movement within the material.[131] This phenomenon suggests the presence of zinc nanoparticles. In contrast, the sacran

aqueous solution did not exhibit any significant absorption peak, implying that sacran may have a role in reducing the zinc precursor to zinc nanoparticles.

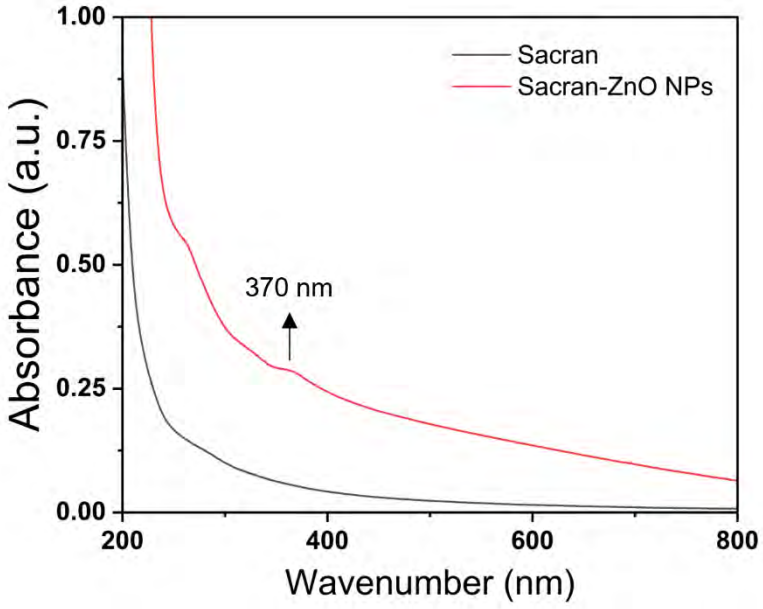

Fig. 74. Uv-vis spectra of sacran and sacran-ZnO NPs solution.

4.3.7. Swelling Behavior as a Function of the Sacran-Xerogels and Sacran-ZnO nanocomposite Xerogels with varying crosslinking content.

The ordered arrangement of molecules in a liquid crystalline phase can create more efficient pathways for water absorption, leading to improved swelling properties. Consequetly, the swelling behavior of sacran-ZnO nanocomposite xerogels with identical ZnO NPs content exhibited a significant dependency on the concentration of the crosslinking agent (DVS), which was systematically varied from low to high (DVS-to-OH ratios 0.43 to 1.10), as illustrated in Fig. 75. Notably, sacran-ZnO nanocomposite xerogels with a DVS-to-OH ratio of 0.43 displayed pronounced hydrophilicity owing to the substantial presence of unreacted hydroxyl groups (-OH) available for interaction. Consequently, these xerogels demonstrated remarkable water absorption capability, reaching up to 1890 ± 54% within the initial 10 minutes. Subsequently, the water uptake stabilized, with the content increasing to 1945 ± 40% after 30 minutes. As the DVS crosslinking content increased, the swelling degree of the xerogels progressively decreased. This

effect is due to the increased density of chemical crosslinks, which reinforces the three-dimensional network formed by the orientation of sacran molecules. The results were subsequently compared with sacran physically crosslinked by annealing at 100°C, which exhibited a swelling percentage of 240.8 ± 55% after 30 minutes, indicating the weaker water holding capabilities and fewer available hydroxyl groups to enhance water absorption capacity.

4.3.8. Swelling Behavior of Sacran-Xerogels and Sacran-ZnO nanocomposite Xerogels as a Function pH.

Tumors are recognized for their distinct microenvironment, characterized by features like acidic pH (around 5.6) and elevated levels of hydrogen peroxide (H_2O_2) , posing significant challenges for cancer therapy [132]. Additionally, in wound care, an elevation in alkaline pH (reaching pH 10) often signals whether a wound will progress to a non-healing or chronic state [133]. We proceeded to examine how changes in pH affected the swelling behavior of our fabricated xerogels. For this investigation, we selected sample S1, a sacran-ZnO nanocomposite xerogel with a DVS-to-OH ratio of 0.49, due to its remarkable swelling rate. We evaluated the impact of pH variations from 2 to 12 on the gel's expansion characteristics, as illustrated in Fig. 8. The sacran-ZnO nanocomposite xerogel displayed its highest swelling propensity around pH 12, likely influenced by the polysaccharide's inherent functional group pKa values. Typically, amino groups possess a pKa value of approximately 6.5, while carboxylic acids within the sacran structure exhibit a pKa value of approximately 5. In extremely acidic environments (pH < 3), the presence of counterions (such as $H_2PO_4^-$ or Cl^-) shields the $-NH_3^+$ groups reducing repulsion and leading to decreased swelling, while the deprotonation of sulfates (SO_3^-) influences the swelling behavior. Around pH 3, the swelling behavior is predominantly influenced by the protonation of sacran's amino groups, resulting in increased swelling. As pH exceeds 5, the ionization of carboxylic acid groups occurs. Between pH 5 and pH 7, there may be hydrogen interactions between $-NH_2$ and $-COOH$ or between $-NH_3^+$ and $-COO^-$, facilitating ionic crosslinking, which may inhibit the enhancement of the swelling rate. At higher pH values (around pH 8), the carboxylic acid groups undergo ionization, leading to electrostatic repulsion and consequently enhancing swelling. When pH exceeds 10, the hydroxyl groups become ionized due to their pKa value (approximately 12).

Substantial swelling occurs as a consequence of the deprotonation of hydroxyl groups, leading to an increase in volume attributed to osmotic effects and charge repulsion.

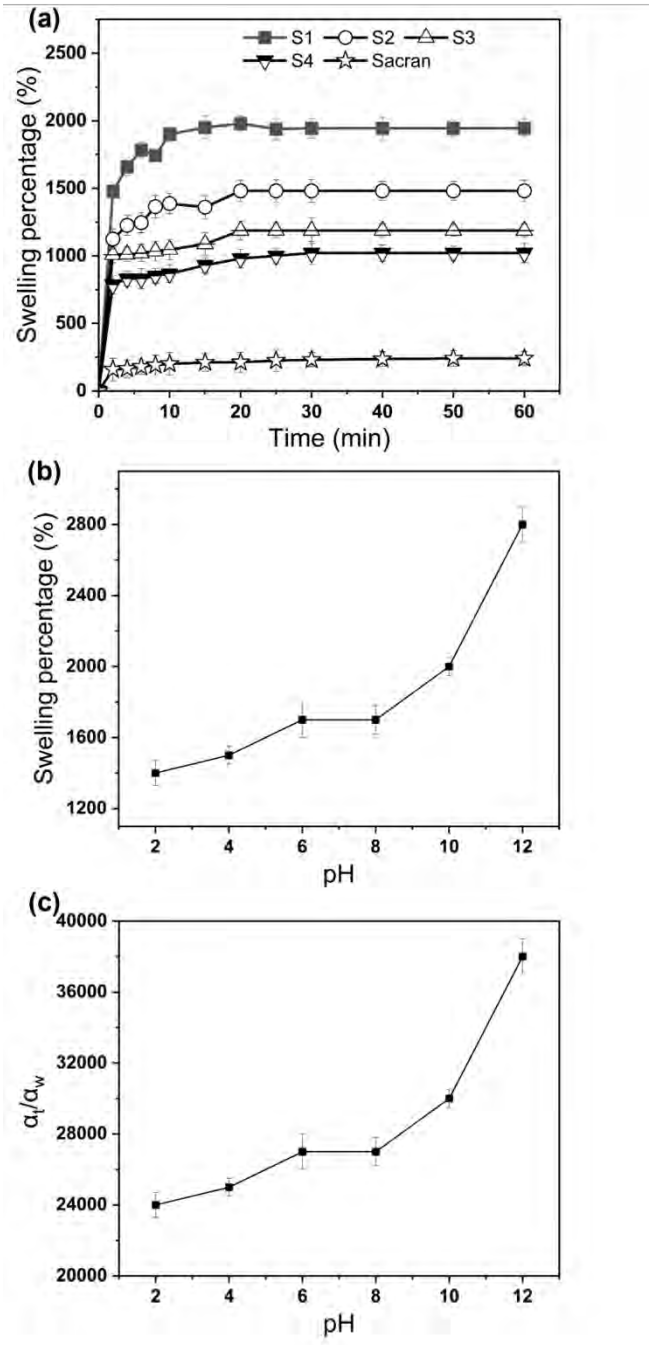

Fig. 76. Swelling behavior of the sacran-ZnO nanocomposite xerogels with the identical ZnO content at 20% w/w and different ratios of DVS/OH 0.43 (S1), 0.63 (S2), 0.83 (S3), and 1.10 (S4). (a). Swelling properties of sacran-ZnO nanocomposite xerogels across various pH levels (b). and anisotropic swelling ratio (c). Measurement was performed three times for each sample.

4.3.9. Mechanical characterization of Sacran-Xerogels and Sacran-ZnO nanocomposite Xerogels.

Given that the ordered arrangement of molecules in a liquid crystal (LC) phase can enhance mechanical strength, we conducted tensile strength tests on the hydrated samples (Fig. 77a). This investigation aimed to assess how the presence of the DVS crosslinking agent and the incorporation of ZnO nanoparticles (NPs) influence the properties of the xerogels, particularly in terms of their potential as cancer-selective materials. As shown in Fig. 77b, the tensile modulus of sacran-ZnO nanocomposite xerogels exhibits a linear increase from 0.47 ± 0.03 MPa to 0.86 ± 0.06 MPa, which is more than 1.6 times higher than that of sacran gel physically crosslinked by thermal treatment at 100°C. Among the samples tested, S4 (with a DVS-to-OH ratio of 1.10) demonstrated the highest tensile modulus.

The ultimate strength and elongation at break, as shown in Fig. 77c and d, followed a similar trend, except for sample S4. S4 exhibited an ultimate strength of 0.14 ± 0.01 MPa and an elongation at break of 23.18 ± 4.05%, indicating lower strength, flexibility, elasticity, and toughness compared to the optimal sample S3 (with a DVS-to-OH ratio of 0.83). This reduction in performance is likely due to rapid and uneven crosslinking throughout the gel, leading to regions with varying crosslink densities and creating inhomogeneities. Such inhomogeneities can cause phase separation within the gel, where denser, polymer-rich regions form. These regions may scatter light differently from the surrounding material, resulting in a change from transparency to a milky or translucent appearance, as seen in Fig. 58. Additionally, the reduction in porosity, as observed in the swelled gel in Fig. 61j, may result in decreased ability to accommodate stresses effectively.

Among the samples evaluated, S3 (with a DVS-to-OH ratio of 0.83) demonstrated the highest resistance to applied force, achieving an ultimate strength of 0.18 ± 0.02 MPa. At the breaking point, it exhibited a maximum elongation of 49.0 ± 2.7%. The observed toughness arises from the formation of a robust network facilitated by ether linkages between the hydroxyl groups of sacran and DVS vinyl groups. In contrast, an improper balance between DVS and OH leads to the creation of a less resilient structure,

diminishing its ability to withstand stress. For example, in sample S2, characterized by a DVS-to-OH ratio of 0.63, ultimate strength levels measured 0.11 ± 0.01 MPa, with a break point at 39.2 ± 2.0%. Similarly, sample S1, featuring a DVS-to-OH ratio of 0.43, demonstrated ultimate strength levels around 0.08 ± 0.01 MPa, with a break point at 32.5 ± 1.3%. These mechanical properties are attributed to the highly hydrophilic nature of the gels, as evidenced by the swelling behavior analysis (Fig. 76), which results in a less resilient polymer network. The sacran-ZnO nanocomposite xerogels exhibit mechanical properties that are 2-3 times stronger than those of sacran gel physically crosslinked by thermal treatment at 100°C.

In conclusion, the results indicate that S3, with its superior elongation at break, enhanced ductility, and higher ultimate strength, is the optimal choice for practical applications requiring toughness, flexibility, and durability. Its ability to withstand significant deformations and impacts makes S3 a more dependable option for further development and use.

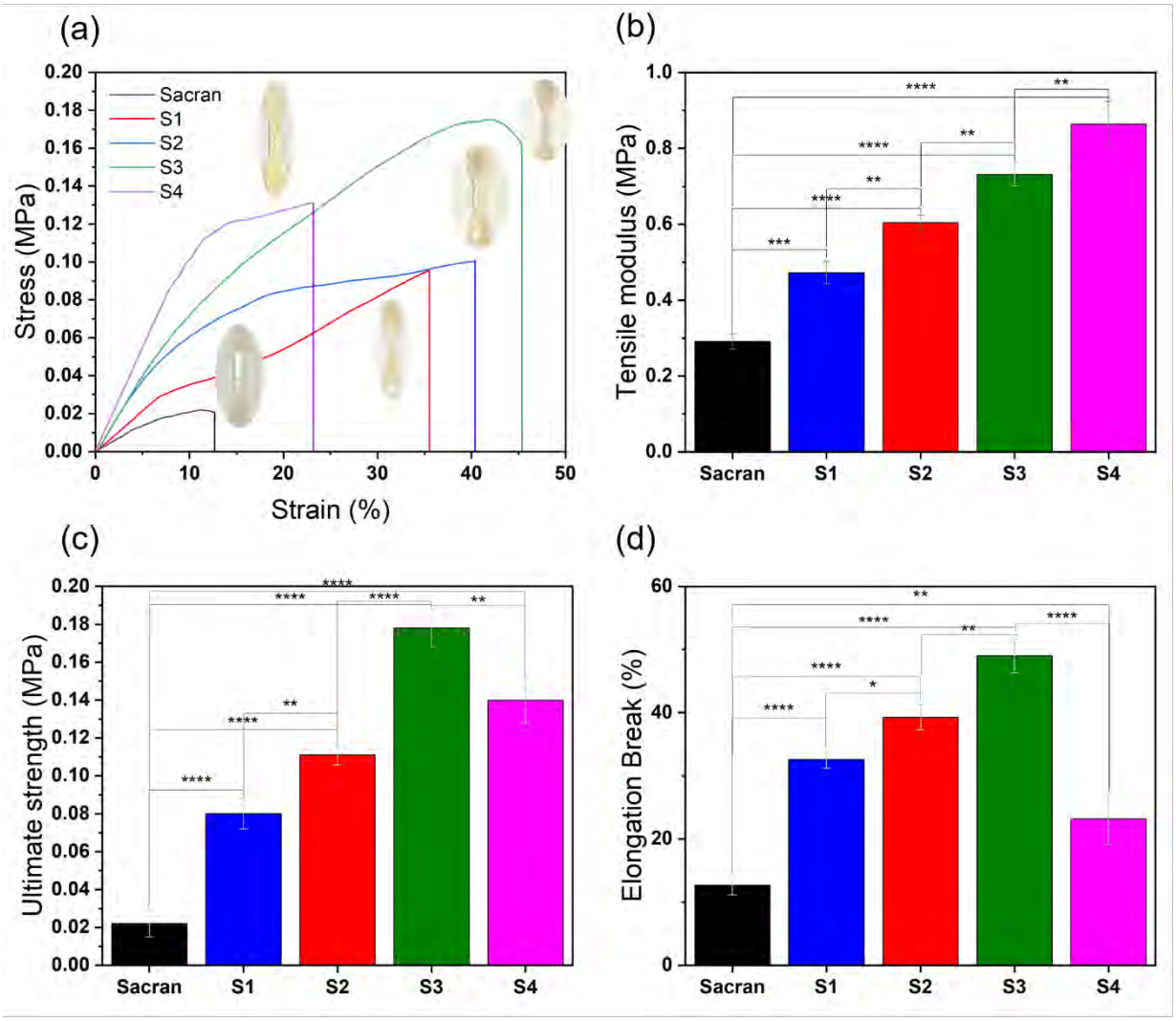

Fig 77. (a) The mechanical test of sacran-ZnO nanocomposite xerogels with different DVS-to-OH ratios 0.43 (S1), 0.63 (S2), 0.83 (S3), and 1.10 (S4) in their hydrated state; inset: actual samples. (b) Bar graphs representing tensile modulus. (c) Bar graphs indicating the ultimate strength. (d) Bar graphs indicating the elongation at break. Data are presented as mean ± standard deviation (n=4). Statistical significance was assessed using one-way ANOVA followed by Tukey's test, with significance levels indicated as ****p<0.0001, ***p<0.001, *p<0.05, and ns (not significant) compared to all other samples.

4.3.10. The Release of ZnO NPs through the Porous Structure of the Sacran-ZnO Nanocomposite Xerogel

The Sacran-ZnO nanocomposite xerogel, with a DVS-to-OH ratio of 0.83 and 20% w/w ZnO NPs, was selected as the sample to evaluate the release of ZnO nanoparticles (NPs). A graph was plotted to show the cumulative concentration of ZnO NPs over time, determining the total duration for complete ZnO NP leaching. The results indicated that all ZnO NPs were removed from the composite gel after 7 hours. The concentration of ZnO NPs in each xerogel was identified using the UV-vis technique and is displayed in the accompanying table.

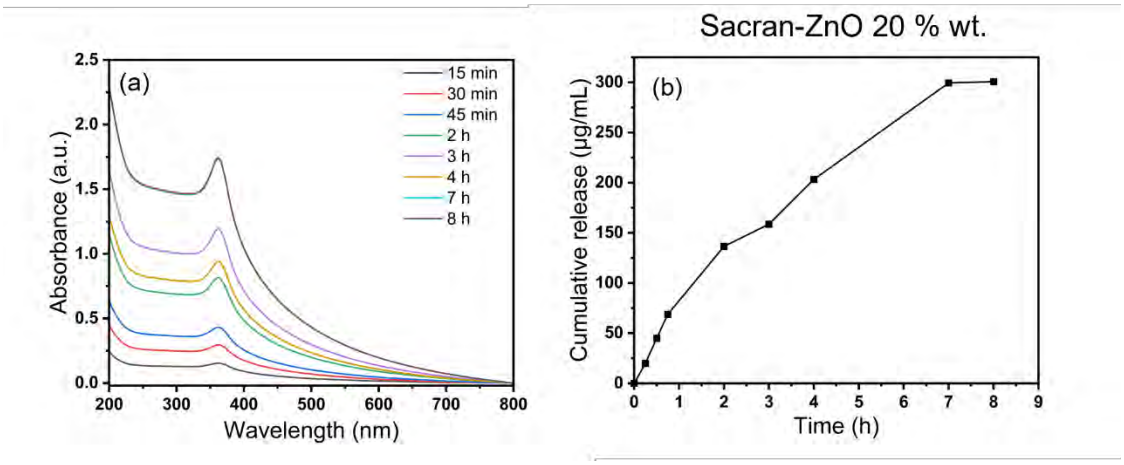

Fig. 78. UV-vis spectra of ZnO NPs released from the composite xerogel at 20% w/w over time (a), and the plot of cumulative ZnO NP release versus time (b).

Table 15. The concentration of each composite xerogel was estimated using the UV-vis technique

Nanocomposite xerogels	Concentration (µg/mL)
Sacran-ZnO 20 % wt.	300.6
Sacran-ZnO 15 % wt.	217.4
Sacran-ZnO 10 % wt.	173.5
Sacran-ZnO 5 % wt.	111.3
Sacran-ZnO 0 % wt.	0

4.3.11. Cytotoxicity and Cell Adhesion of Sacran-ZnO Nanocomposite Xerogels on Primary Dermal Fibroblasts (HDFa)

The adhesion capacity of sacran-ZnO nanocomposite xerogels with varying ZnO nanoparticle concentrations (0 to 20% w/w) was studied. After a 72-hour incubation period, the xerogels were stained with EthD-1, red fluorescence and calcein AM, green fluorescence to evaluate cell viability distribution. From literature reviews, it is evident that fibroblasts are generally tolerant to ROS generation from ZnO NPs compared to other types of cell-line such as carcinoma, and epithelial [122, 134]. We investigated the cytotoxicity of sacran-ZnO nanocomposite xerogels extraction toward normal cells (HDFa) and compared the results with cancellous cells (A549). HDFa cells exhibit lower cytotoxicity than A549 cells as displayed in Fig. 79a. This provides evidence that ZnO NPs are more likely to dissolve, releasing Zn^{2+} ions, which can be internalized by cells and cause cytotoxic effects, including mitochondrial damage in acidic environment. Other researchers have observed that using alginate containing ZnO nanoparticles or even ZnO nanofibers does not show toxicity toward human keratinocyte cells [122], [135], [136], [137]. Therefore, sacran-ZnO nanocomposite xerogels have high potential for selective toxicity toward cancer cells due to their unique microenvironment, unlike that of fibroblasts or keratinocytes. Fig. 79b shows that HDFa cells can grow and adhere to sacran-ZnO nanocomposite gels with less cytotoxicity compared to A549 cells. This is because the micro- and nanoscale patterns present in liquid crystalline structures mimic the extracellular matrix, providing a favorable surface topography for cell attachment, migration, and differentiation[138]. Under control culture conditions, HDFa cells exhibit a spread-out, elongated morphology, likely due to extensions of the cell membrane. However, fibroblasts adhering to sacran-ZnO nanocomposite xerogels with different ZnO concentrations show a more rounded shape due to differences in the mechanical properties of the gels compared to the rigid culture plate.

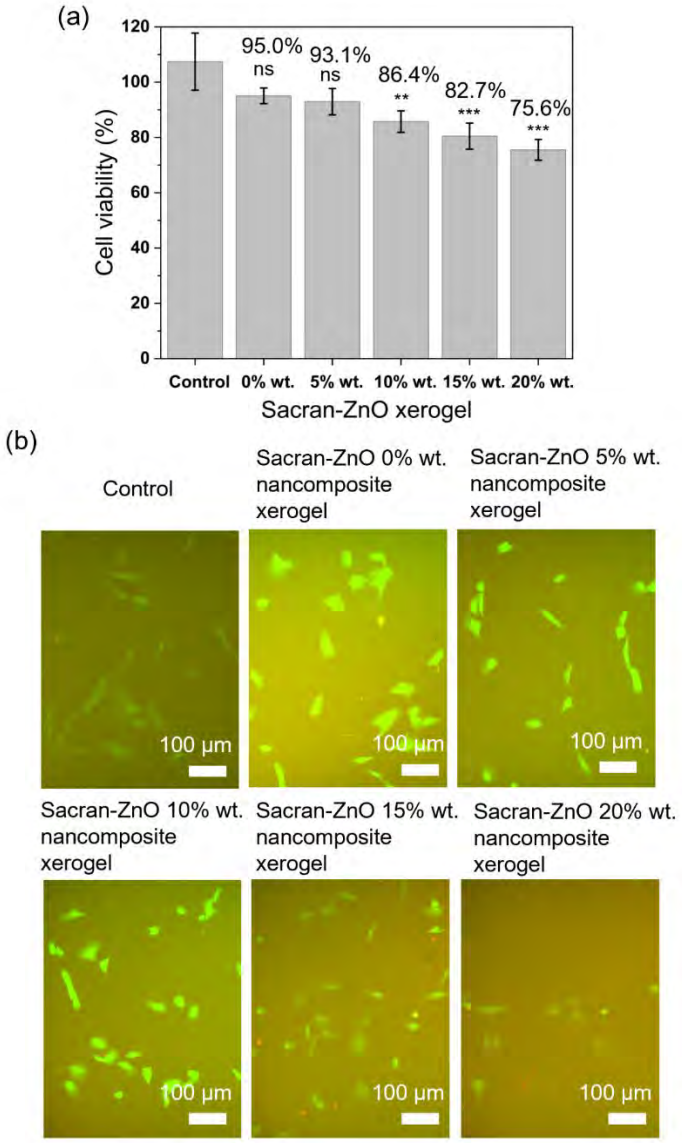

Fig. 79. Cytotoxicity test of sacran-ZnO nanocomposite xerogels with different ZnO wt% extracts on HDFa cells (a). Cell adhesion of HDFa cells on sacran-ZnO nanocomposite xerogels with different ZnO wt% (from 0 to 20% w/w) (b). Data are presented as mean ± standard deviation (n=4). Statistical significance was assessed using one-way ANOVA followed by Tukey's test, with significance levels indicated as ****p<0.0001, ***p<0.001, *p<0.05, and ns (not significant) compared to the control for each sample.

4.3.12. Cytotoxicity test of sacran-ZnO nanocomposite xerogels against human lung cancer cells (A549)

The findings from earlier sections indicate that sacran-ZnO nanocomposite xerogels exhibit superior mechanical stability, along with notable water absorbency, particularly when the DVS-to-OH ratio is 0.83. Therefore, we opted to utilize this specific xerogel and varied the concentration of ZnO nanoparticles to conduct cytotoxicity tests against human lung cancer (A549).

The sacran-ZnO nanocomposite xerogel, synthesized at a DVS-to-OH ratio of 0.83, was extracted with varying ZnO concentrations (0%, 5%, 10%, 15%, and 20% wt.) in 24-well plates containing cell medium (DMEM + 10% FBS). After 72 hours of incubation, the extracts were were introduced into 24-well plates with A549 cells and incubated for an additional 24 hours to assess cytotoxicity. Cell viability was measured using the MTT assay. The results revealed that incorporating varying concentrations of ZnO NPs into sacran xerogels influenced cell viability (Fig. 80a). Sacran xerogel without ZnO NP incorporation exhibited high compatibility with the A549 cell line, with cell viability at approximately 93.0%. However, sacran-ZnO nanocomposite xerogels with 5%, 10%, 15%, and 20% wt. of ZnO showed decreased cell viability, measured at 81.9%, 68.7%, 52.4%, and 25.5%, respectively.

A549 cells underwent staining with EthD-1, red fluorescence and calcein AM, green fluorescence to evaluate cell viability distribution. The results of cell staining, illustrating living and dead cells, are presented in Fig. 80b. The control group exhibited minimal cell death. In sacran gels with 0% wt. of ZnO nanoparticles, slight cell damage was observed, indicated by the presence of red dots, highlighting the high cell compatibility of sacran xerogels. Conversely, sacran nanocomposite xerogels containing different concentrations of ZnO nanoparticles exhibited an increasing number of dead cells as the ZnO weight percentage increased. Cells treated with sacran-ZnO nanocomposite xerogel containing 20% wt. of ZnO nanoparticles exhibited significantly higher numbers of dead cells (red dots), indicating the potential harmful effects of the extracts on A549 cancer cells. Therefore, sacran-ZnO nanocomposite xerogels hold promise for further applications as wound dressing material.

The underlying reason is that ZnO nanoparticles (NPs) can exhibit cytotoxicity in cancer cells due to the acidic environment. This environment can cause oxidative stress, the dissolution of ZnO NPs, Zn^{2+} internalization, and mitochondrial damage [134].

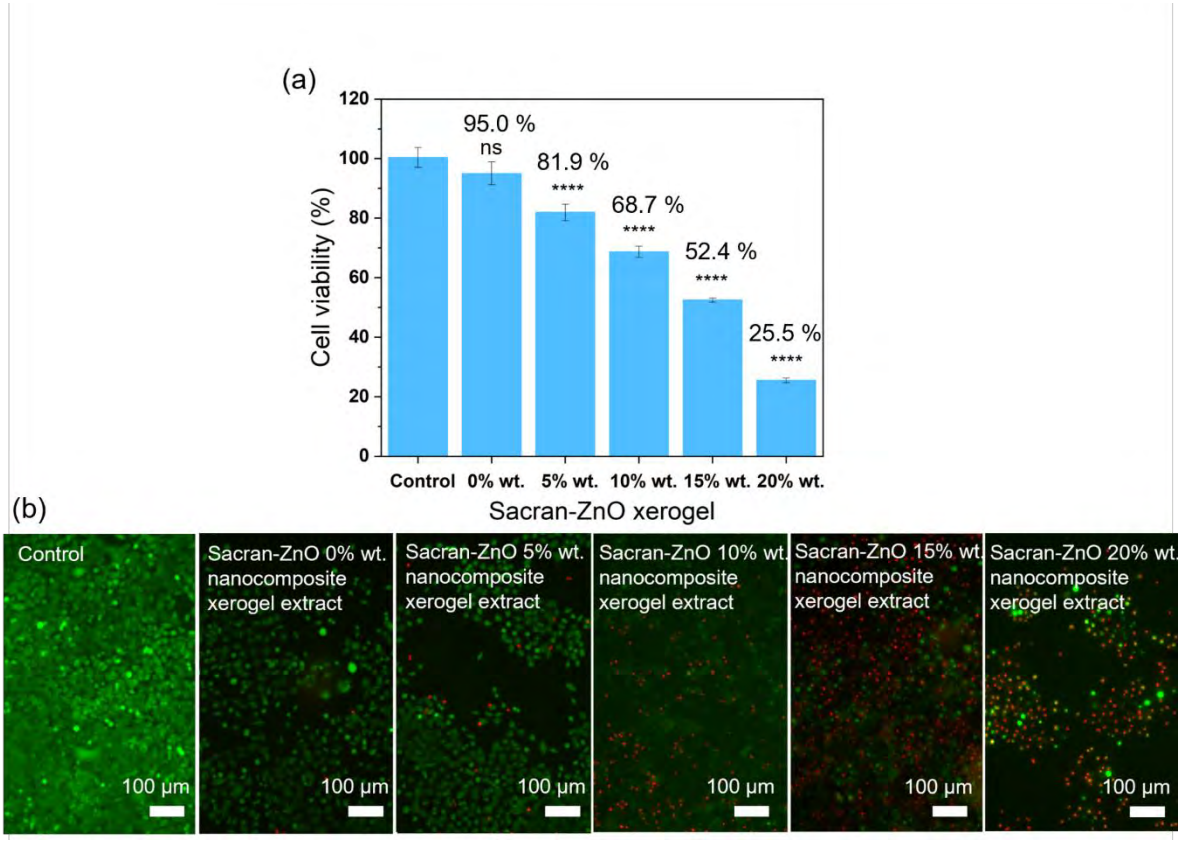

Fig. 80. Cytotoxicity test of sacran-ZnO nanocomposite xerogels with different ZnO wt% (a). Visual alive/dead A549 cells treated with sacran-ZnO nanocomposite xerogels with different ZnO wt% (from 0 to 20% w/w) (b). Data are presented as mean ± standard deviation (n=4). Statistical significance was assessed using one-way ANOVA followed by Tukey's test, with significance levels indicated as ****p<0.0001, ***p<0.001, *p<0.05, and ns (not significant) compared to the control for each sample.

4.4 Conclusion

The development and characterization of sacran-ZnO nanocomposite xerogels have shown promising potential for cancer-selective toxicity applications. Through a systematic investigation, it was observed that sacran could be utilized as the stabilizing agent in LC state for ZnO nanoparticle formation with sizes ranging from 25 to 70 nm. The incorporation of ZnO nanoparticles into sacran matrices significantly influenced the physicochemical properties of the resulting xerogels.

The swelling behavior of the sacran-ZnO nanocomposite xerogels was thoroughly studied, revealing the impact of pH variations on their performance. The presence of ZnO nanoparticles contributed to the overall swelling tendency, with higher DVS-to-OH ratios leading to decreased swelling rates, as indicated by the experimental results.

Mechanical testing demonstrated the importance of the DVS-to-OH ratio in determining the mechanical properties of the xerogels. Optimal ratios of 0.83 resulted in xerogels with enhanced tensile strength and resistance to applied stress, highlighting the significance of precise control over the crosslinking density during synthesis.

Cell viability studies conducted using primary dermal fibroblasts (HDFa) and A549 cancer cells provided valuable insights into the biocompatibility and selective toxicity of the sacran-ZnO nanocomposite xerogels. The results indicated varying degrees of cytotoxicity depending on the concentration of ZnO nanoparticles, with higher concentrations exhibiting increased toxicity towards cancer cells. In contrast, the gels did not negatively affect the dermal fibroblast cells. This suggests the potential of sacran-ZnO nanocomposite xerogels as a cancer-selective therapeutic material.

4.5 References

105. Fountoulaki, S.; Daikopoulou, V.; Gkizis, P. L.; Tamiolakis, I.; Armatas, G. S.; Lykakis, I. N., Mechanistic Studies of the Reduction of Nitroarenes by NaBH4 or Hydrosilanes Catalyzed by Supported Gold Nanoparticles. *ACS Catal.* **2014,** *4* (10), 3504-3511.

106. Arif, M.; Shahid, M.; Irfan, A.; Nisar, J.; Wu, W.; Farooqi, Z. H.; Begum, R., Polymer microgels for the stabilization of gold nanoparticles and their application in the catalytic reduction of nitroarenes in aqueous media. *RSC Adv.* **2022,** *12* (9), 5105-5117.

107. Kemas, C. U.; Ngwuluka, N. C.; Ochekpe, N. A.; Nep, E. I., Starch-based xerogels: Effect of acetylation on Physicochemical and rheological properties. *Int. J. Biol. Macromol.* **2017,** *98*, 94-102.

108. de Resende, M. A.; Pedroza, G. A.; Macêdo, L. H. G. M. C.; de Oliveira, R.; Amela-Cortes, M.; Molard, Y.; Molina, E. F., Design of polyurea networks containing anticancer and anti-inflammatory drugs for dual drug delivery purposes. *J. Appl. Polym. Sci.* **2022,** *139* (16).

109. Ibeaho, W. F.; Chen, M.; Shi, J.; Chen, C.; Duan, Z.; Wang, C.; Xie, Y.; Chen, Z., Multifunctional Magnetic Hydrogels Fabricated by Iron Oxide Nanoparticles Mediated Radical Polymerization. *ACS Applied Polymer Materials* **2022,** *4* (6), 4373-4381.

110. Islam, F.; Wong, S. Y.; Li, X.; Arafat, M. T., Pectin and mucin modified cellulose-based superabsorbent hydrogel for controlled curcumin release. *Cellulose* **2022,** *29* (9), 5207-5222.

111. Pei, Q.; Han, Q.; Tang, F.; Wu, J.; Xu, S.; Zhang, M.; Ding, A., Gallic-Acid-Modified Naphthalimide Containing Disulfide Bond as Reduction-Responsive Supramolecular Organogelator. *ChemistrySelect* **2022,** *7* (17), e202201296.

112. Cheeyattil, S.; Rajan, A.; Radhakrishnan, M., Curcumin-infused xerogel-based nutraceutical development and its 4D shape-shifting behavior. *J. Food Sci.* **2023,** *88* (2), 810-824.

113. Yu, Y.; Chau, Y., One-Step "Click" Method for Generating Vinyl Sulfone Groups on Hydroxyl-Containing Water-Soluble Polymers. *Biomacromolecules* **2012,** *13* (3), 937-942.

114. Mondal, S.; Das, S.; Nandi, A. K., A review on recent advances in polymer and peptide hydrogels. *Soft Matter* **2020,** *16* (6), 1404-1454.

115. Kong, J.-H.; Oh, E. J.; Chae, S. Y.; Lee, K. C.; Hahn, S. K., Long acting hyaluronate – exendin 4 conjugate for the treatment of type 2 diabetes. *Biomaterials* **2010,** *31* (14), 4121-4128.

116. Bae, J. W.; Lee, E.; Park, K. M.; Park, K. D., Vinyl Sulfone-Terminated PEG−PLLA Diblock Copolymer for Thiol-Reactive Polymeric Micelle. *Macromolecules* **2009,** *42* (10), 3437-3442.

117. Yadollahi, M.; Farhoudian, S.; Barkhordari, S.; Gholamali, I.; Farhadnejad, H.; Motasadizadeh, H., Facile synthesis of chitosan/ZnO bio-nanocomposite hydrogel beads as drug delivery systems. *Int. J. Biol. Macromol.* **2016,** *82*, 273-278.

118. Yadollahi, M.; Namazi, H.; Aghazadeh, M., Antibacterial carboxymethyl cellulose/Ag nanocomposite hydrogels cross-linked with layered double hydroxides. *Int. J. Biol. Macromol.* **2015,** *79*, 269-277.

119. Nagaraja, K.; Tae Hwan, O., Green synthesis of Multifunctional Zinc oxide Nanoparticles from Cordia myxa gum; and their Catalytic Reduction of Nitrophenol, Anticancer and Antimicrobial Activity. *Int. J. Biol. Macromol.* **2023,** *253*, 126788.
120. Wirunchit, S.; Koetniyom, W., ZnO Nanoparticles Synthesis and Characterization by Hydrothermal Process for Biological Applications. *physica status solidi (a)* **2023,** *220* (10), 2200364.
121. Ngatu, N. R.; Okajima, M. K.; Yokogawa, M.; Hirota, R.; Eitoku, M.; Muzembo, B. A.; Dumavibhat, N.; Takaishi, M.; Sano, S.; Kaneko, T.; Tanaka, T.; Nakamura, H.; Suganuma, N., Anti-inflammatory effects of sacran, a novel polysaccharide from Aphanothece sacrum, on 2,4,6-trinitrochlorobenzene–induced allergic dermatitis in vivo. *Annals of Allergy, Asthma & Immunology* **2012,** *108* (2), 117-122.e2.
122. Amornwachirabodee, K.; Okajima, M. K.; Kaneko, T., Uniaxial Swelling in LC Hydrogels Formed by Two-Step Cross-Linking. *Macromolecules* **2015,** *48* (23), 8615-8621.
123. Saosamniang, P.; Singh, M.; Ali, M. A.; Takada, K.; Okajima, M. K.; Kaneko, T., Gold nanoparticle morphology adjusted as high-performance catalyses in supergiant dispersant. *Surfaces and Interfaces* **2024,** *45*, 103904.
124. Elumalai, K.; Velmurugan, S., Green synthesis, characterization and antimicrobial activities of zinc oxide nanoparticles from the leaf extract of Azadirachta indica (L.). *Appl. Surf. Sci.* **2015,** *345*, 329-336.
125. Lin, B.; Chen, H.; Liang, D.; Lin, W.; Qi, X.; Liu, H.; Deng, X., Acidic pH and High-H2O2 Dual Tumor Microenvironment-Responsive Nanocatalytic Graphene Oxide for Cancer Selective Therapy and Recognition. *ACS Appl. Mater. Interfaces* **2019,** *11* (12), 11157-11166.
126. Ono, S.; Imai, R.; Ida, Y.; Shibata, D.; Komiya, T.; Matsumura, H., Increased wound pH as an indicator of local wound infection in second degree burns. *Burns* **2015,** *41* (4), 820-824.
127. Dodero, A.; Scarfi, S.; Pozzolini, M.; Vicini, S.; Alloisio, M.; Castellano, M., Alginate-Based Electrospun Membranes Containing ZnO Nanoparticles as Potential Wound Healing Patches: Biological, Mechanical, and Physicochemical Characterization. *ACS Appl. Mater. Interfaces* **2020,** *12* (3), 3371-3381.
128. Vandebriel, R. J.; De Jong, W. H., A review of mammalian toxicity of ZnO nanoparticles. *Nanotechnol Sci Appl* **2012,** *5*, 61-71.

129. High Resolution XPS of Organic Polymers: The Scienta ESCA300 Database (Beamson, G.; Briggs, D.). *J. Chem. Educ.* **1993,** *70* (1), A25.
130. Gobbo, P.; Mossman, Z.; Nazemi, A.; Niaux, A.; Biesinger, M. C.; Gillies, E. R.; Workentin, M. S., Versatile strained alkyne modified water-soluble AuNPs for interfacial strain promoted azide–alkyne cycloaddition (I-SPAAC). *Journal of Materials Chemistry B* **2014,** *2* (13), 1764-1769.
131. Elumalai, K.; Velmurugan, S., Green synthesis, characterization and antimicrobial activities of zinc oxide nanoparticles from the leaf extract of Azadirachta indica (L.). *Appl. Surf. Sci.* **2015,** *345*, 329-336.

132. Lin, B.; Chen, H.; Liang, D.; Lin, W.; Qi, X.; Liu, H.; Deng, X., Acidic pH and High-H2O2 Dual Tumor Microenvironment-Responsive Nanocatalytic Graphene Oxide for Cancer Selective Therapy and Recognition. *ACS Appl. Mater. Interfaces* **2019,** *11* (12), 11157-11166.
133. Ono, S.; Imai, R.; Ida, Y.; Shibata, D.; Komiya, T.; Matsumura, H., Increased wound pH as an indicator of local wound infection in second degree burns. *Burns* **2015,** *41* (4), 820-824.
134. Vandebriel, R. J.; De Jong, W. H., A review of mammalian toxicity of ZnO nanoparticles. *Nanotechnol Sci Appl* **2012,** *5*, 61-71.
135. Dodero, A.; Alloisio, M.; Castellano, M.; Vicini, S., Multilayer Alginate–Polycaprolactone Electrospun Membranes as Skin Wound Patches with Drug Delivery Abilities. *ACS Appl. Mater. Interfaces* **2020,** *12* (28), 31162-31171.
136. Paul, K. B.; Singh, V.; Vanjari, S. R. K.; Singh, S. G., One step biofunctionalized electrospun multiwalled carbon nanotubes embedded zinc oxide nanowire interface for highly sensitive detection of carcinoma antigen-125. *Biosens. Bioelectron.* **2017,** *88*, 144-152.
137. Yazdi, A. S.; Guarda, G.; Riteau, N.; Drexler, S. K.; Tardivel, A.; Couillin, I.; Tschopp, J., Nanoparticles activate the NLR pyrin domain containing 3 (Nlrp3) inflammasome and cause pulmonary inflammation through release of IL-1α and IL-1β. *Proceedings of the National Academy of Sciences* **2010,** *107* (45), 19449-19454.
138. Chi, L.; Wolff, J. J.; Laremore, T. N.; Restaino, O. F.; Xie, J.; Schiraldi, C.; Toida, T.; Amster, I. J.; Linhardt, R. J., Structural Analysis of Bikunin Glycosaminoglycan. *Journal of the American Chemical Society* **2008,** *130* (8), 2617-2625.

CHAPTER V

General Conclusion

The synthesis and application of sacran-based materials, particularly in the realm of nanocomposites, hold promising prospects across various fields. **In Chapter 2**, we explored the unique attributes of sacran, a supergiant polysaccharide, which plays a pivotal role in the controlled formation of anisotropic gold nanoplates (AuNPLs). Sacran's multifunctional properties, including its molecular weight, sulfate groups, carboxylates, and hydroxyl groups, enable it to function as both a reducing and stabilizing agent during AuNPL synthesis. The main factors influencing particle sizes are sacran-to-$HAuCl_4$ weight ratios and temperature, which can be tuned to control the size of AuNPLs. Interestingly, our findings indicate that higher concentrations of sacran, which typically serve as larger synthesis templates, did not necessarily result in larger sizes of AuNPLs, suggesting a negligible influence of the template effect. Moreover, sacran acts as a stabilizing medium for AuNPLs under extreme ionic and pH conditions, contributing to the uniformity of their properties and their potential applications in catalysis, sensing, and photothermal therapy. However, it's important to note that this simple method for AuNPL synthesis may not achieve high shape purity and uniformity.

Chapter 3 explores the collaborative role of sacran, monodispersed seeds, and iodide anions in both the generation and morphology control of gold nanotriangles (AuNTs). This innovative approach demonstrated sacran's proficiency as a dual-action agent, serving as both a reducing and stabilizing component, resulting in the production of highly uniform AuNTs with remarkable catalytic capabilities. The synthesis process, conducted at room temperature and easily adjustable for morphology control, represents a significant improvement over existing methods. The unique geometry of AuNTs, with their anisotropic structure, exposes a greater number of active sites for catalytic reactions. Their increased surface area enhances the interaction between the catalyst and reactants. Additionally, the sharp corners and edges of AuNTs generate strong localized surface plasmon resonances (LSPRs), leading to heightened electromagnetic field enhancement near the surface. This phenomenon promotes enhanced adsorption of reactant molecules and facilitates electron transfer during catalytic reactions, thereby boosting catalytic activity. Furthermore, the crystallographic facets of AuNTs, such as

(110) and (111), exhibit differing surface energies, which impact their surface reactivity. Certain facets may display higher catalytic activity due to their unique atomic arrangements and electronic properties, providing preferential sites for catalytic reactions compared to Au nanospheres (AuNSs), which are typically dominated by (111) facets. In contrast, Au nanospheres (AuNSs) synthesized using higher concentrations of sacran undergo surface reconstruction of surface atoms to achieve a more stable configuration and minimize surface energy upon the onset of catalytic reactions, such as with 4-nitrophenol. This process involves the exchange of sacran capping with reactant molecules, resulting in lower catalytic activity. The exceptional catalytic stability and performance of sacran-mediated AuNTs position them as promising candidates for various applications in biomedicine and plasmonic photothermal therapy.

In Chapter 4, the focus shifted to the development and characterization of sacran-ZnO nanocomposite xerogels for biomedical applications. Sacran demonstrated its efficacy as a green reducing agent for the formation of ZnO nanoparticles, with the resulting nanocomposite xerogels exhibiting enhanced physicochemical properties. The swelling behavior and mechanical properties of sacran-ZnO nanocomposite xerogels were systematically studied, emphasizing the importance of precise control over crosslinking density. Furthermore, cell viability studies revealed varying degrees of cytotoxicity, suggesting the potential of sacran-ZnO nanocomposite xerogels as wound dressing material.

In summary, the comprehensive characterization and evaluation of sacran-based materials presented in this study underscore their versatility and potential across diverse biomedical applications. From controlled synthesis of metal nanoparticles to the development of nanocomposite xerogels with tailored properties, sacran emerges as a valuable biomaterial with wide-ranging implications in biomedicine and beyond. Further exploration and optimization of sacran-based materials hold promise for addressing pressing challenges in drug delivery, tissue engineering, and other biomedical domains.

List of Publications

Journals:

First author:

- Saosamniang, P.; Singh, M.; Ali, M. A.; Takada, K.; Okajima, M. K.; Kaneko, T. *Surfaces and Interfaces* **2024,** 45, 103904.

- Chapter IV: under the preparation to submit.

Co-author:

- R. Urano, P. Saosamniang, T. Kaneko, M. Kawai, G. Joshi, T. Mitsumata, *Soft. Matter*. 2022, 18, 9242-9248.

Conferences:

1.Poster "Sacran reducers form gold nanoparticles with tuned size and morphology" Pruetsakorn Saosamniang, Maninder Singh, Maiko K. Okajima, and Tatsuo Kaneko. Centennial Hall, Kyushu University, Fukuoka, JAPAN**.** August 3-6, 2022.

2.Poster "Morphology control gold nanoparticles by functional supergiant polysaccharide sacran" Pruetsakorn Saosamniang, Maninder Singh, Maiko K. Okajima, and Tatsuo Kaneko. Spring 2019 71st Symposium on Macromolecules. Sapporo, Hokkaido university, JAPAN. September 5 – 7, 2022.

3.Oral "Morphology Control of Anisotropic Gold Nanoparticles by Mega-reducer of Polysaccharides with Dual Anions" Pruetsakorn Saosamniang, Maninder Singh, Maiko K. Okajima, and Tatsuo Kaneko. 13th SPSJ International Polymer Conference. Sapporo, Hokkaido, JAPAN. July 18-21, 2023.